REPUBLIQUE DU CAMEROUN
Paix-Travail-Patrie
****
UNIVERSITE DE YAOUNDE I
****
CENTRE DE RECHERCHE ET DE FORMATION DOCTORALE EN SCIENCES, TECHNOLOGIES ET GEOSCIENCES
****
UNITE DE RECHERCHE ET DE FORMATION DOCTORALE PHYSIQUES ET APPLICATIONS
****
P.O Box : 812, Yaoundé
Email : crfd_stg@uy1.uninet.cm

REPUBLIC OF CAMEROON
Peace-Work-Fatherland
****
UNIVERSITY OF YAOUNDE I
****
POSTGRADUATE SCHOOL FOR SCIENCE, TECHNOLOGY AND GEOSCIENCE
****
RESEARCH AND POSTGRADUATE TRAINING UNIT FOR PHYSICS AND APPLICATIONS
****
P.O Box : 812, Yaoundé
Email : crfd_stg@uy1.uninet.cm

Laboratory of Mechanics, Materials and Structures

NONLINEAR DYNAMICS OF AN HYBRID ENERGY HARVESTER SYSTEM WITH NON-SMOOTH BEHAVIOR AND FRACTIONAL PROPERTIES

Thesis

Submitted and defended publicly in fulfillment of the requirements for the degree of

Doctor of Philosophy in Physics

Option: **Mechanics and complex systems**

By

SENGHA Ghislain Gérard

Registration number: **11W1381**

Master of Science in Physics

Under the supervision of

KOFANE Timoléon Crépin

Professor

University of Yaoundé I

Year 2022

UNIVERSITE DE YAOUNDE I
UNIVERSITY OF YAOUNDE I

FACULTE DES SCIENCES
FACULTY OF SCIENCE

DEPARTEMENT DE PHYSIQUE
DEPARTMENT OF PHYSICS

ATTESTATION DE CORRECTION DE LA THESE DE DOCTORAT/Ph.D

Nous, Professeur **KENFACK JIOTA Aurélien** et Professeurs **BEN-BOLIE Germain Hubert, DJUIDJE KENMOE Germaine epse ALOYEM KAZE, NKAM TCHOUOBIAP Serge Eric** et **FEWO Serge Ibraid** respectivement Président et Examinateurs du jury de la Thèse de Doctorat/Ph.D de Monsieur **SENGHA Ghislain Gérard** Matricule **11W1381**, préparée sous la direction du Professeur **KOFANE Timoléon Crépin,** intitulée : « **La dynamique non-linéaire d'un système de récupérateur d'énergie hybride ayant un comportement discontinu et des propriétés fractionnaires**», soutenue le **Mercredi, 21 décembre 2022**, en vue de l'obtention du grade de Docteur/Ph.D en Physique, Spécialité **Mécanique et système complexe** attestons que toutes les corrections demandées par le Jury de soutenance ont été effectuées.

En foi de quoi, la présente attestation lui est délivrée pour servir et valoir ce que de droit.

Fait à Yaoundé le : ....22 DEC 2022.....

Les Examinateurs

Pr. BEN-BOLIE Germain Hubert

Pr. DJUIDJE KENMOE Germaine epse ALOYEM KAZE

Pr. NKAM TCHOUOBIAP Serge Eric

Le Président du Jury

Pr. KENFACK JIOTA Aurélien

Pr. FEWO Serge Ibraid

Le Chef de Département de Physique

UNIVERSITE DE YAOUNDE I
FACULTE DES SCIENCES
Le Chef de Département
DEPARTEMENT DE PHYSIQUE

Njaka Jean-Marie Emmanuel
Professeur

NONLINEAR DYNAMICS OF AN HYBRID ENERGY HARVESTER SYSTEM WITH NON-SMOOTH BEHAVIOR AND FRACTIONAL PROPERTIES

Submitted in partial fulfillment of the requirements
for the degree of Doctor of Philosophy (Ph.D.) in Physics
at the University of Yaoundé I

By

SENGHA Ghislain Gérard
Postgraduate School of Science, Technology and Geosciences,
University of Yaounde I, P.O. Box 812, Yaounde, Cameroon
Registration Number: ***11W1381***

Under the supervision of

Prof. Timoléon Crépin KOFANE
Professor, University of Yaounde I

"Il est bon d'attendre en silence le secours de l'Eternel."

Lamentations 3:26

Dedications

↬ *To my father SENGA André and my Mother DENGAMON Jeanne Suzanne;*

↬ *To my wife KATCHIAMATCHI Félicité Prudence;*

↬ *To my children SENGHA DENGAMON Kétia Rolissia De suze.*

Acknowledgments

- First of all, I thank the Almighty Lord for the strength he is providing me with and the mercy he is having on me since my childhood.

- Many thanks to Pr. KOFANE Timoléon Crépin, for his time, patience, for his constant encouragement and invaluable direction in the preparation of this thesis. This work wouldn't have made even a half as formidable door-stop without his pointed advices and valuable suggestions. His rectitude, his sympathetic attitude and his encouragements enabled me to broaden my knowledge and improve my research skill and capability. I am very grateful.

- I would like to thank each member of jury who has accepted to evaluate the present work. Many thanks to the president of jury, Pr. KENFACK JIOTA Aurélien and the honorable members, Pr. BEN-BOLIE Germain Hubert, Pr. DJUIDJE KENMOE Germaine epse ALOYEM KAZE, Pr. MKAM TCHOUOBIAP Serge Eric and Pr. FEWO Serge Ibraïd.

- I would like to thank the Pr. SIEWE SIEWE Martin, Pr. TABI Conrad Bertrand and my Mentor Dr. FOKOU KENFACK Wilson, for his continued support in the world of research. His intellectual and material contribution to this thesis is one of the factors of his success. I also salute his scientific rigor and dedication to science.

- I would like to sincerely thank all those who have dedicated their time to teach me a part of what they knew, from the primary school to the University, with a particular emphasis on the teaching staff of the Departments of Physics of the Universities of Yaounde I and Bangui.

- I am particularly impressed and grateful to my teachers Pr. WOAFO Paul, Pr.

TCHAWOUA Clément, Pr. NDJAKA Jean-Marie, Pr. SAIDOU, Pr. ZEKENG Serge, Pr. ENYEGUE A NYAM Françoise, Pr. BODO Bertrand, Pr. VONDOU DEBERTINI Appolinaire, Pr. ROUAUD, Pr. SISSA MAGALE Laurent, Pr. SILLA SEMBALA, Pr. MBOLIGUIPA Jean, Pr. NGANA Félix, Pr. SONGUELE Julien, Pr. OUMAROU SANDA, Pr. KONDJI Yvon, Dr. TSIOFACK, Dr. GOMPE, Dr. NDJI-VON Kluge Paul, Dr. MACKPAGNEN, Dr. BESSE Yvon, Dr. KOYANGBO Ghislain, Dr BOUANA Landry, M. Alain Pépin LOUMOUNDJI for their teaching and permanent encouragements.

- I wish to express my deepest obligations to my father SENGA André and my mother DENGAMON Jeanne Suzanne, who always pray for my success in all aspects of life. It is indeed because of their prayers and their financial supports that i have been able to achieve this work.

- Particular thanks to my cherished Mrs. SENGA, born FEINGUIZA Antonnette, SANWI Marie Annick, MALEGUEME Moise, YOMBO Jean-Claude, SENGHA DOWADIA Marlène, Mrs. NGANA, born LINDA Mireille Eulalie. SENGHA Arnold, SENGHA Aphrodite, SENGHA BADJI Vivien, SENGHA Bibi, SENGHA Fleurie, SENGHA Dieu-béni, SENGHA Jerry, SENGHA DENGUAMON Michael, SENGHA Morel, SENGHA Caleb, MALEKOUDOU Fleury Winner, GREGAM Marina,GREGAM Linéker, GREGAM Tchieng.

- I thank all my classmate from the Higher Teachers' Training College of Yaounde and Bangui.

- Fruitful discussions with my present Ph.D. mates are also to be appreciated: NDOUVADE Ulrich Vivien, NDOUGA Anatole, KOYANDOULOU Corneille, Dr. MOKEM FOKOU Igor, GAZAMBETI Yvon, Dr. NDJOMATCHOUA Frank Thomas, DONGMO TSOPGUE Patrice, Dr. NJOMON MBONG Thierry, Dr. GNINZANLONG Carlos Lawrence, Dr. FOUPOUAPOUOGNIGNI OUMAROU, Dr. EYEBE Guy Joseph, Dr. TEMGOUA DJOUATSA Diane, Dr. DJAZET Alain, Dr. FOPOSSI André-Marie, Dr. FOKOU Martin, Dr. ZAORO Rodax, Dr. OMON Yves, Mr. BISSA-HOLO Rufin.

- I thank my friends MBETIMANGUE Jean-Hermas, BEFIO Judith and the DOTE's familly.

- I am grateful to my colleagues of University of Bangui with whom spent a nice time during the development of this work.

- My deep gratitude goes to all my family (brothers, uncles, nieces, nephews, cousins, ...) and to my friends.

  Those whose names are not here mentioned shouldn't feel omitted.

Contents

List of Figures

Abstract

We study in this thesis a system with energy harvester behavior. First of all, this system is modeled by non-smooth coupled oscillators subjected to harmonic and random excitations, secondly by non-smooth coupled oscillators with fractional properties and subjected to harmonic excitation. We propose a modified harmonic balance method to study the dynamics of these oscillators under harmonic driving. Then, the probabilistic response of the system under bounded and colored noise excitations is tackled through the stochastic averaging method. We show that the proposed modified harmonic balance technique is very effective in parameters regime for which the system output waveform is nearly sinusoidal. In this parameters regime, the harvester performance is improved for optimum nonlinear magnetic coupling coefficients and for weak nonlinearities and damping in the harvester mechanical part. Under random excitations, we find in the weak parameters regime that, the probability density functions (PDFs) for the coupled oscillators amplitudes illustrate a single-peak mode and exhibit phenomenological transitions as the noisy excitations parameters vary. The mean output powers (MOPs) linearly increase with the colored noises intensities, and the piezoelectric MOP especially shows a resonance effect as the bounded noise level increases. Contrariwise, probed with Monte Carlo simulation, we find that the system exhibits the stochastic P-bifurcation for large parameters of coupling and nonlinearity; parameters' regime for which the harvester under purely harmonic driving demonstrates low performance. For the model accounting for fractional properties, we seek within this dissertation the effects of fractional derivatives' orders (FDOs) on the harvesting behavior of the system by the mean of the above harmonic balance method. Then, a numerical confirmation is obtained by the mean of the Newton-Leipnik algorithm. The FDOs effects on the chaotic response and their implication on the harvesting characteristic of the system are also analyzed. For low amplitude excitations,

it is found that, depending on the excitation frequency's band, the power generated by the mean of the electromagnetic transduction mechanism can be maximized either by increasing or reducing the order of the fractional derivative related to the electromagnetic circuit. Contrariwise, the performance of the piezoelectric conversion mechanism is improved by increasing the order of the fractional derivative related to the piezoelectric circuit, irrespective of the excitation frequency. For large amplitude excitations, proper choices of FDOs enable the system to exhibit a regular behavior instead of a chaotic one, so as to harvest a useful power of regular waveform.

Keywords: Electromechanical system; Stochastic averaging method; Stochastic P-bifurcation; Fractional derivative; Harmonic balance method; Chaos.

Résumé

Nous étudions dans cette thèse un système ayant un comportement de récupérateur d'énergie. Tout d'abord, ce système est modélisé par des oscillateurs couplés discontinus soumis à des excitations harmoniques et aléatoires, ensuite par des oscillateurs couplés discontinus avec des propriétés fractionnaires et soumis à une excitation harmonique. Nous proposons une méthode de balance des harmoniques modifiée pour étudier la dynamique de ces oscillateurs sous excitation harmonique. Puis, la réponse probabiliste du système soumis aux bruits borné et colorés est abordée par la méthode de la moyenne stochastique. Nous montrons que la méthode de balance des harmoniques modifiée proposée est adaptée dans le régime de paramètres pour lequel la forme d'onde de la réponse du système est presque sinusoïdale. Dans ce régime de paramètres, la performance du récupérateur est améliorée pour des coefficients de couplage magnétique non linéaire optimaux et pour de faibles non-linéarités puis des amortissements dans la partie mécanique. Sous des excitations aléatoires, nous trouvons dans le régime des paramètres faibles que les fonctions de densité de probabilité (PDF) pour les amplitudes des oscillateurs couplés illustrent un mode à pic unique et présentent des transitions phénoménologiques; lorsque les paramètres des bruits varient. Les puissances moyennes de sortie (MOP) augmentent linéairement avec les intensités des bruits colorés, la MOP piézoélectrique montre un effet de résonance lorsque le niveau du bruit borné augmente. A l'inverse, grâce à la simulation de Monte Carlo; nous constatons que le système présente une bifurcation phénoménologique pour de grands paramètres de couplage et de non-linéarité ; pour le régime des paramètres pour lequel, le récupérateur sous une excitation purement harmonique présente de faibles performances. Pour le modèle tenant compte des propriétés fractionnaires, nous recherchons dans cette thèse les effets des ordres des dérivés fractionnaires (FDOs) sur le comportement du récupérateur par la méthode de balance des harmoniques ci-dessus. De ce fait,

une confirmation numérique est obtenue à l'aide de l'algorithme de Newton-Leipnik. Les effets des FDOs sur la réponse chaotique et leur implication sur la caractéristique de récolte du système sont également analysés. Pour des excitations de faible amplitude, on constate que, selon la bande de fréquence de l'excitation, la puissance générée grâce au mécanisme de transduction électromagnétique peut être maximisée soit en augmentant soit en réduisant l'ordre de la dérivée fractionnaire liée au circuit électromagnétique. A l'inverse, les performances du mécanisme de conversion piézoélectrique sont améliorées en augmentant l'ordre de la dérivée fractionnaire liée au circuit piézoélectrique, quelle que soit la fréquence d'excitation. En ce qui concerne les excitations de grande amplitude, le choix approprié des FDOs permet au système de présenter un comportement régulier au lieu d'un comportement chaotique, de manière à récolter une puissance utile de forme d'onde régulière.

Mots clés: Système électromécanique hybride ; méthode de moyenne stochastique; Bifurcation phénoménologique ; dérivée fractionnelle; méthode de balance harmonique; Chaos

List of Abbreviations

FDOs: Fractional Derivatives' Orders;

PDFs: Probability Density Functions;

MOPs: Mean Output Powers;

RF: Radio Frequency;

VEH: Vibrational Energy Harvester;

NSB: Non Smooth behavior;

HEHNS: Hybrid Energy Harvester Non Smooth;

MENS: Micro Electromechanical System;

FO: Fractional Order;

General Introduction

In light of the abusive exploitation of natural resources to develop the economy and the galloping demography, the idea of sustainable development was proposed in the 1970*s* and has been put forward over the years. Sustainable development is defined as a mode of development that meets current needs without sacrificing the future for Meadows, Randers and Behrens [1]. This is possible through a rational management between man, nature and economy. Furthermore, with the effect of global warming, the need to reduce the carbon footprint has been promoted worldwide. This requires the replacement and modernization of current energy methods with methods that do not emit carbon dioxide (clean energy).

According to record (U.S. Energy Information Administration (EIA) International Energy Statistics 2010), 84% of current energy consumption is due to fossil fuels [2]. It is also predicted that stored fossil fuel will only last another 100 years if we do not change the way we produce energy. Therefore, according to British Petroleum and Royal Dutch Shell (Shell says record profits to be used to boost alternatives, 2006), by 2050, one-third of the world's energy will have to come from alternative energy sources, which is the only way to survive beyond the 21st century [3].

The literature contains hundreds of articles and several textbooks on developments in this research area [4–10, 12–19]. Alternative energy sources include biomass energy, wind energy, solar energy, geothermal energy, hydroelectric energy and mechanical vibration energy sources. The latter, mechanical vibration, is an attractive energy source in certain circumstances. The idea of harvesting energy using microelectromechanical systems (MEMS) has developed over the last two decades, with the development of miniaturized systems with micro-sensors placed on the structure. These sensors can provide information about the health of the structure, so that monitoring and control

are possible. For example, a sensor network can be applied to the bridge to assess its structural health. But to perform such an assessment, the sensors must be powered to send signals to the bridge structure and send the data back to the monitoring center.

Among the previous energy sources, vibration energy harvester (VEH) technology uses mechanical vibrations as the primary energy source, and the transduction mechanisms include electromagnetic [20, 21], piezoelectric [22, 23], triboelectric [24], and electrostatic [25–27]. This area of research has grown rapidly, both in the number of research papers and textbooks [4–10,13–19,28–35] and in the diversity of potential applications. The harvested energy can, in fact, be provided to a variety of low-power portable electronic devices to recharge their batteries or to enable remote operations [35]. Research in this area of scientific investigation is primarily aimed at improving the efficiency and performance of vibration energy sensors by seeking appropriate system design, using better materials and structures, and taking advantage of nonlinear phenomena.

To this aim, several researchers have used nonlinear effects to broaden the bandwidth of vibration energy sensors and thus improve the performance of the system. Erturk et al. [30], Harne and Wang [31], Vocca et al. [32] and Zhou et al. [34] to name a few, have reported that unlike linear sensors, nonlinear bistable sensors show promising results with improved frequency bandwidth. Therefore, the bistable configuration of their potential energy should be taken into account by the designer, as shown by Ramlan et al. [33]. Siewe and Buckjohn [36] and Stanton et al. [37] used Melnikov theory to study the performance of nonlinear bistable harvesters by analyzing the critical condition for homo-clinic bifurcation and inter-well dynamics as a function of system parameters. In fact, nonlinear bistable systems can exhibit, by instantaneous action, a large amplitude well-crossing motion with an increase in the harvested power benefit. The effects of random environmental fluctuations or noise on the performance of nonlinear sensors have also been widely studied [5, 7, 8, 38–40]. It has been recognized that the stochastic resonance phenomenon is advantageous for increasing energy production [7, 38–40]. Indeed, linear harvesters amplify ambient vibrations according to their natural frequency [29], but their efficiency decreases considerably in the vicinity of this frequency. Following Siewe et al. [4], we consider that the interaction between the mechanical and electrical parts of a harvester using an electromagnetic conversion mechanism is of a nonlinear type. This

assumption leads to nonlinear magnetic coupling between the two parts of the harvester considered in this dissertation.

Apart from nonlinearity, in nature, some systems have been modeled by differential equations with non-smooth behavior. Systems with non-smooth behavior or switching systems are ubiquitous in various research areas such as population dynamics [41–44] , control theory [45–48], tribology [49,50] for example, the modeling of such systems results in non-smooth differential equations. These systems have received much attention in the last two decades and several books have been devoted to them [51, 52]. In the context of energy harvesting systems, non-smooth models appear in studies of electromagnetic harvesters with plugs having impact characteristics [16, 53, 54].

In addition to taking into account nonlinear characteristics and non-smooth behavior (NSB) in the modeling of dynamical systems in general, and vibrational energy harvesting systems in particular, another way to develop more realistic models is to take into account the memory effect of certain materials through fractional derivatives. The FDOs date back to the time of Leibniz and L'Hospital, who both engaged in a controversy over the possibility of a non-integer order derivative. From that time to the present, considerable effort has been invested by scientists in establishing a solid foundation for fractional calculus, and hundreds of publications and textbooks [55–74] are now available in the literature on this subject. Many modern examples of its applications can be found in several scientific fields ranging from biology to robotics, and from chemistry to economics and finance. In physics, specifically in the field of vibrational energy harvesting, Fokou et al. [75] recently discussed the performance of a fractionally derived, nonlinearly damped piezoelectric loop beam subjected to a purely harmonic excitation. It was found that the order of the fractional derivative plays an important role in the response of the system. Foupouapouognigni et al. [76, 77] studied an electromechanical energy harvesting system with fractional properties subjected to harmonic excitation using the harmonic balance method. They showed that by increasing the order of the fractional derivative, the output power is maximized. Kwuimy et al. [78] considered an electromechanical system, acting as an energy harvester, with a fractional order (FO) current-voltage relationship for the electrical part and a fractional power law in the restoring force of its mechanical part. From their studies, it is found that the resonance amplitude of the mechanical vibration

depends significantly on the order of the fractional derivative. Cao et al. [59] considered a system with a fractional order viscoelastic material for an energy harvesting perspective and showed that the FO property of the material enhances both the high-energy chaotic motion and the inter-well periodic oscillation. These recent non-exhaustive developments in the field of vibrational energy harvesting show that taking into account hysteresis and/or the memory effect by the fractional derivative influences the system performance. It is therefore interesting to continue this analysis and study the effects of FO inductances on the response of our hybrid energy harvester with NSB and possessing a nonlinear magnetic coupling.

This thesis aims at investigating the effect of the nonlinear magnetic coupling on the efficiency of a class of hybrid VEH device whose mechanical damping possesses a NSB. It also investigates the effects on the harvested powers, of the parameters of non-smoothness and nonlinearities, under harmonic excitation, with the aim of determining parameters regime for which the device may be optimally designed. As other issue, this dissertation studies the effect on the harvested powers of environmental random fluctuations, which are inherent in the system. Moreover, we extend this study by accounting of fractional properties of some elements of the harvester's circuitry. We then investigate the effects of the fractional properties on the harmonic response of the system and study the consequence on energy harvesting. At last this thesis also explores the effects of fractional properties on chaotic regime of such a class of hybrid vibration energy harvester.

To reach the above mentioned aims, the remainder of this thesis is organized as follows:

♣ In chapter 1, we make a literature review and describe the state of the art on the batteries and the energy harvesting devices by insisting on the works achieved in the field of vibration energy harvesters. We describe the main transduction mechanisms and introduce terminologies used through out this dissertation such as *hybrid harvesters*, *non-smoothness* etc.

♣ The second chapter is devoted to the modeling and the methodology. In this chapter, we first of all provide the reader with the system description and the modeling assumptions, then both models used to study the energy harvesting system under consideration in this work are derived. At last, a methodology framework is provided, where we

present and develop analytical and numerical methods used within this dissertation.

♣ The last chapter presents our results with discussions. This chapter is divided into three sections: Firstly, we study the system harmonic and chaotic responses. Then, we secondly study the noise effects on the system response. The last section focuses on the fractional properties' effects on the system dynamics.

Finally, we end this work with a general conclusion in which we present our main results, then establish the scientific breakthroughs gained during this work as well as the prospects for future investigations.

Chapter 1

Literature review

Motivation of the study

The mechanical systems are subject to surrounding vibrations that could be exploited to harvest energy by using suitable generators. Since transducers convert mechanical energy into electrical energy, the energy produced could be stored and used in apparatus that do not consume enough energy for which autonomy is a priority.

Thus, the batteries that initially favored the development of portable electronic devices have become a brake on this progression, particularly because of maintenance problems. In the figure (Fig. 1.1) shows us the improvement in the performance of the components of portable computers between 1990 and 2003 on a logarithmic scale [12, 77]. This graph shows very clearly that the performance of the batteries evolves more slowly than all other components of the computer. Not only that the energy density is not an exponential evolution of time, but it even seems to reach a certain saturation. This trend poses a problem for the alternative energy source. It should be noted that these do not only stop on small devices but also they allow the use of energy in large devices, such as: Thermal sources, space foundries [79] etc. But the harvesting of small energies that can be used to automate devices that do not require enough energy is the major concern of researchers at this time when electronics is essential in everyday life [12, 77].

The VEHs systems mainly use three types of conversion: piezoelectric, electrostatic and electromagnetic. Electrostatic VEH are widely used for low power wireless applications and lend themselves to miniaturization through the use of MEMS [80]. But

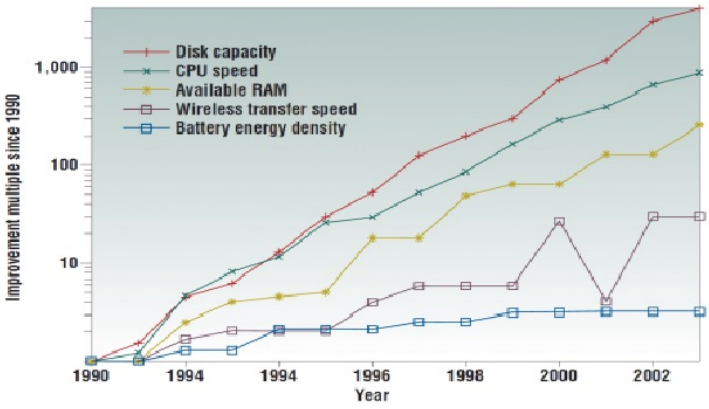

Figure 1.1: Increase of capability of various electronic capabilities over time [77].

we must not lose sight of thermoelectricity, photovoltaic. Each one has its advantages and disadvantages in relation to the vibratory source that gave birth to it and the space required. The energy harvester are generally designed to optimize the frequencies that correspond to those of the excitation. These mechanical resonators have a low damping (important quality factor), which causes a great loss of the electrical power collected as soon as a slight deviation of the excitation frequency from the resonance frequency occurs. In order to overcome these losses in systems with natural frequency control, a solution has been developed for these situations. This allows the use of energy conversion over a wide frequency range. Not only hybrid systems cause non-smooth, chaos in the systems, the introduction of non-linearities in these hybrid systems is the cause of discontinuity so that non-smoothness (NS) can significantly improve the efficiency, output voltage, which allows to increase the power of the systems.

1.1 Introduction

The harvesters energies are a technology destined to capture the energy coming from the surrounding (or from the human activity) to be able to transform it into energy to make devices work in autocracy. With this in mind, the world's concern is to reduce the pollution in the surrounding caused by the use of energy. Thus, the VEH is becoming a current research axis. This clean energy allows to reduce the consumption in electronic systems, which allows to self-power the sensors and the remote data acquisition systems.

In fact, in some situations the amplitude of vibrations can be large, for example, the vibrations of high civil engineering installations: buildings, bridges, railroads, we can add to that the ocean waves, the vibrations of vehicles and even human movements. Thus in this work, the objective is to recover the energies whose vibration amplitude is low enough for the use of electronic devices with low energy consumption (*wearable*) especially in micro electromechanical system ($MENS$). Currently, most of the VEH are linear. These harvesting have a low bandwidth in the vicinity of their resonance frequencies. Most ambient vibration frequencies vary randomly over a wide range of frequencies. Therefore, increasing the bandwidth of the harvesters energies is one of the most critical problems in practice. Therefore, the idea in this work is to use hybrid nonlinear and the harvesters energies non-smooth [81]. The systems that have been widely studied are mostly smooth. However, in this thesis we are interested in nonlinear and non-smooth hybrid systems. In this first chapter, we will start with a brief presentation of the history of the harvesting energy. Under the topic of the VEH, we will present some applications from radiation, human thermoelectricity, human movements. Also, the piezoelectric, electrostatic and electromagnetic conversions that take place in energy harvesters will be presented, as well as techniques and proven method for implementing fractional derivatives.

1.1.1 History in the harvester energy systems

In 1770, a French researcher named Abraham-Louis Perrelet, used the harvesting energy around the human arm movement to design a completely autonomous watch with an automatic pedometer winder. It was for the first time in the history of mankind that someone harvested energy produced in the environment [82] later in 1826 was the work of Abbot R. Haüy [83], for report on his work on mineralogy. Thomas Johann Seebeck found a current flowing in a closed circuit consisting of two different metals that are maintained at temperature gradients [84, 85]. The production of electricity from magnetism, known as electromagnetic induction discovered since 1831 in the work of Joseph Henry and Michael Faraday [86]. In October of the same year, Faraday invented the first direct current generator consisting of a copper plate rotating between magnetic poles [87]. After the work of Edmund Becquere in 1839 on the photovoltaic effect [88], the first large surface of the solar cell was built since 1894 by Charles Fritts which was coated with a

layer of selenium and a thin layer of gold [89]. After the development of quantum light theory and solid state physics in the 1900th [90], the photovoltaic effect became more accessible and understandable. Similarly, the basic thermoelectric effects were studied macroscopically, and their applicability to thermometry, power generation, and building refrigeration was innovated [90]. Energy harvesting has existed for centuries in the form of wind and water mills, passive solar energy systems [91], etc. In 1880, the first observation of energy harvesting was in the form of a charge. The couple Pierre and Jacques Curie proved experimentally that some crystals exhibit a superficial charge when subjected to mechanical stress. This phenomenon is called piezoelectricity [85].

The first step of mechanical-mechanical conversion is provided by a mechanical resonator allowing the conversion of mechanical vibrations harvester from the external environment (ambient or controlled) into a relative motion between the source of the vibrations and the mass. These vibrations are transmitted to an electromechanical device capable of converting them into electrical energy, but this energy is not directly exploitable, that is why an extraction circuit is mandatory to allow the conversion of the alternative electrical energy into useful electrical energy.

Finally, a storage device for the harvester energy is used to guarantee a durable operation of the device to be supplied even in case of absence of the source of vibrations. The VEH necessarily includes a mechanical structure, often in the form of a mass-spring system. Indeed, two types are possible for this type of generator, resonant and non-resonant:

- In the case of a resonant generator, it is used for applications where the amplitude of vibration is small compared to the possible displacement of the mass and the efficiency drops as soon as one moves away from the resonance frequency since the bandwidth is narrow [89].

-In the second case, i.e. the non-resonant generator, it is intended for applications with a large amplitude of vibration compared to the limit oscillation of the mechanical system and where the vibrations are distributed over a wide band towards the low frequencies [93]. Knowing the energy harvesting can also be from human and animal activity or through the environment as solar energy, wind energy, energy from the thermoelectricity of man. The mechanical harvester energy by these generators cannot be converted finally

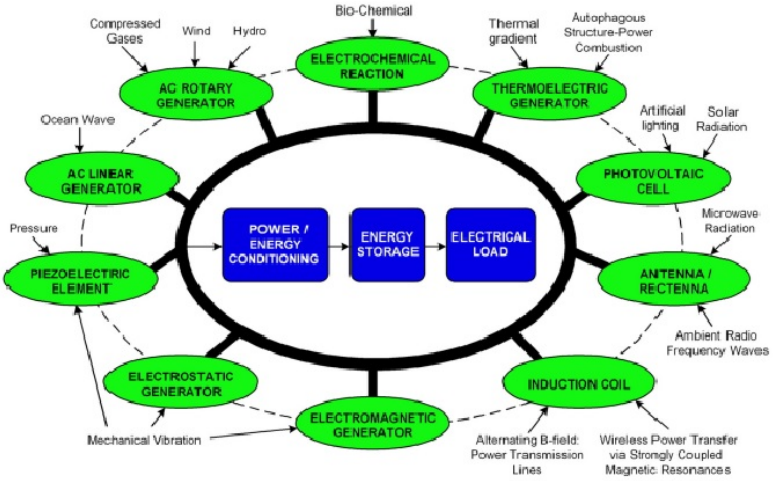

Figure 1.2: Representation of the different types of vibratory energy [92].

into electrical energy because of the energy losses (Fig. 1.2).

-For each harvester source, there is always a suitable energy converter to transform the input energy into useful energy of the desired form, classified into six main forms of conventional energy as: electrical energy, thermal energy, mechanical energy, nuclear energy, chemical energy and radiant energy Fig. 1.2.

1.1.1.1 Harvester energy from human activity

Humans can also produce energy from their activity, store and dissipate energy for consumption in portable electronic devices. The harvesting energy from human activity is a major concern that has prompted researchers as many devices are used, carried by or dragged by humans. Starner [94] and Turri and Poulin [95] have found in their human works on energy harvesting that the mechanical power developed during simple muscular activities such as typing on a computer keyboard, walking, turning a crank, hold with the hand produces energy. There are also many sources of energy harvesting from humans, such as breathing, arterial pressure to name only a few. This comparison justifies the idea of creating energy generating devices which allow to create electrical energy from a voluntary and specific movement of the man. Several examples of practical realizations are cited. These devices are generally conceived on the principle of the dynamo which uses a lever or a crank allowing to put in movement a generator of direct current.

The power generated can reach a few Watts which makes it possible to power most

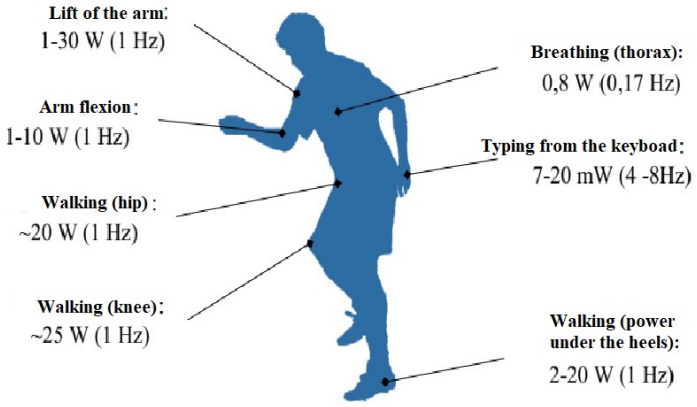

Figure 1.3: Energy losses due to mechanical conversions [96].

portable electronic systems. Niu et al [97, 98] have detailed that energy can be harvested by natural movements, it is the energy associated with the movement of the heels, the twisting of the joints or the displacement of the center of inertia of the body (Fig. 1.3).

1.1.1.2 The thermoelectricity

The difference in temperature between two points can be used to harvest energy by heat transfer. The Carnot cycle allows us to calculate the maximum theoretical efficiency of apparatus making use of such principale of device using such principale [99]. This efficiency is given by the relation (1.1), where T_c is the high temperature and T_a the low temperature. This expression shows that the efficiency is very low in the case of small temperature differences. For example, between a human body at $37°C$ and a room at $20°C$, we can not expect to obtain an efficiency greater than 5.5%.

$$P_s = h(T_c - T_a). \tag{1.1}$$

Nevertheless, (micro) generators have been developed in this case and their efficiency is generally less than 10% for heat transfers from $200°C$ to $20°C$ and less than 1% for heat transfers from $40°C$ to $20°C$ compared to this principle. Toriyama et al [77] have developed a micro-cell capable of delivering a few μW. Also, Douseki et al. [100] have developed an autonomous wireless communication system drawing its energy from the temperature difference between the ambient environment and the human body or cold water. For this application, the output power of the thermoelectric generator was 1.6

mW.

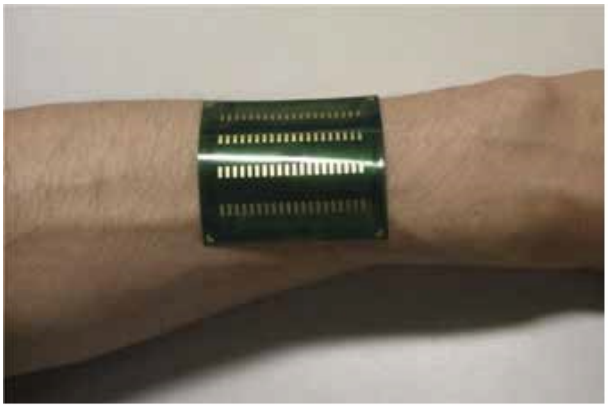

Figure 1.4: Hybrid prototype, fabricated on flexible substrate and taking advantage of both thermal gradient and solar energy [101].

Some industrial applications use thermoelectric generators. Among them is the hybrid prototype both thermal and solar see (Fig. 1.4). This watch uses 10 thermoelectric modules that generate enough microwatts to maintain the mechanical movement of the watch from the thermal gradient between the ambient air and the human body.

1.1.1.3 Harvester energy from radiation

The inhabitants of planet earth (both plant and animal) have been using energy from the sun since the beginning of their existence. There is also a large family of energy sources from radiation which are solar radiation in the visible range, infrared radiation, radio waves and nuclear emissions:

In Hamakawa's work, he summarizes the source is solar radiation can be converted directly into electricity from photovoltaic cells [102] see (Fig.1.5). The energy inputs of the light radiation are quite varied depending on the type of weather. For example, light rays are of the order of 10 to 100 mW/cm^2 for sunny weather and 10 to 100 mW/cm^2 in an office, and only 10 to 100 $\mu W/cm^2$ for artificial light (laboratory prototype on a smaller surface) [103]. These energies are harvested and converted into usable energy [104, 105]. It is also important to know that the efficiency of the cells varies between 10 and 25%, we can estimate that the power density generated by a photovoltaic generator varies between 10 $\mu W cm^{-2}$ (indoor) and 10-25 mW. cm^{-2} (outdoor).

Infrared radiation can be collected with solar panels adapted to this wavelength. It is usually emitted by very hot bodies (above 800K). This limits the usage possibilities to some very particular cases.

Hertzian waves (in other words, radio waves) can provide a significant amount of energy, provided that one is close to a transmitter. For this reason, the available energy decreases with the square of the distance separating the source from the generator.

$$p = \frac{E^2}{Z_0}, \tag{1.2}$$

With p the received power per cm^2 related to the electric field E and the radiation resistance of free space Z_0 (377Ω). For this Yeatman [106] gave the power for an electric field 1 V/m which is equal to 026 $\mu W/m^{-2}$ yet a nearby source did not exceed a few V/m. Thus, for a network with a large superficie, either extremely powerful sources are required (the question of the harmfulness of the electromagnetic bombardment then arises) or the network must be gridded with several sources.

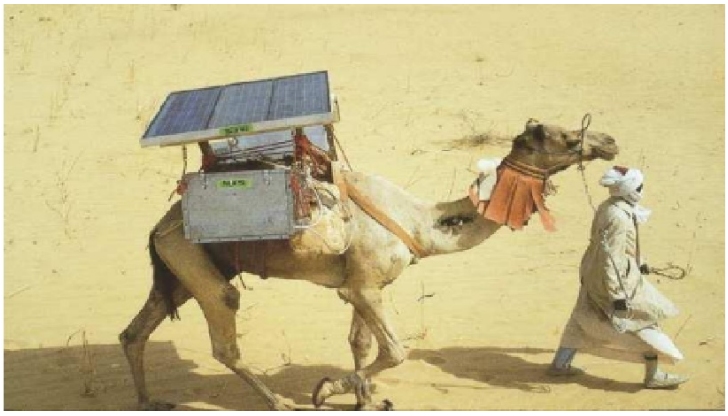

Figure 1.5: Example of a self-powered system [107].

Nuclear radiation also has rather limited applications. Natural sources are generally too weak to hope to power anything (on the order of $fW.cm^{-2}$). On the other hand, artificial sources can sometimes be used (this was for example the case in certain generations of pacemakers) with nevertheless the risks due to radioactivity that we know, for instance in the case of peamaker generators [108].

1.1.1.4 Harvester energy from wind

To obtain wind energy, the kinetic energy of the wind is used to create mechanical power. A generator converts this power into electricity so that it can be used for the benefit of humanity. Recently, there has been much debate among experts about the different types of electricity generation. There is no doubt that wind power is one of the pioneers of technological breakthroughs that could lead to more efficient energy production. On the face of it, the future of wind energy looks promising. This may be the case, but there are also disadvantages that need to be taken into account. The advantages of wind energy are more obvious than the disadvantages. The main advantages are an unlimited,

(a) Vertical wind turbine

(b) Horizontal wind turbine

Figure 1.6: Wind turbine.

free and renewable resource [77] (the wind itself), the economic value, the maintenance cost and the location of the wind harvesting facilities. First of all, wind is an unlimited, free and renewable resource, see Fig. 1.6. Wind is a natural phenomenon and harvesting the kinetic energy of the wind does not affect wind currents or cycles in any way. Secondly, harvesting wind energy is a clean and non-polluting way to generate electricity. Unlike other types of power installations, it emits no air pollutants or greenhouse gases. Their installations are very heavy and expensive then their elicits are dangerous with the birds.

1.2 Transduction techniques

The conversions of mechanical vibratory energy into electrical energy are ensured by several types of electromechanical transducers which vary according to the objective. Indeed, these transducers are based essentially on three techniques [29]: electromagnetic, piezoelectric and electrostatic.

1.2.1 Piezoelectricity and piezoelectric transduction mechanism

Piezoelectricity has been defined by Briscoe and Dunn [82, 109] as the application of a mechanical force on certain materials with piezoelectric characteristics which polarize, thus producing useful electrical power of the order of μW to $100mW$ and capable of powering certain electronic devices. Now, piezo means in Greek to squeeze, to press, hence some materials have the property to polarize under the effect of a mechanical stress [110]. We find this case in loudspeakers and piezoelectric folders; it is the direct effect. However, the reverse or reversible piezoelectric effect occurs under the effect of an applied electric field that deforms the material, which we find in sensors, accelerometers and microphones [111].

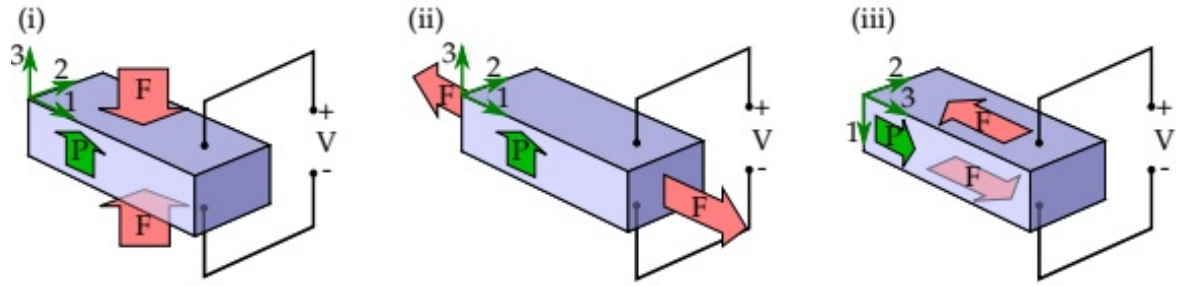

Figure 1.7: The direct piezoeletric effect [112].

One of the first applications of piezoelectric materials was the emission of ultrasound, for military purposes. Oscillators and filters based on piezoelectric crystals have been designed for applications in telephony and broadcasting. The first patent for the application of piezoelectric for non-destructive testing was filed in 1942. The first multi-element ultrasound probe for medical ultrasound was built in 1967. At this time,

the use of piezoelectric can be grouped into three families [113]: power applications, signal applications and ignition devices. In the first family we find sonars, machining and cutting devices, transformers and piezoelectric motors (Fig. 1.7). The second family includes ultrasound probes, non-destructive testing devices, as well as frequency references, loudspeakers and piezoelectric microphones. Ignition devices are a separate family. The role of the piezoelectric is to generate a spark by being stressed. In the different fields of application mentioned, piezoelectric can be used as sensors (microphones, ultrasound probes) or actuators (motors, speakers). The piezoelectric energy harvesters represent a new class of devices in the family of power family of power applications. In this case, we are talking about the use of piezoelectric materials as transducers, with the energy conversion efficiency in the foreground.

1.2.2 Piezoelectric transduction

Some piezoelectric materials are able to polarize electrically by applying a mechanical stress to [107, 110, 111, 114]. Exploiting this phenomenon, we find that most energy harvesting systems are based on the piezoelectric transducer, which is mathematically modeled by the thermodynamic principle [115, 116]. Therefore, the electrical behavior of piezoelectric materials are governed by Hooke's law [109] given by the relationship :

$$D = \varepsilon E, \tag{1.3}$$

where D is the charge displacement density, ε is the permittivity and E is the applied electric field. Hooke's law is defined by :

$$S = sT, \tag{1.4}$$

with S the strength, s is a compliance and T is a stress. From the following two equations, we have:

$$\begin{cases} \{E\} = \left[S^E\right]\{T\} + [d]\{E\} \\ \{D\} = [d^t]\{T\} + \left[\varepsilon^T\right]\{E\} \end{cases} \tag{1.5}$$

where $[d]$ is the piezoelectric matrix of the direct effect, $[d^t]$ is the matrix describing the inverse piezoelectric effect, E indicates the electric field of the system, T indicates a

strength field and t determines the transposed matrix. The piezoelectric coefficients; d_{ij}, e_{ij}, g_{ij}, h_{ij} are given by:

$$\begin{cases} d_{ij} = \left(\frac{\partial D_i}{\partial T_j}\right)^E = \left(\frac{\partial S_j}{\partial E_i}\right)^T \\ e_{ij} = \left(\frac{\partial D_i}{\partial S_j}\right)^E = \left(\frac{\partial T_j}{\partial E_i}\right)^S \\ g_{ij} = \left(\frac{\partial E_i}{\partial T_j}\right)^D = \left(\frac{\partial S_j}{\partial D_i}\right)^T \\ h_{ij} = \left(\frac{\partial E_i}{\partial S_j}\right)^D = \left(\frac{\partial T_j}{\partial D_i}\right)^S \end{cases} \tag{1.6}$$

Then we find the cohabitation of the direct piezoelectric effect and the inverse piezoelectric effect. A simplified method to describe the direct and inverse piezoelectric effects is represented by the electromechanical equation governing the behavior of piezoelectric materials namely [117] :

$$\begin{bmatrix} D \\ S \end{bmatrix} = \begin{bmatrix} d & \varepsilon \\ s & d \end{bmatrix} \begin{bmatrix} T \\ E \end{bmatrix}, \tag{1.7}$$

with the variables defined as follow:

-Electrical displacement or induction (C/m): $D = dT + \varepsilon E$

-Strain: $S = sT + dE$

-The complacency or elastic susceptibility (m^2/N): s

-The electrical permittivity (F/m) : ε

-The piezoelectric constant which expresses the proportionality between the charge and the deformation at zero or constant field (C/N) or (m/V) : d

-The electric field (V/m) : E

-The strength (N/m^2) : T.

When a piezoelectric energy generator is modeled, one of the characteristics that must be taken into account is the operating mode. Thus there are three piezoelectric operating modes [118, 119] :

-Transverse mode (d_{33} mode);

-Longitudinal mode (mode d_{31}) ;

- Piezotronic mode.

These different deformation modes of piezoelectric materials are the transverse mode d_{31} and the longitudinal mode d_{33}. The transverse mode is generally found on piezoelectric patches, where the electric field is perpendicular to the direction of me-

chanical stress, while the longitudinal mode is found on piezoelectric patches where the electric field and strength are collinear to the polarization [120]. The third mode of operation which is the piezotronic mode appeared with the discovery of nanotechnology (ZnO nanowire) with the n-type the conductivity [121]. This mode is due to the piezoelectric potential, a Schottky barrier is created between the piezoelectric nanowire and the electrode which regulates the flow of electrons [119]. Thus, the generator harvesting energy, it can be represented as a series circuit consisting of a voltage source with a capacitor. According to Thevenin and Norton's theorem, it can also be represented as a parallel circuit composed of a current source with a capacitor. If there is no charge displacement $D = 0$, we can conclude that the piezoelectric material is in open circuit. With respect to the equation (1.7) between the voltage and the electric field we have

$$V_{\infty} = -E \times h_p = \frac{d \times \sigma \times h_p}{\varepsilon} = -V_{cst} \times \sigma \times h_p, \tag{1.8}$$

where V_{co} is the open circuit voltage generated by the piezoelectric material, V_{cst} the constant voltage associated with the piezoelectric coefficient d by the relation :

$$d = \varepsilon \times V_{cst}, \tag{1.9}$$

For the parallel circuit, the short-circuit current can be obtained by short-circuiting the electrodes of a piezoelectric material and in the case where $E = 0$, the electrical displacement is obtained from the relation (1.7) where :

$$D = d \times \sigma, \tag{1.10}$$

The short circuit current (i_{cc}) which is proportional to the derivative is :

$$i_{cc} = \dot{D} \times S_p = d \times \dot{\sigma} \times S_p, \tag{1.11}$$

and the short circuit electrical charge is also proportional to the strength which is :

$$Q_{cs} = d \times \sigma \times S_p. \tag{1.12}$$

Most ambient mechanical vibrations have vibration frequencies below 100 Hz [122]. For this reason, the majority of the work focuses on piezoelectric transducers which normally operate at low frequencies, but the disadvantage of this type of transducer is the large size and their low power level.

1.2.3 Electromagnetic transduction mechanism

Electromagnetic induction is probably the best known of all electromechanical transductions: it is found at all scales of electrical energy production, from the simple dynamo for a pocket lamp to the nuclear power plant. Its fundamental operating principle is described by Faraday's law (or Lenz-Faraday):

$$e = \oint_c \overrightarrow{E} \cdot \overrightarrow{dl} = -\frac{\partial}{\partial t} \iint_s \overrightarrow{B} \cdot \overrightarrow{dS}, \tag{1.13}$$

This law describes the appearance of an "electromotive strength", $e = \oint_c \overrightarrow{E} \cdot \overrightarrow{dl}$, homogeneous to a voltage, along a closed contour in a fixed conductor (C) during the time variation of the magnetic flux

$$\phi = \iint_s \overrightarrow{B} \cdot \overrightarrow{dS}, \tag{1.14}$$

crossing the surface bounded by this contour. In other words :

$$e = -\frac{\partial \phi}{\partial t}. \tag{1.15}$$

This relation is also known in its local form, established by James Clerk Maxwell in 1861, which is one of the four fundamental laws of electromagnetism (Maxwell-Faraday law), given by :

$$\overrightarrow{rot}(\overrightarrow{E}) = -\frac{\partial \overrightarrow{B}}{\partial t}, \tag{1.16}$$

In practice, in an electromagnetic generator, a voltage is induced at the terminals of a coil crossed by a magnetic flux variable in time, which is the consequence of the relative movement between an inductor (like a permanent magnet) and an armature (coils), illustrated by Fig.1.8,

The electromagnetic energy harvester energy use permanent magnets to generate the magnetic flux (the alternative being to use active structures,

the electromagnets, which require an electrical supply). These magnets are made of "hard magnetic" materials, which have the particular property of being able to maintain a non-zero magnetic polarization even in the absence of external excitation. The magnetic field thus permanently generated is called the remanent field of the magnet, and can reach high values up 1.4 T for neodymium-iron-boron NdFeB magnets.

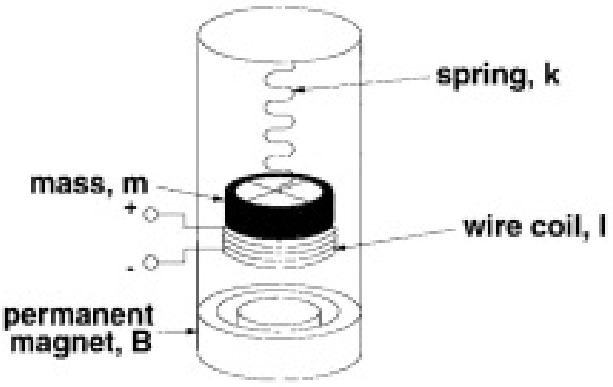

Figure 1.8: Electromagnetic generator from the Massachusetts Institute of Technology (R. Amirtharajah, P. Chandrakasan,...) made with discrete components [112].

1.2.4 Electrostatic transduction technique

An electrostatic transducer consists of a capacitor whose two charged plates can more away from each other under the effect of mechanical vibrations. The capacitance of this capacitor depends on its mechanical characteristics such as the area of overlap of the electrodes and the distance between the electrodes, it also depends on the dielectric material that separates the two plates. It is defined by the following expression:

$$C = \varepsilon_0 \varepsilon_r \frac{s}{d}, \tag{1.17}$$

with :

-ε_0: Permittivity of vacuum,

-ε_r: Permittivity of the dielectric between the two plates of the capacitor,

-s: The area of overlap of the armatures,

-d: Distance between electrodes.

As shown in equation (1.17), the capacitance C can be varied as a function of the dielectric permittivity or by varying the geometrical parameters (overlap area of the electrodes and inter-electrode distance) of the capacitor with the help of some mechanical movements of the transducer.

In this section, we are interested in the vertical and lateral movements which are the two most used mechanical movements in the literature. Two designs of electrostatic transducers appear in Fig. 1.9. Electrostatic transducers require a high potential difference to

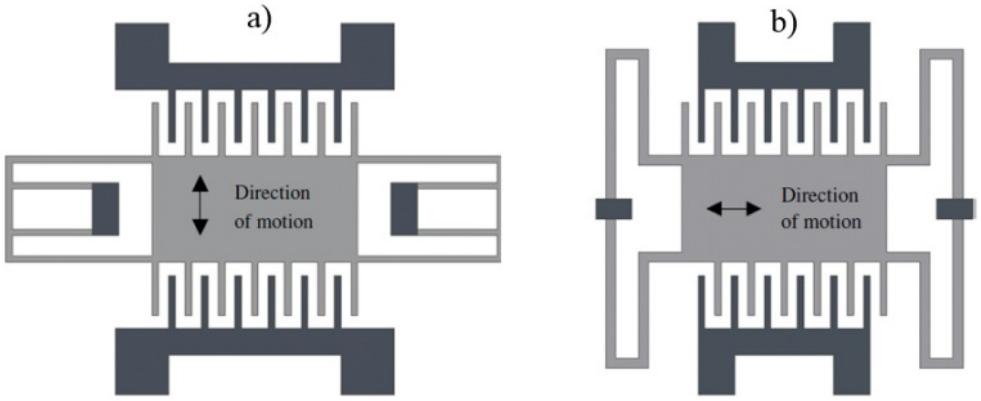

Figure 1.9: Two possible design realizations of electrostatic transducers depending on orientation of strain field for harvesting [77].

be maintained across the two sets of electrodes shown in light and dark in Fig. 1.9. As the transducer strains, the gap between the electrodes is changed, resulting in a change of capacitance

1.3 The hybrid harvester energy

1.3.1 Hybrid definition and general structures

By definition, a hybrid power system is a combination of at least two or more types of energy sources [11, 12, 77, 123–125]. Thus, they can be represented in Fig. 1.10. This is a rather general structure on which sources and loads can be added or removed depending on the topology of the system. It is the combination of thermal (fuel: petrol, diesel, oil...), electrical, piezoelectric, electromagnetic, electrostatic generators, batteries constitute the auxiliary sources.

The load is supplied by the power source for steady-state operation and high current demands are handled by the power source. In addition, for drive systems, the power electronics makes it possible to harvest energy during certain operating phases instead of dissipating it as heat.

Small-scale energy harvesting is one of the solutions to the problems of the growing number of portable devices [126, 127]. An inherent problem is the intermittent nature of

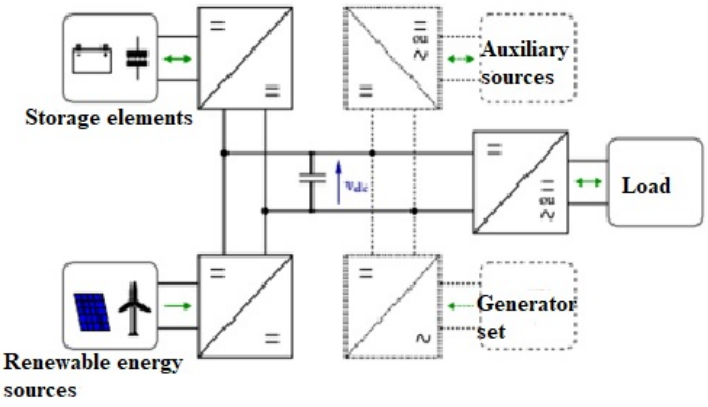

Figure 1.10: General structure of a hybrid electric system [132].

the ambient power source. It is possible that the operational reliability of portable devices may be compromised if the ambient power source is unavailable for a long period of time.

1.3.2 Hybrid piezoelectric and electromagnetic materials

The simplest integration of these technologies was seen in the work of Wischke et al. [128]. They proposed a piezoceramic bimorph cantilever beam configuration with magnets acting as tip mass. As the beam vibrated, the magnets passed through a coil. This configuration is unique because not only are two different technologies used, but each has its own resonance. If tuned appropriately, this type of hybrid technology can be very effective to the harvesting energy over a wider band. An effort has also been made to use the energy harvested by the magnet to tune the piezoelectric stiffness. Karami [129] developed a similar cantilever beam with piezoelectric patches near the base. The tip mass was also a magnet, but its unique configuration interacted with a fixed magnet to induce a voltage in a coil located between the two. The piezoelectric plates and the magnets attached to the tip harvested energy separately. This transducer had a natural frequency of about $10Hz$ and was capable of such a small resonance due to the large size of the beam 152mm length.

Foupouapouognigni et al. studied two systems harvesters and make comparison between the output power generated by the piezoelectric circuit, electromagnetic, they confirmed that the power harvest by the hybrid system was high [77]. Yang et al. in 2010 proposed a hybrid electromagnetic and piezoelectric energy harvester that used a can-

tilever structure containing multilayer piezoelectric materials as a beam, magnets as a tip mass and coils near the magnets [130]. They include type one and two, with magnetic pole direction using the z-axis and plane coils located in the horizontal and vertical plane. Type three has magnetic pole direction using along the y axis and the plane coil located in the vertical plane. Each prototype uses 2, 4 and 6 magnets. Consequently, the output power of type 3 devices with 6 magnets and 2.5 g acceleration at 310Hz frequency for piezoelectric mechanism and electromagnetic mechanisms are 176 W and 0.19 W respectively. Sang et al. in 2012 made a cantilever structure of hybrid energy harvesting system with maximum load power of 10.7 mW at the resonance frequency of 50 Hz and the acceleration of 0.4 g [131]. As a result, the output power from hybrid system with the optimal load of 50 increased by 81.4 in comparison to standalone electromagnetic mechanisms.

1.4 Fractional systems

The FO systems have received considerable interest in many areas of applied science and engineering. These systems are usually described by FO differential equations. Because of these irrational functions, fractional order systems have been marginally studied. As they do not have exact analytical solutions, numerical and approximation techniques are widely used for their solution, analysis and implementation. The FO modeling consists of describing the physical phenomena associated with devices whose behavior can be governed by partial differential equations.

The applications of the theory of fractional calculus in both basic science and engineering are very diverse [66, 134–136]. They are appearing more and more frequently in various fields of research. Electrical machines are ubiquitous components in electrical energy systems and networks, whether for generation (power stations) or for industrial or domestic use, including transport. With the increasing electrification of the main industrial fields, electric actuators can be found in high power networks as well as in smaller ones (embedded or island networks) [137, 138].

1.4.1 Fractional derivative in the circuit elements

Recent research contributions have shown evidence of mechanical elements and electrical components whose dynamics is well described by FO differential equations or FO power law. In fact, considerable amount of research in fractional calculus has been published in engineering and applied science literature. In a cylindrical shape [133] that here we follow classical derivation of the components of the circuit, while introducing generalized constitutive for D and B.

1.4.1.1 Fractional resistor

According to [133], they considered a lossy material in the form of a cylinder of length x and cross-section of area S. Assume a constant electric field in the direction of the cylinder axis z. The voltage $u(t)$ between the boundary of the cylinder is

$$u\left(t\right)=\int_{0}^{x}\varepsilon z dl=\varepsilon z x, \tag{1.18}$$

with the total current $i(t)$ is

$$i\left(t\right)=\int_{0}^{x}Jz dl, \tag{1.19}$$

with J the electric current density defined as:

$$J\left(x,t\right)=\lambda_{\alpha}D_{t}^{1-\alpha}\varepsilon\left(x,t\right), \tag{1.20}$$

where $0<\alpha\leq 1$. Assume (1.20) is valid is thus follows that

$$i\left(t\right)=S\lambda_{\alpha}D_{t}^{1-\alpha}\varepsilon\cdot z, \tag{1.21}$$

where S is the area of the section (1.21) can be rewritten as

$$i\left(t\right)=\frac{S\cdot\lambda_{\alpha}}{x}D_{t}^{1-\alpha}u\left(t\right), \tag{1.22}$$

so,

$$R_{\alpha}=\frac{x}{S\cdot\lambda_{\alpha}}. \tag{1.23}$$

it follows that the fractional resistor satisfies the Curie's law

$$i\left(t\right)=\frac{1}{R_{\alpha}}D_{t}^{1-\alpha}u\left(t\right) \tag{1.24}$$

Notice that if $\alpha=1$, we have the classical law

$$u=Ri. \tag{1.25}$$

1.4.1.2 Fractional inductor

Recall here in the previous subsection on electromagnetism, according to Ampere's law and faraday's law of induction, namely

$$i\left(t\right)=\oint H\cdot tdl, \tag{1.26}$$

$$\oint \varepsilon\cdot tdl=-\frac{d}{dt}\int_{S}B\cdot nds, \tag{1.27}$$

The corresponding generalized constitutive relation between the magnetic field intensity H and the magnetic field B is

$$\mu_{\gamma}H=D_{t}^{1-\gamma}B, \tag{1.28}$$

$0<\gamma\leq 1$.

For the inductor it is considered a toroidal frame of rectangular cross section. The inner and outer radii of the frame are r_1 and r_2 respectively, and the height is h. A coil consisting of n turns of wire is tightly wound on the frame. There is a current of magnitude $i(t)$, t . 0 in the conducting wire.

Set cylindrical coordinates such that the z-axis is the axis of symmetry and the frame is located between $r=r_1$ and $r=r_2$. Let C_r be a circular path within the toroidal frame of radius r with $r_1<r<r_2$. As customary, we assume axis symmetry so that the magnetic field $B\equiv B(r,z,t)$ only depends on r, z, t and where t is the unit tangent to C_r. By Ampere's law applied to the surface of the disc bounded by C_r, we have:

$$ni\left(t\right)=\int_{c_r}H\cdot tdl \tag{1.29}$$

Substituting B from (1.29) we obtain

$$\mu_\gamma n i\left(t\right) = D_t^{1-\gamma} \int_{c_r} B \cdot tdl. \tag{1.30}$$

After applicating of the Riemann-Liouville integral of order $1-\gamma$ we are led to

$$\mu_\gamma n J_t^{1-\gamma} i\left(t\right) = \int_{c_r} B \cdot tdl. \tag{1.31}$$

If B is the magnitude of the magnetic field in the direction of t,

$$\int_{c_r} B \cdot tdl = \int_0^{2\pi} B\left(r,z,t\right)dl = 2\pi r B\left(r,z,t\right), \tag{1.32}$$

hence

$$B\left(r,z,t\right) = \frac{\mu_\gamma n}{2\pi r} J_t^{1-\gamma} i\left(t\right), \tag{1.33}$$

Let us apply Faraday's law to one such surface S. Then the normal to this surface is $n = t$. So if $u_S(t)$ is the induced voltage

$$u_S\left(t\right) = -\frac{d}{dt}\int_S B \cdot nds \tag{1.34}$$

$$u_S\left(t\right) = -\frac{d}{dt}\int_0^h \int_{r_1}^{r_2} B\left(r,z,t\right) drdz, \tag{1.35}$$

$$u_S\left(t\right) = -\frac{\mu_\gamma n}{2\pi}\int_0^h \int_{r_1}^{r_2} \frac{1}{r} drdz \frac{d}{dt} J_t^{1-\gamma} i\left(t\right), \tag{1.36}$$

$$u_S\left(t\right) = -\frac{\mu_\gamma nh}{2\pi} \log\left({}^{r_2}\!/_{r_1}\right) D_t^\gamma i\left(t\right) \tag{1.37}$$

Let u be the total voltage dropped. Since there are n such coils, we have

$u\left(t\right) = L_\gamma D_t^\gamma i\left(t\right)$, this relation is a generalization of the governing equation of an inductor where $L_\gamma = \frac{\mu_\gamma nh}{2\pi} \log\left({}^{r_2}\!/_{r_1}\right)$.

1.4.1.3 Fractional capacitor

Following [133], consider two parallel plates confining a lossy material. Both plates have charge of equal magnitude but opposite sign. If distance between the plates is small compared with their size, there is no charge in the region between the plates. Charge

will reside mostly in the inner surfaces of the plates. The electric field is normal to the plates away from the edges, say in the x direction, and zero in the interior of the plates. Consequently, in the region between the plates the first Maxwell's equation

$$\nabla.D = \rho, \tag{1.38}$$

becomes

$$\nabla.D = 0. \tag{1.39}$$

We propose the constitutive law

$$D = \epsilon_\beta D_t^{1-\beta}\varepsilon, \tag{1.40}$$

since $\varepsilon = -\nabla\phi$, the potential $\phi(x, y, z) \equiv \phi(x)$ solves the equation

$$D_x D_t^{1-\beta} D_x \phi = 0, \tag{1.41}$$

we have

$$D_x \left(\frac{1}{\Gamma(\beta)} t^{\beta-1} D_x \phi \right) = 0, \tag{1.42}$$

and for $t > 0$,

$D^2\phi = 0$.

Let the plates be at $x = a$ and $x = b$. As customary, suppose that the potentials are constant on each plate and are $\phi(a) = u_a$ and $\phi(b) = u_b$

$$\phi(x) = \frac{(u_b - u_a) + bu_a - au_b}{b - a}, \tag{1.43}$$

$$\varepsilon = \frac{u_{ab}}{b - a}, \tag{1.44}$$

where $u_{ab} = u_b - u_a$.

Now choose δ such that $\delta << \mid b - a \mid$ and construct the cylindrical surface S_C, with axis in the x-direction. The plane top and bottom, of area S, are at $x = a + \frac{\delta}{2}$ and $x = a - \frac{\delta}{2}$.

From the integral form of equation (1.38) in the region confined by S_C we obtain

$$qS = \int_{S_C} D.nds \tag{1.45}$$

where q is the constant surface density of charge, positive on $x = a$. Let $u(t) = u_{ab}H(t)$ and $Q(t)$ the total charge on the frame at $x = a$, namely $Q(t) = qSH(t)$. From (1.40) and (1.44) we have

$$Q = \frac{\epsilon_\beta A}{b-a} D_t^{1-\beta} u. \tag{1.46}$$

We are led to a generalized governing equation of a capacitor

$$Q\left(t\right) = C_\beta D_t^{1-\beta} u\left(t\right), \tag{1.47}$$

with

$$C_\beta = \frac{\epsilon_\beta A}{b-a} \tag{1.48}$$

However, some floating fractional modeling coils and capacitor have been realized using massive ferromagnetic nuclei [77]. Also capacitors Fig. 1.11 are modeling in in chemical reactions between different materials shown in [139, 140], in fig(d)a new half-order capacitor based on fractal structures is modeled [141] and in (d), the values of α in the capacitor C are: $\alpha = 0.81$ and $C = 2.7nF$ [142].

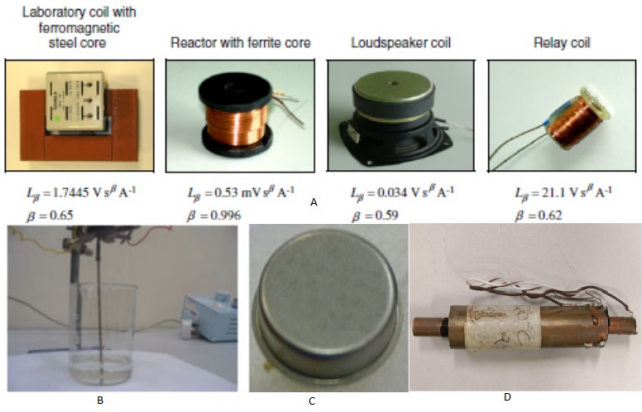

Figure 1.11: Floating fractional-order capacitor [77].

1.4.2 Brief review of fractional energy harvesting systems

Many recent studies revealed that FO nonlinear dynamical systems, in various applications, display rich and complex behaviors. Foupouapouognigni et al [76, 77] studied an electromechanical energy harvesting system with fractional properties subjected to harmonic excitation using the harmonic balance method. They showed that by increasing the

order of the fractional derivative, the output power is maximized. Bagley et al. [143, 144] pointed out that half-order fractional derivative models can quite well describe the frequency dependence damping of viscoelastic materials. Markris et al. [145] presented a fractional derivative Maxwell model for a viscous damper and validated their model using experimental results. Cao et al. [59] recently considered an energy harvesting system with FO nonlinear viscoelastic material. They showed that the FO property of the material enhances high-energy chaotic motion as well as inter-well periodic oscillation. Kwuimy et al. [78] proposed an electromechanical energy harvesting system with a fractional order current voltage relationship for the electrical circuit and fractional power law in the restoring force of its mechanical part. The authors showed that under a single-well potential configuration, for a small amplitude of the perturbation, as the order of derivative increases, the resonant amplitude of mechanical vibration decreases while the bending degree remains fairly constant. For a large amplitude of the perturbation, the output power increased, this is due to the hardening effects.

However, under a double-well configuration, the fractional power stiffness strongly affects the crossing well dynamics and consequently the output electrical power. Ducharne et al. [146] built and energy harvesting devices based on piezoelectric Ericsson cycles in a piezoceramic material. They showed that by coupling an electric field and mechanical excitation on Ericsson-based cycles, the amplitude of the harvested energy can be highly increased, and can reach a maximum close to 100 times its initial value. Kelly et al. [147] have applied the fractional Kelvin model to predict the seismic response of natural rubber bearings. Ngueuteu et al. [58] considered an electromechanical system having a fractional order capacitor and modeled by a FO Duffing-quintic equation. They studied its dynamics and synchronization, and concluded that the FO component can strongly affect the performance of the system, especially the route to chaos and the onset of synchronization. Atanackovic et al. [148] considered the forced oscillations of a rod having FO viscoelastic physical properties, Deng et al. [149] and Hosseini et al. [150] considered the stochastic analysis of column of viscoelastic material. They concluded that for both white noise and colored noise, the fractional order μ of viscoelastic materials plays an important role in the system stability.

1.5 Non-smooth systems, concept and definition

1.5.1 Concept and definition

Non-smooth systems are generally characterized by repeated vibrations and impacts between system components at mostly rough surfaces (Fig. 1.12). It has recently received more attention due to their high conversion efficiency, simple manufacturing, wide choice of materials, cost effectiveness and wide variety of applications [151].

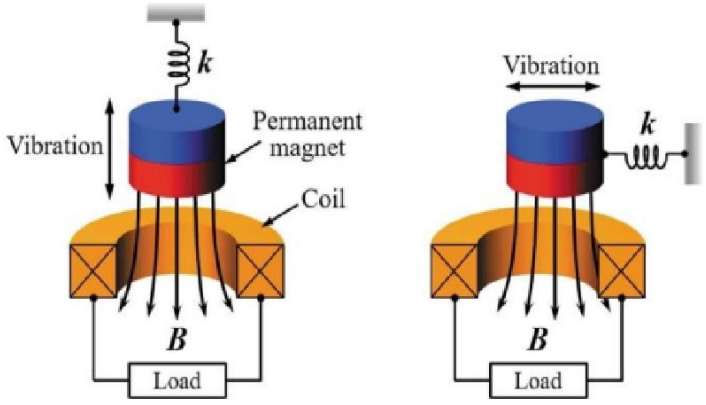

Figure 1.12: Schematic diagrams of a typical "Magnet in line coil electromagnetic energy harvesters (EEH)" and a typical Magnet across coil EEH proposed by Toshiyoshi et al. [159].

The non-smooth system appears in many engineering applications, such as hand-held percussion machines, pile-driving machines, periodic friction between rotor blades and stators in turbo-machinery, braking systems in automobiles, and cutting and grinding machines [152]. The non-smooth systems are complex nonlinear phenomena for which many models especially in systems with electromechanical couplings that accurately describe the transfer of energy from the mechanical domain to the electrical domain.

In this section, we will take inspiration from the magnetic levitation device proposed by Mann and Sims provided in Fig. 1.13 to describe the mathematical modeling and the equation of motion which will allow us to introduce the non-smoothness in the system. The modeling of the mechanical part of the Mann and Sims device is described by the figure below.

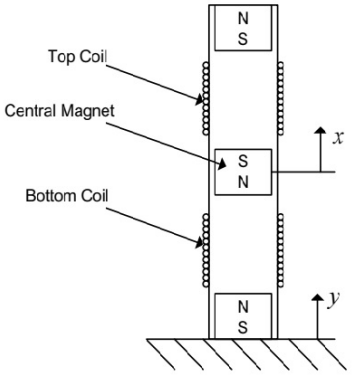

Figure 1.13: Device proposed by Mann and Sims [150].

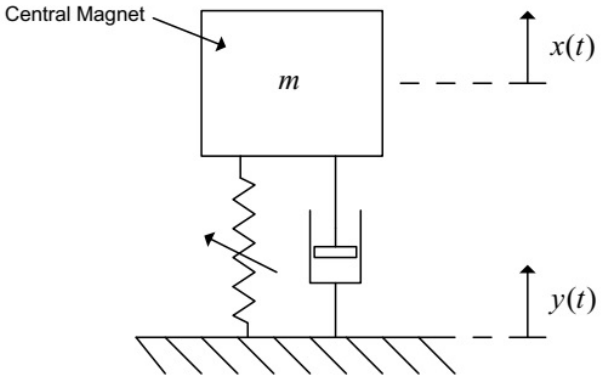

Figure 1.14: Schematic of energy harvester mechanical component [153].

Using the approaches of the mechanical component of the Mann and Sims device [153] shown in the figure (Fig. 1.14) above where the spring represents the nonlinear magnetic restoring force, the dashpot represents a viscous damper, and x and y represent the displacements of the central magnet and the base respectively. The equation of motion of this system is derived as follows:

$$m\ddot{x} = -c\left(\dot{x} - \dot{y}\right) - k_0\left(x - y\right) - k_1\left(x - y\right)^3 - mg, \tag{1.49}$$

where m is the mass of the central magnet, k_0 is the linear stiffness, k_1 is the cubic stiffness, c is the viscous damping, and g is gravity. This can then be rewritten in terms of relative displacement. By setting $z = x - y$, the equation of motion can be written as follows:

$$m\ddot{x} + c\dot{z} + k_0 z + k_1 z^3 = -mg, \tag{1.50}$$

It should be noted here that the magnetic restoring forces have been modeled as a third degree polynomia in [153]. In practice, models of dipolar, distributed or point-loaded magnets are available (see [154]). However, it will be shown in the following sections that a reliable model has been obtained through the use of the spring force with cubic nonlinearity.

1.5.2 Non-smooth modelling

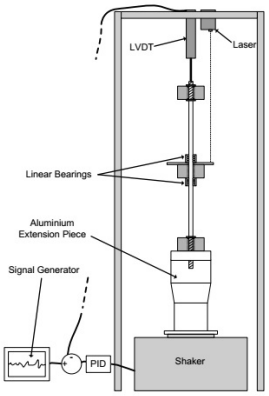

Figure 1.15: Schematic of experimental apparatus used to investigate the mechanical properties of the device [153].

It is agreed by Mann and Sims that after the first tests the response of the device was very sensitive to the effects of friction (non-smooth). This was despite the use of linear bearings to reduce the friction between the central magnet and the aluminum rod (as shown in Fig. 1.15). Therefore, the equation of motion of the device was rewritten as follows

$$m\ddot{x} + c\dot{z} + k_0 z + k_1 z^3 + F = -mg, \tag{1.51}$$

where F has been chosen to represent the force on the central magnet due to friction witch are many models. Among these, Coulomb, hyperbolic tangent... The Coulomb friction model have the properties non-smooth.

Knowing that Coulomb's damping model was used to reproduce the friction present in the system and among his oldest and best known friction models, is the restoring force due to friction, given by the following friction formula :

$$F = F_c sgn(\dot{z}) \tag{1.52}$$

where F_c is a parameter to be identified and sgn represents the sign function :

$$sign\,(\dot{z}) = \begin{cases} 1 & \text{if } \dot{z} > 0 \\ -1 & \text{if } \dot{z} < 0 \end{cases} \tag{1.53}$$

With 1 if $\dot{z} > 0$, -1 if $\dot{z} < 0$ only one parameter, the obvious advantage of the Coulomb damping model is its simplicity, although it is unable to model some of the phenomena that are typically associated with systems subject to friction (this is discussed further with respect to the LuGre model [155]). In addition, the non-smoothness of the sign function at zero can make the analysis difficult.

It is interesting to note that some systems deliberately exploit discontinuities, while others attempt to avoid them. For example, percussion and pile-driving machines utilize discontinuities, while turbomachines and braking systems are designed to avoid discontinuities. However, examples of non-smoothness systems can be found in almost all types of vibration-based harvesting energy. Yamapi et al. [54] considered the dynamics and chaos control of a self-sustaining electromechanical device with and without discontinuities and found that there is room for improvement in the results obtained in their device. Savi et al. [156] exploited non-smoothness for harvesting energy based on piezoelectric vibrations, using non-smooth nonlinearities to obtain a broadband harvesting system. Frequency response analysis has shown the sensitivity of the generated power to the stiffness of the support and the gap, which contribute to defining the energy harvesting capability. Ottman et al. [157] have analyzed a non-smooth current converter to obtain a power-cycle relationship. Using the parameters of the piezoelectric element and the converter, it is possible to determine the optimal duty cycle where the power harvested is maximum for the level of mechanical excitation. Weiss et al. [158] studied a vibrational energy sensor between two elasto-plastic main oscillators and coupled to a nonlinear energy sink with a non-smooth potential. This sensor shows a satisfactory result of a harvested power of

about 325%. Triboelectric [159] sensors mostly characterized by the non-smoothness give very satisfactory results in energy harvesting.

1.6 Conclusion

In this chapter, a detailed review of ambient energy sources and some transduction mechanisms were presented in order to understand the concepts and techniques of energy harvesting. The system under consideration in this thesis possesses a hybrid conversion mechanism and exploits the non-smoothness and fractional property to harvest energy. In Chapter II, we will present a modeling of the different studied systems as well as the analytical and numerical methods used in this thesis.

Chapter 2

Model and methodology

Introduction

The present chapter aims at deriving a model of peculiar energy harvesting apparatus which possesses a damping with non-smooth behavior, then at providing another model which, in addition, accounts for fractional properties of the inductances within the device. This chapter also aims at discussing the analytical and the numerical methods used in order to study the models' responses and to analyze the harvesting behavior of the system. To reach these aims, fundamental laws namely the Newton's second law of motion and the Kirchhoff's laws are used for modeling. We next provide the analytical developments based on the above mentioned models and the main numerical methods used in this work.

2.1 Modeling of the non-smooth type hybrid energy harvesting device

We consider in this work an electromechanical device. Precisely, the system under consideration is a hybrid energy harvester making use of both electromagnetic and piezoelectric conversions and whose mechanical part possesses a damping with discontinuous behavior. This device is sketched in Fig. 2.1. We derive in the following paragraphs two mathematical models to study the dynamics of this device.

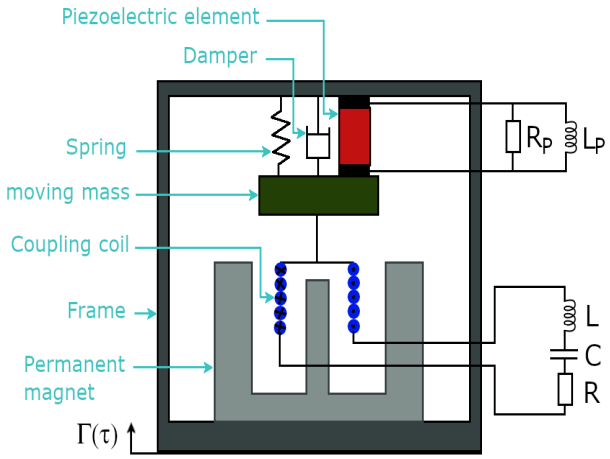

Figure 2.1: Sketch of the energy harvester.

2.1.1 The first mathematical model

The mechanical part of the device is composed of a suspended mass m, whose motion is determined by the inherent forces of the damped mass-spring system and the inertial forces acting on the system. $\Gamma(\tau)$ is the time-dependent acceleration of the frame (or base). From the Newton's second law, the motion of the mass is described by Eq. (2.1)

$$m\frac{d^2X}{d\tau^2} = -\mu_0\frac{dX}{d\tau} - F_P + F_L - m\Gamma(\tau), \tag{2.1}$$

with X the relative displacement of the mass with respect to the frame; F_P the global restoring force due to the spring and the piezoelectric element; F_L the Laplace force; $-m\Gamma(\tau)$ the inertial force and $\mu_0\dot{X}$ the damping forces originating from friction, air resistance, etc. As the simplest and the mostly used model of the friction is discontinuous [54, 153], in the present system, the magnitude of the damping forces also depends on the movement direction of the suspended mass in such a way that $\mu_0 = \begin{cases} \mu_0^+ & \text{if } \dot{x} > 0 \\ \mu_0^- & \text{if } \dot{x} < 0 \end{cases}$. The discontinuity is due to the intrinsic characteristics of the device.

The electrical part consists of two components: the piezoelectric and the electromagnetic circuits. The piezoelectric circuit is formed of the piezoelectric element, an inductor with inductance L_P and the load resistance R_P. However, the electromagnetic circuit consists of a linear inductor L, a linear capacitor of capacitance C, and a linear resistor R. Using the Kirchhoff's laws, these two circuitries can be described by the

following equations:

$$i_P = \frac{v}{R_P} + \frac{1}{L_P}\int v d\tau, \tag{2.2a}$$

$$L\frac{d^2q}{d\tau^2} + R\frac{dq}{d\tau} + \frac{1}{C}q + E_L = 0, \tag{2.2b}$$

where i_P and v are respectively the current and the voltage across the electrodes of the piezoelectric element, E_L the Lenz electromotive voltage and q, the instantaneous electrical charge.

The harvester's mechanical part and electromagnetic circuit interact through the air-gap of a permanent magnet which creates a radial magnetic field $\vec{B}$. The relationship between the magnitude B of that magnetic field and the coil position (related to X), established by Tomlinson [160], is given as:

$$B = B_0\left(1 - \left(\frac{X + X_0}{X_{\max}}\right)^2\right), \tag{2.3}$$

where B_0 is the highest intensity that the field B reaches, X_0 is the armature initial position, and X_{max} is the maximum amplitude. Thence, the motion of the mechanical part should take into account the relationship between the Laplace force and the current given by

$$F_L = \alpha_0\left(1 - \left(\frac{X + X_0}{X_{max}}\right)^2\right)\frac{dq}{d\tau}, \tag{2.4}$$

and the expression of the global restoring force [161], namely

$$F_P = \left(k_0 X + k_1 X^2 + k_2 X^3 + \alpha v\right). \tag{2.5}$$

k_0 is the global linear stiffness of the system's mechanical part. Parameters k_1 and k_2 define the nonlinearity of the spring. In the electromagnetic circuit, the Lenz electromotive voltage E_L is defined as:

$$E_L = \kappa_0\left(1 - \left(\frac{X + X_0}{X_{\max}}\right)^2\right)\frac{dX}{d\tau}, \tag{2.6}$$

while the current i_P, across the piezoelectric element, is related to the mass displacement X by:

$$i_P = \alpha\frac{dX}{d\tau} - C_P\frac{dv}{d\tau}. \tag{2.7}$$

Parameters α and C_P have been thoroughly defined in [18]. They are respectively referred to as *force factor* and *blocking capacitance* of the piezoelectric insert. α_0 and κ_0 are coefficients of adjustment of dimension. They depend on B_0 and the coil geometrical parameters.

The complete mathematical model that describes the physical model of Fig. 2.1 is obtained by replacing Eqs. (2.4), (2.5), (2.6) and (2.7) into Eqs. (2.1) and (2.2). Thence, setting $\omega_m = \sqrt{\frac{k_0}{m}}$, $\omega_e = \sqrt{\frac{1}{LC}}$, $\omega_P = \sqrt{\frac{1}{L_P C_P}}$, $x = \frac{X}{l}$, $y = \frac{q}{Q_0}$, $z = \frac{v}{V_0}$, where l, Q_0 and V_0 are respectively the reference length, charge and voltage; and with the time transformation $t = \omega_e \tau$, one obtains the following dimensionless equations:

$$\begin{aligned} &\ddot{x} + \left(\nu_1 + \nu_2 \text{sign}\left(\dot{x}\right)\right)\dot{x} + \omega_1^2 x + \lambda_1 x^2 + \lambda_2 x^3 + \delta z \\ &\quad + \left(\gamma_0 + \gamma_1 x + \gamma_2 x^2\right)\dot{y} = f(t), \end{aligned} \tag{2.8a}$$

$$\ddot{y} + \mu_e \dot{y} + y + \left(\beta_0 + \beta_1 x + \beta_2 x^2\right)\dot{x} = 0, \tag{2.8b}$$

$$\ddot{z} + \mu_P \dot{z} + \omega_3^2 z + \eta \ddot{x} = 0, \tag{2.8c}$$

with the dimensionless parameters given by

$$\begin{aligned} &\nu_1 = \frac{\mu_0^+ + \mu_0^-}{2m\omega_e},\ \omega_1 = \frac{\omega_m}{\omega_e},\ \lambda_1 = \frac{k_1 l}{m\omega_e^2},\ \gamma_0 = -\frac{\alpha_0 Q_0}{ml\omega_e}\frac{X_{\max}^2 - X_0^2}{X_{\max}^2},\ \gamma_1 = \frac{2\alpha_0 X_0 Q_0}{m\omega_e X_{\max}^2}, \\ &\gamma_2 = \frac{\alpha_0 l Q_0}{m\omega_e X_{\max}^2},\ \delta = \frac{\alpha V_0}{ml\omega_e^2},\ \lambda_2 = \frac{k_2 l^2}{m\omega_e^2},\ \mu_e = \frac{R}{L\omega_e},\ \beta_0 = \frac{\kappa_0 l}{LQ_0\omega_e}\frac{X_{\max}^2 - X_0^2}{X_{\max}^2}, \\ &\beta_1 = -\frac{2\kappa_0 l^2 X_0}{LQ_0\omega_e X_{\max}^2};\ \beta_2 = -\frac{\kappa_0 l^3}{LQ_0\omega_e X_{\max}^2},\ \mu_P = \frac{1}{R_P C_P \omega_e},\ \omega_3 = \frac{\omega_P}{\omega_e},\ \eta = -\frac{\alpha l}{C_P V_0}, \\ &\nu_2 = \frac{\mu_0^+ - \mu_0^-}{2m\omega_e}. \end{aligned} \tag{2.9}$$

The excitation function $f(t)$ is related to the frame motion acceleration as

$$f(t) = -\frac{\Gamma(\tau)}{l\omega_e^2}. \tag{2.10}$$

We assume throughout this thesis that $\Gamma(\tau)$ is formed of a harmonic function with constant amplitude, that is to say $f(t)$ can be mathematically expressed as

$$f(t) = F_0 \cos(\varphi(t)), \tag{2.11}$$

with F_0, the amplitude of the excitation and $\varphi(t)$ its phase. Let us notice that the over dot denotes the derivatives with respect to the dimensionless time t.

2.1.2 Model accounting for fractional properties: The second mathematical model

As we remind in the introductory part of this dissertation, the existence of ideal inductance in reality is merely a hypothesis. Inductance for real world application is built by conductor loops or coils. The ideal relation between the current through and voltage across the inductor, namely

$$v(t) = L\frac{di}{dt} \tag{2.12}$$

does not describe the real world inductance accurately. Several methods were proposed in the literature to model an inductor taking into account the losses due to ohmic resistance, eddy-current and hysteresis. In the field of mechanics, the behavior of magnetic core coils is comparable to that of viscoelastic materials [162] and this motivated to use fractional calculus to model coils. So, the fractional derivatives are used for modeling coils and showed that such models provide clearly more realistic description than the conventional model [3]. Therefore, we once more consider our apparatus whose schematic description is provided in Fig. 2.1, yet we assume that the coils within the electrical subsystem exhibit fractional properties. In short, this means we now use fractional derivatives for modeling both coils within the system.

The voltage and current within the piezoelectric circuit now obey the following equations:

$$i_1 = \frac{v}{R_P}, \tag{2.13a}$$

$$v = L_P\frac{d^\theta i_2}{d\tau^\theta}, \tag{2.13b}$$

$$i_P = i_1 + i_2, \tag{2.13c}$$

where i_P and v are still respectively the current and the voltage across the electrodes of the piezoelectric element, i_1 and i_2 are the currents flowing through the load resistor and the inductor respectively. θ $(0 < \theta < 1)$ is the order of the fractional derivative with respect to time τ. Replacing Eqs. (2.13a) and (2.13b) into Eq. (2.13c) one obtains

$$\frac{d^\theta i_P}{d\tau^\theta} = \frac{1}{R_P}\frac{d^\theta v}{d\tau^\theta} + \frac{v}{L_P} \tag{2.14}$$

Let us recall the relation between the current across the piezoelectric element i_P and the mass displacement X given by Eq. (2.7). Replacing Eq. (2.7) into the left hand side of Eq. (2.14) and then, applying the operator $\frac{d^{1-\theta}}{d\tau^{1-\theta}}$ on the resulting equation yields:

$$\frac{1}{R_P}\frac{dv}{d\tau}+\frac{1}{L_P}\frac{d^{1-\theta}v}{d\tau^{1-\theta}}=\alpha\frac{d^2X}{d\tau^2}-C_P\frac{d^2v}{d\tau^2}. \tag{2.15}$$

The current-voltage relation of the coil in the electromagnetic circuit is also of the form $v_L = L\frac{d^\epsilon i}{d\tau^\epsilon}$. Therefore, using the Kirchhoff's laws, the electromagnetic circuit is now described by the following equation:

$$L\frac{d^{1+\epsilon}q}{d\tau^{1+\epsilon}}+R\frac{dq}{d\tau}+\frac{1}{C}q+E_L=0, \tag{2.16}$$

where ϵ $(0<\epsilon<1)$ is the parameter describing the fractional property of the coil within the electromagnetic circuit. Other quantities of Eq. (2.16) remain the same. That is to say, the Lenz electromotive voltage E_L is still defined through Eq. (2.6).

As in the previous subsection, the motion of the mass in the mechanical part of the harvester is described by Eq. (2.1). The Laplace force F_L and the global restoring force F_P are respectively given by Eq. (2.4) and Eq. (2.5). The equation describing the mechanical part of the device thus remains unchanged.

Replacing Eq. (2.6) into Eq. (2.16) then setting, as previously, $\omega_m=\sqrt{\frac{k_0}{m}}$, $\omega_e=\sqrt{\frac{1}{LC}}$, $\omega_P=\sqrt{\frac{1}{L_PC_P}}$, $x=\frac{X}{l}$, $y=\frac{q}{Q_0}$, $z=\frac{v}{V_0}$, with the time transformation $t=\omega_e\tau$, one obtains the following dimensionless equations resulting from Eqs. (2.1), (2.16) and (2.15) respectively:

$$\begin{aligned}&\ddot{x}+\left(\nu_1+\nu_2\text{sign}\left(\dot{x}\right)\right)\dot{x}+\omega_1^2x+\lambda_1x^2+\lambda_2x^3+\delta z\\&\qquad+\left(\gamma_0+\gamma_1x+\gamma_2x^2\right)\dot{y}=f(t),\end{aligned} \tag{2.17a}$$

$$r_1D_t^{1+\epsilon}y+\mu_e\dot{y}+y+\left(\beta_0+\beta_1x+\beta_2x^2\right)\dot{x}=0, \tag{2.17b}$$

$$\ddot{z}+\mu_P\dot{z}+r_2D_t^{1-\theta}z+\eta\ddot{x}=0, \tag{2.17c}$$

with the additional dimensionless parameters given by

$$r_1=\frac{1}{\omega_e^{1-\epsilon}},\quad r_2=\frac{\omega_P^2}{\omega_e^{1+\theta}}. \tag{2.18}$$

The equation Eq. (2.17) and Eq. (2.8) are the two mathematical models to be used in the remaining part of this thesis. Let us remark that in the particular case where

$\epsilon = 1$ and $theta = 1$, Eq. (2.17) and Eq. (2.8) overlap. The potentials of the harvester mechanical and electrical parts are given by

$$V(x) = \frac{\omega_1^2}{2}x^2 + \frac{\lambda_1}{3}x^3 + \frac{\lambda_2}{4}x^4, \quad V(y) = \frac{1}{2}y^2 \text{ and } V(z) = \frac{\omega_3^2}{2}z^2. \tag{2.19}$$

$V(y)$ and $V(z)$ are harmonic potentials. The conditions $\lambda_2 > 0$ and $\lambda_1^2 - 4\lambda_2\omega_1^2 > 0$ hold in the remainder of this dissertation so that $V(x)$ is a bistable potential.

2.2 The research methods

We provide in this section the analytical developments used in this thesis to study the system dynamics and to analyze the system harvesting behavior.

2.2.1 Analytical methods

2.2.1.1 Modified harmonic balance method

The harmonic balance method (HBM) is generally used to calculate the periodic solution. It consists of finding a solution in the form of a Fourier series. In this way, the nonlinear differential equations are transformed into a nonlinear algebraic system. However, when the non-linearities are complex, the derivation of the algebraic system becomes very complex. Other methods have been proposed to solve this problem, such as the incremental harmonic balance method [163] or the alternative harmonic balance method [164], but they require a very large amount of time for the calculation of the solution. In order to solve this problem, the authors [165] have proposed an alternative strategy to apply the classical HBM method with a large number of harmonics. The basic idea is to reformulate the original system into a new system where the nonlinearities are quadratic polynomials. This leads to a quadratic nonlinear system to which the application of the HBM method is simpler. Furthermore, the quadratic transformation allows the use of the numerical asymptotic method (MAN). The MAN method has several advantages: it provides continuous solutions, the continuity is very robust and the control of the step length is automatic and always-optimal [166, 167]. This method is detailed in the work of Cochelin et al. [165].

In this thesis, we propose a slightly modified harmonic balance method that takes into account the discontinuous nature of the models equations. This so called *modified harmonic balance method* is applied to both models in the subsequent paragraphs to determine the amplitudes of approximate analytical solutions.

We seek approximate analytical solutions of both Eqs. (2.8) and (2.17) when the excitation is purely sinusoidal, that is to say

$$\varphi(t) = \omega t, \tag{2.20}$$

with ω the excitation frequency. To this end, the approximate solution is taken, consistently to the harmonic balance method, in the form:

$$x(t) = a_1 \cos(\omega t) + a_2 \sin(\omega t), \tag{2.21a}$$

$$y(t) = b_1 \cos(\omega t) + b_2 \sin(\omega t), \tag{2.21b}$$

$$z(t) = c_1 \cos(\omega t) + c_2 \sin(\omega t). \tag{2.21c}$$

Let $a = \sqrt{a_1^2 + a_2^2}$, $b = \sqrt{b_1^2 + b_2^2}$ and $c = \sqrt{c_1^2 + c_2^2}$, the amplitudes of the preceding harmonic solution.

2.2.1.1.1 Case of the first model

Replacing Eq. (2.21) into Eq. (2.8) and neglecting the terms of higher harmonics yields:

$$\left(\left(\frac{3\lambda_2}{4} - \frac{\lambda_1\gamma_2}{2\gamma_1}\right)a^2 + \omega_1^2 - \omega^2\right)a_1 + (\nu_1 \pm \nu_2)\,\omega a_2 + \left(\frac{1}{4}\omega\gamma_2 a^2 + \gamma_0\omega\right)b_2 + \delta c_1 = F_0, \tag{2.22a}$$

$$-(\nu_1 \pm \nu_2)\,\omega a_1 + \left(\left(\frac{3\lambda_2}{4} - \frac{\lambda_1\gamma_2}{2\gamma_1}\right)a^2 + \omega_1^2 - \omega^2\right)a_2 - \left(\frac{1}{4}\omega\gamma_2 a^2 + \gamma_0\omega\right)b_1 + \delta c_2 = 0, \tag{2.22b}$$

$$\left(1 - \omega^2\right)b_1 + \mu_e\omega b_2 + \left(\frac{\omega\beta_2}{4}a^2 + \beta_0\omega\right)a_2 = 0, \tag{2.22c}$$

$$-\mu_e\omega b_1 + \left(1 - \omega^2\right)b_2 - \left(\frac{\omega\beta_2}{4}a^2 + \beta_0\omega\right)a_1 = 0, \tag{2.22d}$$

$$\left(\omega_3^2 - \omega^2\right)c_1 + \mu_P\omega c_2 - \eta\omega^2 a_1 = 0, \tag{2.22e}$$

$$-\mu_P\omega c_1 + \left(\omega_3^2 - \omega^2\right)c_2 - \eta\omega^2 a_2 = 0. \tag{2.22f}$$

Combining the six preceding equations, one can show that depending on the value taken by the sign function, the amplitude a is either the root of the algebraic equation

$\Gamma^+(a) = 0$ or $\Gamma^-(a) = 0$, where the polynomial functions $\Gamma^\pm$ are defined as

$$\Gamma^\pm(a) = \chi_{10}a^{10} + \chi_8 a^8 + \chi_6^\pm a^6 + \chi_4^\pm a^4 + \chi_2^\pm a^2 - 256F_0^2. \tag{2.23}$$

The coefficients of these polynomials are given in the appendix A. The approximate amplitude of the harvester mechanical part's oscillation can be taken as the average of the roots yielded by the equations $\Gamma^+(a) = 0$ and $\Gamma^-(a) = 0$. Once this amplitude is determined, the amplitudes of the electrical part's oscillations are given by:

$$b = \frac{\left|\beta_0 + \frac{1}{4}\beta_2 a^2\right| \omega a}{\sqrt{\mu_e^2\omega^2 + \left(1-\omega^2\right)^2}}, \tag{2.24a}$$

$$c = \frac{|\eta|\omega^2 a}{\sqrt{\mu_P^2\omega^2 + \left(\omega_3^2 - \omega^2\right)^2}}. \tag{2.24b}$$

2.2.1.1.2 Case of the second model

Here we derive an approximate analytical solution of Eq. (2.17) in the form (2.21) given above. When replacing Eq. (2.21) into Eq. (2.17), we have to approximately evaluate $D_t^{1+\epsilon}[y(t)]$ and $D_t^{1-\theta}[z(t)]$. Among the numerous definitions of the fractional derivatives, we use the Caputo's definition [55] given as:

$$\begin{aligned} D_t^\epsilon[y(t)] &= \frac{1}{\Gamma(1-\epsilon)}\int_0^t (t-s)^{-\epsilon}\dot{y}(s)ds \\ &= \frac{1}{\Gamma(1-\epsilon)}\int_0^t s^{-\epsilon}\dot{y}(t-s)\,ds, \end{aligned} \tag{2.25}$$

where $\Gamma(\cdot)$ is the gamma function and $0 < \epsilon < 1$. Replacing Eq. (2.21b) into Eq. (2.25), one obtains

$$\begin{aligned} D_t^\epsilon[y(t)] &= D_t^\epsilon[b_1\cos(\omega t) + b_2\sin(\omega t)] \\ &= \frac{1}{\Gamma(1-\epsilon)}\int_0^t s^{-\epsilon}\left(-b_1\omega\sin\left(\omega(t-s)\right)\right)ds \\ &\quad + \frac{1}{\Gamma(1-\epsilon)}\int_0^t s^{-\epsilon}b_2\omega\cos\left(\omega(t-s)\right)ds. \end{aligned} \tag{2.26}$$

Making the variable change $u = \omega s$ and setting $I_1 = \int_0^{\omega t}\frac{\cos u}{u^\epsilon}du$ and $I_2 = \int_0^{\omega t}\frac{\sin u}{u^\epsilon}du$, it can be shown that

$$D_t^\epsilon[y(t)] = \frac{\omega^\epsilon}{\Gamma(1-\epsilon)}\left[(-b_1I_1 + +b_2I_2)\sin(\omega t) + (b_1I_2 + b_2I_1)\cos(\omega t)\right]. \tag{2.27}$$

Using the approximation

$$I_1 \approx \Gamma(1-\epsilon)\sin\left(\epsilon\frac{\pi}{2}\right) \quad \text{and} \quad \mathrm{I}_2 \approx \Gamma(1-\epsilon)\cos\left(\epsilon\frac{\pi}{2}\right), \tag{2.28}$$

we finally obtain

$$D_t^{\epsilon}[y(t)] = \omega^{\epsilon}\left[(b_1\cos(\omega t)+b_2\sin(\omega t))\cos\left(\epsilon\frac{\pi}{2}\right)+(b_2\cos(\omega t)-b_1\sin(\omega t))\sin\left(\epsilon\frac{\pi}{2}\right)\right]. \tag{2.29}$$

Thence, differentiating with respect to time t, we have the following expression of $D_t^{1+\epsilon}[y(t)]$

$$\begin{aligned} D_t^{1+\epsilon}[y(t)] &= \frac{d}{dt}D_t^{\epsilon}[y(t)] \\ &= \omega^{1+\epsilon}\left[(-b_1\sin(\omega t)+b_2\cos(\omega t))\cos\left(\epsilon\frac{\pi}{2}\right)\right. \\ &\quad \left.-(b_1\cos(\omega t)+b_2\sin(\omega t))\sin\left(\epsilon\frac{\pi}{2}\right)\right]. \end{aligned} \tag{2.30}$$

We express $D_t^{1-\theta}[z(t)]$ in the same way as above. It follows that

$$\begin{aligned} D_t^{1-\theta}[z(t)] = \omega^{1-\theta}&\left[(c_1\cos(\omega t)+c_2\sin(\omega t))\cos\left((1-\theta)\frac{\pi}{2}\right)\right. \\ &\left.+(c_2\cos(\omega t)-c_1\sin(\omega t))\sin\left((1-\theta)\frac{\pi}{2}\right)\right]. \end{aligned} \tag{2.31}$$

In order to derive the algebraic equations that verify the amplitudes, let us substitute Eq. (2.21) into Eq. (2.17). We have to take Eqs. (2.30) and (2.31) into account and neglect the terms of higher harmonics. We obtain the following linear system:

$$\left(\left(\frac{3\lambda_2}{4}-\frac{\lambda_1\gamma_2}{2\gamma_1}\right)a^2+\omega_1^2-\omega^2\right)a_1+(\nu_1\pm\nu_2)\,\omega a_2+\left(\frac{1}{4}\omega\gamma_2a^2+\gamma_0\omega\right)b_2+\delta c_1=F_0, \tag{2.32a}$$

$$-(\nu_1\pm\nu_2)\,\omega a_1+\left(\left(\frac{3\lambda_2}{4}-\frac{\lambda_1\gamma_2}{2\gamma_1}\right)a^2+\omega_1^2-\omega^2\right)a_2-\left(\frac{1}{4}\omega\gamma_2a^2+\gamma_0\omega\right)b_1+\delta c_2=0, \tag{2.32b}$$

$$(1-r_1\varsigma_2)\,b_1+(\mu_e\omega+r_1\varsigma_1)\,b_2+\left(\frac{\omega\beta_2}{4}a^2+\beta_0\omega\right)a_2=0, \tag{2.32c}$$

$$-(\mu_e\omega+r_1\varsigma_1)\,b_1+(1-r_1\varsigma_2)\,b_2-\left(\frac{\omega\beta_2}{4}a^2+\beta_0\omega\right)a_1=0, \tag{2.32d}$$

$$\left(r_2\varrho_2-\omega^2\right)c_1+(\mu_P\omega+r_2\varrho_1)c_2-\eta\omega^2a_1=0, \tag{2.32e}$$

$$-(\mu_P\omega+r_2\varrho_1)c_1+\left(r_2\varrho_2-\omega^2\right)c_2-\eta\omega^2a_2=0, \tag{2.32f}$$

where we set

$$\varsigma_1 = \omega^{1+\epsilon}\cos\left(\frac{\pi\epsilon}{2}\right), \quad \varsigma_2 = \omega^{1+\epsilon}\sin\left(\frac{\pi\epsilon}{2}\right),$$
$$\varrho_1 = \omega^{1-\theta}\cos\left(\frac{\pi\theta}{2}\right), \quad \varrho_2 = \omega^{1-\theta}\sin\left(\frac{\pi\theta}{2}\right). \tag{2.33a}$$

Using some elementary algebra, one can show from the preceding system that depending on the value taken by the sign function, the amplitude a is either the root of the algebraic equation $H^+(a) = 0$ or $H^-(a) = 0$, where the polynomial functions $H^\pm$ are defined as

$$H^\pm(a) = \iota_{10}a^{10} + \iota_8 a^8 + \iota_6^\pm a^6 + \iota_4^\pm a^4 + \iota_2^\pm a^2 - 256F_0^2. \tag{2.34}$$

The coefficients of these polynomials are provided in the appendix A. The approximate amplitude of the harvester mechanical part's oscillation can be taken as the average of the roots yielded by the equations $H^+(a) = 0$ and $H^-(a) = 0$. From the above algebra, it is also shown that the amplitudes b and c of the electrical part's oscillations relate to amplitude a as follows:

$$b = \frac{\left|\beta_0 + \frac{1}{4}\beta_2 a^2\right|\omega a}{\sqrt{\left(1 - r_1\varsigma_2\right)^2 + \left(\mu_e\omega + r_1\varsigma_1\right)^2}}, \tag{2.35a}$$

$$c = \frac{|\eta|\omega^2 a}{\sqrt{\left(r_2\varrho_2 - \omega^2\right)^2 + \left(\mu_P\omega + r_2\varrho_1\right)^2}}. \tag{2.35b}$$

To evaluate the amplitude a of the mechanical vibration, the roots a^+ and a^- of the respective polynomials $H^+(a)$ and $H^-(a)$ are calculated by the mean of the Newton-Raphson algorithm. Then amplitude a is estimated as $a = \frac{a^+ + a^-}{2}$. Once amplitude a is determined, the amplitudes of the electrical oscillations are deduced through Eq. (2.35).

2.2.1.2 The stochastic averaging technique

Complicated motions of the frame has been described in the literature as a summation of a harmonic motion and a noisy term. Specifically, we assume here that these motions' acceleration are of constant amplitude, with noisily fluctuating phase angle $\varphi(t)$ of average frequency ω. $\varphi(t)$ reads

$$\varphi(t) = \omega t + \sqrt{\frac{2}{\tau_1}}W(t) + \Phi, \tag{2.36}$$

where τ_1 is a positive constant interpreted as the correlation time of the random driving excitation $f(t)$. Specifically, $\sqrt{\frac{2}{\tau_1}}$ represents the randomness level in the phase of $f(t)$. $W(t)$ is a standard Wiener process and Φ is a random variable uniformly distributed within $[0;\pi[$ and independent of $W(t)$. In its present form, the random excitation $f(t)$ is referred to as bounded noise in the literature [168–175] and will be henceforth denoted by $\xi_1(t)$ for notation convenience. In addition, the fundamental property of the electrical components to be effective noise source (such as thermal noise, shot noise, $1/f$ noise etc.) is now taken into consideration and modeled by additive colored noises $\zeta_2(t)$ and $\zeta_3(t)$. The model equation (2.8) can therefore be rewritten as:

$$\begin{aligned}&\ddot{x} + (\nu_1 + \nu_2 \text{sign}\,(\dot{x}))\,\dot{x} + \omega_1^2 x + \lambda_1 x^2 + \lambda_2 x^3 + \delta z \\ &\quad + \left(\gamma_0 + \gamma_1 x + \gamma_2 x^2\right)\dot{y} = \xi_1(t), \qquad (2.37a)\\ &\ddot{y} + \mu_e \dot{y} + y + \left(\beta_0 + \beta_1 x + \beta_2 x^2\right)\dot{x} = \zeta_2(t), \qquad (2.37b)\\ &\ddot{z} + \mu_P \dot{z} + \omega_3^2 z + \eta \ddot{x} = \zeta_3(t), \qquad (2.37c)\end{aligned}$$

with the cross-covariance matrix $R(s)$ of the random excitation vector $(\xi_1(t), \zeta_2(t), \zeta_3(t))$, defined by:

$$\begin{aligned}R_{11}(s) &= \frac{F_0^2}{2}\exp\left(-\frac{|s|}{\tau_1}\right)\cos(\omega s)\,, \qquad (2.38a)\\ R_{22}(s) &= \frac{D_2}{\tau_2}\exp\left(-\frac{|s|}{\tau_2}\right), \qquad (2.38b)\\ R_{33}(s) &= \frac{D_3}{\tau_3}\exp\left(-\frac{|s|}{\tau_3}\right), \qquad (2.38c)\\ R_{ij}(s) &= 0, \quad i \neq j. \qquad (2.38d)\end{aligned}$$

D_2 and D_3 respectively represent the intensities of the colored noises excitations $\zeta_2(t)$ and $\zeta_3(t)$, and τ_2 and τ_3 stand for their correlation time. In the remainder of this subsection, we determine the stationary probability distribution for the amplitudes by the mean of the stochastic averaging technique. Consistently to this method, let's consider the following variable change:

$$\begin{aligned}&\vartheta_1(t) = \omega_1 t + \phi_1(t), \quad \vartheta_2(t) = t + \phi_2(t), \quad \vartheta_3(t) = \omega_3 t + \phi_3(t),\\ &x(t) = a(t)\cos(\vartheta_1(t)), \quad y(t) = b(t)\cos(\vartheta_2(t)), \quad z(t) = c(t)\cos(\vartheta_3(t)), \qquad (2.39)\\ &\dot{x}(t) = -\omega_1 a(t)\sin(\vartheta_1(t)), \quad \dot{y}(t) = -b(t)\sin(\vartheta_2(t)), \quad \dot{z}(t) = -\omega_3 c(t)\sin(\vartheta_3(t)).\end{aligned}$$

Replacing relations (2.39) into system (2.37) and after some algebraic manipulations, the system (2.37) takes the following form:

$$\dot{a} = f_1(U,t) + g_{11}(U,t)\xi_1(t), \tag{2.40a}$$

$$\dot{\phi}_1 = f_2(U,t) + g_{21}(U,t)\xi_1(t), \tag{2.40b}$$

$$\dot{b} = f_3(U,t) + g_{32}(U,t)\zeta_2(t), \tag{2.40c}$$

$$\dot{\phi}_2 = f_4(U,t) + g_{42}(U,t)\zeta_2(t), \tag{2.40d}$$

$$\dot{c} = f_5(U,t) + g_{51}(U,t)\xi_1(t) + g_{53}(U,t)\zeta_3(t), \tag{2.40e}$$

$$\dot{\phi}_3 = f_6(U,t) + g_{61}(U,t)\xi_1(t) + g_{63}(U,t)\zeta_3(t), \tag{2.40f}$$

where $U = (a, \phi_1, b, \phi_2, c, \phi_3)$ is the state vector. The functions f_i, and g_{ij} are defined in the appendix B.

The state vector of system (2.40) can be approximated by a diffusive Markov process vector by the mean of the central limit theorem [177]. The later process vector is governed by the following Itô equations:

$$da = m_1 dt + \sigma_1 dW_1, \tag{2.41a}$$

$$d\phi_1 = m_2 dt + \sigma_2 dW_2, \tag{2.41b}$$

$$db = m_3 dt + \sigma_3 dW_3, \tag{2.41c}$$

$$d\phi_2 = m_4 dt + \sigma_4 dW_4, \tag{2.41d}$$

$$dc = m_5 dt + \sigma_5 dW_5, \tag{2.41e}$$

$$d\phi_3 = m_6 dt + \sigma_6 dW_6, \tag{2.41f}$$

where the drift coefficients m_i and the diffusion coefficients σ_i are given in annexe B. $W_i(t)$, $(i = 1, 2, ..., 6)$ are six independent standard Wiener processes.

With the knowledge of the drift and diffusion coefficients, it is clear that the amplitude processes a, b and c are decoupled from the phase processes. The transition probability densities $P_a(a,t|a_0,t_0)$, $P_b(b,t|b_0,t_0)$, and $P_c(c,t|c_0,t_0)$ for the amplitudes a, b and c respectively, can therefore be determined separately instead of joint transition probability densities. They are governed by the following uncoupled Fokker-Planck-Kolmogorov (FPK) equations:

$$\frac{\partial P_a}{\partial t} = -\frac{\partial}{\partial a}\left(m_1 P_a\right) + \frac{1}{2}\frac{\partial^2}{\partial a^2}\left(\sigma_1^2 P_a\right), \tag{2.42}$$

$$\frac{\partial P_b}{\partial t} = -\frac{\partial}{\partial b}\left(m_3 P_b\right) + \frac{1}{2}\frac{\partial^2}{\partial b^2}\left(\sigma_3^2 P_b\right) \tag{2.43}$$

and

$$\frac{\partial P_c}{\partial t} = -\frac{\partial}{\partial c}\left(m_5 P_c\right) + \frac{1}{2}\frac{\partial^2}{\partial c^2}\left(\sigma_5^2 P_c\right). \tag{2.44}$$

Setting $\frac{\partial P_a}{\partial t} = 0$, $\frac{\partial P_b}{\partial t} = 0$ and $\frac{\partial P_c}{\partial t} = 0$ and following Zhu [178], the stationary solutions $P_a(a)$, $P_b(b)$ and $P_c(c)$ of Eqs. (2.42), (2.43) and (2.44), referred to as stationary transition PDFs are given by:

$$P_a(a) = \frac{N_a}{\sigma_1^2}\exp\left[2\int\frac{m_1}{\sigma_1^2}da\right], \tag{2.45}$$

$$P_b(b) = \frac{N_b}{\sigma_3^2}\exp\left[2\int\frac{m_3}{\sigma_3^2}db\right] \tag{2.46}$$

and

$$P_c(c) = \frac{N_c}{\sigma_5^2}\exp\left[2\int\frac{m_5}{\sigma_5^2}dc\right], \tag{2.47}$$

where N_a, N_b and N_c are the normalization constants. With the knowledge of m_1, m_3, m_5, σ_1, σ_3 and σ_5, the transition stationary PDFs can be expressed as:

$$P_a(a) = \frac{\nu_1}{\sigma_1^2}a\exp\left(-\frac{\nu_1}{2\sigma_1^2}a^2\right), \tag{2.48}$$

$$P_b(b) = \frac{\mu_e}{\sigma_3^2}b\exp\left(-\frac{\mu_e}{2\sigma_3^2}b^2\right), \tag{2.49}$$

and

$$P_c(c) = \frac{\mu_P}{\sigma_5^2}c\exp\left(-\frac{\mu_P}{2\sigma_5^2}c^2\right). \tag{2.50}$$

2.2.2 Numerical methods

Obtaining analytical solution of ordinary or stochastic differential equations is in most cases, the most difficult challenge in continuous time dynamics. Since most ordinary differential equations are not soluble analytically, numerical integration is the only way to obtain information about the trajectory. Different methods have been proposed and used in an attempt to more accurately solve various types of differential equations. However there are a handful of methods known and used universally (i.e., Runge-Kutta, Adams-Bashforth and Backward Differentiation Formula methods). All these methods discretize the differential system to produce a discrete system of equation or map. They obtain different maps from the same differential equation with the same aim; that is the dynamics

of the map should correspond closely to the dynamics of the differential equation. In this work, we mainly use the fourth order Runge-Kutta algorithm and the second order stochastic Runge-Kutta algorithm to numerically solve the first model (Eq. (2.8)). The fractional order Newton-Leipnik algorithm is mainly used to compute the response of the second model (Eq. (2.17)). Other routines used in this thesis to numerically analyzed the response of those models such as the routine to evaluate the PDFs and that to estimate the Lyapunov exponent for instance are based on the above algorithms. It is therefore necessary to discuss these three algorithms in the following paragraphs.

2.2.2.1 The fourth-order Runge-Kutta algorithm

The fourth order Runge-Kutta is a much more locally accurate method. Let's consider the following problem

$$\begin{cases} \dfrac{dy}{dt} = f(t, y), \\ y(t_0) = \alpha, \end{cases} \tag{2.51}$$

and define h to be the normalized integration time step size and set $t_i = t_0 + ih$. Then the following sequence of operations

$$\begin{aligned} &U_0 = \alpha, \\ &U_{i+1} = U_i + \frac{h}{6}(k_1 + 2k_2 + 2k_3 + k_4), \quad \text{for i} = 0, 1, ..., \text{n} - 1, \end{aligned} \tag{2.52}$$

computes an approximate solution, that is $U_n \approx y(t_n)$. k_1, k_2, k_3 and k_4 are the coefficients which have to be evaluated in each stage of the loop (of the fourth order Runge-Kutta algorithm) by the formulas below:

$$\begin{aligned} k_1 &= f(t_i, U_i), \\ k_2 &= f(t_i + \frac{h}{2}, U_i + \frac{h}{2}k_1), \\ k_3 &= f(t_i + \frac{h}{2}, U_i + \frac{h}{2}k_2), \\ k_4 &= f(t_i + h, U_i + hk_3). \end{aligned} \tag{2.53}$$

In order to use this algorithm to solve the model equation (2.8), this equation is put in the standard form defined by Eq. (2.51), that is to say, in the following form:

$$\begin{aligned}
\dot{x} = &\quad u,\\
\dot{u} = &\quad -\left(\nu_1+\nu_2\text{sign}(u)\right)u-\omega_1^2x-\lambda_1x^2-\lambda_2x^3-\delta z-\left(\gamma_0+\gamma_1x+\gamma_2x^2\right)v\\
&\quad +F_0\cos\left(\varphi(t)\right),\\
\dot{y} = &\quad v,\\
\dot{v} = &\quad -\mu_e v-y-\left(\beta_0+\beta_1x+\beta_2x^2\right)u,\\
\dot{z} = &\quad w,\\
\dot{w} = &\quad -\mu_P w-\omega_3^2z+\eta\left[\left(\nu_1+\nu_2\text{sign}(u)\right)u+\omega_1^2x+\lambda_1x^2+\lambda_2x^3+\delta z\right.\\
&\quad \left.+\left(\gamma_0+\gamma_1x+\gamma_2x^2\right)v-F_0\cos\left(\varphi(t)\right)\right],\\
\dot{\varphi} = &\quad \omega.
\end{aligned} \tag{2.54}$$

2.2.2.2 The stochastic Runge-Kutta algorithm

Several Runge-Kutta-like algorithm has been developed in the literature to solve stochastic differential equation. Let us consider the following stochastic dynamical system

$$\begin{cases}
\dfrac{dx}{dt} = f(t,x,y),\\
\dfrac{dy}{dt} = g(t,x,y)+\xi(t),
\end{cases} \tag{2.55}$$

with the initial conditions defined as

$$\begin{cases}
x(t_0) = x_0,\\
y(t_0) = y_0,
\end{cases} \tag{2.56}$$

and where $\xi(t)$ is the white Gaussian noise with statistical properties $\langle\xi(t)\rangle = 0$ and $\langle\xi(t)\xi(t+\tau)\rangle = 2D\delta(\tau)$. Setting $t_i = t_0+ih$, $x(t_i) = x_i$ and following Honeycutt [179], the second-order Runge-Kutta like algorithm to compute an approximate solution of the above problem is given as follows:

$$\begin{aligned}
x_{i+1} &= x_i+\frac{h}{2}\left(F_1+F_2\right),\\
y_{i+1} &= y_i+\frac{h}{2}\left(G_1+G_2\right)+(2Dh)^{\frac{1}{2}}\psi,\ \text{ for i} = 0,1,...,\text{n}-1.
\end{aligned} \tag{2.57}$$

The coefficients F_1, F_2, G_1 and G_2 are evaluated in each stage of the loop as follows

$$\begin{aligned} F_1 &= f\left(t_i, x_i, y_i\right), \\ G_1 &= g\left(t_i, x_i, y_i\right), \\ F_2 &= f\left(t_i + h, x_i + hF_1, y_i + hG_1 + (2Dh)^{\frac{1}{2}}\psi\right), \\ G_2 &= g\left(t_i + h, x_i + hF_1, y_i + hG_1 + (2Dh)^{\frac{1}{2}}\psi\right), \end{aligned} \tag{2.58}$$

and ψ is a normally distributed random number evaluated in each stage of the loop.

To verify the consistency of the analytical treatment provided in section 2.2.1.2, the stationary transition PDFs for the amplitudes $a(t)$, $b(t)$ and $c(t)$ are obtained through the Monte-Carlo simulations by computing a long time evolution of the random amplitudes $a(t)$, $b(t)$ and $c(t)$ with the above second order stochastic Runge-Kutta algorithm [179]. To this aim, following Honeycutt [179, 180], Eq. (2.37) is transformed into the following stochastic dynamical system:

$$\left\{\begin{aligned} \dot{x} &= u, \\ \dot{u} &= -\left(\nu_1 + \nu_2 \text{sign}(u)\right) u - \omega_1^2 x - \lambda_1 x^2 - \lambda_2 x^3 - \delta z - \left(\gamma_0 + \gamma_1 x + \gamma_2 x^2\right) v \\ &\quad + F_0 \cos\left(\varphi(t)\right), \\ \dot{y} &= v, \\ \dot{v} &= -\mu_e v - y - \left(\beta_0 + \beta_1 x + \beta_2 x^2\right) u + \zeta_2(t), \\ \dot{z} &= w, \\ \dot{w} &= -\mu_P w - \omega_3^2 z + \eta\left[\left(\nu_1 + \nu_2 \text{sign}(u)\right) u + \omega_1^2 x + \lambda_1 x^2 + \lambda_2 x^3 + \delta z\right. \\ &\quad \left. + \left(\gamma_0 + \gamma_1 x + \gamma_2 x^2\right) v - F_0 \cos\left(\varphi(t)\right)\right] + \zeta_3(t), \\ \dot{\varphi} &= \omega + \sqrt{\frac{2}{\tau_1}}\chi_1(t), \\ \dot{\zeta}_2 &= -\frac{1}{\tau_2}\zeta_2 + \frac{\sqrt{2D_2}}{\tau_2}\chi_2(t), \\ \dot{\zeta}_3 &= -\frac{1}{\tau_3}\zeta_3 + \frac{\sqrt{2D_3}}{\tau_3}\chi_3(t), \end{aligned}\right. , \tag{2.59}$$

with $\chi_i(t)$ ($i \in \{1, 2, 3\}$), the normalized sources of Gaussian white noise. Their statistical properties are: $\langle \chi_i(t) \rangle = 0$ and $\langle \chi_i(t)\chi_j(t+s) \rangle = \delta_{ij}\delta(s)$. Let's remind that the amplitudes are numerically computed as: $a(t) = \sqrt{(x(t))^2 + \frac{(\dot{x}(t))^2}{\omega_1^2}}$, $b(t) = \sqrt{(y(t))^2 + (\dot{y}(t))^2}$ and $c(t) = \sqrt{(z(t))^2 + \frac{(\dot{z}(t))^2}{\omega_3^2}}$.

2.2.2.3 The fractional order Newton-Leipnik algorithm

In the last part of subsection 2.2.1.1, the amplitudes of the response of the model equation (2.17) are analytically derived. In order to estimate these amplitudes by the mean of direct numerical integrations of system (2.17), each equation of system (2.17) can be decomposed into a set of equations of lower degree as follows:

$$\dot{x} = u, \tag{2.60a}$$

$$\dot{u} = G\left(x, u, v, z, t\right), \tag{2.60b}$$

$$\dot{y} = v, \tag{2.60c}$$

$$D_t^{\epsilon} v = \frac{1}{r_1}\left(-\mu_e v - y - \left(\beta_0 + \beta_1 x + \beta_2 x^2\right) u\right), \tag{2.60d}$$

$$\dot{z} = w, \tag{2.60e}$$

$$D_t^{1-\theta} z = \psi, \tag{2.60f}$$

$$\dot{w} = -\mu_P w - r_2 \psi - \eta G\left(x, u, v, z, t\right), \tag{2.60g}$$

where $G\left(x, u, v, z, t\right) = -\left(\nu_1 + \nu_2 sign\left(u\right)\right) u - \omega_1^2 x - \lambda_1 x^2 - \lambda_2 x^3 - \delta z - \left(\gamma_0 + \gamma_1 x + \gamma_2 x^2\right) v + f\left(t\right)$. Using the fractional order Newton-Leipnik algorithm [62, 68], the above set of equations can be written in the following discretized form:

$$x_k = x_{k-1} + h u_{k-1}, \tag{2.61a}$$

$$u_k = u_{k-1} + h G\left(x_{k-1}, u_{k-1}, v_{k-1}, z_{k-1}, t_{k-1}\right), \tag{2.61b}$$

$$y_k = y_{k-1} + h v_{k-1}, \tag{2.61c}$$

$$v_k = \left[\frac{1}{r_1}\left(-\mu_e v_{k-1} - y_k - \left(\beta_0 + \beta_1 x_k + \beta_2 x_k^2\right) u_k\right)\right] h^{\epsilon} - \sum_{j=1}^{k} c_j^{(\epsilon)} v_{k-j}, \tag{2.61d}$$

$$\psi_{k-1} = \left[z_{k-1} + h w_{k-1} + \sum_{j=1}^{k} c_j^{(1-\theta)} z_{k-j}\right] \frac{1}{h^{1-\theta}}, \tag{2.61e}$$

$$z_k = z_{k-1} + h w_{k-1}, \tag{2.61f}$$

$$w_k = w_{k-1} + h\left[-\mu_p w_{k-1} - r_2 \psi_{k-1} - \eta G\left(x_{k-1}, u_{k-1}, v_{k-1}, z_{k-1}, t_{k-1}\right)\right], \tag{2.61g}$$

where h is the integration (or time) step defined such as $t_k = t_{k-1} + h$ and x_k denotes $x(t_k)$. The coefficients $c_j^{(\epsilon)}$ are computed by the following recursive relations:

$$c_0^{(\epsilon)} = 1, \quad c_j^{(\epsilon)} = \left(1 - \frac{1+\epsilon}{j}\right) c_{j-1}^{(\epsilon)}. \tag{2.62}$$

$c_j^{(1-\theta)}$ are computed in a similar way. By the mean of the above set of equations ((2.61a)-(2.61g)), numerical solution of system (2.17) is evaluated with time step $h = 0.001$ and null initial conditions. This computation, done usng MATLAB software, is excessively time consuming due to the memory effect. After computing a long time evolution of the state variables $x(t)$, $y(t)$ and $z(t)$; if $x(t)$, $y(t)$ and $z(t)$ exhibit a sine waveform, then the peak-to-peak lengths $x_{max} - x_{min}$, $y_{max} - y_{min}$ and $z_{max} - z_{min}$ are evaluated and the amplitudes a, b and c are extracted as $a = \frac{x_{max}-x_{min}}{2}$, $b = \frac{y_{max}-y_{min}}{2}$ and $c = \frac{z_{max}-z_{min}}{2}$. Note that x_{max}, y_{max} and z_{max} are respectively the upper peaks of $x(t)$, $y(t)$ and $z(t)$, while x_{min}, y_{min} and z_{min} are their lower peaks. With such a procedure, the amplitudes can be directly numerically evaluated with increasing frequency for instance, to obtain the frequency-response curves.

2.2.2.4 Other numerical methods

Other numerical methods used in this thesis are subsequently utilized after using those discussed in the subsections above to compute the models' responses. Apart from the MATLAB routine which helps us to plot all the curves in the remainder of this dissertation, other numerical methods allow us to compute Lyapunov exponents, to draw bifurcation map and to evaluate histograms (for computation of PDFs through Monte-Carlo simulations).

Conclusion

This chapter was devoted, on the one hand, to the modeling of the non-smooth type hybrid energy harvesting device under consideration in this work, and on the other hand, to the description of the main methods used to solve the resulting model equations. In the first section of this chapter, the classical laws (Newton's second law of motion and Kirchhoff's law) enabled us to derive equations which describes the dynamical behavior of the energy harvester. The first set of equations which we refer to as *first model*, consists of three second-order coupled ordinary differential equations. The first equation of this model is non-smooth and subjected to an excitation due to the vertical acceleration of the harvester frame. In the first model, the excitation was considered to be purely harmonic.

Then, assuming that the frame motion acceleration noisily fluctuates and that the electrical components of the electrical part of the harvester are noise sources, the first model gave birth to a slightly different model: a stochastic dynamical system. We also assumed that the current-voltage relationship of the inductances within the system is of fractional order. This assumption led to a fractional order dynamical system which we refer to as *second model*. Then, in the second section, the analytical and the numerical methods used in this dissertation to determine responses of the models have been discussed. The key research methods used to analyze these responses throughout the remainder of this dissertation, have been pointed out. In the next chapter, we will provide the outputs of the different methods discussed in this chapter, thence we will investigate the effects of the intrinsic characteristics of the device on its harvesting behavior.

Chapter 3

Results and Discussion

Introduction

In the previous chapters, we have provided generalities on energy harvesting systems and have defined concepts such as vibrational energy harvester, hybridity, non-smoothness and fractional calculus. We have also derived two main mathematical models of the dynamical behavior of the hybrid energy harvester device under consideration in this work, then we have pointed out the main methods used to reach our goals. In the present chapter, we bring out our results: In section 3.1, we use the first model of our non-smooth type hybrid harvester to study its harmonic and chaotic response. Remarkable effects on the harvested powers of peculiar parameters such as parameter of non-smoothness and that of nonlinearities are investigated. We then study in section 3.2 the effect on the harvested powers of environmental random fluctuations by the mean of analytical and numerical treatments carried out on the counterpart of the first model which accounts for noises. At last, the hybrid energy harvester exhibits fractional properties. Its dynamics is analytically and numerically studied with respect to FDOs by the mean of the second model. The essential aim of this section is to investigate the effects of the fractional properties on the harmonic response of the system and study the consequence on energy harvesting. We also explore the effects of fractional properties on chaotic regime of such a class of hybrid vibration energy harvester.

3.1 Harvester's harmonic and chaotic response

3.1.1 Potential configuration

We use unless otherwise specified the following physical parameters values throughout this dissertation: $k_0 = 250\,\mathrm{N\,m^{-1}}$, $k_1 = 225\,\mathrm{N\,m^{-2}}$, $k_2 = 50\,\mathrm{N\,m^{-3}}$, $\alpha_0 = 500\,\mathrm{N\,A^{-1}}$, $\kappa_0 = 10\,\mathrm{V\,m^{-2}\,s}$, $\mu_0^+ = 7\,\mathrm{Kg\,s^{-1}}$, $\mu_0^- = 5\,\mathrm{Kg\,s^{-1}}$, $m = 0.4\,\mathrm{Kg}$, $\alpha = 4.0 \times 10^{-3}\,\mathrm{A\,m^{-1}\,s}$, $C_P = 250.0 \times 10^{-9}\,\mathrm{F}$, $R_P = 5000\,\Omega$, $L_P = 50\,\mathrm{H}$, $L = 4.0\,\mathrm{H}$, $C = 0.100 \times 10^{-3}\,\mathrm{F}$, $R = 200\,\Omega$, $X_0 = 1.0 \times 10^{-3}\,\mathrm{m}$, $l = 20.0 \times 10^{-3}\,\mathrm{m}$, $X_{max} = 50.0 \times 10^{-3}\,\mathrm{m}$, $Q_0 = 1.0 \times 10^{-4}\,\mathrm{C}$ and $V_0 = 5\,\mathrm{V}$. Thence, the dimensionless parameters of the different mathematical models can be computed by the mean of formulas given in Eqs. (2.9) and (2.18). In the remainder of this dissertation, values of some physical parameters are monitored with the aim of varying specific dimensionless parameters.

With the above physical parameters, the potential $V(x)$ of the mechanical part of the system has three equilibria among which only one is unstable. This bistable potential is portrayed in Fig. 3.1. The presence of bi-stability makes the system capable of switching

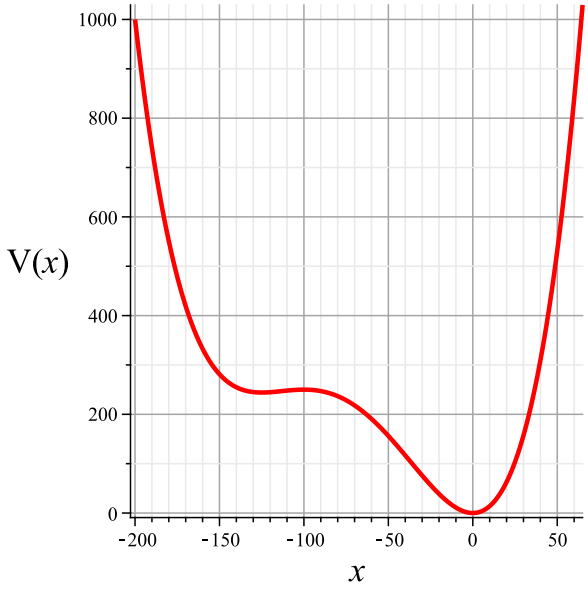

Figure 3.1: Potential energy configuration of the mechanical part of the system.

between stable states.

3.1.2 Response amplitude of harmonic oscillatory motion

3.1.2.1 Resonance and multiple resonance of each part of the device

In this paragraph, because of the complexity of the analytical determination of roots of polynomials $\Gamma^{\pm}$, which are of degree 10, we use the Newton-Raphson algorithm to determine those roots. Thence, amplitude a is determined and a semi-analytical evaluation of amplitudes b and c is obtained by the mean of formulas (2.21c) and (2.21b). These amplitudes can also be directly estimated by the mean of numerical integration of Eq. (2.8) with the fourth-order Runge-Kutta algorithm. The results of our calculations are provided in Figs. 3.2 and 3.3. In Figure 3.2, are depicted the analytical and the numerical frequency-response curves. The agreement between both results illustrates the effectiveness of present analytical treatment. However, this consistency does not hold irrespectively of the values of non-smoothness (damping) coefficients ν_1 and ν_2. Yet, good agreement appears in the range of damping parameters for which the system's response is harmonic. It can be seen in Figure 3.2 that the mechanical vibrations, as well as the electrical oscillations, exhibit a resonance behavior. In low-frequency regime, the amplitude of the electromagnetic oscillations is larger than that of the piezoelectric ones. The opposite is observed in the high-frequency regime.

In the figure below, the blue and green solid lines are analytically obtained from the smooth version of system (2.8) in cases $\mu_0 = \mu_0^+$ and $\mu_0 = \mu_0^-$ respectively. For Figs. 3.2(a), (b) and (c), the thick red curves and the black dots are analytical and numerical results obtained from system (2.8). For Fig. 3.2(d), blue and green dotted lines represent trajectories obtained with initial conditions ($x = 0.2$, $\dot{x} = 0$, $y = 0$, $\dot{y} = 0$, $z = 0$, $\dot{z} = 0$) and ($x = -0.2$, $\dot{x} = 0$, $y = 0$, $\dot{y} = 0$, $z = 0$, $\dot{z} = 0$) respectively, the red solid line stands for the limit-cycle. Parameters are $\nu_1 = 0.3$, $\nu_2 = 0.05$, $\mu_e = 1.0$, $\mu_P = 16.0$, $\omega_1 = 0.5$, $\omega_3 = 5.66$, $\lambda_1 = 0.0045$, $\lambda_2 = 0.00002$, $\gamma_0 = -0.125$, $\gamma_1 = 0.002$, $\gamma_2 = 0.02$, $\beta_0 = 10.0$, $\beta_1 = -0.16$, $\beta_2 = -1.6$, $\delta = 0.001$, $\eta = -64.0$ and $F_0 = 0.02$.

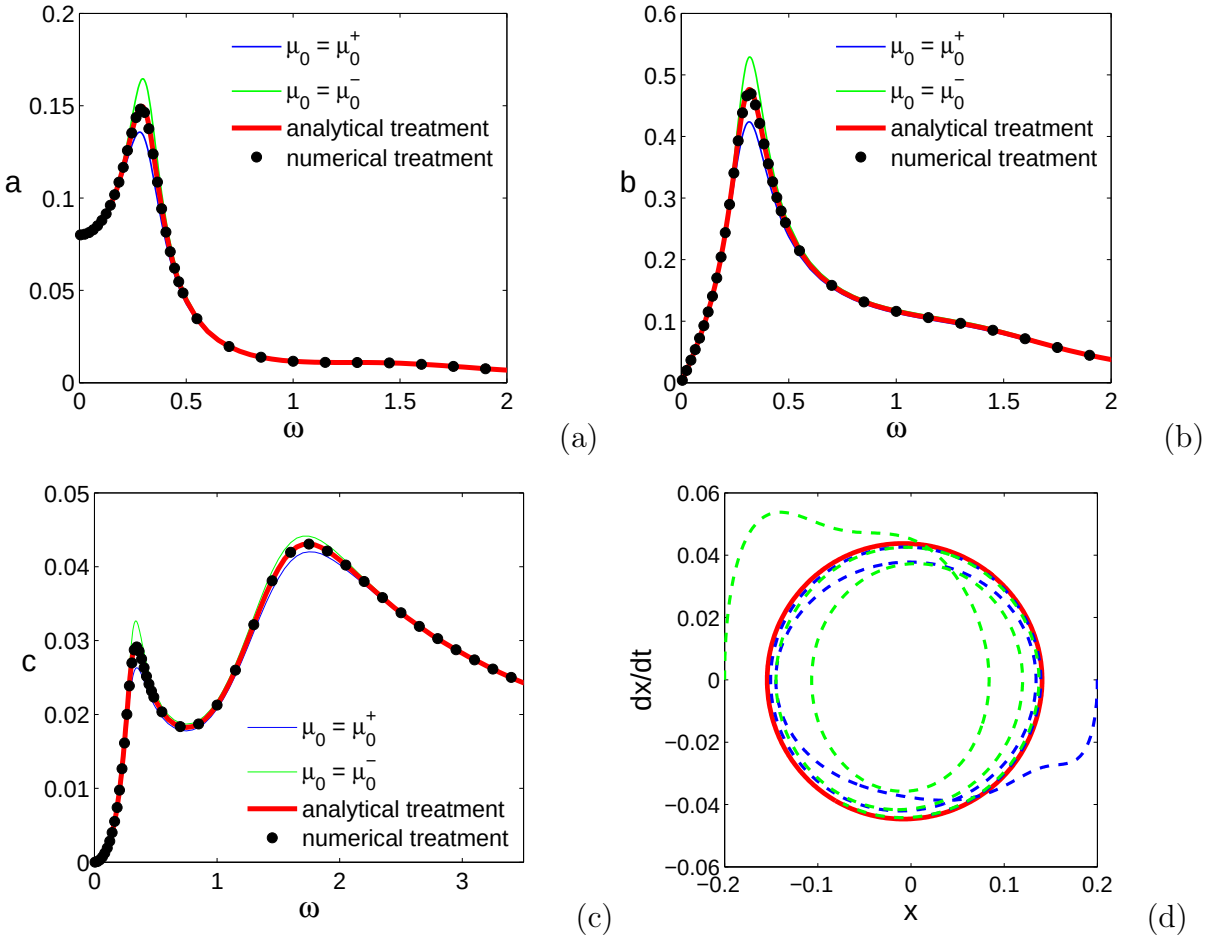

Figure 3.2: Frequency-response curves: amplitudes of (a) mechanical vibrations, (b) electromagnetic vibrations and (c) piezoelectric ones versus driving frequency and (d) phase space structure of the mechanical oscillator.

3.1.2.2 Effect of the damping, nonlinearity, coupling coefficient and excitation strength on piezoelectric oscillation amplitude

In Figs. 3.3(a) and (b), the frequency-response curves, the amplitudes of these oscillations monotonously decrease as the damping parameter ν_1 or the nonlinear parameter λ_2 increases. However, the vibrations also plainly show a resonant structure as the coupling parameter γ_2 is varied in Fig. 3.3(c). The figure Fig.3.3(d)), the amplitude of the oscillations increases monotonically as a function of force excitation. Note that we have monitored the magnetic coupling factor α_0 and the damping parameter μ_0^+, to vary γ_2 and ν_1 respectively. For instance, to obtain Fig. 3.3(a), parameter μ_0^+ is varied. This variation involves that of ν_1 and ν_2. Then, the amplitude is computed and plotted with respect to ν_1. The variations of the amplitudes of mechanical and electromagnetic oscillations have the same trend as the variations provided in Fig. 3.3. The thick solid lines stand for the analytical result while cycles result from direct computation of system (2.8). Other parameters in Fig. 3.2 are kept unchanged and $\omega = 0.3$.

3.1.3 Effect of both amplitude and frequency of the harmonic excitation on the output powers of the device

The output (or harvested) power is an essential quantity in any energy harvesting device. These devices are designed to operate in the parameters' regime that delivers an optimum output power. For the present system, which involves two transduction mechanisms, we define the electromagnetic and the piezoelectric output powers respectively as:

$$\tilde{P}_1 = R\left(\frac{dq}{d\tau}\right)^2 \quad \text{and} \quad \tilde{P}_2 = \frac{v^2}{R_P}. \tag{3.1}$$

Setting

$$P_1 = \frac{LC}{RQ_0^2}\tilde{P}_1 = \dot{y}^2 \quad \text{and} \quad P_2 = \frac{R_P}{V_0^2}\tilde{P}_2 = z^2, \tag{3.2}$$

the corresponding dimensionless output powers, their maximum values (or magnitudes) P_{1max} and P_{2max} are evaluated as:

$$P_{1\,\max} = \frac{\omega}{\pi}\int_0^{\frac{2\pi}{\omega}} \dot{y}^2 dt \quad \text{and} \quad P_{2\,\max} = \frac{\omega}{\pi}\int_0^{\frac{2\pi}{\omega}} z^2 dt. \tag{3.3}$$

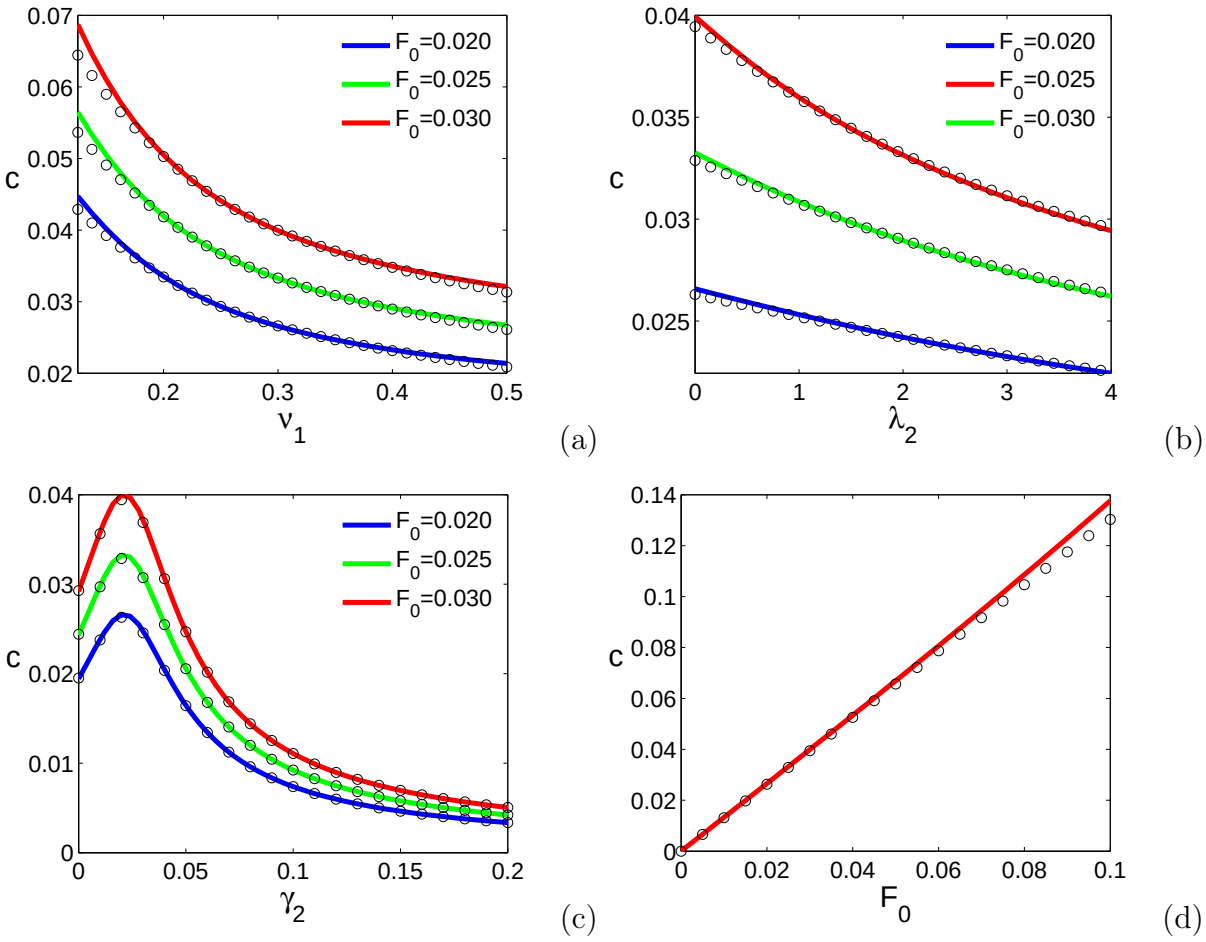

Figure 3.3: Amplitude of the piezoelectric oscillations versus (a) damping, (b) nonlinearity and (c) coupling coefficients, and versus (d) the excitation strength.

They are related to the amplitudes b and c of the electrical vibrations. The variations of these output powers versus the excitation frequency and strength are depicted in Fig. 3.4.

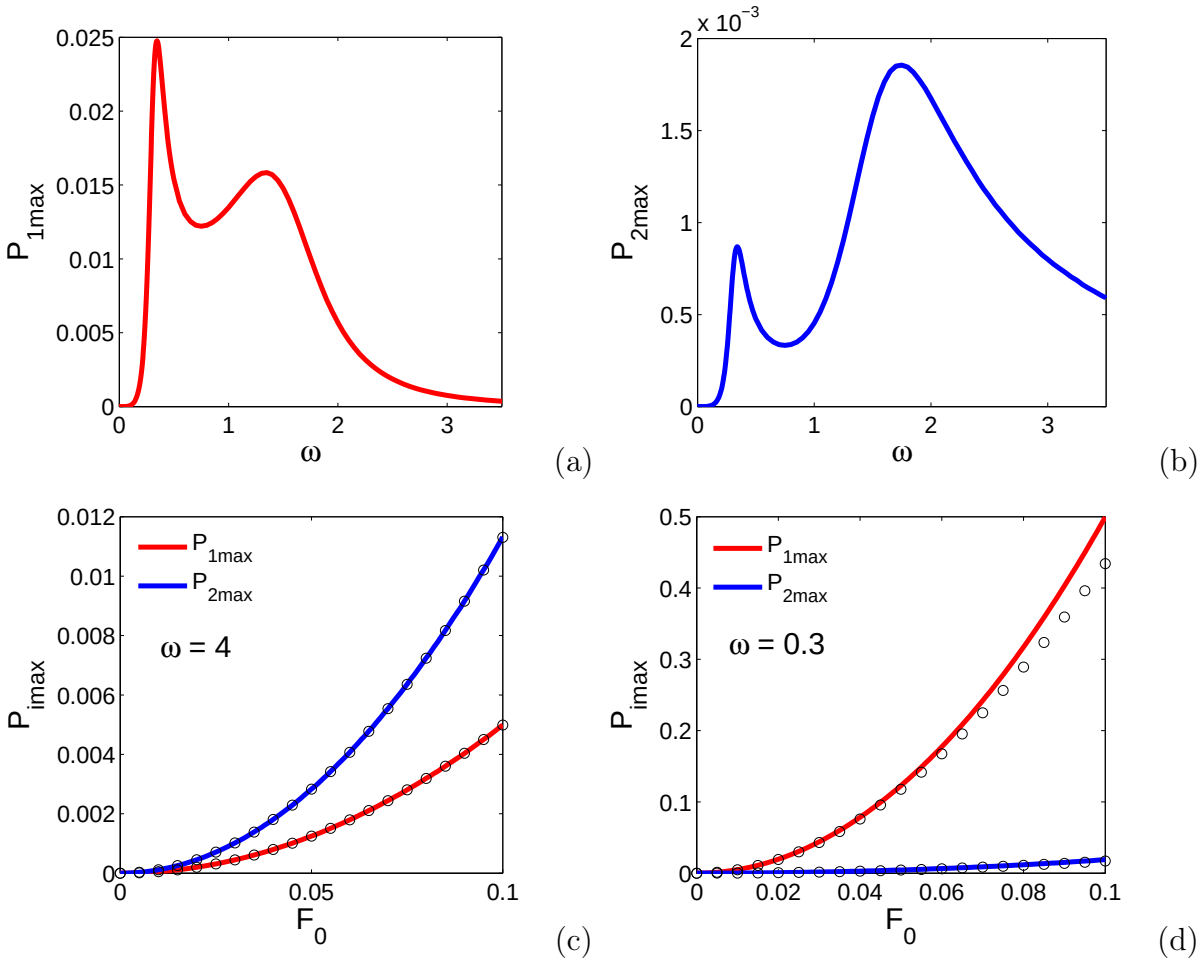

Figure 3.4: Output powers versus the excitation's frequency and strength. (a,b) Output power versus excitation frequency and (c,d) Output power versus excitation strength.

Parameters in Fig. 3.2 are kept unchanged unless otherwise specified. The thick solid lines correspond to the analytical result while cycles result from direct computation of system (2.8). Figs. 3.4(a) and (b) indicate that the harvested powers are considerably affected by the driving frequency. In fact, there are some frequencies at which the output powers exhibit a resonant behavior. For instance, in the present parameters regime (that is to say, parameters used in Fig. 3.4), the piezoelectric output power reaches its extreme peak nearly at $\omega = 1.75$. However, at this frequency, as well as in low-frequency regime,

the electromagnetic harvested power is larger than the piezoelectric output power. By inspection of figures 3.4(c) and (d), it is clear that the opposite remark is drawn in the high-frequency regime. Superimposing the curves provided in Fig. 3.4(a) and Fig. 3.4(b), one notes that the later remark holds when $\omega > 3$. Moreover, these output powers monotonously increase with the excitation strength irrespective of the driving frequency as illustrated in Figs. 3.4(c) and (d) checking the figure Fig.3.3(d)). Yet, they monotonously decrease while the damping and the nonlinearity coefficients ν_1 and λ_2 are varied, checked the figure Fig.3.3(a)) and Fig.3.3(b)) . These observations suggest that the transduction mechanisms would be more efficient if the nonlinearities in the mechanical part of the system are reduced and if the mechanical vibrations are under-damped.

To firmly characterize effects of the magnetic coupling and non-smoothness coefficients on the system efficacy, on the one hand, and to firmly compare both transduction mechanisms on the other hand, we define the efficiencies related to both transduction mechanisms in the following paragraph.

3.1.4 Effect of both magnetic coupling and non-smoothness coefficients on the system efficacy

The instantaneous input power, namely the power of the inertial force acting on the moving mass, is expressed as:

$$\tilde{P}_{in} = -m\Gamma(\tau)\frac{dX}{d\tau}. \tag{3.4}$$

Setting

$$P_{in} = \frac{1}{ml^2\omega_e^3}\tilde{P}_{in} = \dot{x}f(t) \tag{3.5}$$

the corresponding dimensionless input power, the normalized efficiency ρ is simply defined by the relation $\rho = \frac{P_{out\,\max}}{P_{in\,\max}}$; where $P_{in\,\max}$ is the magnitude of the dimensionless input power from the driving vibrations and $P_{out\,\max}$ is the magnitude of the dimensionless power delivered to the electrical load. In the present work, $P_{out\,\max}$ represents either the electromagnetic output power magnitude $P_{1\,\max}$ or the piezoelectric output power magnitude $P_{2\,\max}$. We therefore define two normalized efficiencies, which are related to both transduction mechanisms exhibited by the present harvester. It follows from the above

relations that the normalized efficiencies for the electromagnetic and the piezoelectric mechanisms are respectively expressed as:

$$\rho_1 = \frac{b^2\omega}{F_0 a} \quad \text{and} \quad \rho_2 = \frac{c^2}{F_0 a\omega}. \tag{3.6}$$

Note that the normalized efficiencies, as defined above, are not necessarily lower than the unity. However, their variations with the system's parameters have the same trends as the variations of the genuine efficiencies. In fact, it can be shown that the later quantities are related to the normalized efficiencies as follows:

$$\tilde{\rho}_1 = \frac{RQ_0^2}{ml^2\omega_e}\rho_1, \qquad \tilde{\rho}_2 = \frac{V_0^2}{R_P ml^2\omega_e^3}\rho_2. \tag{3.7}$$

Varying μ_0^+ and α_0 in the ranges $[0; 15]$ and $[0; 20]$ respectively, particularly affects the non-smoothness parameter ν_1 and the nonlinear coupling coefficient γ_2. The variation of both later quantities affects the vibrational amplitudes and consequently, it affects the efficiencies. The variations of efficiencies $\tilde{\rho}_1$ and $\tilde{\rho}_2$ with respect to γ_2 and ν_1 are plotted in Fig. 3.5. In Fig. 3.5(a), the upper surface stands for $\tilde{\rho}_1$; the efficiency (in percentage) of the electromagnetic transduction mechanism, while the lower one represents $\tilde{\rho}_2$, the efficiency of the piezoelectric transduction mechanism. Parameters in Fig. 3.2 are kept unchanged unless otherwise specified, $F_0 = 0.03$, $\omega = 0.3$ for Fig. 3.5(a) and $\omega = 4$ for Fig. 3.5(b). This result has been obtained for $\omega = 0.3$. Conversely, in Fig. 3.5(b) obtained with $\omega = 4$, the upper surface represents $\tilde{\rho}_2$ and the lower one stands for $\tilde{\rho}_1$. It is therefore clear from Fig. 3.5 that in the low frequency regime, the electromechanical mechanism is more efficient that the piezoelectric one for a broad range of parameters γ_2 and ν_1 even if both efficiencies are very small. The opposite is observed in the high frequency regime. Moreover, by reducing the mechanical damping and by choosing the best nonlinear magnetic coupling coefficient, the efficiencies of both transduction mechanisms are improved.

3.1.5 Transition to chaos

3.1.5.1 Lyapunov exponent and numerical threshold for chaotic motion

As mentioned above, the excitation strength can be increased to improve the efficacy of the device as long as its response remains harmonic. However, as reported

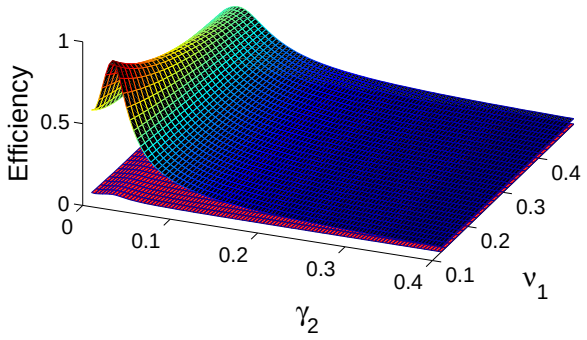

(a)

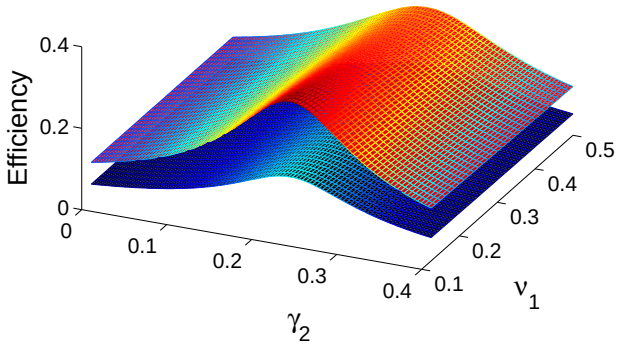

(b)

Figure 3.5: Efficiency versus γ_2 and ν_1.

within several papers in the literature, the excitation strength may considerably affect the response's regime of the system. In other words, increasing the excitation strength may induce the transition from periodic oscillations to chaotic ones; whereas periodic vibrations are preferable for external power storage circuitry because they are more regular in waveform. It is therefore necessary to assess the threshold of F_0 for the onset of chaos. To this end, we compute the largest Lyapunov exponent [186], which is a major indicator of predicting instability and emergence of chaos.

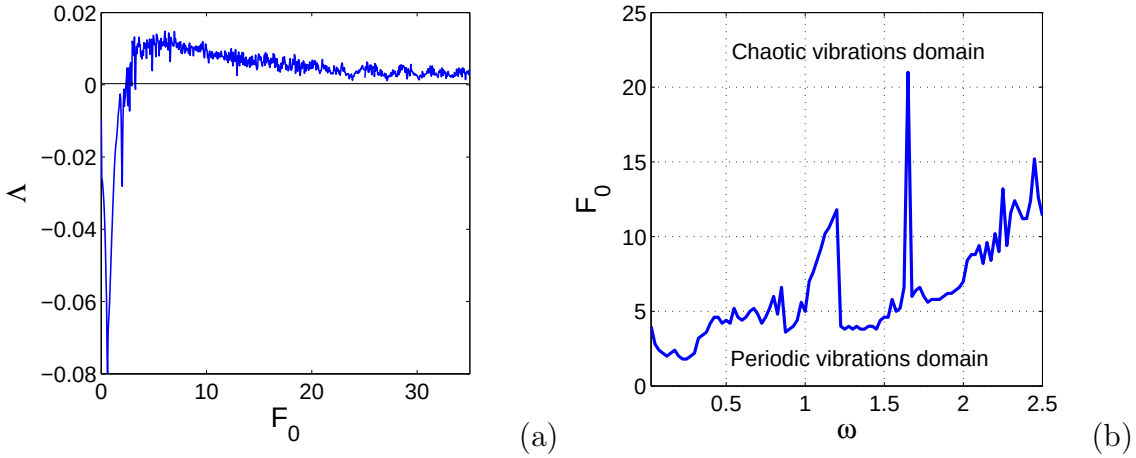

Figure 3.6: Largest Lyapunov exponent and transition curve from regular to chaotic vibrations.

Assume that the state vector of the differential system (2.8) is subjected to a small perturbation vector denoted $\overrightarrow{Z}(t) = (x_1(t), u_1(t), y_1(t), v_1(t), z_1(t), w_1(t))$. Specifically, $\overrightarrow{Z}(t)$ represents a slight variation of the state vector of Eq. (2.8), and thus obeys the variational system resulting from (2.8). Solving system (2.8) and its related variational system by the mean of the fourth-order Runge-Kutta algorithm, the largest Lyapunov exponent Λ is computed as:

$$\Lambda = \lim_{t \to +\infty} \frac{1}{t} \ln \left(\frac{\|Z(t)\|}{\|Z(0)\|} \right), \tag{3.8}$$

where $Z(t)$ is the perturbation vector at time t, $Z(0)$ is a given initial perturbation vector and $\|\cdot\|$ denotes the norm. The results of our computation are reported in Fig. 3.6. Fig. 3.6(a) provides the variation of the largest Lyapunov exponent with respect to F_0 for $\omega = 0.3$ and the parameters in Fig. 3.2 are kept unchanged. It is seen that for $F_0 \leq 2$, Λ

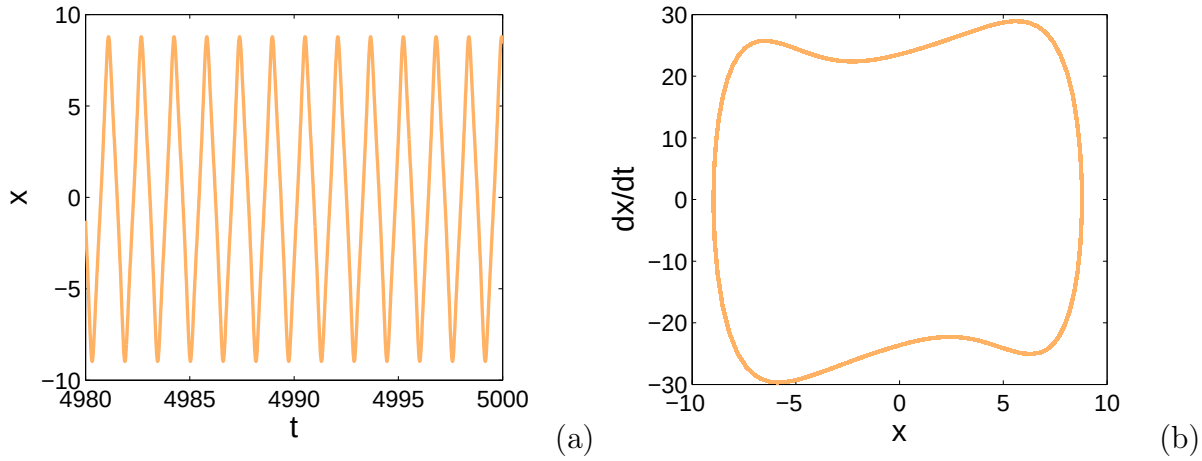

Figure 3.7: Time series and phase space diagram curve from regular vibrations. (a) periodic oscillations and (b) state space diagram.

is negative and the device exhibits periodic vibrations which could be harmonic. Beyond $F_0 = 3.5$, it is seen in Fig. 3.6(a) that Λ is positive. Therefore, nearby trajectories starting with almost the same initial conditions exponentially diverge in the course of time, that is to say, trajectories are high sensitive to initial conditions and chaotic vibrations take place. These vibrations are probably made of interwell jumps. In Fig. 3.6(b) is depicted, in the parameter space (ω, F_0), the transition curve from periodic vibrations to chaotic ones. This result has been obtained by seeking the threshold values of ω and F_0 for which Λ changes sign. It provides a good insight of the domain in which periodic orbits of high energy can be obtained. As a matter of fact, it is seen that the harvester can sustained periodic high-energy orbits at large excitation frequencies. For instance, the system exhibits a periodic intrawell vibration for $\omega = 4$ and $F_0 = 50$ see in Fig. 3.7. Such vibration yields a high energy harvesting performance.

3.1.5.2 Phase portrait and time evolution

To verify the result provided in Fig. 3.6(b), we compute the time series of system (2.8) for parameters taken in the periodic vibrations domain and for parameters taken in the chaotic vibrations domain also. The results are respectively depicted in Figs. 3.8(a) and (c) and Figs. 3.8(b) and (d). Figs. 3.8(a) and (c) show the state space diagram and the corresponding time series for a periodic vibration obtained with $\omega = 0.5$ and $F_0 = 4$.

Fig. 3.8(a) specifically illustrates the limit cycle toward which converge the phase space trajectories. It is not worth mentioning that the initial conditions are null for the time series of Fig. 3.8(c). Contrariwise, the phase space diagram of Fig. 3.8(b) reveals chaotic behavior and the corresponding time series provided in Fig. 3.8(d) exhibit sensitivity to initial conditions. As a matter of fact, the blue solid line results from null initial conditions while the black one results from initial conditions $(10^{-8}, 0, 0, 0, 0, 0)$. These results are obtained with $\omega = 0.5$ and $F_0 = 6$. Other parameters are those used in Fig. 3.2.

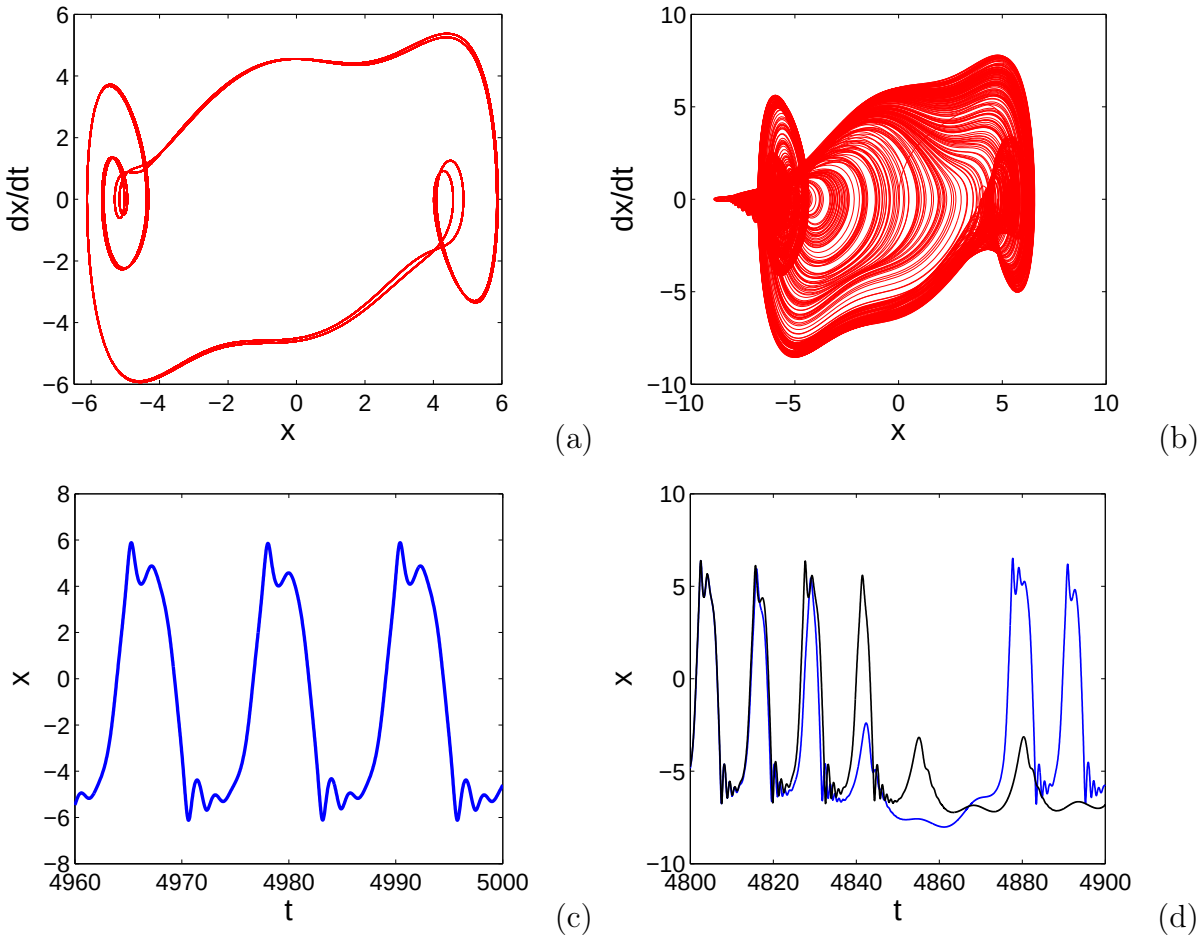

Figure 3.8: Phase space diagrams and corresponding time series illustrating regular and chaotic dynamics.

.

3.1.6 Concluding remarks

Conclusively, the main objectives of this section was to investigate the effects of (a) the nonlinear magnetic coupling and (b) the parameters of non-smoothness and nonlinearities, on the performance of a hybrid vibration energy harvester with a non-smooth mechanical damping. By the mean of a modified harmonic balance method, we have obtained the stationary harmonic response of the system to harmonic excitation. Using this response, we have then investigated the system's performance. We found that, the electromagnetic and piezoelectric transduction mechanisms are improved and the harvester efficiencies, increased, by weakening the nonlinearities and the damping of the harvester mechanical part and by choosing peculiar nonlinear magnetic coupling coefficients. Increasing the harmonic excitation strength is useful to augment the harvested powers, however, it can not be increased beyond a threshold value when one desires a harvested power of regular waveform. In fact, augmenting it further induces transition to chaotic behavior, and results in a non-periodic harvested power, which is inappropriate for energy storage devices.

3.2 Noise effects on the system response and efficiency

3.2.1 Stationary probability density functions for the amplitudes

Clearly, it comes out from the analytical development provided in section 2.2.1.2 that the stationary PDFs (Eqs. (2.48), (3.4) and (3.5)) have, each of them, a unique peak irrespective of the values of the system parameters. The amplitude c_m for which the peak of the probability density function P_c (for instance) is reached, is obtained by solving $\frac{dP_c}{dc} = 0$. It yields

$$c_m = \frac{\sigma_5}{\sqrt{\mu_P}}. \tag{3.9}$$

The distributions of amplitudes $a(t)$, $b(t)$ and $c(t)$, obtained from the present analytical treatment, are thus only unimodal. Moreover, the average oscillatory amplitude of the

harvester's piezoelectric part is given by

$$\langle c \rangle = \int_0^{+\infty} cP_c(c)dc. \tag{3.10}$$

Phenomenological transitions, consisting in a modification of the position and the width of the PDF's peak, common to other models for vibration energy harvesting systems [4,9], are also observed in the present model. Specifically, the position of the PDF extreme point; c_m for instance, increases (moves away from zero) and the peak $P_c(c_m)$ becomes lower (decreases) as the modulation amplitude F_0 increases (see Fig. 3.9). Similar transitions appear when the noises' intensities and the correlation times vary.

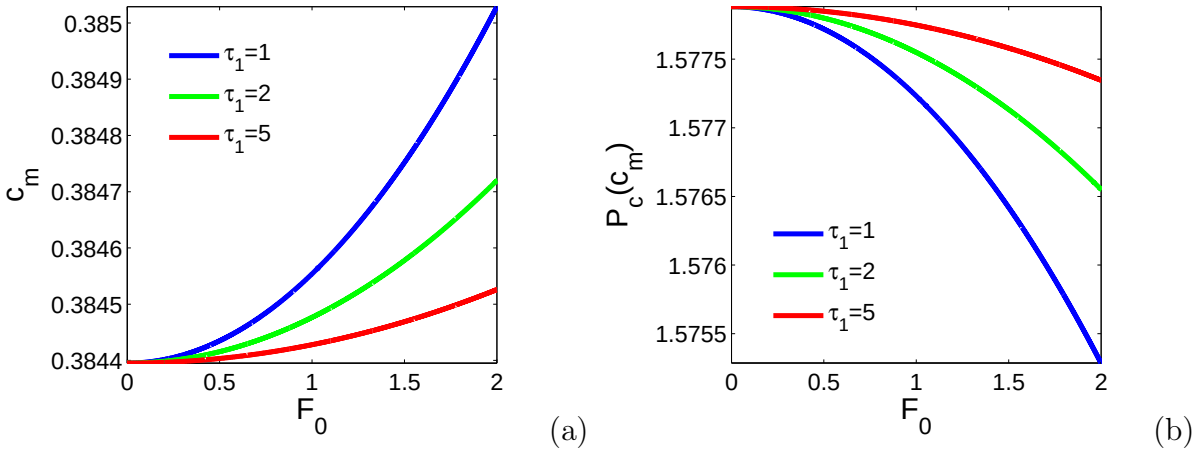

Figure 3.9: Variation of the peak position (a) and (b) the extreme point of PDF P_c versus the modulation amplitude F_0 for different values of the correlation time τ_1.

To check the consistency of the analytical technique of derivation of PDFs, the stationary transition PDFs for the amplitudes are obtained through the Monte-Carlo simulations based on the the computation of a long time evolution of the random amplitudes $a(t)$, $b(t)$ and $c(t)$ with the second order stochastic Runge-Kutta algorithm [179], as described in section 2.2.1.2. These results are superimposed to the analytically obtained ones, provided in Fig. 3.10. Parameters are $\nu_1 = 0.03$, $\nu_2 = 0.005$, $\mu_e = 0.01$, $\mu_P = 0.016$, $\omega_1 = 1.0$, $\omega_3 = 5.66$, $\lambda_1 = 0.0045$, $\lambda_2 = 0.00002$, $\gamma_0 = -0.00125$, $\gamma_1 = 0.00002$, $\gamma_2 = 0.0002$, $\beta_0 = 0.10$, $\beta_1 = -0.0016$, $\beta_2 = -0.016$, $\delta = 10^{-6}$, $\eta = -0.064$, $\omega = 0.3$, $D_2 = 0.1$, $\tau_2 = 4.5$, $D_3 = 0.1$ and $\tau_3 = 0.1$. It is clearly shown in Fig. 3.10 that the preceding approximate analytical treatment agrees with the numerical result. However, other

results of our computations show that the agrement between both approaches appears only in the weak damping, nonlinearity and coupling parameters regime. When coupling and nonlinearity parameters are no longer sufficiently small, stochastic averaging method can no longer be trusted [4, 177]. As a matter of fact, the analytically predicted PDFs (Eqs. (2.48), (3.4) and (3.5)) are independent of the nonlinearity and coupling coefficients λ_i, β_i and γ_i, while numerically computed PDFs may be sensitive to these parameters. We therefore resort to numerical simulations to investigate the effects of the noises' parameters, the coupling and the nonlinear coefficients on the probability density functions, the mean amplitudes and the mean output power of the transducer.

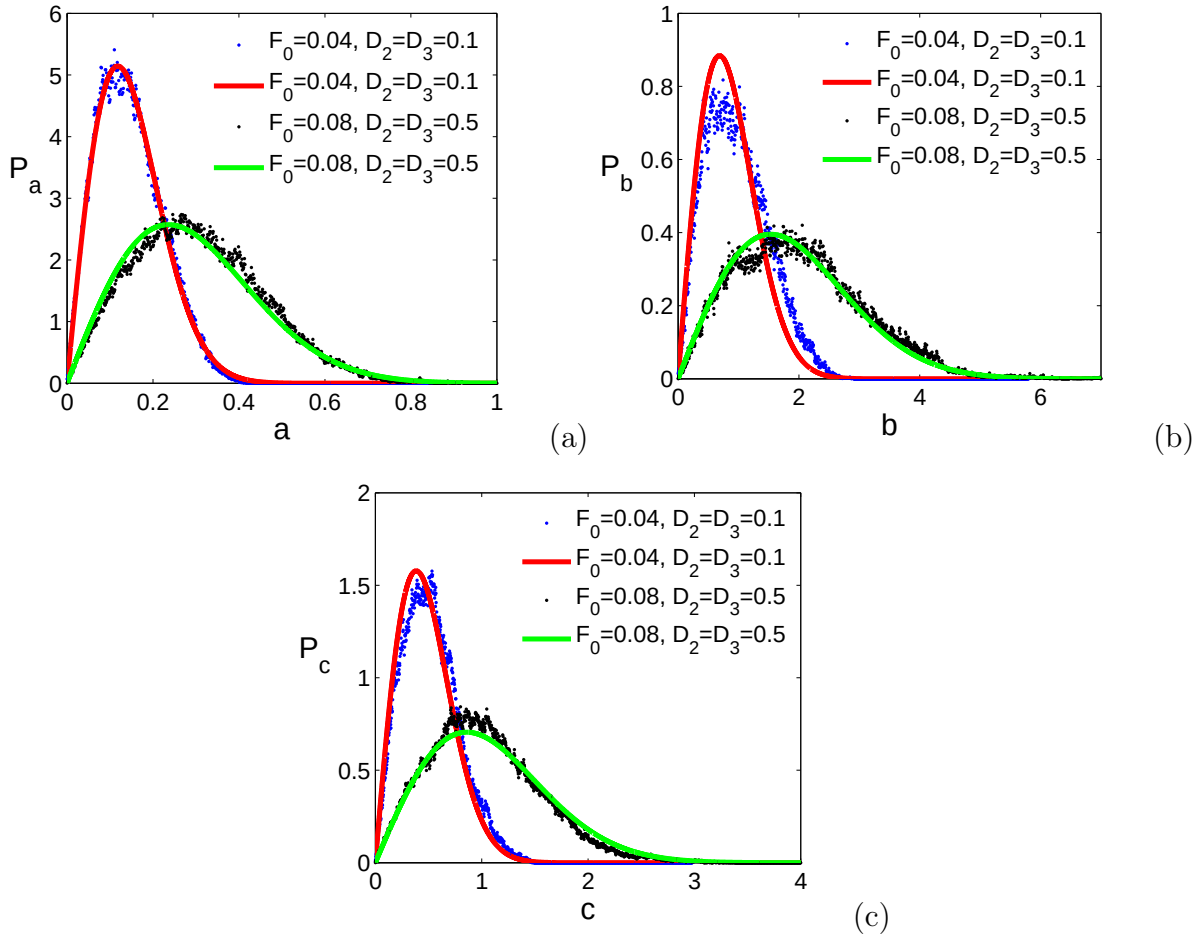

Figure 3.10: Stationary probability density functions for amplitudes. Thick solid lines result from the averaging technique, while dots result from direct computation.

3.2.2 Effect of nonlinearity: Stochastic P-bifurcation

Some of the results of our computations are provided in Fig. 3.11. These results are obtained with large coupling parameters and large parameters of nonlinearity, by the mean of Monte-Carlo simulations. Parameters are $\nu_1 = 0.03$, $\nu_2 = 0.005$, $\mu_e = 0.01$, $\mu_P = 0.016$, $\omega_1 = 1.0$, $\omega_3 = 5.66$, $\lambda_1 = 6.2$, $\gamma_0 = -12.5$, $\gamma_1 = 0.2$, $\gamma_2 = 2.0$, $\beta_0 = 10.0$, $\beta_1 = -0.16$, $\beta_2 = -1.6$, $\delta = 0.001$, $\eta = -64.0$, $F_0 = 0.02$, $\omega = 0.3$, $\tau_1 = 5$, $D_2 = 0.5$, $\tau_2 = 4.5$, $D_3 = 0.5$ and $\tau_3 = 0.1$. Fig. 3.11(a) shows the PDF for amplitude a, numerically obtained with different values of λ_2. It is seen that the shape of this PDF considerably depends on λ_2 while, for the same parameters used in this figure, the analytically derived PDF for amplitude a (given by Eq. (2.48)) does not depend on λ_2 and has the same shape as the PDFs provided in Fig. 3.10, however, with a higher peak. In Fig. 3.11(b), the PDF for amplitude c obtained from simulations is depicted. We notice that this PDF, or precisely the height of its peak, also depends on λ_2. However, its analytically obtained counterpart (which can be plotted using Eq. (3.5)) is independent of λ_2 and has a higher peak. The PDF for amplitude b, obtained numerically with parameters of Fig. 3.11, also depends on λ_2 and has a shape similar to that of P_c. Summarily, by plotting the analytically derived PDFs P_a and P_c and superimposing to their counterparts given in Figs. 3.11(a) and (b), it appears a considerable gap, in terms of shape and peak height, between the analytically predicted PDFs and the numerically computed ones. Therefore, the numerical and the analytical treatments do not agree for parameters used in Fig. 3.11. In addition, varying λ_2 which is a parameter of the harvester mechanical part, has affected the PDFs P_b and P_c for the amplitudes b and c of the harvester electrical part, because the coupling strength is considerable. Similarly, it can be shown that varying the "mechanical noise" parameters (τ_1 for instance) affects the PDFs P_b and P_c. As stated above, the results to be trusted is that provided by the Monte-Carlo simulations. Moreover, when the nonlinear coefficients are increased, one witnesses transitions in the shape of the probability distributions. As a matter of fact, when λ_2 varies, the PDF P_a bifurcates from a unimodal shape (or single-peak mode) to a bimodal shape (double-peak mode) as demonstrated in Fig. 3.11(a). This qualitative change of the density of an invariant measure related to a stochastic dynamical system, is termed in the framework of stochastic bifurcation theory as stochastic

P-bifurcation. This phenomenon is not theoretically predicted by the stochastic averaging technique. In fact, it comes out from the above analytical treatment that the PDFs have, each of them, only one peak irrespective of values of system's parameters. However, in the hard coupling regime where the stochastic averaging technique is no longer prominent, stochastic P-bifurcation appears in the mechanical part of the harvester as λ_2 varies. At the same time, the electrical part of the harvester only exhibits phenomenological transitions which consist in a modification of the position and the width of the peak of the PDFs. That is to say, the PDF P_c, as well as P_b remain unimodal as observed in Fig. 3.11(b). A similar switch from the unimodal shape to a bimodal one may also be observed in the electrical part of the harvester when the noise intensity (D_2 for instance) is varied and the other parameters, properly set.

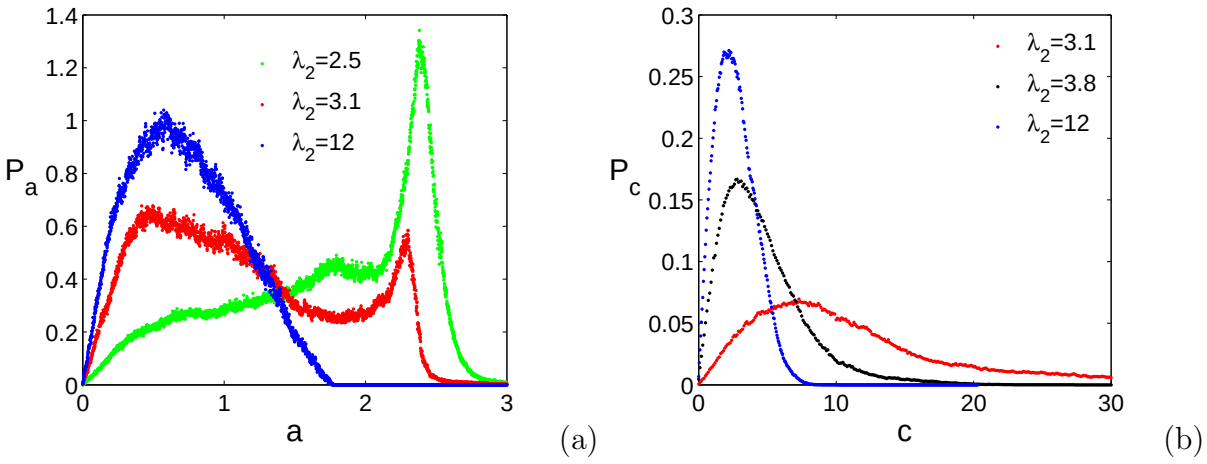

Figure 3.11: Probability density functions for amplitudes: Stochastic P-bifurcation exhibited in the hard coupling and nonlinearity parameters regime.

3.2.3 Average output powers under bounded noise and colored noise excitations

From the formulas of the dimensionless electromagnetic and piezoelectric output powers given in Eq. (3.2), it follows that their mean values are respectively related to the mean square values of the electric current (across resistor R) and the voltage (across R_P)

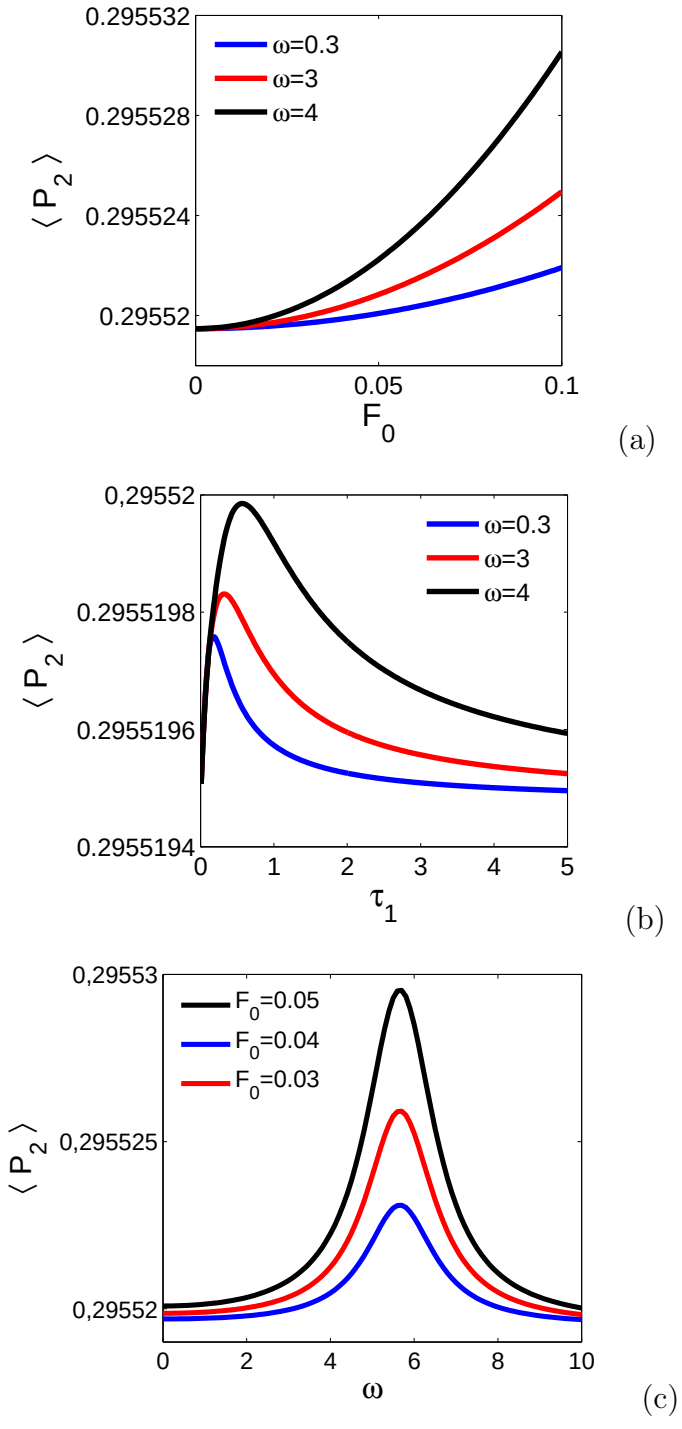

Figure 3.12: Dimensionless average output power of the piezoelectric circuitry versus (a) bounded noise amplitude, (b) bounded noise relaxation time and (c) frequency.

and can be expressed as:

$$\langle P_1\rangle = \int_0^{+\infty} b^2 P_b(b)db, \qquad \langle P_2\rangle = \int_0^{+\infty} c^2 P_c(c)dc. \tag{3.11}$$

Hence, it follows that

$$\langle P_1\rangle = \frac{2\sigma_3^2}{\mu_e}, \qquad \langle P_2\rangle = \frac{2\sigma_5^2}{\mu_P}. \tag{3.12}$$

From the knowledge of the expressions of σ_3 and σ_5, it easily appears that the mean output powers $\langle P_1\rangle$ and $\langle P_2\rangle$ monotonously increase with the colored noise intensities D_2 and D_3 respectively. In addition, $\langle P_1\rangle$ decreases as τ_2 and μ_e vary. The variations of the average output power $\langle P_2\rangle$, of the piezoelectric part of the harvester, with respect to the bounded noise parameters are computed and given in Fig. 3.12. $D_2 = 0.1$, $D_3 = 0.1$, $F_0 = 0.02$ for Fig. 3.12(b), other parameters are those used in Fig. 3.10. One can see that, $\langle P_2\rangle$ monotonously increases with the bounded noise amplitude F_0. Moreover, it exhibits a resonance effect as the relaxation time τ_1 or the frequency ω of the bounded noise varies. Therefore, there exists a proper level of noise, determined by the quantity $\sqrt{\frac{2}{\tau_1}}$ (see Fig. 3.12(b)) and an optimum excitation frequency (see Fig. 3.12(c)) for which the mean output power is maximized. Fig. 3.12(b) demonstrates that the standard deviation of the amplitude of piezoelectric vibrations exhibits a single-peak mode as $\sqrt{\frac{2}{\tau_1}}$ varies. This resonance behavior correspond to the stochastic resonance phenomenon. It arises in several systems ranging from electronic systems [187, 188] to biological systems [189–191] and, as far as the present system is concerned, a particular attention has to be paid to it in further studies.

3.2.4 Concluding remarks

This section focused on the investigation of the effect of environmental random fluctuations on the mean output powers. Under bounded and colored noise excitation, we derived the stationary PDFs for the amplitudes of the mechanical and the electrical parts of the harvester, by the mean of the stochastic averaging procedure. We found that in the parameters' regime for which the averaging technique is meaningful, that is to say, in the regime of weak coupling, damping and nonlinearity parameters, the stationary PDFs only exhibited a single-peak mode as the system's parameters varied. This result has

been verified by the Monte Carlo simulation. Moreover, we found in such parameters' regime that the mean output powers increase with the colored noises' intensities and the harvester piezoelectric part output power exhibits a resonance behavior as some bounded noise parameter vary. This behavior demonstrates that, for fixed colored noise intensities, the performance of the harvester piezoelectric part is maximized for optimum bounded noise relaxation time and average frequency. This result reveals the stochastic resonance phenomenon. For large coupling parameters, that is, in the parameter regime for which stochastic averaging technique is meaningless, we found by the mean of the Monte Carlo simulation that by increasing a particular parameter of nonlinearity, the stochastic P-bifurcation appears in the mechanical part of the energy harvester. This result sustains the idea of Siewe *et al.* [4] according to which the stochastic P-bifurcation can be exhibited by a stochastic dynamical system although not predicted theoretically by the stochastic averaging technique. The present work enables designers to get an insight on the constraint to be tackled in order to improve the device performance.

3.3 Fractional properties' effects on the system dynamics

3.3.1 Fractional derivatives orders' effects on the harmonic oscillatory regime

In the subsequent paragraphs, we consider the mathematical model (2.17) referred to as *second model*. Varying the frequency of the excitation, the amplitudes a, b and c of its approximate harmonic solution are evaluated as mentioned in section 2.2.1.1 and the so-called *frequency-response curves* are plotted in Fig. 3.13. Parameters are $\nu_1 = 0.3$, $\nu_2 = 0.05$, $\mu_e = 1.0$, $\mu_P = 16.0$, $\omega_1 = 0.5$, $\lambda_1 = 0.0045$, $\lambda_2 = 0.00002$, $\gamma_0 = -0.125$, $\gamma_1 = 0.002$, $\gamma_2 = 0.02$, $\beta_0 = 10.0$, $\beta_1 = -0.16$, $\beta_2 = -1.6$, $\delta = 0.001$, $\eta = -64.0$, $\omega_e = 50.0$, $\omega_P = 282.84$ and $F_0 = 0.02$. These are curves depicting the variations of the oscillators' amplitudes versus the excitation frequency. In a similar way, the variations of these amplitudes with respect to parameters ϵ and θ are provided (in solid lines) in Fig. 3.14. Moreover, the *amplitude-response curves*, which illustrate the oscillations amplitudes

variation with respect to the excitation amplitude, are depicted with solid lines in Fig. 3.15.

Analyzing Fig. 3.13, one can notice the variation of the amplitudes with increasing ϵ and θ. Moreover, Fig. 3.13 illustrates a resonance structure whose number of peak and peak high are affected by both ϵ and θ. Specifically, the variation of the amplitudes with respect of ϵ considerably depends on the frequency ω. As a matter of fact, as we can notice in Fig. 3.13(c), in low-frequency regime ($\omega < 1$ for instance), the amplitude c decreases with increasing ϵ; whereas, the amplitude c increases with ϵ in the high-frequency regime. This remark can be drawn by comparing the green solid line and the blue dotted line of Fig. 3.13(c). A similar analysis can be made by observing Figs. 3.13(a) and (b). It is clearly shown in Fig. 3.13(c) that c increases with θ. To further probe the evolution of the amplitudes with respect to ϵ and θ, let's evaluate both analytically and numerically the amplitudes as ϵ increases on the one hand, and as θ grows on the other hand. Some of the results obtained in the low-frequency regime ($\omega = 0.3$) are provided in Fig. 3.14. The solid thick curves result from analytical treatment, while circles and dots are obtained through numerical simulations. $\theta = 0.6$ for Figs. 3.14(a) and (c), $\epsilon = 0.8$ for Figs. 3.14(b) and (d) and $\omega = 0.3$. Other parameters in Fig. 3.13 are kept unchanged. Contrariwise to Fig. 3.13(b), Fig. 3.14(b) demonstrates that amplitude b varies with θ (see the insert in Fig. 3.14(b)), however this variation is slow. Fig. 3.14(a) approves the observation that can be made on Fig. 3.13(b), according to which amplitude b increases with ϵ in the low-frequency regime. Fig. 3.14(c) shows that the variation of amplitude c with respect to ϵ is not monotonic, however this variation confirms the observation made on Fig. 3.13(c) because, in the low-frequency regime, the value of amplitude c obtained with $\epsilon = 0.4$ is greater than that obtained with $\epsilon = 1$. Fig. 3.14(d) shows that amplitude c monotonically increases with θ as suggested by Fig. 3.13(c). Note that in the low-frequency regime, amplitude a slowly increases with θ. Its variation with ϵ is similar to that of c. It was enough to provide in this report the variation of amplitudes with respect to ϵ and θ, in the high-frequency regime. The results provided in Fig. 3.14 have been obtained with sufficiently small excitation amplitude F_0. One can see in this figure that numerical results (represented by circles) have the same trend as analytical results (represented by solid lines). This agreement in term of trend and the gap between both

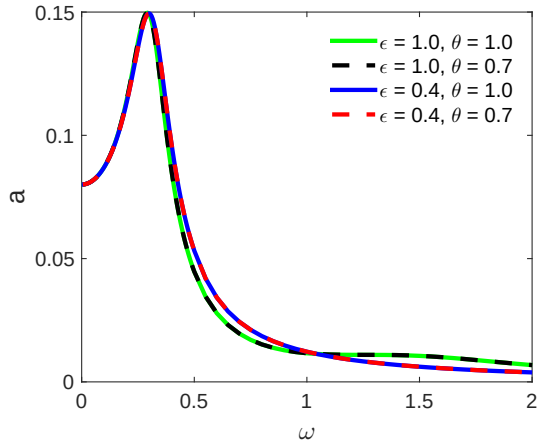

(a)

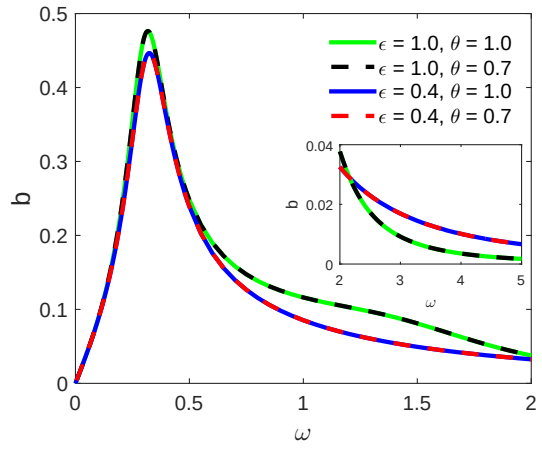

(b)

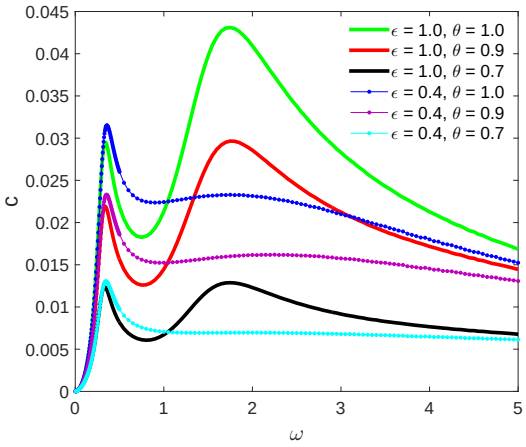

(c)

Figure 3.13: Frequency-response curves: amplitudes of (a) mechanical vibrations, (b) electromagnetic vibrations and (c) piezoelectric ones versus driving frequency; for various FDOs ϵ and θ. These results are analytically obtained.

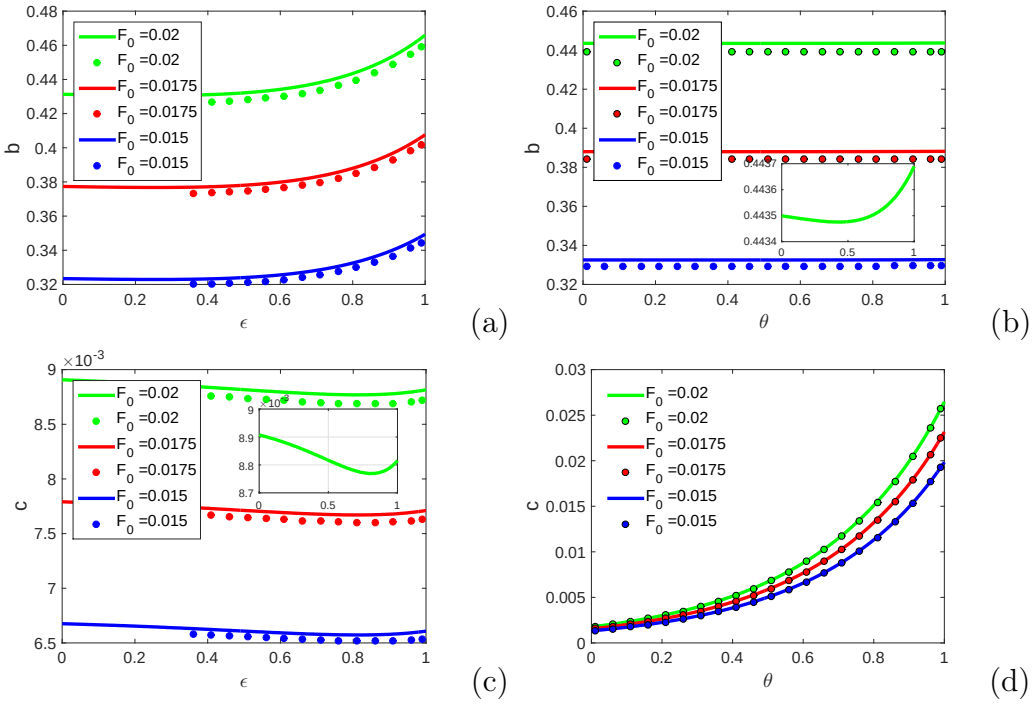

Figure 3.14: Amplitudes of (a,b) electromagnetic vibrations and (c,d) piezoelectric ones versus FDOs.

analytical and numerical results may depend on the system parameters. Inspecting Fig. 3.15, we note that the amplitudes increase with the excitation amplitude as suggested through Fig. 3.14. Note that solid lines stand for analytical results while circles stand for numerical results. Solid thick lines result from analytical method and circles result from direct numerical integrations of system (2.17). Parameters in Fig. 3.13 are kept unchanged unless otherwise specified and $\omega = 0.3$. It is clear, analyzing Fig. 3.15, that the gap between both results drastically depends on the excitation amplitude F_0. The more F_0 increases, the more the gap augments. When F_0 increases further, the trends of both results do no longer agree. This is due to the fact that, the more F_0 increases, the more the system's output deviates from harmonics oscillations.

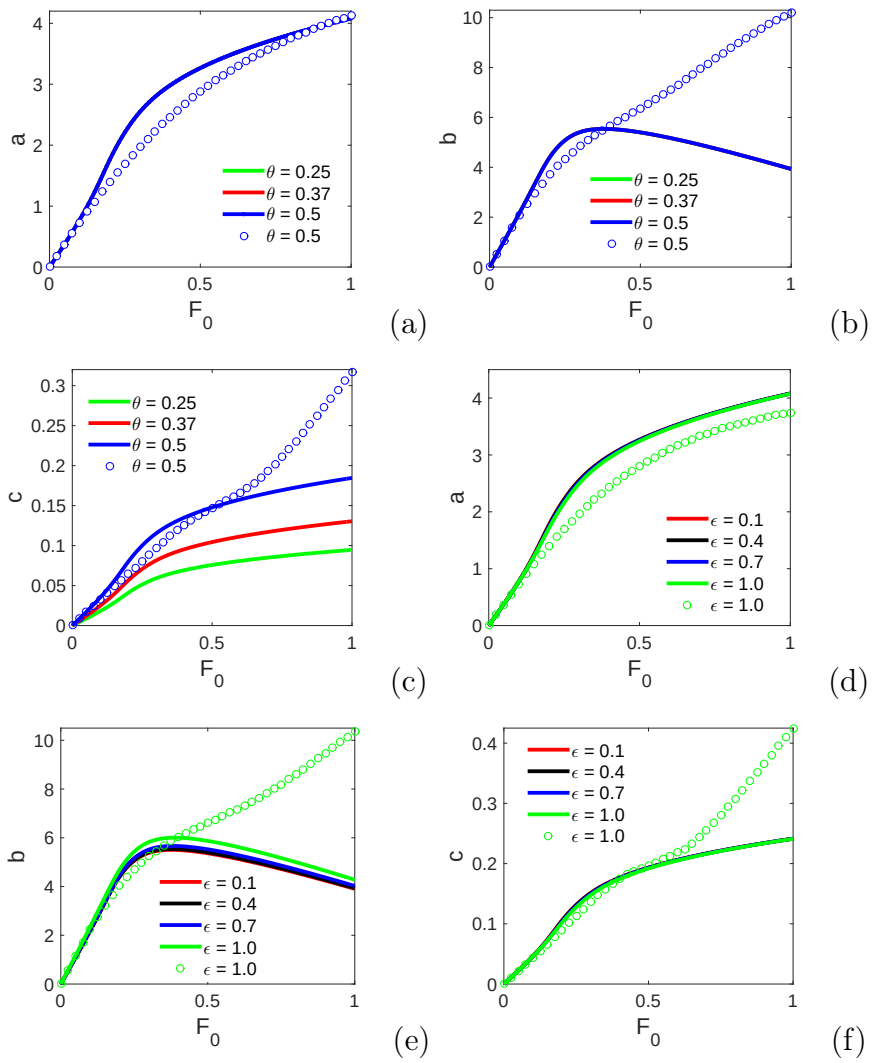

Figure 3.15: Amplitude-response curves: amplitudes of (a) mechanical vibrations, (b) electromagnetic vibrations and (c) piezoelectric ones versus excitation strength.

3.3.2 Fractional order properties and consequences on energy harvesting

We are interested in this section in studying the influence of the orders ϵ and θ of the fractional derivatives upon the harvested powers on the one hand and upon the efficiencies of both transduction mechanisms on the other hand. Following [22], we respectively define, for the present hybrid energy harvester, the electromagnetic and the piezoelectric output powers as follows:

$$\tilde{P}_1 = R\left(\frac{dq}{d\tau}\right)^2 \quad \text{and} \quad \tilde{P}_2 = \frac{v^2}{R_P}. \tag{3.13}$$

Define the corresponding dimensionless output powers

$$P_1 = \frac{LC}{RQ_0^2}\tilde{P}_1 = \dot{y}^2 \quad \text{and} \quad P_2 = \frac{R_P}{V_0^2}\tilde{P}_2 = z^2, \tag{3.14}$$

their maximum values (or magnitudes) P_{1max} and P_{2max} are evaluated as:

$$P_{1\,\max} = \frac{\omega}{\pi}\int_0^{\frac{2\pi}{\omega}} \dot{y}^2 dt \quad \text{and} \quad P_{2\,\max} = \frac{\omega}{\pi}\int_0^{\frac{2\pi}{\omega}} z^2 dt. \tag{3.15}$$

They are related to the amplitudes b and c of the electrical vibrations. It has been shown above that the fractional orders ϵ and θ affect the vibrations amplitudes in general. Specifically, the influence of ϵ on the amplitudes strongly depends on the excitation frequency. Consequently, output powers are affected by fractional orders as well and their variations may considerably be dictated by the value of the oscillation frequency ω. To ascertain these combined effects of the FDOs and excitation frequency, the output powers have been evaluated for several values of ϵ, θ and ω. The results, depicted in Fig. 3.16, illustrate the 3-dimensional variations of output powers versus ω and ϵ on the one hand, and versus ω and θ on the other hand.

As suggested by the dependence of the amplitudes on fractional derivatives orders, figures 3.16(a)-3.16(d) demonstrate that the harvested powers also depend on ϵ and θ. By inspection of Figs. 3.16(a) and (b), it is clear that the variation of the output powers with fractional derivative order (FDO) ϵ depends on the frequency regime. As a matter of fact, depending on the frequency band, output powers can increase or can decrease with ϵ. This is clearly illustrated in the inserts within Figs. 3.16(a) and (b). In these

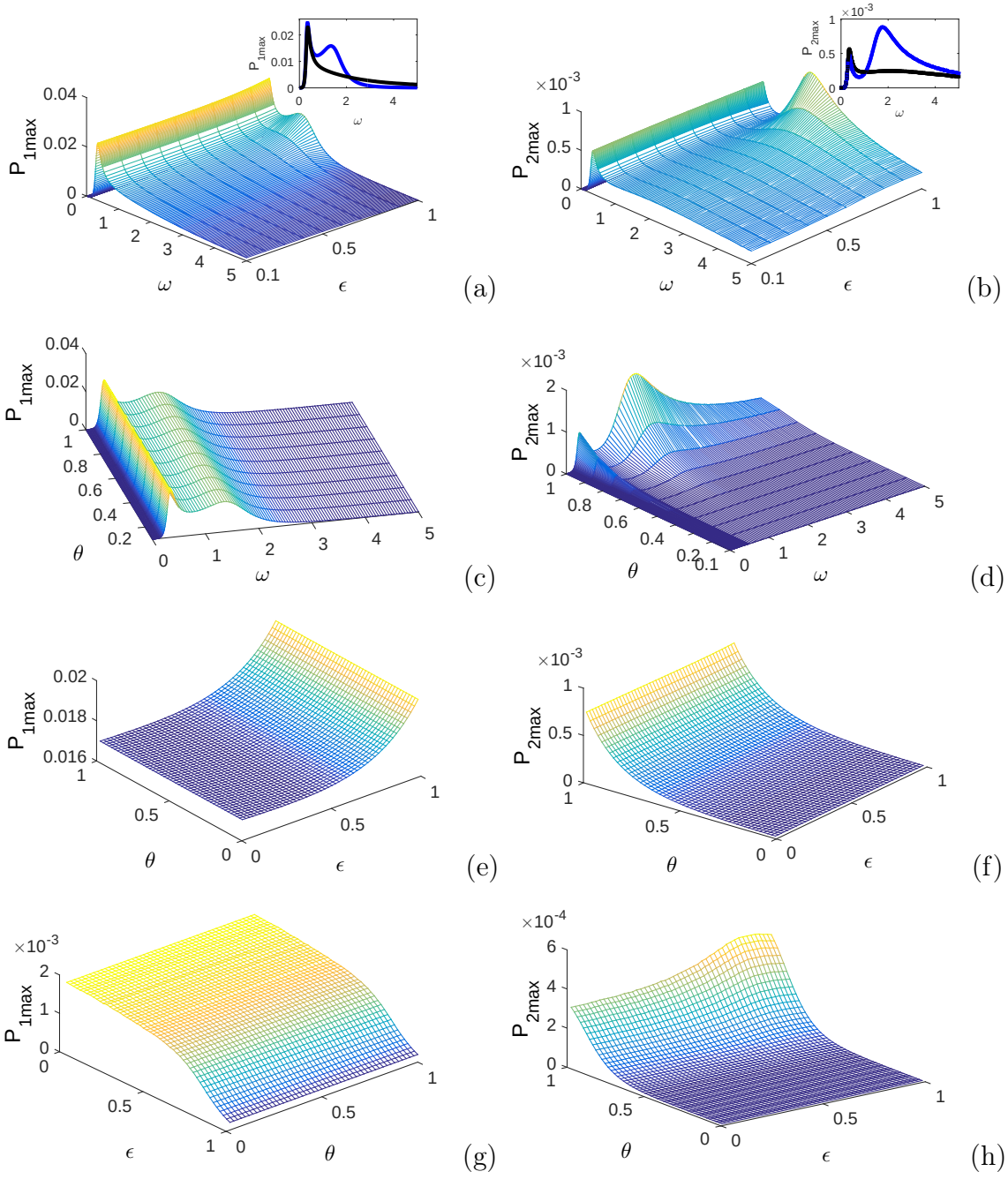

Figure 3.16: Output powers versus excitation frequency and FDOs.

inserts are plotted and superimposed the output powers for two values of ϵ, namely $\epsilon = 0.1$ (black solid line) and $\epsilon = 1$ (blue solid line). We notice that the electromagnetic harvested power increases with ϵ in the low-frequency regime, that is to say $0 < \omega < 2$ for instance. Contrariwise, it decreases with ϵ in the high-frequency regime. As for the piezoelectric output power, it rather decreases with ϵ in the low-frequency regime, that is for $0 < \omega < 1$ for instance. Conversely, it increases with ϵ for greater values of ω. Moreover, the output powers of the present harvester exhibit a resonant behavior as its counterpart without fractional properties. However, the number of resonant peaks and the peak height strongly depend on orders of fractional derivatives. In fact, for parameters used in this report, the piezoelectric output power exhibits two peaks. The first one is reached nearly at $\omega = 0.3$ and the second one at $\omega = 1.75$. As ϵ increases, the height of the first resonant peak slowly decreases while that of the second peak quickly increases (see Fig. 3.16(b) and insert therein). The electromagnetic output power progressively escapes the one-peak mode to join the two-peaks mode with increasing ϵ as observed in Fig. 3.16(a) and in insert therein. It is remarked observing Figs. 3.16(c) and (d) that the electromagnetic output power is less influenced by θ while the piezoelectric output power quickly increases with θ irrespective of the frequency band. Figures 3.16(e) and (f) have been obtained with $\omega = 0.3$. These figures clearly show that at very low frequency, the electromagnetic harvested power is more sensitive to ϵ than it is to θ. In fact, it monotonously increases with ϵ as remarked above. Conversely, the piezoelectric harvested power is more sensitive to θ than it is to ϵ. As expected, it monotonously increases with θ. As for Figs. 3.16(g) and (h), they were obtained with $\omega = 4$. Figure 3.16(g) confirms that P_{1max} rather decreases with ϵ for large values of the driving frequency. Figure 3.16(h) confirms that P_{2max} always increases with θ irrespective of ω.

It is worth noticing that, for very low frequencies, the electromagnetic harvested power is larger than the piezoelectric output power irrespective of the fractional orders. This can be verify by superimposing surfaces provided in Fig. 3.16(e) and Fig. 3.16(f). For greater frequencies, there is an area in (ϵ, θ) plane within which the piezoelectric output power is larger, and, another area where the electromagnetic harvested power is larger. This remark is ascertained by superimposing the results provided in Fig. 3.16(g) and Fig. 3.16(h).

Let's now define the efficiencies related to both transduction mechanisms with the purpose of comparing these transduction mechanisms on the one hand, and firmly characterizing the fractional derivatives orders' effects on the system efficacy on the other hand. To this end, define as in reference [22] the instantaneous input power

$$\tilde{P}_{in} = -m\Gamma(\tau)\frac{dX}{d\tau}, \tag{3.16}$$

that is the power of the inertial force acting on the moving mass, and letting

$$P_{in} = \frac{1}{ml^2\omega_e^3}\tilde{P}_{in} = \dot{x}f(t) \tag{3.17}$$

the corresponding dimensionless input power, the normalized efficiency ρ is defined by the relation $\rho = \frac{P_{out\,\max}}{P_{in\,\max}}$; where $P_{in\,\max}$ is the magnitude of the dimensionless input power from the driving vibrations and $P_{out\,\max}$ is the magnitude of the dimensionless power delivered to the electrical load. Note that $P_{out\,\max}$ represents either the electromagnetic output power magnitude $P_{1\,\max}$ or the piezoelectric output power magnitude $P_{2\,\max}$. Thence, we define two normalized efficiencies, which are related to both transduction mechanisms exhibited by the harvester. It follows that the normalized efficiencies for the electromagnetic and the piezoelectric transduction mechanisms are respectively expressed as:

$$\rho_1 = \frac{b^2\omega}{F_0 a} \quad \text{and} \quad \rho_2 = \frac{c^2}{F_0 a\omega}. \tag{3.18}$$

It is worth noticing that the variations of the normalized efficiencies with the system parameters have the same trends as the variations of the genuine efficiencies, which are expressed as follows:

$$\tilde{\rho}_1 = \frac{RQ_0^2}{ml^2\omega_e}\rho_1, \qquad \tilde{\rho}_2 = \frac{V_0^2}{R_P ml^2\omega_e^3}\rho_2. \tag{3.19}$$

The genuine efficiencies are analytically evaluated for several values of the fractional derivatives orders and for three different values of the frequency. Results are depicted in Fig. 3.17, that is the 3-Dimensional plot of efficiencies $\tilde{\rho}_1$ and $\tilde{\rho}_2$ (in percentage) with respect to ϵ and θ. In Fig. 3.17(a), the upper surface stands for $\tilde{\rho}_1$; the efficiency of the electromagnetic transduction mechanism, while the lower one represents $\tilde{\rho}_2$, the efficiency of the piezoelectric transduction mechanism. This result has been obtained for $\omega = 0.3$. Conversely, in Figs. 3.17(b) and 3.17(c) respectively obtained with $\omega = 4$ and $\omega = 10$ with $F_0 = 0.02$, there exists an area of the $(\epsilon - \theta)$ plane within which $\tilde{\rho}_1$ is greater than $\tilde{\rho}_2$,

and another area within which the opposite is observed. It therefore comes out from Fig. 3.17 that in the low-frequency regime, the electromagnetic mechanism is more efficient that the piezoelectric one irrespective of ϵ and θ. Moreover, for low frequencies, ϵ can be augmented to especially improve the electromagnetic mechanism while θ can be increased to improve the piezoelectric one. Contrariwise, for greater frequencies, augmenting ϵ results in reducing the efficacy of the electromagnetic transduction mechanism. This can be also achieved to render the electromagnetic mechanism less efficient than the piezoelectric one. Moreover, an appropriate choice of ϵ and θ, in the high frequency regime, enables the present hybrid energy harvester to achieve mechanisms of similar efficacy.

Let us note in addition that, when the excitation strength F_0 increases, while remaining weak, the transduction mechanisms efficiencies monotonously increase irrespective of the fractional derivatives orders and irrespective of the driving frequency. As the transition to chaos, which is not always desirable, is expected with increasing F_0 on the one hand, and as increasing F_0 enables to improve the efficiencies on the other hand, it is necessary to investigate the effects of orders of fractional derivatives on the chaotic behavior of the system.

3.3.3 Fractional derivatives orders' effects onto chaotic response and energy harvesting perspectives

Unlike the non-fractional counterpart of system 2.17, simulating system 2.17 is very time consuming due to the memory effect as we did not make use of the short memory principle throughout all this report. This constraint rendered simulations very cumbersome, especially when the fractional derivatives orders are lower than 0.4. In addition, due to the above constraint assessing the maximum Lyapunov exponent [186], which is an indicator commonly used to predict emergence of chaotic response of a dynamical system, is very cumbersome on the one hand; and on the other hand, this number as legally defined has no direct meaning because the system dimension could be undetermined. Therefore, to investigate the response type of the present system, as the excitation strength and the fractional derivatives orders evolve, we can make use of other indicators for qualitatively characterizing the dynamical behavior like the power spectral

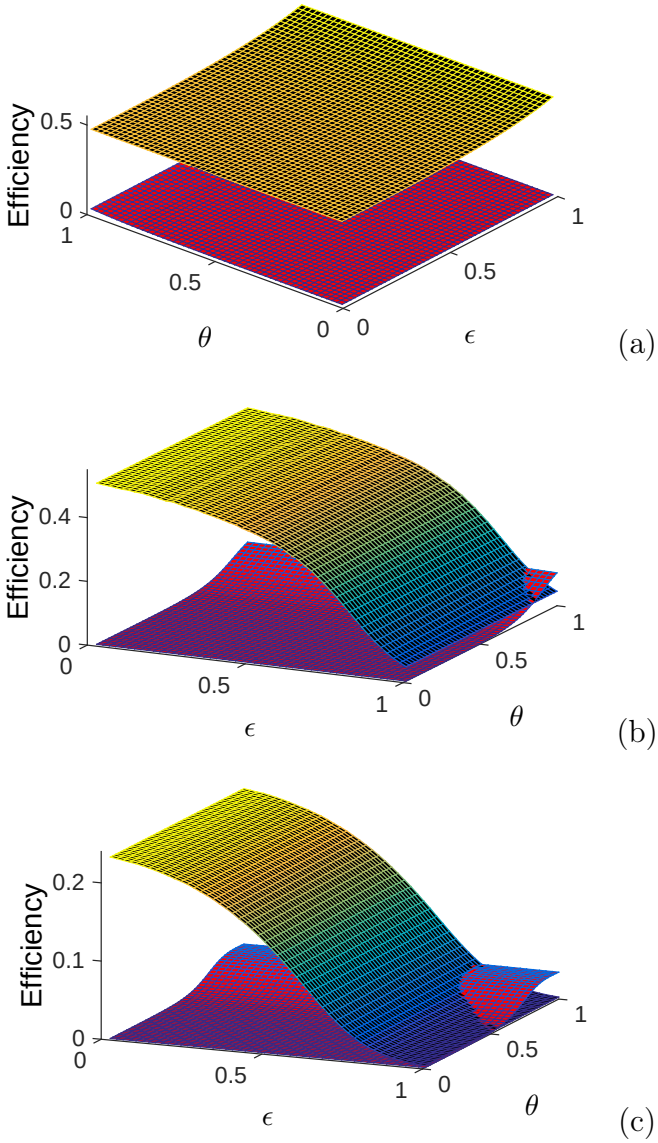

Figure 3.17: Efficiency versus ϵ and θ.

density, the $0-1$ test, the poincaré map, the basin of attraction and the bifurcation diagram. We made several computations by the mean of the fractional order Newton-Leipnik algorithm, however due to the conciseness constraint, we only provided bifurcation diagrams in the present work. Unless otherwise specified, we used the initial conditions $(x_0, u_0, y_0, v_0, z_0, w_0) = (0, 0, 0, 0, 0, 0)$ throughout the simulations. The results are provided in Figs. 3.18 and 3.19.

It comes out from computations that the present system, like its non-fractional counterpart, exhibits a rich dynamical behavior that mainly depends on the amplitude and frequency of the excitation. Figure 3.18 illustrates a qualitative change in the system response as the excitation amplitude varies through the corresponding bifurcation diagram. As expected, periodic vibrations are exhibited for small values of F_0. These vibrations are almost harmonic when F_0 is sufficiently small. Other waveforms such as relaxation oscillations appear as F_0 increases. When F_0 increases further, a transition from periodic to non-periodic vibrations occurs. Figure 3.18(a) has been obtained with $\epsilon = 1$ and $\theta = 1$ by the mean of the fourth-order Runge Kutta algorithm. It is a bifurcation diagram of the non-fractional counterpart of system (2.17). One can see that when F_0 increases more, we observe in this figure another transition from non-periodic motion to periodic motion which is subsequently followed by another transition to non-periodic motion. Figure 3.18(b) has been obtained with $\epsilon = 0.90$ and $\theta = 0.80$. In this figure, similar transition from non-periodic vibrations to periodic ones, subsequently follows by another transition to non-periodic motion only occurs once. Comparing Fig. 3.18(a) and Fig. 3.18(b), we clearly remark that the region corresponding to periodic motion depends on the FDOs. As a matter of fact, regular motion appears within the region $F_0 \in [12.12; 12.34]$ on Fig. 3.18(b), while on Fig. 3.18(a), in the same region appear non-periodic vibrations which are found to be chaotic.

To further probe the effect of FDOs, we studied the qualitative evolution of the system response with increasing FDOs and, to this end, corresponding bifurcation diagrams are provided in Figs. 3.19(a) and 3.19(c). The results depicted in Figs. 3.19(a)-(d) are obtained with $F_0 = 12.25$. For such a value of the excitation amplitude, the non-fractional version of system (2.17) exhibits a chaotic vibration. However, as it is seen in Fig. 3.19(a), when the FDO θ varies with fixed ϵ ($\epsilon = 0.90$), this chaotic vibration

can give birth to regular motion for peculiar values of θ. For instance, for $\theta = 0.97$ with $\epsilon = 0.90$ one obtains the time series depicted in Fig. 3.19(b) (blue solid line). The insert within this figure represents the corresponding state space diagram. This is a fractional order-induced periodic oscillation. Similarly, when ϵ varies for fixed θ ($\theta = 0.97$), as one can notice by analyzing Fig. 3.19(c), there are peculiar values of ϵ for which the behavior of the system's response switch from chaotic to regular. As expected, this phenomenon appears at $\epsilon = 0.90$. Other periodic motions appear at $\epsilon = 0.685$, $\epsilon = 0.73$ and $\epsilon = 0.92$. These values of ϵ are not exhaustive. They rather give an overview of the tight domains of ϵ where regular motions are expected to occur. As a matter of fact, since the diagram of Fig. 3.19(c) has been obtained with the ϵ step of 0.005, by analyzing this figure, it follows that the domains of ϵ within which regular oscillations are expected to occur correspond to $\epsilon \in]0.680; 0.690[\cup]0.725; 0.735[\cup]0.895; 0.905[\cup]0.915; 0.925[$. In the domains complementary to the above ones, chaotic oscillations are expected to appear. For instance, for $\epsilon \in [0.905; 0.915]$, the harvester is expected to exhibit non-regular oscillations which are highly sensitive to initial conditions. These are chaotic motions which involve long displacements from the initial state $(0, 0, 0, 0, 0, 0)$ due to the fact that the excitation amplitude is sufficiently large. In such regime of oscillation, the instantaneous output power can reach very large values, however it is not regular in waveform. In order to ascertain the preceding discussion, we computed various time series of system (2.17) for ϵ taken in the domain corresponding to chaotic vibrations. The result obtained with $\epsilon = 0.91$ (for θ fixed at 0.97) is provided in Fig. 3.19(d). In this figure, the blue solid line starts with null initial conditions while the green solid curve initiates with $(x_0, u_0, y_0, v_0, z_0, w_0) = (10^{-8}, 0, 0, 0, 0, 0)$. Both curves are initially superimposable, however at the long run, they completely diverge from one another. This motion is therefore highly sensitive to the initial conditions, which is another signature of chaotic behavior. The insert within Fig. 3.19(d) is the state space diagram corresponding to the previous motion, obtained with null initial conditions. It is not worth mentioning that the results depicted in Fig. 3.19 have been obtained with the time step $h = 0.005$ (to solve system (2.17)), the ϵ step of 0.005 and θ step of 0.005; while the result provided in Fig. 3.18 is obtained with the time step $h = 0.01$ and the step of 0.1 for F_0.

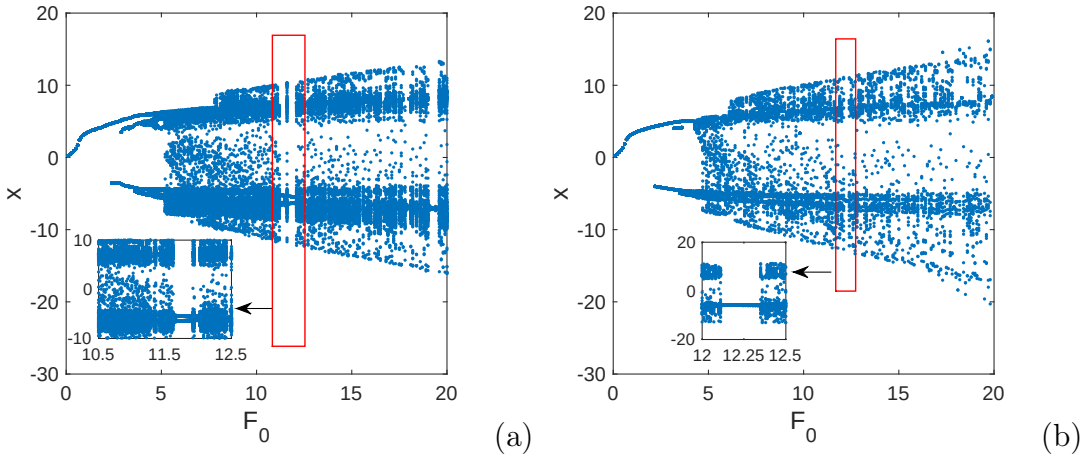

Figure 3.18: Bifurcation diagrams versus the excitation strength for different couples (ϵ, θ).

3.3.4 Concluding remarks

Summarily, we mainly investigated in this section the effects of FDOs, on the performance of a hybrid vibration energy harvester with a non-smooth mechanical damping. By the mean of a modified harmonic balance method, we have obtained the stationary harmonic response of the system. We have then investigated the harvester performance by the mean of this response. In the harmonic oscillatory regime, we found that FDOs astonishingly affect the device efficiency in the sense that: an increase of the FDO θ results, irrespective of the frequency, in the increase of the output voltage of the piezoelectric circuitry, and consequently leading to the increase of the corresponding output power. In addition, the derivative order θ slightly affects the electromagnetic output power in a non-monotonic way. The influence of the FDO ϵ on the electromagnetic output power significantly depends on the frequency. Indeed, in low-frequency regime, the electromagnetic output power increases with ϵ. However, in high-frequency regime, the decrease of ϵ leads to large values of the output power for the electromagnetic circuitry and thence, improves the performance of the electromagnetic transduction mechanism. The variation of ϵ also slightly affects the piezoelectric harvested power in a non-monotonic way irrespective of the frequency. The efficiency of the electromagnetic transduction mechanism is more sensitive to ϵ while that of the piezoelectric transduction mechanism is more sensitive to θ.

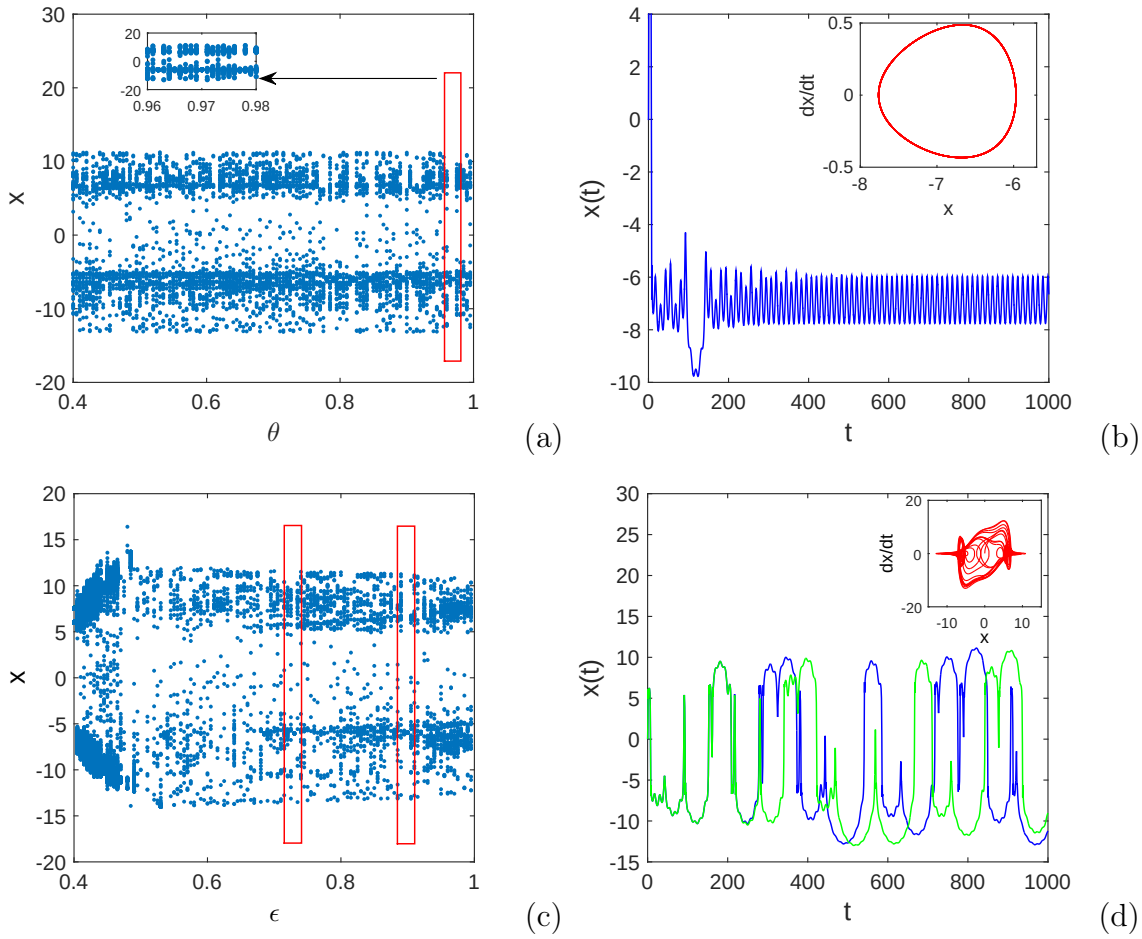

Figure 3.19: Bifurcation diagrams versus the FDOs and time series illustrating regular and chaotic dynamics.

.

Monitoring the FDOs in high-frequency band is useful to render the piezoelectric transduction mechanism more efficient than the electromagnetic one or to get transduction mechanisms of similar performance.

Apart from harmonic oscillations which are delivered by the harvester when the excitation strength is sufficiently small, the system exhibits a richer dynamical behavior especially when the excitation amplitude is increased. In fact, we found through numerical simulations that the harvester may be excited to a degree so as to exhibit non-regular or chaotic behavior. These chaotic output voltages contain large value instantaneous voltages and may yield substantially greater root mean square output powers, but such chaotic or aperiodic voltages may hardly yield a useful electrical power because they are irregular in waveform. We also found that for large excitation strength, a proper choice of the FDOs can be used to draw the system to a regular behavior and thus to prevent the emergence of chaotic vibrations. In short, it comes out of this section that: fractional derivatives' orders (FDOs) astonishingly affect the device efficiency, monitoring FDOs enables to achieve conversion mechanisms of similar performance, chaotic behavior appears for large harmonic excitation amplitudes, and this chaotic behavior can be overcome by a proper choice of the FDOs.

3.4 Discussion

Sustainable power generation is the major interest of investigations in the field of energy harvesting systems as well as in this work. It may be achieved by converting ambient energy into electrical energy. Among possible sources of ambient energy [181], we are concerned in this work with the transformation of mechanical vibrations. Several techniques aiming at improving the work performance of vibration energy harvesters have been developed in the past two decades. Some important techniques are, for instance, preloading technique [182], bi-stability [183], hybridization [184], stochastic excitation [7, 8, 22]. Apart from the above-mentioned methods, recent advances in fractional calculus lately allowed some investigators [59, 75, 76, 78] to search the effects of fractional order components on the performance of vibration energy harvesters. The present work, like the work reported in Ref. [76], focuses on this task by considering a fractional order induc-

tor in the electrical part of the system. In other works [75, 78], the capacitor within the electrical part of the harvester is assumed to be of fractional order. The intent of these investigations is, of course, to search how the fractional properties can be beneficial in enhancing the harvester performance. In this work, as it is commonly found in the works on fractional-order energy harvesting systems [59, 75, 76, 78], fractional order derivative may effectively enhance the performance of the harvester. However, this can be achieved only for peculiar operating conditions. For instance, in Ref. [78], the harvester efficiency is improved only for a large amplitude of perturbation by exploiting the hardening behavior of the system. In this work, the performance of the system is strongly affected by the excitation frequency. In low-frequency regime, increasing the FDO ϵ within $]0, 1[$ results in enhancing one of the output powers. However, such findings reveals that the standard inductor ($\epsilon = 1$) is more appropriate than an inductor exhibiting fractional properties. A similar result is highlighted by Foupouapouognigni *et al.* [76]. Contrariwise, unlike the findings commonly highlighted so far [76, 78], the output power related to the electromagnetic circuitry decreases with the FDO for an appropriate range of the excitation frequency. In this case, the fractional order inductor is better than a standard inductor, and diminishing the FDO rather improves the efficiency of the system. It has also been reported as in this work, by calculating basins of attraction and bifurcation diagrams, that fractional order properties induce a broad spectrum of non-linear behavior connected with sensitivity to the initial conditions and chaos [62]. Energy harvesting systems have been extensively studied for the last two decades and several papers are devoted to them in the literature. Indeed, these papers report studies aiming at improving the performance of energy harvesters. However, as the harvesting performance can be improved in a variety of aspects, each of these studies has its own peculiarity. As a matter of fact, references [181] and [185] are concerned with vibration energy harvesters making use of piezoelectric conversion mechanism while the present work deals with a hybrid harvester with two conversion mechanisms, which are electromagnetic and piezoelectric. The present work studies the role that fractional properties may play in enhancing the performance of a hybrid harvester, while reference [185] studies the response of a piezoelectric harvester with regard to non-smooth nonlinearities. Moreover, it pays attention on the role that can play non-smooth nonlinearities in obtaining a broadband harvesting

capacity. Unlike this work, reference [181] presents a comprehensive review of recently developed piezoelectric energy harvesting techniques for converting mechanical energy into electricity.

Conclusion

The aim of this chapter was to present our results with some discussions. We have solved several problems namely: the investigation of effects on the harvested powers and on device efficiency of non-smoothness coefficient, nonlinear magnetic coupling parameter and parameter of nonlinearities; the study of the effects on harvested powers of environmental random fluctuations modeled by bounded noise and color noise; finally the investigation of the effects of fractional properties on the energy harvesting behavior of the device. During the resolution of these different issues, it appears several results and discussions summarized in concluding remarks.

General Conclusion and Futures Works

⇝ Main Results of the Thesis

This thesis was concerned with a peculiar energy harvesting apparatus possessing non-smooth behavior and a nonlinear coupling between its mechanical part and its electrical part. We have studied the effects of nonlinearity, discontinuity, noise and fractional derivatives' orders on the device dynamics and their consequences on the device harvesting behavior. We have organized our dissertation in three chapters.

In the first chapter, we have reviewed the literature on the hybridity concept, non-smoothness, fractional derivative and the notion of transduction in energy harvester.

The second chapter was devoted to the modeling and the methodological framework. We described the device and derived the mathematical models which governs its dynamics there, then we described the numerical and the analytical methods used within this dissertation.

The last chapter was devoted to results and comments. In this chapter, we provided the readers with our principal findings followed by some comments, which are summarized below.

• From the investigation of effects of (a) the nonlinear magnetic coupling and (b) the parameters of non-smoothness and nonlinearities, on the performance of the system, it comes out that the electromagnetic and piezoelectric transduction mechanisms are improved and the harvester efficiencies, increased, by weakening the nonlinearities and the damping of the harvester mechanical part and by choosing peculiar nonlinear magnetic coupling coefficients. Increasing the harmonic excitation strength is useful to augment the harvested powers, however, it can not be increased beyond a threshold value when one desires a harvested power of regular waveform. In fact, augmenting it further induces transition to chaotic behavior, and results in a non-periodic harvested power, which is

inappropriate for energy storage devices.

• From the study of the effects of random fluctuations on the efficiency of the system, we found that in the parameters' regime for which the averaging technique is meaningful, that is to say, in the regime of weak coupling, damping and nonlinearity parameters, the stationary PDFs only exhibited a single-peak mode as the system's parameters varied. This result has been verified by the Monte Carlo simulation. Moreover, we found in such parameters' regime that the mean output powers increase with the colored noises' intensities and the harvester piezoelectric part output power exhibits a resonance behavior as some bounded noise parameter vary. This behavior demonstrates that, for fixed colored noise intensities, the performance of the harvester piezoelectric part is maximized for optimum bounded noise relaxation time and average frequency. This result reveals the stochastic resonance phenomenon. For large coupling parameters, that is, in the parameter regime for which stochastic averaging technique is meaningless, we found by the mean of the Monte Carlo simulation that by increasing a particular parameter of nonlinearity, the stochastic P-bifurcation appears in the mechanical part of the energy harvester. This result sustains the idea of Siewe *et al.* [4] according to which the stochastic P-bifurcation can be exhibited by a stochastic dynamical system although not predicted theoretically by the stochastic averaging technique. The present work enables designers to get an insight on the constraint to be addressed in order to improve the device performance.

• In the framework of the investigation of the effects of fractional properties on the harvesting behavior of the device, we found that FDOs astonishingly affect the device efficiency in the sense that: an increase of the FDO θ results, irrespective of the frequency, in the increase of the output voltage of the piezoelectric circuitry, and consequently leading to the increase of the corresponding output power. In addition, the derivative order θ slightly affects the electromagnetic output power in a non-monotonic way. The influence of the FDO ϵ on the electromagnetic output power significantly depends on the frequency. Indeed, in low-frequency regime, the electromagnetic output power increases with ϵ. However, in high-frequency regime, the decrease of ϵ leads to large values of the output power for the electromagnetic circuitry and thence, improves the performance of the electromagnetic transduction mechanism. The variation of ϵ also slightly affects the piezoelectric harvested power in a non-monotonic way irrespective of the frequency. The

efficiency of the electromagnetic transduction mechanism is more sensitive to ϵ while that of the piezoelectric transduction mechanism is more sensitive to θ. Monitoring the FDOs in high-frequency band is useful to render the piezoelectric transduction mechanism more efficient than the electromagnetic one or to get transduction mechanisms of similar performance. Apart from harmonic oscillations which are delivered by the harvester when the excitation strength is sufficiently small, the system exhibits a richer dynamical behavior especially when the excitation amplitude is increased. In fact, we found through numerical simulations that the harvester may be excited to a degree so as to exhibit non-regular or chaotic behavior. These chaotic output voltages contain large value instantaneous voltages and may yield substantially greater root mean square output powers, but such chaotic or aperiodic voltages may hardly yield a useful electrical power because they are irregular in waveform. We also found that for large excitation strength, a proper choice of the FDOs can be used to draw the system to a regular behavior and thus to prevent the emergence of chaotic vibrations.

$\rightsquigarrow$ **Open problems and future directions**

The work carried out in this dissertation and the results so far obtained are a source of encouragement for other studies. Other points of interest may be solved in the future.

• In this thesis, we have only achieved theoretical investigations. It would also be interesting to implement the real-world apparatus of the harvester under consideration in this work, then carry out an experimental study in order to verify the theoretical results so far obtained in this work.

• The mathematical models provided in this thesis have to be refined. In fact, a more realistic model should concomitantly takes fractional properties of the circuit elements and random fluctuations or noise into consideration.

Bibliography

[1] *Energy-harvesting chips: The quest for everlasting life. http* : *//www.eetasia.com/ART* − 8800378146 − 765245 − *NT* − 27*d*0*I*882.*HTM*. (2005).

[2] *Shell says record profits to be used to boost alternatives*. Retrieved from Deutsche Presse-Agentur. (2006).

[3] *U.S. Energy Information Administration (EIA) International Energy Statistics*. Retrieved from U.S. Energy Information Administration (EIA): *http* : *//www.eia.gov/cfapps/ipdbproject/IEDIndex*3.*cfm*. (2010).

[4] M. S. Siewe, W. F. Kenfack and T. C. Kofane *Probabilistic response of an electromagnetic transducer with nonlinear magnetic coupling under bounded noise excitation*. Chaos Solitons & Fractals. **124** (2019) 26.

[5] M. F. Daqaq, *On intentional introduction of stiffness nonlinearities for energy harvesting under white Gaussian excitations*. Nonlinear Dyn. **69** (2012) 1063.

[6] F. Cottone, H. Vocca and L. Gammaitoni, *Nonlinear energy harvesting*. Phys. Rev. Lett. **102** (2009) 080601.

[7] G. Litak, M.I. Friswell and S. Adhikari, *Magnetopiezoelastic energy harvesting driven by random excitations*. Appl. Phys. Lett. **96** (2010) 214103.

[8] F. Cottone, L. Gammaitoni, H. Vocca, M. Ferrari and V. Ferrari, *Piezoelectric buckled beams for random vibration energy harvesting*. Smart Mater. Struct. **21** (2012) 035021.

[9] T. Yang, J. Liu and Q. Cao, *Response analysis of the archetypal smooth and discontinuous oscillator for vibration energy harvesting*. Physica A: Statistical Mechanics and its Applications **507** (2018) 358.

[10] I.S.M. Fokou, C.N.D. Buckjohn, M.S. Siewe and C. Tchawoua, *Probabilistic distribution and stochastic P-bifurcation of a hybrid energy harvester under colored noise*. Commun. Nonlinear Sci. Numer. Simulat. **56** (2018) 177.

[11] T. Wacharasindhu and J. W. Kwon, *A micromachined energy harvester from a keyboard using combined electromagnetic and pieoelectrique conversion*. Journal of Micromechanics and Microengineering. **18** (2008) 104016.

[12] I.S.M. Fokou, *Nonlinear characterization of some wireless energy harvesters*. (Thesis of University of Yaounde 1, Cameroon. 2019).

[13] S. Xiao and Y. Jin, *Response analysis of the piezoelectric energy harvester under correlated white noise*. Nonlinear Dyn. **90** (2017) 2069.

[14] M. Xu, X. Jin, Y. Wang and Z. Huang, *Stochastic averaging for nonlinear vibration energy harvesting system*. Nonlinear Dyn. **78** (2014) 1451.

[15] H. Li, W. Qin, C. Lan, W. Deng and Z. Zhou, *Dynamics and coherence resonance of tri-stable energy harvesting system*. Smart Mater. Struct. **25** (2016) 015001.

[16] M. Borowiec, G. Litak and S. Lenci, *Noise effected energy harvesting in a beam with stopper*. Int J of Structural Stability and Dynamics **14** (2014) 1440020.

[17] W. Martens, U. von Wagner and G. Litak, *Stationary response of nonlinear magnetopiezoelectric energy harvester systems under stochastic excitation*. Eur. Phys. J. **222** (2013) 1665.

[18] X. Wang, *Frequency Analysis of Vibration Energy Harvesting Systems*. (Academic Press, 2016).

[19] S. Beeby and N. White, *Energy Harvesting for Autonomous Systems*. (Artech House, 2010).

[20] I. Sari, T. Balkan and H. Kulah, *An electromagnetic micro power generator for wide-band environmental vibrations*. Sens. Act. A **145** (2008) 405.

[21] R. Torah, P. Glynne-Jones, M. Tudor, T. O'Donnell, S. Roy and S. Beeby, *Self-powered autonomous wireless sensor node using vibration energy harvesting*. Meas. Sci. Technol. **19** (2008) 125202.

[22] G. G. Sengha, W. F. Kenfack, M. S. Siewe, C. B. Tabi and T. C. Kofane, *Dynamics of a non-smooth type hybrid energy harvester with nonlinear magnetic*. Commun. Nonlinear Sci. Numer. Simulat. **124** (2019) 26.

[23] E. E. Aktakka and K. Najafi, A *micro inertial energy harvesting platform with self-supplied power management circuit for autonomous wireless sensor nodes*. IEEE J. Solid-State Circuits **49** (2014) 2017.

[24] C. Sano, H. Mitsuya, S. Ono, K. Miwa, H. Toshiyoshi and H. Fujita, *Triboelectric energy harvesting with surface-charge-fixed polymer based on ionic liquid*. Sci. Technol. Adv. Mater. **19** (2018) 317.

[25] P. D. Mitcheson, P. Miao, B. H. Stark, E. M. Yeatman, A. S. Holmes and T. C. Green, *MEMS electrostatic micropower generator for low frequency operation*. Sens. Act. A **115** (2004) 523.

[26] Y. Sakane, Y. Suzuki and N. Kasagi, *The development of a high-performance perfluorinated polymer electret and its application to micro power generation*. J. Micromech. Microeng. **18** (2008) 104011.

[27] Y. Suzuki, *Recent progress in MEMS electret generator for energy harvesting*. IEEJ Trans. **6** (2011) 101.

[28] C. N. D. Buckjohn, M. S. Martin, I. S. M. Fokou, C. Tchawoua and T.C. Kofane, *Investigating bifurcations and chaos in magnetopiezoelastic vibrating energy harvesters using Melnikov theory*. Phys. Scr. **88** (2013) 015006.

[29] C. B. Williams and R. B. Yates, *Analysis Of A Micro-electric Generator For Microsystems*. Sensors and Actuators A: Physical **52** (1996) 8.

[30] A. Erturk, J. Hoffmann and D. J. Inman, *A piezomagnetoelastic structure for broadband vibration energy harvesting*. Appl. Phys. Let. **94** (2009) 128.

[31] R. L. Harne and K. W. Wang, *A review of the recent research on vibration energy harvesting via bistable systems*. Smart Mater. and Struct. **22** (2013) 23001.

[32] H. Vocca, I. Neri, F. Travasso and L. Gammaitoni, *Kinetic energy harvesting with bistable oscillators*. Applied Energy **97** (2012) 771.

[33] R. Ramlan, M. J. Brennan, B. R. Mace and I. Kovacic, *Potential benefits of a nonlinear stiffness in an energy harvesting device*. Nonlinear Dyn. **59** (2010) 545.

[34] S. Zhou, J. Cao, D. J. Inman, Ji. Lin, S. Liu and Z. Wang, *Broadband tristable energy harvester: Modeling and experiment verification*. Applied Energy **133** (2014) 33.

[35] A. Erturk and D. J. Inman, *Piezoelectric Energy Harvesting*. (Wiley, Chichester, 2011)

[36] M. S. Siewe and C. N. D. Buckjohn, *Heteroclinic motion and energy transfer in coupled oscillator with nonlinear magnetic coupling*. Nonlinear Dyn. **75** (2014) 903.

[37] S. C. Stanton, B. P. Mann and B. A. Owens, *Melnikov theoretic methods for characterizing the dynamics of the bistable piezoelectric inertial generator in complex spectral environments*. Phys. D **241** (2012) 711.

[38] R. Zheng, K. Nakano, H. Hu, D. Su and M. P. Cartmell, *An application of stochastic resonance for energy harvesting in a bistable vibrating system*. J Sound Vib **333** (2014) 2568.

[39] H. T. Li, W. Qin, W. Deng and R. Tian, *Improving energy harvesting by stochastic resonance in a laminated bistable beam*. Eur. Phys. J. Plus **131** (2016) 1.

[40] K. Nakano, M. P. Cartmell, H. Hu and R. Zheng, *Feasibility of energy harvesting using stochastic resonance caused by axial periodic force*. J. Mech. Eng. **60** (2014) 314.

[41] F. Dercole, F. Della Rossa, A. Colombo and Y. A. Kuznetsov, *Two degenerate boundary equilibrium bifurcations in planar Filippov systems*. Siam J. Applied Dynamical Systems **10** (2011) 1525.

[42] F. Dercole, A. Gragnani and S. Rinaldi, *Bifurcation analysis of piecewise smooth ecological models*. Theoretical Population Biology **72** (2007) 197.

[43] Y. A. Kuznetsov, S. Rinaldi and A. Gragnani, *One-parameter bifurcations in planar Filippov systems*. International Journal of Bifurcation and chaos **13** (2003) 2157.

[44] J. L. Gouze and T. Sari, *A class of piecewise linear differential equations arising in biological models*. Dynamical Systems **17** (2002) 299.

[45] V. I. Utkin, *Sliding Modes in Control and Optimization*, (Springer-Verlag, 1992).

[46] V. I. Utkin, *Sliding mode control design principles and applications to electric drives*. IEEE Transactions on Industrial Electronics **40** (1993) 23.

[47] G. Bartolini, F. Parodi, V. I. Utkin and T. Zolezzi, *The simplex method for nonlinear sliding mode control*. Mathematical Problems in Engineering **4** (1999) 461.

[48] V. A. Yakubovich, G. A. Leonov and A.Kh. Gelig, *Stability of Stationary Sets in Control Systems with Discontinuous Nonlinearities*. (World Scientific, 2004).

[49] P. Kowalczyk and P. T. Piiroinen, *Two-parameter sliding bifurcations of periodic solutions in a dry-friction oscillator*. Physica D **237** (2008) 1053.

[50] M. Guardia, S. J. Hogan and T. M. Seara, *An analytical approach to codimension-2 sliding bifurcations in the dry-friction oscillator*. Siam J. Appl. Dyn. Syst. **9** (2010) 769.

[51] R. I. Leine and H. Nijmeijer, *Dynamics and Bifurcations of Non-Smooth Mechanical Systems*. (Springer-Verlag, Berlin, 2004).

[52] V. Acary and B. Brogliato, *Numerical Methods for Nonsmooth Dynamical Systems, Applications in Mechanics and Electonics*. (Springer-Verlag, Berlin, 2008).

[53] M. S. M. Soliman, E. M. Abdel-Rahman, E. F. El-Saadany and R. R. Mansour, *A design procedure for wideband micropower generators*. J. Mircoelectromech. Syst. **18** (2009) 1288.

[54] R. Yamapi and S. Bowong, *Dynamics and chaos control of the self-sustained electromechanical device with and without discontinuity*. Commun Nonlinear Sci Numer Simulat **11** (2006) 355.

[55] L. Debnath, *Recent applications of fractional calculus to science and engineering*. Int. J. Math. Sci. **54** (2003) 3413.

[56] F. Duarte and J. A. T. Machado, *Chaotic phenomena and fractional-order dynamics in the trajectory control of redundant manipulators*. Nonlinear Dyn. **29** (2002) 315.

[57] O. Agrawal, *Application of Fractional Derivatives in Thermal Analysis of Disk Brake*. Nonlinear Dyn. **38** (2004) 191.

[58] G. M. Ngueuteu and P. Woafo, *Dynamics and synchronization analysis of coupled fractional-order nonlinear electromechanical systems*. Mech. Res. Commun. **46** (2012) 20.

[59] J. Cao, S. Zhou, D. J. Inman and Y. Chen, *Chaos in the fractionally damped broadband piezoelectric energy generator*. Nonlinear Dyn. **80** (2015) 1705

[60] J. A. T. Machado, M. F. Silva, R. S. Barbosa, I.S. Jesus, C. M. Reis, M. G. Marcos and A. F. Galhano, *Some applications of fractional calculus in engineering*. Math. Probl. Eng. **639801** (2010) 1.

[61] M. F. Silva and J. A. T. Machado, *Fractional order PD^{α} joint control of legged robots*. J. Vib. Control **12** (2006) 1483.

[62] A. Syta, G. Litak, S. Lenci and M. Scheffler, *Chaotic vibrations of the duffing system with fractional damping*. Chaos **24** (2014) 013107.

[63] L. Cveticanin and M. Zukovic, *Melnikov's criteria and chaos in systems with fractional order deflection*. J. Sound Vib. **326** (2009) 768.

[64] K. S. Miller and B. Ross, *An Introduction to the Fractional Calculus and Fractional Differential Equations*. (John Wiley & Sons Inc., New York, 1993).

[65] K. B. Oldham and J. Spanier, *The Fractional Calculus*. (Academic Press, New-York, 1974).

[66] B. Ross, *Fractional Calculus and Applications, volume 457 of Lecture Notes in Mathematics, chapter A brief history and exposition of the fundamental theory of the fractional calculus*. (Springer-Verlag, New-York, 1975).

[67] R. Herrmann, *Fractional Calculus: An Introduction for Physicists*. (GigaHedron, Germany, 2013).

[68] I. Petras, *Fractional-order nonlinear systems: Modelling, analysis and simulation*. (Springer, New York, 2010).

[69] A. Atangana and B.S.T. Alkahtani, *Extension of the resistance, inductance, capacitance electrical circuit to fractional derivative without singular kernel*. Adv. Mech. Eng. **7** (2013) 16.

[70] E. K. Lenzi, R. M. Netoa, A. A. Tateishi, M. K. Lenzi and H. V. Ribeiro, *Fractional diffusion equations coupled by reaction terms*. Phys. A **458** (2016) 9.

[71] J. F. G. Aguilar, H. Y. Martnez, C. C. Ramn, I. C. Ordua, R. F. E. Jimnez and V. H. O. Peregrino, *Modeling of a mass-spring-damper system by fractional derivatives with and without a singular kernel*. Entr. **17** (2015) 6289.

[72] A. Atangana and D. Baleanu, *New fractional derivatives with nonlocal and non-singular kernel: Theory and application to heat transfer model*. Thermal Sci. **20** (2016) 763.

[73] D. Prodanov and J. Delbeke, *A model od space-fractional-order diffusion in the glial scar*. J Theor Biol. **403** (2016) 97.

[74] B. Zhang, B. Ducharne and D. Guyomar. *Inverse model of the piezoelectric ceramic polarization under wide bandwidth mechanical excitations with fractional derivative consideration*. Opt. Quant. Electron **46** (2013) 103110.

[75] I.S.M. Fokou, C.N.D. Buckjohn, M.S. Siewe and C. Tchawoua, *Nonlinear analysis and analog simulation of a piezoelectric buckled beam with fractional derivative*. Eur. Phys. J. Plus **132** (2017) 1.

[76] O. Foupouapouognigni, C.N.D. Buckjohn, M.S. Siewe and C. Tchawoua, *Nonlinear electromechanical energy harvesters with fractional inductance*. Chaos, Solitons and Fractals **103** (2017) 12.

[77] O. Foupouapouognigni, *Hybrid electromagnetic energy harvesting systems exhibiting structural nonlinearities and fractional properties: Contribution to design and optimization* . (Thesis of University of Yaounde 1 Cameroon 2020).

[78] C. A. K. Kwuimy, G. Litak and C. Nataraj, *Nonlinear analysis of energy harvesting systems with fractional order physical properties*. Nonlinear Dyn. **80** (2015) 491.

[79] E. Arroyo, A. Badel and F. Formosa, *Modeling and design of an electromagnetic vibration energy harvester and its dedicated energy extraction circuit.* Proceeding of the IEEE **96** (2012) 1457.

[80] P. Mitcheson, E. Yeatman, G. Rao, A. Holmes and T. Green, *Energy harvesting from human and machine motion for wireless electronic devices* . **9** (2008) 1457.

[81] W. Wang, J. Cao, S. Zhou and J. Lin. Shrier, *Bistable energy harvesting from human motion. In 27th Conference on Mechanical Vibration and Noise*. ASME **8** (2015).

[82] C. Covaci and A. Gonteau, *Piezoelectric Energy Harvesting Solution*. a. Review (sensors) **20** (2008) 3512.

[83] E. Maghsoudi Nia, N. A. Wan Abdullah Zawawi and B. S. Mahinder Singh, *Design of a pavement using piezoelectric materials*. Mater Werkst, **50** (2019) 320.

[84] F. J. Bilatt, P. Schroeder, C. L. Foiles and D. Greil, *Thermoelectric power of materials*. (Plenum Press, New York, 1976).

[85] F. J. Ryan, *A comparison of power harvesting techniques and related energy storage*. (Thèse de doctorat, Dept. Mech. Eng., Virginia Polytechnic Institute and State Univ. Blacksburg, VA, 2007).

[86] R. L. Myers, *The basics of physics. Greenwood Press, Westport*, (Conn, 2006).

[87] R. Elliott, *Electromagnetics : History Theory and Applications.* (Wiley IEEE Press, 1993).

[88] O. Mah, *Fundamentals of photovoltaic materials.* (National Solar Power Research Institute, 1998).

[89] J. M. Damaschke, *Design of a low-input-voltage converter for thermoelectric generator. Industry Applications, IEEE Transactions on.* **33**(1997) 5. 1203.

[90] G. S. Nolas, J. Sharp and H. J. Goldsmid, *Thermoelectrics : basic principles and new materials developments.* (Springer, New York, 2001).

[91] R. Murugavel, *Energy harvesting, white paper.* (Texas instruments, 2008).

[92] *Université virtuelle environnement et développement durable, La maîtrise de la demande d'énergie : état des lieux et perspectives, http : uved. Univperp/.fr /module1 /co / Module maitrise demande .html.* 2013.

[93] T. Starner, *Human-Powered Wearable Computing.* IBM Systems Journal, **35** (1996) 618.

[94] S. Turri and G. Poulin, *Dispositifs electromecaniques permettant l'exploitation de l'énergie des mouvements humains.* (Presented at Journée electrotechniques du club EEA, Cachan, France, 2002).

[95] P. Niu, P. Chapman, R. Riemer, and X. Zhang, *Evaluation of motions and actuation methods for biomechanical energy harvesting.* (Presented at Power Electronics Specialists Conference, 2004. PESC 04. 2004 IEEE 35th Annual, 2004).

[96] J. L. Gonzalez, A. Rubio, and F. Moll, *A prospect on the use of piezoelectric effect to supply power to Wearable electronic devices, International journal of the society of materials engineering for resources.* **10** (2002) 34.

[97] T. Toriyama, M. Yajima, and S. Sugiyama, *Thermoelectric micro power generator utilizing self-standing polysilicometal thermopile, presented at Micro electro Mechanical Systems.* (The 14th IEEE International conference on. 2001).

[98] T. Dousekii, Y. Yoshida, F. Utsunomiya, N. Itoh, and N. Hama, *A battery less wireless systems uses ambient heat with a reversible-power-source compatible CMOS/SOI DC-DC converter, presented at solid-state circuits conference.* (Digest of Technical Papers. ISSCC. 2003 IEEE International. 2003).

[99] O. Puscasu, *Dispositifs innovants pour la récupération de l'énergie thermique.* (Thèse université de Lyon. 2015).

[100] J. A. Paradiso and T. Starner, *Energy scavenging for mobile and wireless electronics, pervasive computing.* **18** (2005) 1268.

[101] M. M. Mounira, *Récupération des déperditions d'énergie dans les complexes industriels et leur conversion en énergie électrique exploitable.* (Thése d'Université Badji Mokhtar Annaba. 2004).

[102] D. Guyomar, A. Badel, C. Richard and E. Lefeuvre, *Vibration control based on a probabilistic nonlinear processing of the piezoelement output voltage, ASME Biennial Conference on Mechanical Vibration and Noise.* (Long Beach, California, USA. 2005).

[103] A. Badel, *Récupération d'énergie et controle vibratoire par éléments piézoélectriques suivant une approche non linéaire.* (Thèse de l'Université de Savoir. 2005).

[104] D. Masotti, A. Costanzo and S. Adami, *Design and realization of a wearable multi-frequency RF energy harvesting system Proceedings of the 5th European Conference on Antennas and Propagation (EUCAP)* . 12034332 (2011) 2162.

[105] V. Talla, S. Pellerano, H. Xu, A. Ravi and Y. Palaskas. *Wi-Fi RF energy harvesting for battery free wearable radio platforms IEEE International Conference on RFID.* (2015) 47.

[106] M. Lallart, A. Badel and D. Guyomar, *Nonlinear semi-passive damping using constant or adaptive voltage sources: A stability analysis, 16th International Conference on Adaptive Structures and Technologies.* (Paris, France 2005).

[107] J. Li and X. Wang, *Research Update, Materials design of implantable nanogenerators for biomechanical energy harvesting.* AP L Materials, **5** (2017) 073801.

[108] B. Zhang, *Model for coupled ferroelectric hysteresis using time fractional operators: Application to innovation energy harvesting*. Thesis INSA Lyon (France) 2014.

[109] J. Briscoe and S. Dunn, *Background. In Nanostructured Piezoelectric Energy Harvesters*. 1st ed.; Springer International Publishing: Berlin/Heidelberg, Germany (2014) 3.

[110] A. N. Maghsoudi, W. Z. Abdullah and S. S. B. Mahinder, *Design of a pavement using piezoelectric materials*. Mater. Werkst. **50** (2019) 320.

[111] J. Feenstra, J. Granstrom and H. Sodano, *Energy harvesting through a backpack employing a mechanically amplified piezoelectric stack*. Mech. Syst. Signal Process. **22** (2008) 521.

[112] M. Deterre *Toward an energy harvester for leadless pacemakers*. (Thesis of University of paris-sud. 2013).

[113] M. Brissaud, *Matériaux piézoélectriques: caractérisation, modélisation et vibration*. (Presses Polytechniques Romandes. 2007).

[114] A. Rjafallah, A. Hajjaji, D. Guyomar, K. Kandoussi, F. Belhora and Y. Boughaleb. *Modeling of polyurethane/lead zirconate titanate composites for vibration energy harvesting*. J. Compos. Mater, **53** (2018) 1.

[115] G. Lippmann, *Principe de la conservation de l'électricité, ou second principe de la théorie des phénomènes électriques*. J. Phys. Theor. Appl. **10** (1881) 381.

[116] S. J. A. Koh, X. Zhao and Z. Suo, *Maximal energy that can be converted by a dielectric elastomer generator*. Appl. Phys. Lett. **94** (2009) 262902.

[117] I. Chopra, *Review of state of art of smart structures and integrated systems*. AIAA J. **40** (2007) 2145.

[118] C. H. Nguyen, U. Hanke and E. Halvorsen, *Actuation of Piezoelectric Layered Beams With d31 and d33 Coupling*. IEEE Trans. Ultrason. Ferroelectr. Freq. Control. **65** (2018) 1.

[119] K. Jenkins, V. Nguyen, R. Zhu and R. Yang, *Piezotronic Effect: An Emerging Mechanism for Sensing Applications*. Sensors. **15** (2015) 22914.

[120] S. Khalid, I. Raouf, A. Khan, N. Kim and H. S. Kim, *A Review of Human-Powered Energy Harvesting for Smart Electronics: Recent Progress and Challenges*. Int. J. Precis. Eng. Manuf. Green Technol. **6** (2019) 821.

[121] X. Wang, J. Zhou, J. Song, J. Liu, N. Xu and Z. L. Wang, *Piezoelectric Field Effect Transistor and Nanoforce Sensor Based on a Single ZnO Nanowire*. Nano Lett. **6** (2006) 2768.

[122] S. Roundy, P. K. Wright and K. S. J. Pister, *Micro-Electrostatic Vibration to Electricity Converters, presented at ASME International Mechanical Engineering Congress Exposition*. (New Orleans, Louisiana, 2002).

[123] S. Delprat, *Evaluation de stratégies de commande pour véhicules hybrides parallèles*. (Thèse de l'Université de Valenciennes et du Hainaut Cambrésis. 2002).

[124] R. Hodkinson and J. Fenton, *Lightweight Electric / Hybrid Vehicule Design* . (ISBN 7506 5092 3, Butterworth Heinemann. 2001).

[125] B. Destraz, *Assistance énergétique à base de supercondensateurs pour véhicules à propulsion électrique et hybride*. (Thèse de l'Université de Lausanne. 2008).

[126] M. K. Stojcev, M. R. Kosanovic and L. R. Golubovic, *Power management and energy harvesting techniques for wireless sensor nodes*. (9th International Conference on Telecommunications in Modern Satellite, Cable, and Broadcasting Services. 2009).

[127] Y. T. He, Y. Q. Li, L. H. Liu and L. Wang, *Solar micro-power system for self-powered wireless sensor nodes, Proceedings of the SPIE-The International Society for Optical Engineering*. **7133** (2008).

[128] M. Wischke, M. Masur, F. Goldschmidtboeing and P. Woias, *Electromagnetic vibration harvester with piezoelectrically tunable resonance frequency*. Journal of Micromechanics and Microengineering, **20** 3 (2010) 1.

[129] M. A. Karami, *Micro-Scale and nonlinear vibrational energy harvesting.* (Virginia Polytechnic Institute and State University. 2011).

[130] B. Yang, C. Lee, W. L. Kee and S. P. Lim, *Hybrid energy harvester based on piezoelectric and electromagnetic mechanisms.* Journal of Micro/Nanolithography, MEMS, and MOEMS. **9** (2010).

[131] S. Yingjun, H. Xueliang, L. Hexiang, and J. Ping, *A Vibration-Based Hybrid Energy Harvester for Wireless Sensor Systems.* Magnetics, IEEE Transactions on. **48** (2012) 4495.

[132] D. Paire *Dimensionnement et gestion d'énergie de systèmes d'entraînements électriques hybrides : application à un ascenseur avec récupération d'énergie.* (Thèse de l'Université de Technologie de Belfort-Montbéliard. 2010).

[133] M. A. Moreles and R. Lainez, *Mathematical modelling of fractional order circuits.* (Physics Class-ph. 2016).

[134] R. Hilfer. *Applications of Fractional Calculus in Physics.* (World Scientific. 2000).

[135] T. Houmor, *Analyse du Chaos dans un Système d'Équations Différentielles Fractionnaires.* (Thèse Doctorat en sciences, Université Mentouri de Constantine. 2014).

[136] J. Sabatier, O. P. Agrawal and J. A. Tenreiro Machado. *Advances in fractional calculus.* (Springer. Berlin. 2007).

[137] S. Racewicz, *Identification et modélisation d'ordre fractionnaire des machines synchrones fonctionnant comme générateur.* (Thèse de doctorat à l'INPC de Grenoble. 2011).

[138] M. Lin, A. K. Srivastava and N. N. Schulz, *A Generic Digital Model of Multiphase Synchronous Generator for Shipboard Power System.* (IEEE Electric Ship Technologies Symposium, ESTS. Arlington, Virginia. 2007).

[139] K. Biswas, S. Sen and P. Dutta, *Modelling of a capacitive probe in a polarizable medium.* Sens. Actuators Phys. **120** (2005) 115.

[140] T. C. Haba, G. L. Loum, J. T. Zoueu and G. Albart, *Use of a component with fractional impedance in the realization of an analogical regulator of order 1/2*. J. Appl. Sci. **8** (2008) 59.

[141] T. C. Haba, G. L. Loum and G. Ablart, *An analytical expression for the input impedance of a fractal tree obtained by a microelectronical process and experimental measurements of its non-integral dimension*. Chaos Solitons Fractals **33** (2007) 364.

[142] A. Buscarino, R. Caponetto, S. Graziani and E. Murgano, *Realization of fractional order circuits by a Constant Phase Element*. European Journal of Control. **4** (2020) 64.

[143] R. L. Bagley and P. J. Torvik, *Fractional calculus a different approach to the analysis of viscoelastically damped structures*. AIAA Journal. **21** (1983) 741.

[144] R. L. Bagley and P. J. Torvik, *Fractional calculus in the transient analysis of viscoelastically damped structures, AIAA Journal*. **23** (1985) 918.

[145] N. Makris and M. C. Constantinou, *Spring-viscous damper systems for combined seismic and vibration isolation, Earthquake Engineering and Structural*. **21** (1992) 649.

[146] B. Zhang, B. Ducharne, D. Guyomar and G. Sebald, *Energy harvesting based on piezoelectric Ericsson cycles in a piezoceramic material*. The European Physical Journal Special Topics. **222** (2013) 1733.

[147] C. G. Koh and J.M. Kelly, *Application of fractional derivatives to seismic analysis of base-isolated models*. Earthquake Engineering and Structural. **19** (1990) 229.

[148] T. M. Atanackovic, S. Pilipovic and D. Zorica, *Forced oscillations of a body attached to a viscoelastic rod of fractional derivative type, International Journal of Engineering Science*. **64** (2013) 54.

[149] J. Deng, W. C. Xie and M. D. Pandey, *Higher-order stochastic averaging to study stability of a fractional viscoelastic column*. Journal of Sound and Vibration. **333** (2014) 6121.

[150] S. M. Hosseini, H. Kalhori, A. Shooshtari and S. N. Mahmoodi, *Analytical solution for nonlinear forced response of a viscoelastic piezoelectric cantilever beam resting on a nonlinear elastic foundation to an external harmonic excitation*. Composites P art B: Engineering. **67** (2014) 464.

[151] C. Jin, D. S. Kia, M. Jones and S. Towfighian, *On the contact behavior of micro-nanostructured interface used in vertical-contact-mode triboelectric nanogenerators*. Nano Energy. **27** (2016) 68.

[152] R. A. Ibrahim, *Vibro-impact dynamics modeling, mapping and applications*. (Springer. Berlin. 2009).

[153] B. P. Mann and N. D. Sims, *Energy harvesting from the nonlinear oscillations of magnetic levitation*. Journal of Sound and Vibration. **329** (2009) 515.

[154] A. J. Sneller and B. P. Mann, *On the nonlinear electromagnetic coupling between a coil and an oscillating magnet*. Journal of Physics D: Applied Physics. **43** (2010).

[155] de Wit, C. Canudas, H. Olsson, K. J. Astrom, and P. Lischinsky, *New model for control of systems with friction*. IEEE Transactions on Automatic Control. **40** (1995) 419.

[156] R. Ai, L. L. S. Monteiro, P. C. C. Monteiro Jr., P. M. C. L. Pacheco and M. A. Savi, *Piezoelectric Vibration-Based Energy Harvesting Enhancement Exploiting Nonsmoothness*. Actuators. **8** (2019) 25.

[157] G. K. Ottman, F. Hofmann and G. A. Lesieutre, *Optimized Piezoelectric Energy Harvesting Circuit Using Step-Down Converter in Discontinuous Conduction Mode*. IEEE Transactions on Power Electronics. **18** (2003) 2.

[158] M. Weiss, M. Chenia, A. T. Savadkoohi, C. H. Lamarque, B. Vaurigaud and A. Hammouda, *Multi-scale energy exchanges between an elasto-plastic oscillator and a light nonsmooth system with external pre-stress*. Nonlinear Dyn. **83** (2016) 109.

[159] F. Yiqiang, *Triboelectric Energy Harvesting and Non-smooth Systems*. (Thesis University of Liverpool. 2019).

[160] G.R. Tomlinson, *Force distortion in resonance testing of structures with electrodynamic vibration exciters*. J. Sound Vib. **63** (1979) 337.

[161] E. Lefeuvre, A. Badel, C. Richard, L. Petit and D. Guyomar, *A comparison between several vibration-powered piezoelectric generators for standalone systems.* Sensor Actuator A. **126** (2006) 405.

[162] I. Schäfer and K. Krüger, *Modelling of lossy coils using fractional derivatives*, Journal of Physics D: Applied Physics. **41** (2008) 045001.

[163] S. L. Lau and Y. K. Cheung, *Amplitude incremental variational principle for nonlinear vibration of elastic systems*. Journal of Applied Mechanics. **48** (1981) 959.

[164] S. Nacivet, C. Pierre, F. Thouverez and L. Jezequel, *A dynamic lagrangian frequency-time method for the vibration of dry-friction-damped systems*. Journal of Sound and Vibration. **265** (2003) 201.

[165] B. Cochelin and C. Vergez, *A high order purely frequency-based harmonic balance formulation for continuation of periodic solutions*. Journal of sound and vibration. **324** (2009) 243.

[166] L. Azrar, B. Cochelin, N. Damil and M. Potier-ferry, *An asymptotic-numerical method to compute the postbuckling behaviour of elastic plates and shells*. International Journal for Numerical Methods in Engineering. **36** (1993) 1251.

[167] B. Cochelin, *A path-following technique via an asymptotic-numerical method. Computers and structures*. **53** (1994) 1181.

[168] M.F. Dimentberg, *Statistical Dynamics of Nonlinear and Time-Varying Systems* (Wiley, New York, 1988).

[169] W.V. Wedig, *Analysis and simulation of nonlinear stochastic systems. In: W. Schiehlen (ed.) Nonlinear Dynamics in Engineering Systems, p. 337.* (Springer, Berlin, 1989)

[170] J.R. Li, W. Xu, X.L. Yang and Z.K. Sun, *Chaotic motion of Van der Pol-Mathieu-Duffing system under bounded noise parametric excitation*. J. Sound Vib. **309** (2008) 330.

[171] C. Gan, *Noise-induced chaos and basin erosion in softening Duffing oscillator*. Chaos Solitons & Fractals. **25** (2005) 1069.

[172] R.L. Stratonovich, *Topics in the Theory of Random Noise, vol. II* (Gordon and Breach, New York, 1967).

[173] R.V. Bobryk and A. Chrzeszczyk, *Transitions induced by bounded noise*. Physica A **358** (2005) 263.

[174] W.Y. Liu, W.Q. Zhu and Z.L. Huang, *Effect of bounded noise on chaotic motion of duffing oscillator under parametric excitation*. Chaos Solitons & Fractals **12** (2001) 527.

[175] A. Onofrio, *Fuzzy oncology: Fuzzy noise induced bifurcations and their application to anti-tumor chemotherapy*. Appl. Math. Lett. **21** (2008) 662.

[176] S. Arathi, S. Rajasekar and J. Kurths, *Characteristics of stochastic resonance in asymmetric dufing oscillator*, International Journal of Bifurcation and Chaos. **21** (2011) 2729.

[177] J.B. Roberts and P.D. Spanos, *Stochastic averaging: an approximate method of solving random vibration problems*. Int. J. of Non-Linear Mechanics **21** (1986) 111.

[178] W. Zhu, *Recent developments and applications of the stochastic averaging method in random vibration*. Appl. Mech. Rev. **49** (1996) s72.

[179] R.L. Honeycutt, *Stochastic Runge-Kutta algorithms. I. White noise*. Phys. Rev. A **45** (1992) 600.

[180] R.L. Honeycutt, *Stochastic Runge-Kutta algorithms. II. Colored noise*. Phys. Rev. A **45** (1992) 604.

[181] Z. Yang, S. Zhou, J. Zu and D. Inman, *High-performance piezoelectric energy harvesters and their applications*. Joule **2** (2018) 642.

[182] E.S. Leland and P.K. Wright, *Resonance tuning of piezoelectric vibration energy scavenging generators using compressive axial preload*. Smart Mater. Struct. **15** (2006) 1413.

[183] Q. He and M.F. Daqaq, *New insights into utilizing bistability for energy harvesting under white noise*. J. Vibrat. Acoust. **137** (2015) 021009.

[184] V.R. Challa, M.G. Prasad and F. T. Fisher, *A coupled piezoelectric- electromagnetic energy harvesting technique for achieving increased power output through damping matching*. Smart Mater. Struct. **18** (2009) 095029.

[185] R. Ai, L.L.S. Monteiro, P.C.C. Monteiro, P.M.C.L. Pacheco and M.A. Savi, *Piezoelectric vibration-based energy harvesting enhancement exploiting nonsmoothness*. Actuators **8** (2019) 1.

[186] A. Wolf, *Quantifying chaos with lyapunouv exponent*. Princeton: Princeton University press. (1986).

[187] R. N. Mantegna and B. Spagnolo, *Stochastic resonance in a tunnel diode*. Phys Rev E. **49** (1994) R1792.

[188] E. Lanzara, R. N. Mantegna, B. Spagnolo and R. Zangara, *Experimental study of a nonlinear system in the presence of noise: the stochastic resonance*. Am J Phys. **65** (1997) 341.

[189] A. La Barbera and B. Spagnolo, *Spatio-temporal patterns in population dynamics*. Phys A. **314** (2002) 120.

[190] A. Fiasconaro, D. Valenti and B. Spagnolo, *Nonmonotonic behavior of spatiotemporal pattern formation in a noisy lotka-volterra system*. Acta Phys Pol B. **35** (2004) 1491.

[191] D. Valenti, L. Tranchina, M. Brai, A. Caruso, C. Cosentino and B. Spagnolo, *Environmental metal pollution considered as noise: effects on the spatial distribution of benthic foraminifera in two coastal marine areas of sicily (southern italy)*. Ecol Model. **213** (2008) 449.

Appendix A

Coefficients of polynomials $\Gamma^{\pm}$ and $H^{\pm}$

The coefficients of polynomials $\Gamma^{\pm}$ are given by:

$$\chi_{10} = \omega^4 {\gamma_2}^2 \beta_2^2 \left(R_5^2 + R_1^2\right),$$

$$\chi_8 = 8\omega^2 \gamma_2 \beta_2 \left(R_5^2 R_6 + R_1^2 R_6 + 4R_1 R_2\right),$$

$$\begin{aligned}\chi_6^{\pm} =& 32\omega^2 \gamma_2 \beta_2 \left(\gamma_0 \omega^2 \beta_0 \left(R_5^2 + R_1^2\right) + R_4^{\pm} R_5 + R_1 R_3\right) \\ &+ 16\left(R_6 R_1 + 4R_2\right)^2 + 16 R_6^2 R_5^2,\end{aligned}$$

$$\begin{aligned}\chi_4^{\pm} =& 128\omega^2 \beta_0 \gamma_0 \left(R_6\left(R_5^2 + R_1^2\right) + 4R_1 R_2\right) + 512 R_3 R_2 \\ &+ 128 R_6 \left(R_1 R_3 + R_4^{\pm} R_5\right),\end{aligned}$$

$$\chi_2^{\pm} = 256\left(\left(\gamma_0 \omega^2 \beta_0 R_1 + R_3\right)^2 + \left(R_4^{\pm} + \gamma_0 \omega^2 \beta_0 R_5\right)^2\right),$$

where

$$R_1 = \frac{1-\omega^2}{\left(1-\omega^2\right)^2 + \mu_e^2 \omega^2},$$

$$R_2 = \frac{3}{4}\lambda_2 - \frac{1}{2}\frac{\lambda_1 \gamma_2}{\gamma_1},$$

$$R_3 = \omega_1^2 - \omega^2 + \frac{\delta\eta\omega^2\left(\omega_3^2 - \omega^2\right)}{\mu_P^2 \omega^2 + \left(\omega_3^2 - \omega^2\right)^2},$$

$$R_4^{\pm} = -\frac{\delta\eta\omega^3 \mu_P}{\mu_P^2 \omega^2 + \left(\omega_3^2 - \omega^2\right)^2} + \left(\nu_1 \pm \nu_2\right)\omega,$$

$$R_5 = -\frac{\mu_e \omega}{\left(1-\omega^2\right)^2 + \mu_e^2 \omega^2},$$

and

$$R_6 = \omega^2 \left(\beta_2\gamma_0 + \gamma_2\beta_0\right).$$

Those of polynomials $H^{\pm}$ are given as follows:

$$\iota_{10} = \omega^4 {\gamma_2}^2 \beta_2^2 \left(\Delta_5^2 + \Delta_1^2\right),$$

$$\iota_8 = 8\omega^2\gamma_2\beta_2 \left(\Delta_5^2\Delta_6 + \Delta_1^2\Delta_6 + 4\Delta_1\Delta_2\right),$$

$$\begin{aligned}\iota_6^{\pm} =& 32\omega^2\gamma_2\beta_2 \left(\gamma_0\omega^2\beta_0 \left(\Delta_5^2 + \Delta_1^2\right) + \Delta_4^{\pm}\Delta_5 + \Delta_1\Delta_3\right) \\ &+ 16\left(\Delta_6\Delta_1 + 4\Delta_2\right)^2 + 16\Delta_6^2\Delta_5^2,\end{aligned}$$

$$\begin{aligned}\iota_4^{\pm} =& 128\omega^2\beta_0\gamma_0 \left(\Delta_6 \left(\Delta_5^2 + \Delta_1^2\right) + 4\Delta_1\Delta_2\right) + 512\Delta_3\Delta_2 \\ &+ 128\Delta_6 \left(\Delta_1\Delta_3 + \Delta_4^{\pm}\Delta_5\right),\end{aligned}$$

$$\iota_2^{\pm} = 256 \left(\left(\gamma_0\omega^2\beta_0\Delta_1 + \Delta_3\right)^2 + \left(\Delta_4^{\pm} + \gamma_0\omega^2\beta_0\Delta_5\right)^2\right),$$

where

$$\Delta_1 = \frac{1 - r_1\varsigma_2}{\left(1 - r_1\varsigma_2\right)^2 + \left(\mu_e\omega + r_1\varsigma_1\right)^2},$$

$$\Delta_2 = \frac{3}{4}\lambda_2 - \frac{1}{2}\frac{\lambda_1\gamma_2}{\gamma_1},$$

$$\Delta_3 = \omega_1^2 - \omega^2 + \frac{\delta\eta\omega^2(r_2\varrho_2 - \omega^2)}{\left(r_2\varrho_2 - \omega^2\right)^2 + \left(\mu_P\omega + r_2\varrho_1\right)^2},$$

$$\Delta_4^{\pm} = -\frac{\delta\eta\omega^2(\mu_P\omega + r_2\varrho_1)}{\left(r_2\varrho_2 - \omega^2\right)^2 + \left(\mu_P\omega + r_2\varrho_1\right)^2} + \left(\nu_1 \pm \nu_2\right)\omega,$$

$$\Delta_5 = -\frac{\mu_e\omega + r_1\varsigma_1}{\left(1 - r_1\varsigma_2\right)^2 + \left(\mu_e\omega + r_1\varsigma_1\right)^2},$$

and

$$\Delta_6 = \omega^2 \left(\beta_2\gamma_0 + \gamma_2\beta_0\right).$$

Appendix B

Derivation of the drift and the diffusion coefficients of diffusive Markov process vector

Let us consider the following stochastic dynamical system

$$\frac{dX_j}{dt} = f_j\left(X,t\right) + g_{jr}\left(X,t\right)\xi_r(t), \tag{B.1}$$

Where $j = 1, 2, ..., n$ and $r = 1, 2, ..., m$ (n is the number of state variables and m is the number of components of the noise vector). Following [177], the state vector of system (B.1) can be approximated by a diffusive Markov process vector. The process vector X is therefore governed by the following Fokker-Planck-Kolmogorov (FPK) equation:

$$\frac{\partial P}{\partial t} = -\frac{\partial}{\partial X_j}\left(a_j P\right) + \frac{1}{2}\frac{\partial^2}{\partial X_j \partial X_k}\left(b_{jk} P\right) \tag{B.2}$$

and the related Itô equations:

$$dX_j = m_j dt + \sigma_{jr} dW_r, \tag{B.3}$$

where a_j and b_{jk} are defined as

$$a_j = \left\langle f_j\left(X,t\right) + \int_{-\infty}^{0} \frac{\partial g_{jr}\left(X,t\right)}{\partial X_k} g_{kl}\left(X,t+\tau\right) R_{rl}\left(\tau\right) d\tau \right\rangle, \tag{B.4}$$

$$b_{jk} = \left\langle \int_{-\infty}^{+\infty} g_{jr}\left(X,t\right) g_{kl}\left(X,t+\tau\right) R_{rl}\left(\tau\right) d\tau \right\rangle. \tag{B.5}$$

The drift and the diffusion coefficients are related to a_j and b_{jk} by the formulas:

$$m_j = a_j, \tag{B.6}$$

$$\sigma_{jr}\sigma_{kr} = b_{jk}. \tag{B.7}$$

$R_{rl}(\tau)$ are the components of the cross-covariance matrix of the noise vector. Note that the repeated index convention is used in the above equations. Also note that $\langle\rangle$ denotes the mean value, defined for a function f of period T as $\langle f(t)\rangle = \frac{1}{T}\int_0^T f(t)dt$. Moreover, P denotes the joint probability density.

Functions f_i and g_{ij} of section 2.2.1.2 are defined as:

$$\begin{aligned} f_1(U,t) = \Bigg[& -\left(\nu_1 - \nu_2 \operatorname{sign}\left(\sin\left(\vartheta_1\right)\right)\right) a \sin\left(\vartheta_1\right) + \frac{\lambda_1 a^2}{\omega_1}\cos^2\left(\vartheta_1\right) \\ & - \left(\gamma_0 + \gamma_1 a\cos\left(\vartheta_1\right) + \gamma_2 a^2\cos^2\left(\vartheta_1\right)\right)\frac{b}{\omega_1}\sin\left(\vartheta_2\right) \\ & + \frac{\lambda_2 a^3}{\omega_1}\cos^3\left(\vartheta_1\right) + \frac{\delta c}{\omega_1}\cos\left(\vartheta_3\right)\Bigg]\sin(\vartheta_1), \end{aligned} \tag{B.8}$$

$$g_{11}(U,t) = -\frac{\sin\left(\vartheta_1\right)}{\omega_1}, \tag{B.9}$$

$$\begin{aligned} f_2(U,t) = \Bigg[& -\left(\nu_1 - \nu_2 \operatorname{sign}\left(\sin\left(\vartheta_1\right)\right)\right)\sin\left(\vartheta_1\right) + \frac{\lambda_1 a}{\omega_1}\cos^2\left(\vartheta_1\right) \\ & - \left(\frac{\gamma_0}{a} + \gamma_1\cos\left(\vartheta_1\right) + \gamma_2 a\cos^2\left(\vartheta_1\right)\right)\frac{b}{\omega_1}\sin\left(\vartheta_2\right) \\ & + \frac{\lambda_2 a^2}{\omega_1}\cos^3\left(\vartheta_1\right) + \frac{\delta c}{\omega_1 a}\cos\left(\vartheta_3\right)\Bigg]\cos(\vartheta_1), \end{aligned} \tag{B.10}$$

$$g_{21}(U,t) = -\frac{\cos\left(\vartheta_1\right)}{\omega_1 a}, \tag{B.11}$$

$$\begin{aligned} f_3(U,t) = & \left[-\mu_e b\sin\left(\vartheta_2\right) - \left(\beta_0 + \beta_1 a\cos\left(\vartheta_1\right) + \beta_2 a^2\cos^2\left(\vartheta_1\right)\right)\omega_1 a\sin\left(\vartheta_1\right)\right] \\ & \times \sin\left(\vartheta_2\right), \end{aligned} \tag{B.12}$$

$$g_{32}(U,t) = -\sin\left(\vartheta_2\right), \tag{B.13}$$

$$\begin{aligned} f_4(U,t) = & \left[-\mu_e\sin\left(\vartheta_2\right) - \left(\beta_0 + \beta_1 a\cos\left(\vartheta_1\right) + \beta_2 a^2\cos^2\left(\vartheta_1\right)\right)\omega_1\frac{a}{b}\sin\left(\vartheta_1\right)\right] \\ & \times \cos\left(\vartheta_2\right), \end{aligned} \tag{B.14}$$

$$g_{42}\left(U,t\right)=-\frac{\cos\left(\vartheta_2\right)}{b}, \tag{B.15}$$

$$\begin{aligned} f_5\left(U,t\right)=-\Bigg[&-\frac{\eta\omega_1}{\omega_3}a\sin\left(\vartheta_1\right)\left(\nu_1-\nu_2\,\mathrm{sign}\left(\sin\left(\vartheta_1\right)\right)\right)\\ &-\frac{b\eta}{\omega_3}\left(\gamma_0+\gamma_1 a\cos\left(\vartheta_1\right)+\gamma_2 a^2\left(\cos\left(\vartheta_1\right)\right)^2\right)\sin(\vartheta_2)\\ &+\frac{\eta\lambda_1}{\omega_3}a^2\cos^2\left(\vartheta_1\right)+\frac{\eta\lambda_2}{\omega_3}a^3\cos^3\left(\vartheta_1\right)\\ &+\mu_P c\sin\left(\vartheta_3\right)+\frac{\eta{\omega_1}^2 a\cos\left(\vartheta_1\right)}{\omega_3}+\frac{\eta\delta c\cos\left(\vartheta_3\right)}{\omega_3}\Bigg]\times\sin(\vartheta_3), \end{aligned} \tag{B.16}$$

$$g_{51}\left(U,t\right)=\eta\frac{\sin\left(\vartheta_3\right)}{\omega_3}, \tag{B.17}$$

$$g_{53}\left(U,t\right)=-\frac{\sin\left(\vartheta_3\right)}{\omega_3}, \tag{B.18}$$

$$\begin{aligned} f_6\left(U,t\right)=-\Bigg[&-\frac{\eta\omega_1}{\omega_3 c}a\sin\left(\vartheta_1\right)\left(\nu_1-\nu_2\,\mathrm{sign}\left(\sin\left(\vartheta_1\right)\right)\right)\\ &-\frac{b\eta}{\omega_3 c}\left(\gamma_0+\gamma_1 a\cos\left(\vartheta_1\right)+\gamma_2 a^2\left(\cos\left(\vartheta_1\right)\right)^2\right)\sin(\vartheta_2)\\ &+\frac{\eta\lambda_1}{\omega_3 c}a^2\cos^2\left(\vartheta_1\right)+\frac{\eta\lambda_2}{\omega_3 c}a^3\cos^3\left(\vartheta_1\right)\\ &+\mu_P\sin\left(\vartheta_3\right)+\frac{\eta{\omega_1}^2 a\cos\left(\vartheta_1\right)}{\omega_3 c}+\frac{\eta\delta\cos\left(\vartheta_3\right)}{\omega_3}\Bigg]\times\cos(\vartheta_3), \end{aligned} \tag{B.19}$$

$$g_{61}\left(U,t\right)=\eta\frac{\cos\left(\vartheta_3\right)}{\omega_3 c}, \tag{B.20}$$

and

$$g_{63}\left(U,t\right)=-\frac{\cos\left(\vartheta_3\right)}{\omega_3 c}. \tag{B.21}$$

The drift and the diffusion coefficients are evaluated by the mean of Eqs.(B.4)-(B.7). The results are given below:

$$m_1=\frac{\tau_1 F_0^2\left(1+\tau_1^2\left(\omega^2+\omega_1^2\right)\right)}{4a\omega_1^2\left(1+\tau_1^2\left(\omega+\omega_1\right)^2\right)\left(1+\tau_1^2\left(\omega-\omega_1\right)^2\right)}-\frac{a\nu_1}{2}, \tag{B.22}$$

$$m_2=\frac{3\lambda_2 a^2}{8\omega_1}, \tag{B.23}$$

$$m_3 = \frac{D_2}{2b\left(1+\tau_2^2\right)} - \frac{\mu_e b}{2}, \tag{B.24}$$

$$m_4 = 0, \tag{B.25}$$

$$m_5 = \frac{\eta^2 F_0^2 \tau_1 \left(1+\tau_1^2\left(\omega^2+\omega_3^2\right)\right)}{4c\omega_3^2\left(1+\tau_1^2\left(\omega+\omega_3\right)^2\right)\left(1+\tau_1^2\left(\omega-\omega_3\right)^2\right)} + \frac{D_3}{2c\omega_3^2\left(1+\omega_3^2\tau_3^2\right)} - \frac{\mu_P c}{2}, \tag{B.26}$$

$$m_6 = -\frac{\eta\delta}{2\omega_3}, \tag{B.27}$$

$$\sigma_1 = \sqrt{\frac{\tau_1 F_0^2\left(1+\tau_1^2\left(\omega^2+\omega_1^2\right)\right)}{2\omega_1^2\left(1+\tau_1^2\left(\omega+\omega_1\right)^2\right)\left(1+{\tau_1}^2\left(\omega-\omega_1\right)^2\right)}} = \sqrt{2a\left(m_1+\frac{a\nu_1}{2}\right)}, \tag{B.28}$$

$$\sigma_2 = \frac{\sigma_1}{a}, \tag{B.29}$$

$$\sigma_3 = \sqrt{\frac{D_2}{1+\tau_2^2}} = \sqrt{2b\left(m_3+\frac{\mu_e b}{2}\right)}, \tag{B.30}$$

$$\sigma_4 = \frac{\sigma_3}{b}, \tag{B.31}$$

$$\sigma_5 = \sqrt{\frac{\eta^2 F_0^2 \tau_1\left(1+{\tau_1}^2\left(\omega^2+\omega_3^2\right)\right)}{2\omega_3^2\left(1+\tau_1^2\left(\omega+\omega_3\right)^2\right)\left(1+\tau_1^2\left(\omega-\omega_3\right)^2\right)} + \frac{D_3}{\omega_3^2\left(1+\omega_3^2\tau_3^2\right)}} = \sqrt{2c\left(m_5+\frac{\mu_P c}{2}\right)}, \tag{B.32}$$

and

$$\sigma_6 = \frac{\sigma_5}{c}. \tag{B.33}$$

List of publications in international refereed journals

G. G. Sengha, W. Fokou Kenfack, M. Siewe Siewe, C.B. Tabi and T.C. Kofane, *Dynamics of a non-smooth type hybrid energy harvester with nonlinear magnetic coupling.* Communications in Nonlinear Science and Numerical Simulation **90** (2020) 105364.

G. G. Sengha, W. Fokou Kenfack, D. J. Owono Bekoa, M. Siewe Siewe, C.B. Tabi and T.C. Kofane, *Fractional properties' effects on a hybrid energy harvesting system dynamics.* Meccanica **56** (2021) 2451.

Commun Nonlinear Sci Numer Simulat 90 (2020) 105364

Contents lists available at ScienceDirect

Commun Nonlinear Sci Numer Simulat

journal homepage: www.elsevier.com/locate/cnsns

Research paper

Dynamics of a non-smooth type hybrid energy harvester with nonlinear magnetic coupling

G.G. Sengha[a,b,c,*], W. Fokou Kenfack[a], M. Siewe Siewe[a], C.B. Tabi[a,d], T.C. Kofane[a]

[a] Laboratory of Mechanics, Department of Physics, Faculty of sciences, University of Yaounde I, Yaounde, P.O. Box 812, Cameroon
[b] Department of Physics, Faculty of sciences, University of Bangui, Bangui, P.O. Box 1450, Central African Republic
[c] The African Center of Excellence in Information and Communication Technologies (CETIC), Yaounde, Cameroon
[d] Department of Physics and Astronomy, Botswana International University of Science and Technology, Private Bag 16, Palapye, Botswana

ARTICLE INFO

Article history:
Received 6 December 2019
Revised 21 May 2020
Accepted 26 May 2020
Available online 27 May 2020

Keywords:
Vibration energy harvesting
Harmonic balance method
Stochastic averaging method
Stochastic P-bifurcation

ABSTRACT

In this paper, a system with energy harvester behavior is modeled by non-smooth coupled oscillators subjected to harmonic and random excitations. A modified harmonic balance method is proposed to study the dynamics of the oscillators under harmonic driving. Then, the probabilistic response of the system under bounded and colored noise excitations is tackled through the stochastic averaging method. We show that the proposed modified harmonic balance technique is very effective in parameters regime for which the system output waveform is nearly sinusoidal. In this parameters regime, the harvester performance is improved for optimum nonlinear magnetic coupling coefficients and for weak nonlinearities and damping in the harvester mechanical part. Under random excitations, we find in the weak parameters regime that, the probability density functions (PDFs) for the coupled oscillators amplitudes illustrate a single-peak mode and exhibit phenomenological transitions as the noisy excitations parameters vary. The mean output powers (MOPs) linearly increase with the colored noises intensities, and the piezoelectric MOP especially shows a resonance effect as the bounded noise level increases. Contrariwise, probed with Monte Carlo simulation, we find that the system exhibits the stochastic P-bifurcation for large parameters of coupling and nonlinearity; parameters' regime for which the harvester under purely harmonic driving demonstrates low performance.

1. Introduction

Vibration-powered energy harvesters are typically, although not exclusively, formed of mass-spring system. These energy harvesters have attracted the attention of researchers in the past recent years. Hundred papers and several text-books reporting developments in this research area are present in the literature [1–14]. In this rich bibliography, investigators have used three main transduction techniques in such generators to extract and convert mechanical energy into electrical energy. These are electromagnetic, piezoelectric, and electrostatic mechanisms. These three fundamental techniques have been shown to be capable of generating typical output power levels in the range of a few microwatts to several milliwatts [14]. Such electric power levels are useful for technological purposes. For instance, they are helpful in micro-electromechanical

* Corresponding author at: Department of Physics, P.O. Box 812, Yaounde, Cameroon
E-mail addresses: senghaghislain2@yahoo.fr (G.G. Sengha), wilsonkenfack@gmail.com (W.F. Kenfack), martinsiewesiewe@yahoo.fr (M.S. Siewe), tabic@biust.ac.bw (C.B. Tabi), tckofane@yahoo.com (T.C. Kofane).

https://doi.org/10.1016/j.cnsns.2020.105364
1007-5704/

systems (MEMS) technology, for the design of ultralow-power consumption sensors, which are low-cost and of low weight because of their small size. This is also justified by a wealth of literature devoted to the concept of vibration harvesting.

It is commonly assumed in most of the works devoted to energy harvesting systems, implementing the electromagnetic conversion mechanism, that the interaction between the mechanical and the electrical parts of the system is due to a radial magnetic field of uniform type only, created in the air-gap of a permanent magnet. However, following Tomlinson [15], this radial magnetic field is a nonlinear function of the coil position. The later consideration, which results in a nonlinear magnetic coupling between both parts of the energy harvester, has only been assumed by few investigators among which Siewe *et al.* [8,16], and the effects of such nonlinear magnetic coupling have not yet been sufficiently probed, to our knowledge. For instance, attention deserves to be paid on the effect of this peculiar magnetic coupling on the harvester efficiency.

Nature systems can't strictly speaking preserve from random fluctuations, which may originate from the system environment or may be inherent in the system. Several reports have predicted energy harvesters response to random signal inputs via stochastic averaging method and/or numerical integration [1–12]. Martens *et al.* [1] and Xu *et al.* [3] studied, by the mean of stochastic averaging procedure, the effects of random environmental fluctuations on the performance of different vibration energy harvesting systems. The systems considered by these investigators make use of the piezoelectric conversion mechanism and are subjected to excitations of white noise character. Borowiec *et al.* [2] numerically studied a frequency broadband nonlinear resonator with energy harvesting outlook, excited by stochastic ground motion. This system was modeled by a non-smooth stochastic differential equations. In reference [8], Siewe and coworkers considered an electromechanical seismograph, with nonlinear magnetic coupling, under the assumption of a stochastic vibration environment. They found that for large magnetic coupling parameters, stochastic P-bifurcation is expected to appear. Another noise-induced behavior referred to as stochastic resonance, reported in a large variety of natural systems [17–21], has been recognized to be an advantageous effect in vibration energy harvesting systems, to maximize the harvested power and achieve high harvesting efficiency [11,22–25].

Systems with non-smooth behavior or switching systems are ubiquitous in nature. In various fields of research such as population dynamics [26–29], control theory [30–33], tribology [34,35] for instance, the modeling of such systems give rise to non-smooth differential equations. These systems, have received a lot of attention during the past two decades and several books have been devoted to them [36,37]. In the context of energy harvesting systems, non-smooth models arise in studies on electromagnetic harvesters with stoppers having impact characteristics [2,38,39].

This paper essentially aims at investigating the effect of the nonlinear magnetic coupling on the efficiency of a class of hybrid vibration energy harvesting device whose mechanical damping possesses a non-smooth behavior. It also investigates the effects on the harvested powers, of the parameters of non-smoothness and nonlinearities, under harmonic excitation, with the aim of determining parameters regime for which the device may be optimally designed. As other issue, this paper studies the effect on the harvested powers of environmental random fluctuations, which are inherent in the system. To meet these expectations the remainder of the paper is organized as follows: In Sect. 2, we provide a schematic description of the harvester and derive the governing equations. In Sect. 3, a modified harmonic balance method is used to derive the stationary harmonic response of the system. Then, the effects on the oscillatory amplitudes, the harvested powers and the system efficiency of some system parameters, especially the magnetic coupling parameter, the excitation strength and the mechanical damping parameter, are investigated by the mean of this analytical treatment. The results are then numerically verified. In Sect. 4, the stochastic averaging procedure enables us to derive the stationary probability densities for the vibration amplitudes, and to express the average output powers. Phenomenological transitions exhibited by the PDFs as the noisy excitations parameters vary are then discussed. The agreement between the analytical result and the Monte Carlo simulation approach is demonstrated in the low parameters regime. In such parameters regime, noises effects on the mean output powers are also discussed. Then stochastic P-bifurcation is investigated in the large coupling parameters regime by the mean of Monte Carlo simulation. Finally, Sect. 5 summarizes the paper.

2. The mathematical model

The system under consideration is a hybrid energy harvester making use of both electromagnetic and piezoelectric conversions and whose mechanical part possesses a damping with discontinuous behavior. This device is sketched in Fig. 1.

The mechanical part is composed of a suspended mass m, whose motion is determined by the inherent forces of the damped mass-spring system and the inertial forces acting on the system. $\Gamma(\tau)$ is the time-dependent acceleration of the frame (or base). From the Newton's second law, the motion of the mass is described by Eq. (1)

$$m\ddot{X} = -\mu_0\dot{X} - F_P + F_L - m\Gamma(\tau), \tag{1}$$

with X the relative displacement of the mass with respect to the frame; F_P, the global restoring force due to the spring and the piezoelectric element; F_L, the Laplace force; $-m\Gamma(\tau)$ the inertial force and $\mu_0\dot{X}$ the damping forces originating from friction, air resistance, etc. Here, the magnitude of the damping forces also depends on the movement direction of the suspended mass in such a way that $\mu_0 = \begin{cases} \mu_0^+ & \text{if } \dot{x} > 0 \\ \mu_0^- & \text{if } \dot{x} < 0 \end{cases}$.

The electrical part consists of two components: the piezoelectric and the electromagnetic circuits. The piezoelectric circuit is formed of the piezoelectric element, an inductor with inductance L_P and the load resistance R_P. However, the electromagnetic circuit consists of a linear inductor L, a linear capacitor of capacitance C, and a linear resistor R. Using the

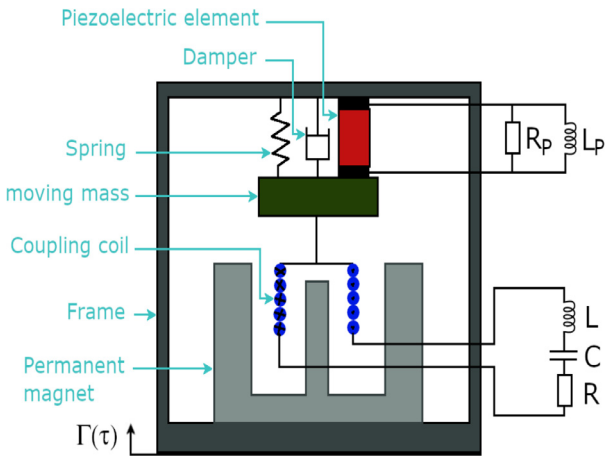

Fig. 1. Sketch of the energy harvester.

Kirchhoff's laws, these two circuitries can be described by the following equations:

$$i_P = \frac{v}{R_P} + \frac{1}{L_P}\int v d\tau, \tag{2a}$$

$$L\frac{d^2q}{d\tau^2} + R\frac{dq}{d\tau} + \frac{1}{C}q + E_L = 0, \tag{2b}$$

where i_P and v are respectively the current and the voltage across the electrodes of the piezoelectric element, E_L the Lenz electromotive voltage and q, the instantaneous electrical charge.

The harvester's mechanical part and electromagnetic circuit interact through the air-gap of a permanent magnet which creates a radial magnetic field $\vec{B}$. The relationship between the magnitude B of that magnetic field and the coil position (related to X), established by Tomlinson [15], is given as:

$$B = B_0\left(1 - \left(\frac{X + X_0}{X_{\max}}\right)^2\right), \tag{3}$$

where B_0 is the highest intensity that the field B reaches, X_0 is the armature initial position, and $X_{\max}$ is the maximum amplitude. Thence, the motion of the mechanical part should take into account the relationship between the Laplace force and the current given by

$$F_L = \alpha_0\left(1 - \left(\frac{X + X_0}{X_{max}}\right)^2\right)\frac{dq}{d\tau}, \tag{4}$$

and the expression of the global restoring force [40], namely

$$F_P = \left(k_0X + k_1X^2 + k_2X^3 + \alpha v\right). \tag{5}$$

k_0 is the global linear stiffness of the system's mechanical part. Parameters k_1 and k_2 define the nonlinearity of the spring. In the electromagnetic circuit, The Lenz electromotive voltage E_L is defined as:

$$E_L = \kappa_0\left(1 - \left(\frac{X + X_0}{X_{\max}}\right)^2\right)\frac{dX}{d\tau}, \tag{6}$$

while the current i_P, across the piezoelectric element, is related to the mass displacement X by:

$$i_P = \alpha\dot{X} - C_P\frac{dv}{d\tau}. \tag{7}$$

Parameters α and C_P have been thoroughly defined in reference [13]. They are respectively referred to as *force factor* and *blocking capacitance* of the piezoelectric insert. α_0 and κ_0 are coefficients of adjustment of dimension. They depend on B_0 and the coil geometrical parameters.

The complete mathematical model that describes the physical model of Fig. 1 is obtained by replacing Eqs. (4), (5), (6) and (7) into Eqs. (1), (2a) and (2b). Thence, setting $\omega_m = \sqrt{\frac{k_0}{m}}$, $\omega_e = \sqrt{\frac{1}{LC}}$, $\omega_P = \sqrt{\frac{1}{L_PC_P}}$, $x = \frac{X}{l}$, $y = \frac{q}{Q_0}$, $z = \frac{v}{V_0}$, where l, Q_0 and V_0 are respectively the reference length, charge and voltage; and with the time transformation $t = \omega_e\tau$, one obtains

the following dimensionless equations:

$$\ddot{x} + (\nu_1 + \nu_2 \text{sign}(\dot{x}))\dot{x} + \omega_1^2 x + \lambda_1 x^2 + \lambda_2 x^3 + \delta z + \left(\gamma_0 + \gamma_1 x + \gamma_2 x^2\right)\dot{y} = f(t), \tag{8a}$$

$$\ddot{y} + \mu_e \dot{y} + y + \left(\beta_0 + \beta_1 x + \beta_2 x^2\right)\dot{x} = 0, \tag{8b}$$

$$\ddot{z} + \mu_P \dot{z} + \omega_3^2 z + \eta \ddot{x} = 0, \tag{8c}$$

with the dimensionless parameters given by

$$\begin{array}{llll} \nu_1 = \frac{\mu_0^+ + \mu_0^-}{2m\omega_e}, & \omega_1 = \frac{\omega_m}{\omega_e}, & \lambda_1 = \frac{k_1 l}{m\omega_e^2}, & \gamma_0 = -\frac{\alpha_0 Q_0}{ml\omega_e}\frac{X_{\max}^2 - X_0^2}{X_{\max}^2}, \quad \gamma_1 = \frac{2\alpha_0 X_0 Q_0}{m\omega_e X_{\max}^2}, \\ \gamma_2 = \frac{\alpha_0 l Q_0}{m\omega_e X_{\max}^2}, & \delta = \frac{\alpha V_0}{ml\omega_e^2}, & \lambda_2 = \frac{k_2 l^2}{m\omega_e^2}, & \mu_e = \frac{R}{L\omega_e}, \quad \beta_0 = \frac{\kappa_0 l}{LQ_0\omega_e}\frac{X_{\max}^2 - X_0^2}{X_{\max}^2}, \quad \nu_2 = \frac{\mu_0^+ - \mu_0^-}{2m\omega_e}, \\ \beta_1 = -\frac{2\kappa_0 l^2 X_0}{LQ_0\omega_e X_{\max}^2}; & \beta_2 = -\frac{\kappa_0 l^3}{LQ_0\omega_e X_{\max}^2}, & \mu_P = \frac{1}{R_P C_P \omega_e}, & \omega_3 = \frac{\omega_p}{\omega_e}, \quad \eta = -\frac{\alpha l}{C_P V_0}. \end{array} \tag{9}$$

The excitation function $f(t)$ is related to the frame motion acceleration as $f(t) = -\frac{\Gamma(\tau)}{l\omega_e^2}$. We assume throughout this report that $\Gamma(\tau)$ is formed of a harmonic function with constant amplitude, i.e. $f(t)$ can be mathematically expressed as $f(t) = F_0\cos(\varphi(t))$, with F_0, the amplitude of the excitation.

The potentials of the harvester mechanical and electrical parts are given by

$$V(x) = \frac{\omega_1^2}{2}x^2 + \frac{\lambda_1}{3}x^3 + \frac{\lambda_2}{4}x^4, \quad V(y) = \frac{1}{2}y^2 \text{ and } V(z) = \frac{\omega_3^2}{2}z^2. \tag{10}$$

$V(y)$ and $V(z)$ are harmonic potentials while potential $V(x)$ can portray a bounded single well, an unbounded single well or a double well. The later case occurs when the conditions $\lambda_2 > 0$ and $\lambda_1^2 - 4\lambda_2\omega_1^2 > 0$ hold, and the potential $V(x)$ has three equilibria among which only one is unstable. These two conditions are assumed in the remainder of this report.

3. System's harmonic and chaotic response

3.1. Amplitude of the harmonic oscillatory response of the system: Modified harmonic balance method

This section aims at seeking an approximate analytical solution of Eq. (8) when the excitation is purely sinusoidal, that is, $\varphi(t) = \omega t$ with ω the excitation frequency. To this end, the approximate solution is taken, consistently to the harmonic balance method, in the form:

$$x(t) = a_1\cos(\omega t) + a_2\sin(\omega t), \tag{11a}$$

$$y(t) = b_1\cos(\omega t) + b_2\sin(\omega t), \tag{11b}$$

$$z(t) = c_1\cos(\omega t) + c_2\sin(\omega t). \tag{11c}$$

Let $a = \sqrt{a_1^2 + a_2^2}$, $b = \sqrt{b_1^2 + b_2^2}$ and $c = \sqrt{c_1^2 + c_2^2}$, the amplitudes of the preceding harmonic solutions. Replacing Eq. (11) into Eq. (8) and neglecting the terms of higher harmonics yields:

$$\left(\left(\frac{3\lambda_2}{4} - \frac{\lambda_1\gamma_2}{2\gamma_1}\right)a^2 + \omega_1^2 - \omega^2\right)a_1 + (\nu_1 \pm \nu_2)\omega a_2 + \left(\frac{1}{4}\omega\gamma_2 a^2 + \gamma_0\omega\right)b_2 + \delta c_1 = F_0, \tag{12a}$$

$$-(\nu_1 \pm \nu_2)\omega a_1 + \left(\left(\frac{3\lambda_2}{4} - \frac{\lambda_1\gamma_2}{2\gamma_1}\right)a^2 + \omega_1^2 - \omega^2\right)a_2 - \left(\frac{1}{4}\omega\gamma_2 a^2 + \gamma_0\omega\right)b_1 + \delta c_2 = 0, \tag{12b}$$

$$\left(1 - \omega^2\right)b_1 + \mu_e\omega b_2 + \left(\frac{\omega\beta_2}{4}a^2 + \beta_0\omega\right)a_2 = 0, \tag{12c}$$

$$-\mu_e\omega b_1 + \left(1 - \omega^2\right)b_2 - \left(\frac{\omega\beta_2}{4}a^2 + \beta_0\omega\right)a_1 = 0, \tag{12d}$$

$$\left(\omega_3^2 - \omega^2\right)c_1 + \mu_P\omega c_2 - \eta\omega^2 a_1 = 0, \tag{12e}$$

$$-\mu_P\omega c_1 + \left(\omega_3^2 - \omega^2\right)c_2 - \eta\omega^2 a_2 = 0. \tag{12f}$$

Combining the six preceding equations, one can show that depending on the value taken by the sign function, the amplitude a is either the root of the algebraic equation $\Gamma^+(a) = 0$ or $\Gamma^-(a) = 0$, where the polynomial functions $\Gamma^{\pm}$ are defined as

$$\Gamma^{\pm}(a) = \chi_{10}a^{10} + \chi_8 a^8 + \chi_6^{\pm}a^6 + \chi_4^{\pm}a^4 + \chi_2^{\pm}a^2 - 256F_0^2. \tag{13}$$

The coefficients of these polynomials are given in the Appendix A. The approximate amplitude of the harvester mechanical part's oscillation can be taken as the average of the roots yielded by the equations $\Gamma^+(a) = 0$ and $\Gamma^-(a) = 0$. Once this

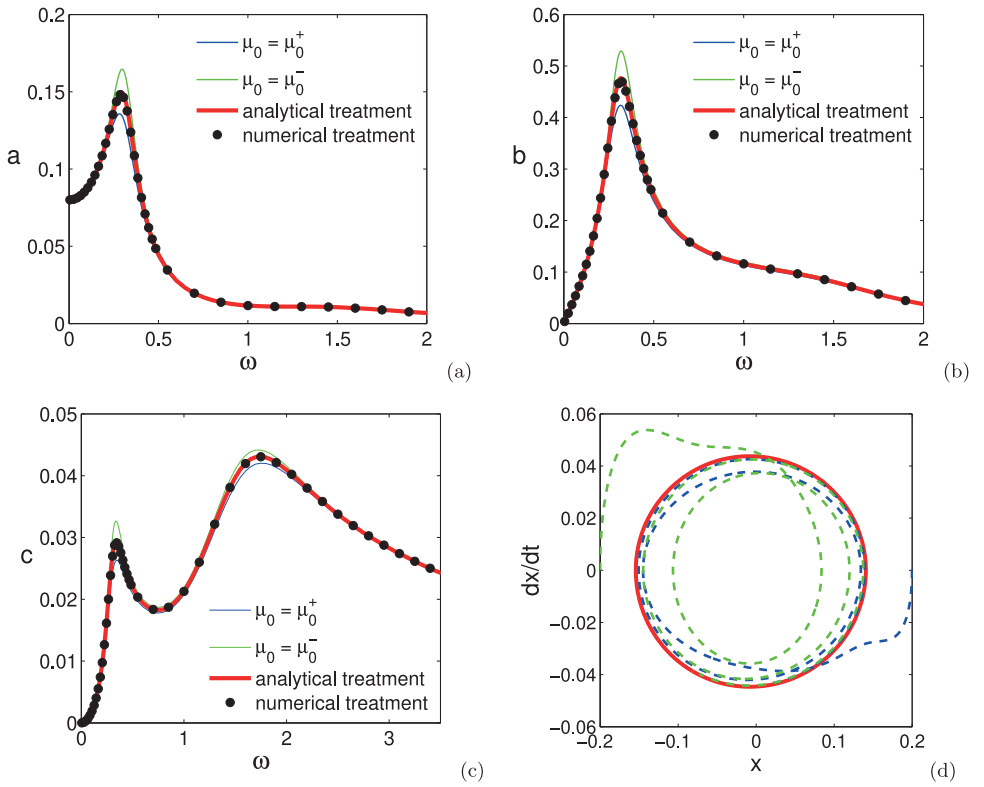

Fig. 2. Frequency-response curves: amplitudes of (a) mechanical vibrations, (b) electromagnetic vibrations and (c) piezoelectric ones versus driving frequency and (d) phase space structure of the mechanical oscillator. The blue and green solid lines are analytically obtained from the smooth version of system (8) in cases $\mu_0 = \mu_0^+$ and $\mu_0 = \mu_0^-$ respectively. For Figs. 2(a), (b) and (c), the thick red curves and the black dots are analytical and numerical results obtained from system (8). For Fig. 2(d), blue and green dotted lines represent trajectories obtained with initial conditions ($x = 0.2$, $\dot{x} = 0$, $y = 0$, $\dot{y} = 0$, $z = 0$, $\dot{z} = 0$) and ($x = -0.2$, $\dot{x} = 0$, $y = 0$, $\dot{y} = 0$, $z = 0$, $\dot{z} = 0$) respectively, the red solid line stands for the limit-cycle. Parameters are $\nu_1 = 0.3$, $\nu_2 = 0.05$, $\mu_e = 1.0$, $\mu_P = 16.0$, $\omega_1 = 0.5$, $\omega_3 = 5.66$, $\lambda_1 = 0.0045$, $\lambda_2 = 0.00002$, $\gamma_0 = -0.125$, $\gamma_1 = 0.002$, $\gamma_2 = 0.02$, $\beta_0 = 10.0$, $\beta_1 = -0.16$, $\beta_2 = -1.6$, $\delta = 0.001$, $\eta = -64.0$ and $F_0 = 0.02$. (For interpretation of the references to colour in this figure legend, the reader is referred to the web version of this article.)

amplitude is determined, the amplitudes of the electrical part's oscillations are given by:

$$b = \frac{\left|\beta_0 + \frac{1}{4}\beta_2 a^2\right|\omega a}{\sqrt{\mu_e^2\omega^2 + \left(1-\omega^2\right)^2}}, \tag{14a}$$

$$c = \frac{|\eta|\omega^2 a}{\sqrt{\mu_P^2\omega^2 + \left(\omega_3^2 - \omega^2\right)^2}}. \tag{14b}$$

By the mean of the Newton-Raphson algorithm, the amplitude a is calculated, hence b and c are deduced. These amplitudes can also be estimated by the mean of numerical integration of Eq. (8) with the fourth-order Runge-Kutta algorithm. The results of our calculations are provided in Figs. 2 and 3. In Fig. 2, are depicted the analytical and the numerical frequency-response curves. The agreement between both results illustrates the effectiveness of present analytical treatment. However, this consistency does not hold irrespectively of the values of non-smoothness (damping) coefficients ν_1 and ν_2. Yet, good agreement appears in the range of damping parameters for which the system's response is harmonic. It can be seen in Fig. 2 that the mechanical vibrations, as well as the electrical oscillations, exhibit a resonance behavior. In low-frequency regime, the amplitude of the electromagnetic oscillations is larger than that of the piezoelectric ones. The opposite is observed in the high-frequency regime. Conversely to frequency-response curves, the amplitudes of these oscillations monotonously decrease as the damping parameter ν_1 or the nonlinear parameter λ_2 increases as illustrated in Figs. 3(a) and (b). However, the vibrations also plainly show a resonant structure as the coupling parameter γ_2 is varied (see Fig. 3(c)). Note that we have monitored the magnetic coupling factor α_0 and the damping parameter μ_0^+, to vary γ_2 and ν_1 respectively. For instance, to obtain Fig. 3(a), parameter μ_0^+ is varied. This variation involves that of ν_1 and ν_2. Then, the amplitude is computed and plotted with respect to ν_1. The variations of the amplitudes of mechanical and electromagnetic oscillations have the same trend as the variations provided in Fig. 3.

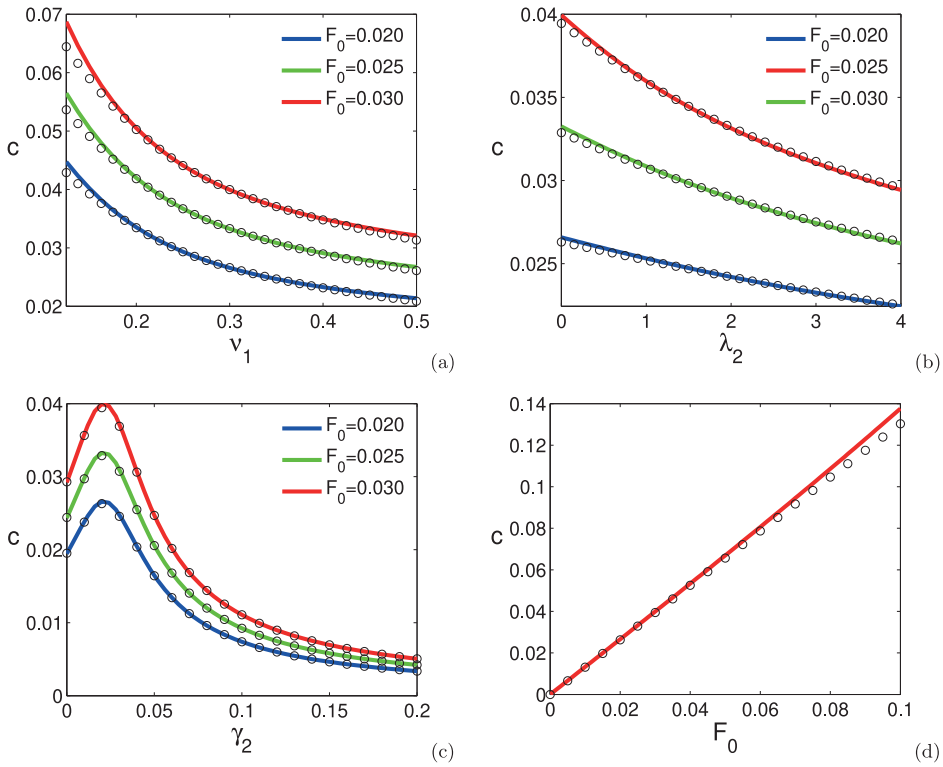

Fig. 3. Amplitude of the piezoelectric oscillations versus (a) damping, (b) nonlinearity and (c) coupling coefficients, and versus (d) the excitation strength. The thick solid lines stand for the analytical result while cycles result from direct computation of system (8). Other parameters in Fig. 2 are kept unchanged and $\omega = 0.3$.

3.2. System efficiency under harmonic excitation

The output (or harvested) power is an essential quantity in any energy harvesting device. These devices are designed to operate in the parameters' regime that delivers an optimum output power. For the present system, which involves two transduction mechanisms, we define the electromagnetic and the piezoelectric output powers respectively as:

$$\tilde{P}_1 = R\left(\frac{dq}{d\tau}\right)^2 \quad \text{and} \quad \tilde{P}_2 = \frac{v^2}{R_P}. \tag{15}$$

Setting

$$P_1 = \frac{LC}{RQ_0^2}\tilde{P}_1 = \dot{y}^2 \quad \text{and} \quad P_2 = \frac{R_P}{V_0^2}\tilde{P}_2 = z^2, \tag{16}$$

the corresponding dimensionless output powers, their maximum values (or magnitudes) P_{1max} and P_{2max} are evaluated as:

$$P_{1\,\max} = \frac{\omega}{\pi}\int_0^{\frac{2\pi}{\omega}} \dot{y}^2 dt \quad \text{and} \quad P_{2\,\max} = \frac{\omega}{\pi}\int_0^{\frac{2\pi}{\omega}} z^2 dt. \tag{17}$$

They are related to the amplitudes b and c of the electrical vibrations. The variations of these output powers versus the excitation frequency and strength are depicted in Fig. 4.

Figs. 4 (a) and (b) indicate that the harvested powers are considerably affected by the driving frequency. In fact, there are some frequencies at which the output powers exhibit a resonant behavior. For instance, in the present parameters regime (that is to say, parameters used in Fig. 4), the piezoelectric output power reaches its extreme peak nearly at $\omega = 1.75$. However, at this frequency, as well as in low-frequency regime, the electromagnetic harvested power is larger than the piezoelectric output power. By inspection of Figs. 4(c) and (d), it is clear that the opposite remark is drawn in the high-frequency regime. Superimposing the curves provided in Fig. 4(a) and Fig. 4(b), one notes that the later remark holds when $\omega > 3$.

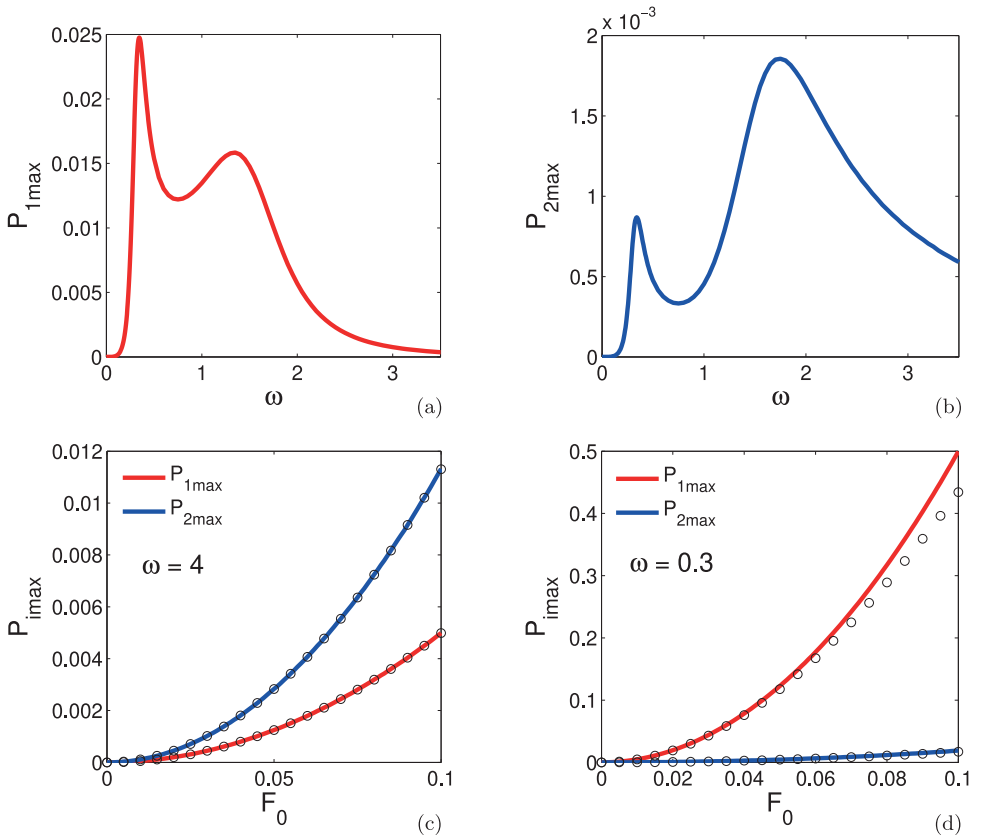

Fig. 4. Output powers versus the excitation's frequency and strength. (a,b) Output power versus excitation frequency and (c,d) Output power versus excitation strength. The thick solid lines correspond to the analytical result while cycles result from direct computation of system (8). Parameters in Fig. 2 are kept unchanged unless otherwise specified.

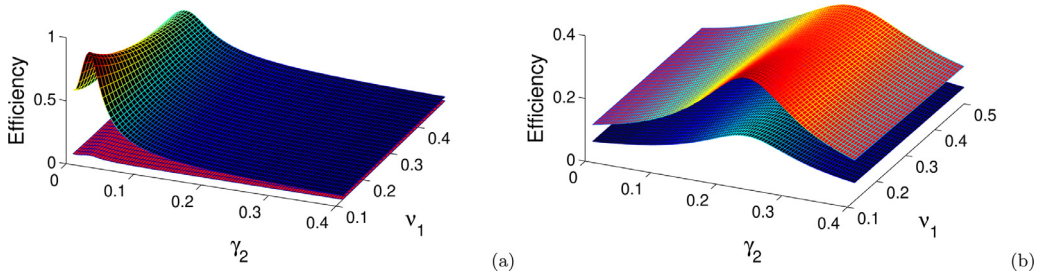

Fig. 5. Efficiency versus γ_2 and ν_1. Parameters in Fig. 2 are kept unchanged unless otherwise specified, $F_0 = 0.03$, $\omega = 0.3$ for Fig. 5(a) and $\omega = 4$ for Fig. 5(b).

Moreover, these output powers monotonously increase with the excitation strength irrespective of the driving frequency as illustrated in Figs. 4(c) and (d). Yet, they monotonously decrease while the damping and the nonlinearity coefficients ν_1 and λ_2 are varied. These observations suggest that the transduction mechanisms would be more efficient if the nonlinearities in the mechanical part of the system are reduced and if the mechanical vibrations are under-damped. To firmly characterize effects of the magnetic coupling and non-smoothness coefficients on the system efficacy, on the one hand, and to firmly compare both transduction mechanisms on the other hand, we define the efficiencies related to both transduction mechanisms in the following paragraph.

The instantaneous input power, namely the power of the inertial force acting on the moving mass, is expressed as:

$$\tilde{P}_{in} = -m\Gamma(\tau)\frac{dX}{d\tau}. \tag{18}$$

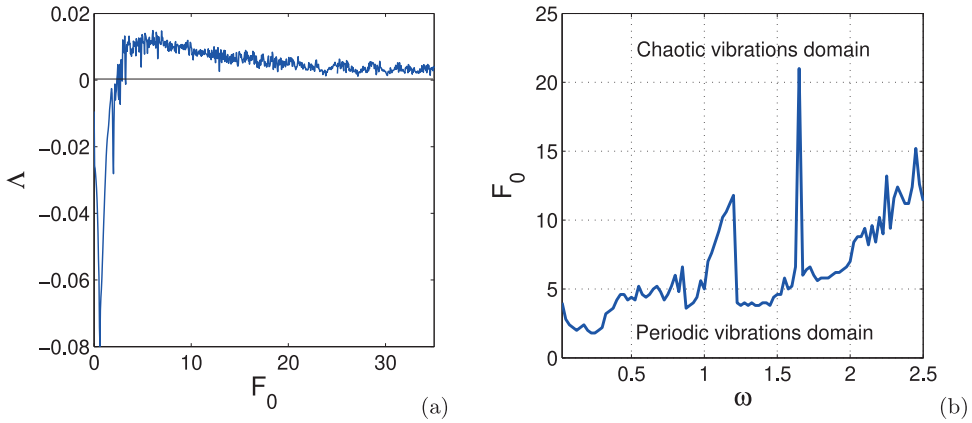

Fig. 6. Largest Lyapunov exponent and transition curve from regular to chaotic vibrations. Parameters in Fig. 2 are kept unchanged and $\omega = 0.3$ for Fig. 6(a).

Setting

$$P_{in} = \frac{1}{ml^2\omega_e^3}\tilde{P}_{in} = \dot{x}f(t) \tag{19}$$

the corresponding dimensionless input power, the normalized efficiency ρ is simply defined by the relation $\rho = \frac{P_{out\,\max}}{P_{in\,\max}}$; where $P_{in\max}$ is the magnitude of the dimensionless input power from the driving vibrations and $P_{out\max}$ is the magnitude of the dimensionless power delivered to the electrical load. In the present work, $P_{out\max}$ represents either the electromagnetic output power magnitude $P_{1\max}$ or the piezoelectric output power magnitude $P_{2\max}$. We therefore define two normalized efficiencies, which are related to both transduction mechanisms exhibited by the present harvester. It follows from the above relations that the normalized efficiencies for the electromagnetic and the piezoelectric mechanisms are respectively expressed as:

$$\rho_1 = \frac{b^2\omega}{F_0 a} \quad \text{and} \quad \rho_2 = \frac{c^2}{F_0 a\omega}. \tag{20}$$

Note that the normalized efficiencies, as defined above, are not necessarily lower than the unity. However, their variations with the system's parameters have the same trends as the variations of the genuine efficiencies. In fact, it can be shown that the later quantities are related to the normalized efficiencies as follows:

$$\tilde{\rho}_1 = \frac{RQ_0^2}{ml^2\omega_e}\rho_1, \qquad \tilde{\rho}_2 = \frac{V_0^2}{R_P ml^2\omega_e^3}\rho_2. \tag{21}$$

Varying μ_0^+ and α_0 in the ranges [0; 15] and [0; 20] respectively, particularly affects the non-smoothness parameter ν_1 and the nonlinear coupling coefficient γ_2. The variation of both later quantities affects the vibrations amplitudes and consequently, it affects the efficiencies. The variations of efficiencies $\tilde{\rho}_1$ and $\tilde{\rho}_2$ with respect to γ_2 and ν_1 are plotted in Fig. 5. In Fig. 5(a), the upper surface stands for $\tilde{\rho}_1$; the efficiency (in percentage) of the electromagnetic transduction mechanism, while the lower one represents $\tilde{\rho}_2$, the efficiency of the piezoelectric transduction mechanism. This result has been obtained for $\omega = 0.3$. Conversely, in Fig. 5(b) obtained with $\omega = 4$, the upper surface represents $\tilde{\rho}_2$ and the lower one stands for $\tilde{\rho}_1$. It is therefore clear from Fig. 5 that in the low frequency regime, the electromechanical mechanism is more efficient that the piezoelectric one for a broad range of parameters γ_2 and ν_1 even if both efficiencies are very small. The opposite is observed in the high frequency regime. Moreover, by reducing the mechanical damping and by choosing the best nonlinear magnetic coupling coefficient, the efficiencies of both transduction mechanisms are improved.

3.3. Numerical study of the transition to chaos

As mentioned above, the excitation strength can be increased to improve the efficacy of the device as long as its response remains harmonic. However, as reported within several papers in the literature, the excitation strength may considerably affect the response's regime of the system. In other words, increasing the excitation strength may induce the transition from periodic oscillations to chaotic ones; whereas periodic vibrations are preferable for external power storage circuitry because they are more regular in waveform. It is therefore necessary to assess the threshold of F_0 for the onset of chaos. To

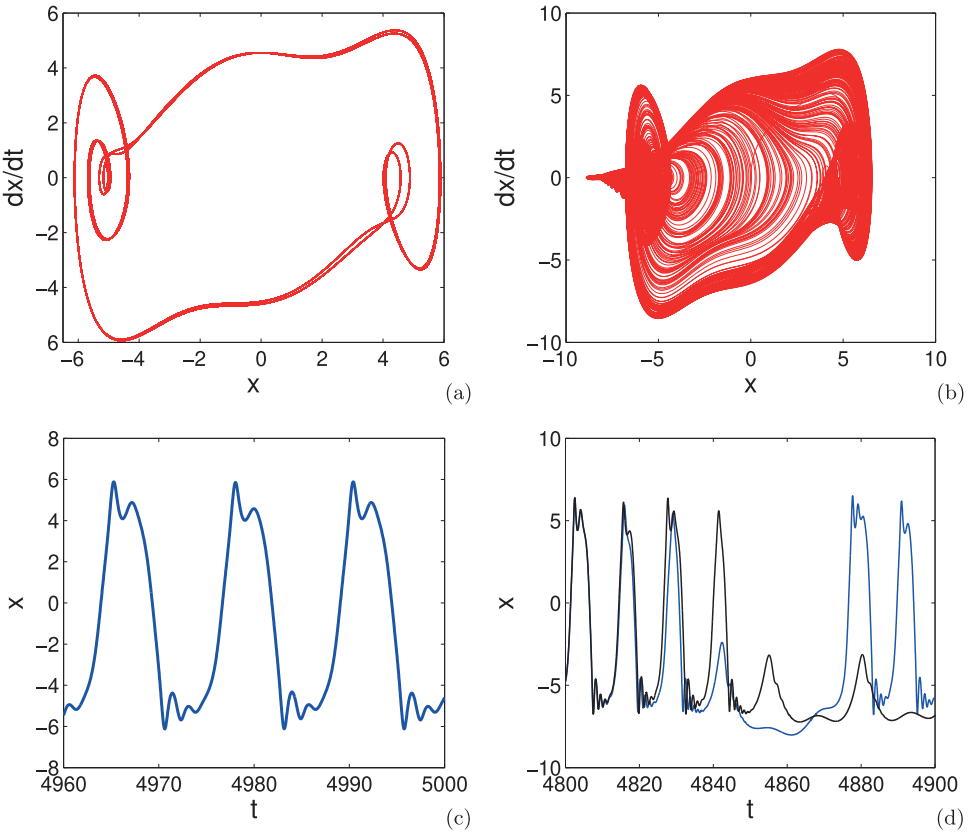

Fig. 7. Phase space diagrams and corresponding time series illustrating regular and chaotic dynamics. (a) State space diagram and (c) periodic oscillations for $\omega = 0.5$ and $F_0 = 4$; (b) state space diagram and (d) chaotic vibrations for $\omega = 0.5$ and $F_0 = 6$. Other parameters are those used in Fig. 2.

this end, we compute the largest Lyapunov exponent [41], which is a major indicator of predicting instability and emergence of chaos.

Assume that the state vector of the differential system (8) is subjected to a small perturbation vector denoted $Z(t) = (x_1(t), u_1(t), y_1(t), v_1(t), z_1(t), w_1(t))$. Specifically, $Z(t)$ represents a slight variation of the state vector of system (8), and thus obeys the variational system resulting from (8). Solving system (8) and its related variational system by the mean of the fourth-order Runge-Kutta algorithm, the largest Lyapunov exponent Λ is computed as:

$$\Lambda = \lim_{t\to+\infty} \frac{1}{t} \ln\left(\frac{\|Z(t)\|}{\|Z(0)\|}\right), \tag{22}$$

where $Z(t)$ is the perturbation vector at time t, $Z(0)$ is a given initial perturbation vector and $\|\cdot\|$ denotes the norm. The results of our computation are reported in Fig. 6. Fig. 6(a) provides the variation of the largest Lyapunov exponent with respect to F_0 for $\omega = 0.3$. It is seen that for $F_0 \leq 2$, Λ is negative and the device exhibits periodic vibrations which could be harmonic. Beyond $F_0 = 3.5$, it is seen in Fig. 6(a) that Λ is positive. Therefore, nearby trajectories starting with almost the same initial conditions exponentially diverge in the course of time, that is to say, trajectories are high sensitive to initial conditions and chaotic vibrations take place. These vibrations are probably made of interwell jumps. In Fig. 6(b) is depicted, in the parameter space (ω, F_0), the transition curve from periodic vibrations to chaotic ones. This result has been obtained by seeking the threshold values of ω and F_0 for which Λ changes sign. It provides a good insight of the domain in which periodic orbits of high energy can be obtained. As a matter of fact, it is seen that the harvester can sustained periodic high-energy orbits at large excitation frequencies. For instance, the system exhibits a periodic intrawell vibration for $\omega = 4$ and $F_0 = 50$. Such vibration yields a high energy harvesting performance.

In order to verify the result provided in Fig. 6(b), we compute the time series of system (8) for parameters taken in the periodic vibrations domain and for that taken in the chaotic vibrations domain. The results are respectively depicted in Figs. 7(a) and (c) and Figs. 7(b) and (d). Figs. 7(a) and (c) show the state space diagram and the corresponding time series for a periodic vibration obtained with $\omega = 0.5$ and $F_0 = 4$. Fig. 7(a) specifically illustrates the limit cycle toward which converge the phase space trajectories. It is not worth mentioning that the initial conditions are null for the time series of Fig. 7(c). Contrariwise, the phase space diagram of Fig. 7(b) reveals chaotic behavior and the corresponding time series provided in

Fig. 7(d) exhibit sensitivity to initial conditions. As a matter of fact, the blue solid line results from null initial conditions while the black one results from initial conditions $(10^{-8}, 0, 0, 0, 0, 0)$. These results are obtained with $\omega = 0.5$ and $F_0 = 6$.

4. Noise effects on the system response and efficiency

4.1. Stochastic averaging technique

Complicated motions of the frame has been described in the literature as a summation of a harmonic motion and a noisy term. Specifically, we assume here that these motions' acceleration are of constant amplitude, with noisily fluctuating phase angle $\varphi(t)$ of average frequency ω. $\varphi(t)$ reads

$$\varphi(t) = \omega t + \sqrt{\frac{2}{\tau_1}} W(t) + \Phi, \tag{23}$$

where τ_1 is a positive constant interpreted as the correlation time of the random driving excitation $f(t)$. Specifically, $\sqrt{\frac{2}{\tau_1}}$ represents the randomness level in the phase of $f(t)$. $W(t)$ is a standard Wiener process and Φ is a random variable uniformly distributed within $[0; \pi[$ and independent of $W(t)$. In its present form, the random excitation $f(t)$ is referred to as bounded noise in the literature [42–49] and will be henceforth denoted by $\xi_1(t)$ for notation convenience. In addition, the fundamental property of the electrical components to be effective noise source (such as thermal noise, shot noise, $1/f$ noise etc.) is now taken into consideration and modeled by additive colored noises $\zeta_2(t)$ and $\zeta_3(t)$. The model equation (8) can therefore be rewritten as:

$$\ddot{x} + (\nu_1 + \nu_2 \text{sign}(\dot{x}))\dot{x} + \omega_1^2 x + \lambda_1 x^2 + \lambda_2 x^3 + \delta z + \left(\gamma_0 + \gamma_1 x + \gamma_2 x^2\right)\dot{y} = \xi_1(t), \tag{24a}$$

$$\ddot{y} + \mu_e \dot{y} + y + \left(\beta_0 + \beta_1 x + \beta_2 x^2\right)\dot{x} = \zeta_2(t), \tag{24b}$$

$$\ddot{z} + \mu_p \dot{z} + \omega_3^2 z + \eta \ddot{x} = \zeta_3(t), \tag{24c}$$

with the cross-covariance matrix $R(s)$ of the random excitation vector $(\xi_1(t), \zeta_2(t), \zeta_3(t))$, defined by:

$$R_{11}(s) = \frac{F_0^2}{2} \exp\left(-\frac{|s|}{\tau_1}\right) \cos(\omega s), \tag{25a}$$

$$R_{22}(s) = \frac{D_2}{\tau_2} \exp\left(-\frac{|s|}{\tau_2}\right), \tag{25b}$$

$$R_{33}(s) = \frac{D_3}{\tau_3} \exp\left(-\frac{|s|}{\tau_3}\right), \tag{25c}$$

$$R_{ij}(s) = 0, \quad i \neq j. \tag{25d}$$

D_2 and D_3 respectively represent the intensities of the colored noises excitations $\zeta_2(t)$ and $\zeta_3(t)$, and τ_2 and τ_3 stand for their correlation time. In the remainder of this section, we determine the stationary probability distribution for the amplitudes by the mean of the stochastic averaging technique. Consistently to this method, let's consider the following variable change:

$$\begin{gathered} \vartheta_1(t) = \omega_1 t + \phi_1(t), \quad \vartheta_2(t) = t + \phi_2(t), \quad \vartheta_3(t) = \omega_3 t + \phi_3(t), \\ x(t) = a(t)\cos(\vartheta_1(t)), \quad y(t) = b(t)\cos(\vartheta_2(t)), \quad z(t) = c(t)\cos(\vartheta_3(t)), \\ \dot{x}(t) = -\omega_1 a(t)\sin(\vartheta_1(t)), \quad \dot{y}(t) = -b(t)\sin(\vartheta_2(t)), \quad \dot{z}(t) = -\omega_3 c(t)\sin(\vartheta_3(t)). \end{gathered} \tag{26}$$

Replacing relations (26) into system (24) and after some algebraic manipulations, the system (24) takes the following form:

$$\dot{a} = f_1(U,t) + g_{11}(U,t)\xi_1(t), \tag{27a}$$

$$\dot{\phi}_1 = f_2(U,t) + g_{21}(U,t)\xi_1(t), \tag{27b}$$

$$\dot{b} = f_3(U,t) + g_{32}(U,t)\zeta_2(t), \tag{27c}$$

$$\dot{\phi}_2 = f_4(U,t) + g_{42}(U,t)\zeta_2(t), \tag{27d}$$

$$\dot{c} = f_5(U,t) + g_{51}(U,t)\xi_1(t) + g_{53}(U,t)\zeta_3(t), \tag{27e}$$

$$\dot{\phi}_3 = f_6(U,t) + g_{61}(U,t)\xi_1(t) + g_{63}(U,t)\zeta_3(t), \tag{27f}$$

where $U = (a, \phi_1, b, \phi_2, c, \phi_3)$ is the state vector. The functions f_i, and g_{ij} are defined in the Appendix B.

The state vector of system (27) can be approximated by a diffusive Markov process vector by the mean of the central limit theorem [50]. The later process vector is governed by the following Itô equations:

$$da = m_1 dt + \sigma_1 dW_1, \tag{28a}$$
$$d\phi_1 = m_2 dt + \sigma_2 dW_2, \tag{28b}$$
$$db = m_3 dt + \sigma_3 dW_3, \tag{28c}$$
$$d\phi_2 = m_4 dt + \sigma_4 dW_4, \tag{28d}$$
$$dc = m_5 dt + \sigma_5 dW_5, \tag{28e}$$
$$d\phi_3 = m_6 dt + \sigma_6 dW_6, \tag{28f}$$

where the drift coefficients m_i and the diffusion coefficients σ_i are given in the appendix. $W_i(t)$, $(i = 1, 2, \ldots, 6)$ are six independent standard Wiener processes.

With the knowledge of the drift and diffusion coefficients, it is clear that the amplitude processes a, b and c are decoupled from the phase processes. The transition probability densities $P_a(a, t|a_0, t_0)$, $P_b(b, t|b_0, t_0)$, and $P_c(c, t|c_0, t_0)$ for the amplitudes a, b and c respectively, can therefore be determined separately instead of joint transition probability densities. They are governed by the following uncoupled Fokker-Planck-Kolmogorov (FPK) equations:

$$\frac{\partial P_a}{\partial t} = -\frac{\partial}{\partial a}(m_1 P_a) + \frac{1}{2}\frac{\partial^2}{\partial a^2}\left(\sigma_1^2 P_a\right), \tag{29}$$
$$\frac{\partial P_b}{\partial t} = -\frac{\partial}{\partial b}(m_3 P_b) + \frac{1}{2}\frac{\partial^2}{\partial b^2}\left(\sigma_3^2 P_b\right) \tag{30}$$

and

$$\frac{\partial P_c}{\partial t} = -\frac{\partial}{\partial c}(m_5 P_c) + \frac{1}{2}\frac{\partial^2}{\partial c^2}\left(\sigma_5^2 P_c\right). \tag{31}$$

Setting $\frac{\partial P_a}{\partial t} = 0$, $\frac{\partial P_b}{\partial t} = 0$ and $\frac{\partial P_c}{\partial t} = 0$ and following Zhu [51], the stationary solutions $P_a(a)$, $P_b(b)$ and $P_c(c)$ of Eqs. (29), (30) and (31), referred to as stationary transition PDFs are given by:

$$P_a(a) = \frac{N_a}{\sigma_1^2}\exp\left[2\int \frac{m_1}{\sigma_1^2} da\right], \tag{32}$$
$$P_b(b) = \frac{N_b}{\sigma_3^2}\exp\left[2\int \frac{m_3}{\sigma_3^2} db\right] \tag{33}$$

and

$$P_c(c) = \frac{N_c}{\sigma_5^2}\exp\left[2\int \frac{m_5}{\sigma_5^2} dc\right], \tag{34}$$

where N_a, N_b and N_c are the normalization constants. With the knowledge of m_1, m_3, m_5, σ_1, σ_3 and σ_5, the transition stationary PDFs can be expressed as:

$$P_a(a) = \frac{\nu_1}{\sigma_1^2} a \exp\left(-\frac{\nu_1}{2\sigma_1^2}a^2\right), \tag{35}$$
$$P_b(b) = \frac{\mu_e}{\sigma_3^2} b \exp\left(-\frac{\mu_e}{2\sigma_3^2}b^2\right) \tag{36}$$

and

$$P_c(c) = \frac{\mu_P}{\sigma_5^2} c \exp\left(-\frac{\mu_P}{2\sigma_5^2}c^2\right). \tag{37}$$

Clearly, it comes out from the above analytical development that the stationary PDFs (Eqs. (35), (36) and (37)) have, each of them, a unique peak irrespective of the values of the system parameters. The amplitude c_m for which the peak of the probability density function P_c (for instance) is reached, is obtained by solving $\frac{dP_c}{dc} = 0$. It yields

$$c_m = \frac{\sigma_5}{\sqrt{\mu_P}}. \tag{38}$$

The distributions of amplitudes $a(t)$, $b(t)$ and $c(t)$, obtained from the present analytical treatment, are thus only unimodal. Moreover, the average oscillatory amplitude of the harvester's piezoelectric part is given by

$$\langle c \rangle = \int_0^{+\infty} c P_c(c) dc. \tag{39}$$

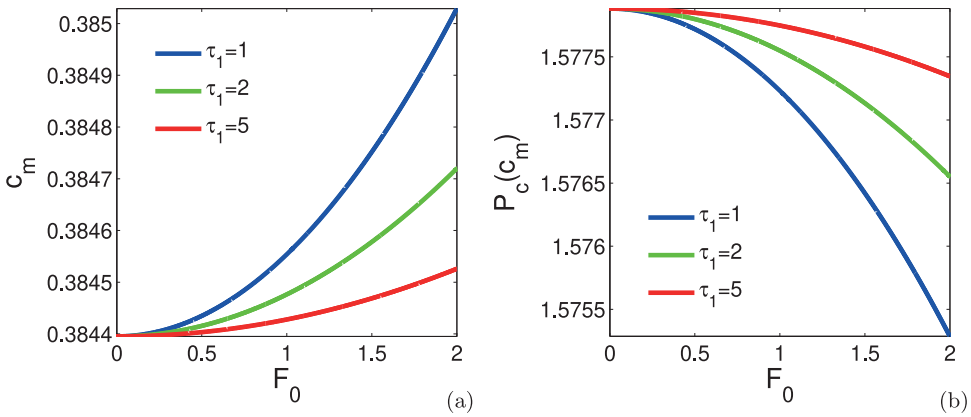

Fig. 8. Variation of (a) the peak position and the (b) extreme point of PDF P_c versus the modulation amplitude F_0 for different values of the correlation time τ_1. Parameters are $\nu_1 = 0.03$, $\nu_2 = 0.005$, $\mu_e = 0.01$, $\mu_P = .016$, $\omega_1 = 1.0$, $\omega_3 = 5.66$, $\lambda_1 = 0.0045$, $\lambda_2 = 0.00002$, $\gamma_0 = -0.00125$, $\gamma_1 = 0.00002$, $\gamma_2 = 0.0002$, $\beta_0 = 0.10$, $\beta_1 = -0.0016$, $\beta_2 = -0.016$, $\delta = 10^{-6}$, $\eta = -0.064$, $\omega = 0.3$, $D_2 = 0.1$, $\tau_2 = 4.5$, $D_3 = 0.1$ and $\tau_3 = 0.1$.

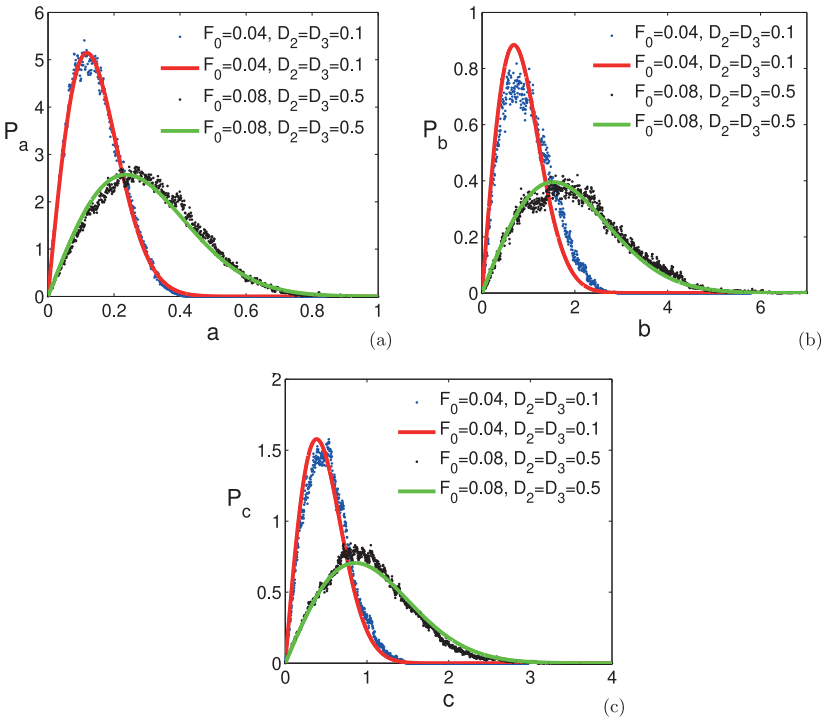

Fig. 9. Stationary probability density functions for amplitudes. Thick solid lines result from the averaging technique, while dots result from direct computation. Parameters are $\nu_1 = 0.03$, $\nu_2 = 0.005$, $\mu_e = 0.01$, $\mu_P = .016$, $\omega_1 = 1.0$, $\omega_3 = 5.66$, $\lambda_1 = 0.0045$, $\lambda_2 = 0.00002$, $\gamma_0 = -0.00125$, $\gamma_1 = 0.00002$, $\gamma_2 = 0.0002$, $\beta_0 = 0.10$, $\beta_1 = -0.0016$, $\beta_2 = -0.016$, $\delta = 10^{-6}$, $\eta = -0.064$, $\omega = 0.3$, $\tau_1 = 1$, $\tau_2 = 4.5$ and $\tau_3 = 0.1$.

Phenomenological transitions, consisting in a modification of the position and the width of the PDF's peak, common to other models for vibration energy harvesting systems [7,8], are also observed in the present model. Specifically, the position of the PDF extreme point; c_m for instance, increases (moves away from zero) and the peak $P_c(c_m)$ becomes lower (decreases) as the modulation amplitude F_0 increases (see Fig. 8). Similar transitions appear when the noises' intensities and the correlation times vary.

To verify the consistency of the above analytical treatment, the stationary transition PDFs for the amplitudes $a(t)$, $b(t)$ and $c(t)$ are obtained through the Monte-Carlo simulations by computing a long time evolution of the random amplitudes $a(t)$, $b(t)$ and $c(t)$ with the second order stochastic Runge-Kutta algorithm [52]. To this aim, following Honeycutt [52,53],

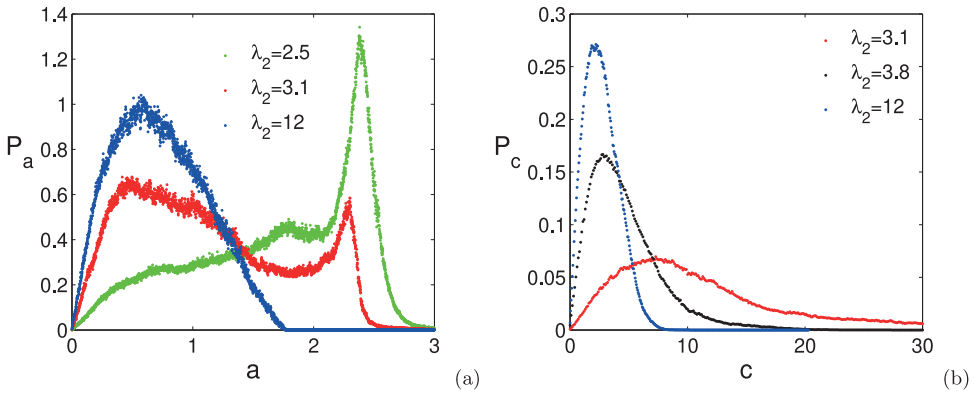

Fig. 10. Probability density functions for amplitudes: Stochastic P-bifurcation exhibited in the hard coupling and nonlinearity parameters regime. Parameters are $\nu_1 = 0.03$, $\nu_2 = 0.005$, $\mu_e = 0.01$, $\mu_P = .016$, $\omega_1 = 1.0$, $\omega_3 = 5.66$, $\lambda_1 = 6.2$, $\gamma_0 = -12.5$, $\gamma_1 = 0.2$, $\gamma_2 = 2.0$, $\beta_0 = 10.0$, $\beta_1 = -0.16$, $\beta_2 = -1.6$, $\delta = 0.001$, $\eta = -64.0$, $F_0 = 0.02$, $\omega = 0.3$, $\tau_1 = 5$, $D_2 = 0.5$, $\tau_2 = 4.5$, $D_3 = 0.5$ and $\tau_3 = 0.1$.

Eq. (24) is transformed into the following stochastic dynamical system:

$$\begin{cases} \dot{x} = & u \\ \dot{u} = & -(\nu_1 + \nu_2 \text{sign}(u))u - \omega_1^2 x - \lambda_1 x^2 - \lambda_2 x^3 - \delta z - \left(\gamma_0 + \gamma_1 x + \gamma_2 x^2\right)v \\ & +F_0 \cos(\varphi(t)) \\ \dot{y} = & v \\ \dot{v} = & -\mu_e v - y - \left(\beta_0 + \beta_1 x + \beta_2 x^2\right)u + \zeta_2(t) \\ \dot{z} = & w \\ \dot{w} = & -\mu_P w - \omega_3^2 z + \eta\Big[(\nu_1 + \nu_2 \text{sign}(u))u + \omega_1^2 x + \lambda_1 x^2 + \lambda_2 x^3 + \delta z \\ & +\left(\gamma_0 + \gamma_1 x + \gamma_2 x^2\right)v - F_0 \cos(\varphi(t))\Big] + \zeta_3(t) \\ \dot{\varphi} = & \omega + \sqrt{\frac{2}{\tau_1}}\chi_1(t) \\ \dot{\zeta}_2 = & -\frac{1}{\tau_2}\zeta_2 + \frac{\sqrt{2D_2}}{\tau_2}\chi_2(t) \\ \dot{\zeta}_3 = & -\frac{1}{\tau_3}\zeta_3 + \frac{\sqrt{2D_3}}{\tau_3}\chi_3(t) \end{cases}, \tag{40}$$

with $\chi_i(t)$ ($i \in \{1, 2, 3\}$), the normalized sources of Gaussian white noise. Their statistical properties are: $\langle \chi_i(t) \rangle = 0$ and $\langle \chi_i(t)\chi_j(t+s) \rangle = \delta_{ij}\delta(s)$. Let's remind that the amplitudes are numerically computed as: $a(t) = \sqrt{(x(t))^2 + \frac{(\dot{x}(t))^2}{\omega_1^2}}$, $b(t) = \sqrt{(y(t))^2 + (\dot{y}(t))^2}$ and $c(t) = \sqrt{(z(t))^2 + \frac{(\dot{z}(t))^2}{\omega_3^2}}$.

It is clearly shown in Fig. 9 that the preceding approximate analytical treatment agrees with the numerical result. However, other results of our computations show that the agrement between both approaches appears only in the weak damping, nonlinearity and coupling parameters regime. When coupling and nonlinearity parameters are no longer sufficiently small, stochastic averaging method can no longer be trusted [8,50]. As a matter of fact, the analytically predicted PDFs (Eqs. (35), (36) and (37)) are independent of the nonlinearity and coupling coefficients λ_i, β_i and γ_i, while numerically computed PDFs may be sensitive to these parameters. We therefore resort to numerical simulations to investigate the effects of the noises' parameters, the coupling and the nonlinear coefficients on the probability density functions, the mean amplitudes and the mean output power of the transducer.

Some of the results of our computations are provided in Fig. 10. These results are obtained with large coupling parameters and large parameters of nonlinearity, by the mean of Monte-Carlo simulations. Fig. 10(a) shows the PDF for amplitude a, numerically obtained with different values of λ_2. It is seen that the shape of this PDF considerably depends on λ_2 while, for the same parameters used in this figure, the analytically derived PDF for amplitude a (given by Eq. (35)) does not depend on λ_2 and has the same shape as the PDFs provided in Fig. 9, however, with a higher peak. In Fig. 10(b), the PDF for amplitude c obtained from simulations is depicted. We notice that this PDF, or precisely the height of its peak, also depends on λ_2. However, its analytically obtained counterpart (which can be plotted using Eq. (37)) is independent of λ_2 and has a higher peak. The PDF for amplitude b, obtained numerically with parameters of Fig. 10, also depends on λ_2 and has a shape similar to that of P_c. Summarily, by plotting the analytically derived PDFs P_a and P_c and superimposing to their counterparts given in Figs. 10(a) and (b), it appears a considerable gap, in terms of shape and peak height, between the analytically predicted PDFs and the numerically computed ones. Therefore, the numerical and the analytical treatments do not agree for parameters used in Fig. 10. In addition, varying λ_2 which is a parameter of the harvester mechanical part, has affected the PDFs P_b and P_c for the amplitudes b and c of the harvester electrical part, because the coupling strength is considerable. Similarly, it

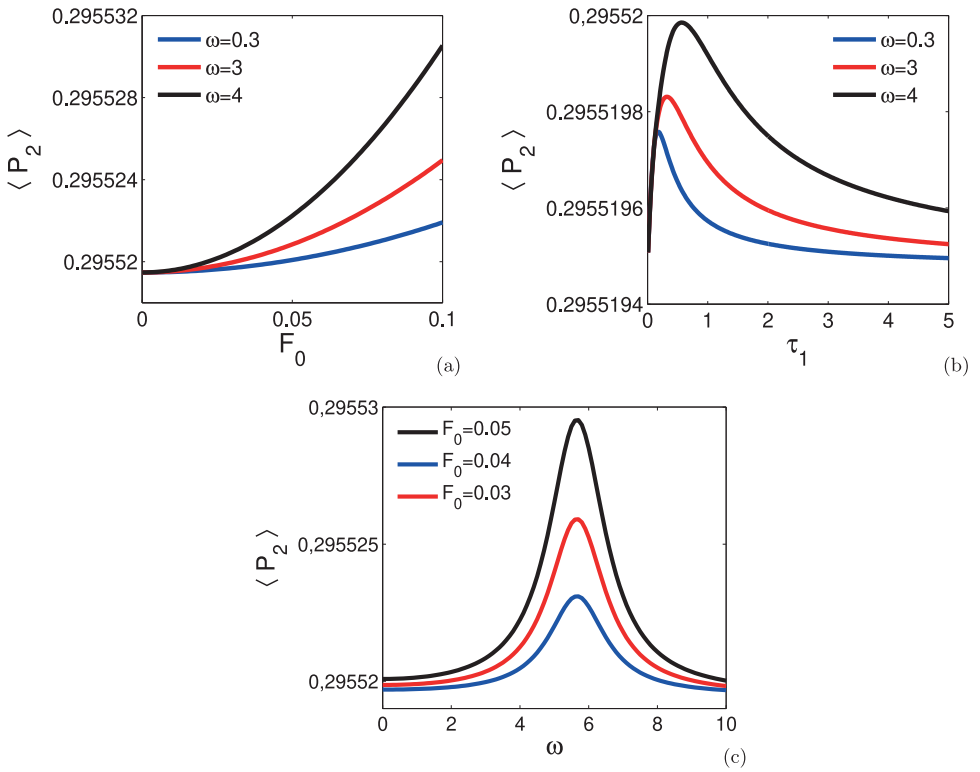

Fig. 11. Dimensionless average output power of the piezoelectric circuitry versus (a) bounded noise amplitude, (b) bounded noise relaxation time and (c) frequency. $D_2 = 0.1$, $D_3 = 0.1$, $F_0 = 0.02$ for Fig. 11(b), other parameters are those used in Fig. 9.

can be shown that varying the "mechanical noise" parameters (τ_1 for instance) affects the PDFs P_b and P_c. As stated above, the results to be trusted is that provided by the Monte-Carlo simulations. Moreover, when the nonlinear coefficients are increased, one witnesses transitions in the shape of the probability distributions. As a matter of fact, when λ_2 varies, the PDF P_a bifurcates from a unimodal shape (or single-peak mode) to a bimodal shape (double-peak mode) as demonstrated in Fig. 10(a). This qualitative change of the density of an invariant measure related to a stochastic dynamical system, is termed in the framework of stochastic bifurcation theory as stochastic P-bifurcation. This phenomenon is not theoretically predicted by the stochastic averaging technique. In fact, it comes out from the above analytical treatment that the PDFs have, each of them, only one peak irrespective of values of system's parameters. However, in the hard coupling regime where the stochastic averaging technique is no longer prominent, stochastic P-bifurcation appears in the mechanical part of the harvester as λ_2 varies. At the same time, the electrical part of the harvester only exhibits phenomenological transitions which consist in a modification of the position and the width of the peak of the PDFs. That is to say, the PDF P_c, as well as P_b remain unimodal as observed in Fig. 10(b). A similar switch from the unimodal shape to a bimodal one may also be observed in the electrical part of the harvester when the noise intensity (D_2 for instance) is varied and the other parameters, properly set.

4.2. Average output powers under bounded noise and colored noise excitations

From the formulas of the non-dimensional electromechanical and piezoelectric output powers given in Eq. (16), it follows that their mean values are respectively related to the mean square values of the electric current (across resistor R) and the voltage (across R_P) and can be expressed as:

$$\langle P_1\rangle = \int_0^{+\infty} b^2 P_b(b)db, \qquad \langle P_2\rangle = \int_0^{+\infty} c^2 P_c(c)dc. \tag{41}$$

Hence, it follows that

$$\langle P_1\rangle = \frac{2\sigma_3^2}{\mu_e}, \qquad \langle P_2\rangle = \frac{2\sigma_5^2}{\mu_P}. \tag{42}$$

From the knowledge of the expressions of σ_3 and σ_5, it easily appears that the mean output powers $\langle P_1\rangle$ and $\langle P_2\rangle$ monotonously increase with the colored noise intensities D_2 and D_3 respectively. In addition, $\langle P_1\rangle$ decreases as τ_2 and μ_e

vary. The variations of the average output power $\langle P_2 \rangle$, of the piezoelectric part of the harvester, with respect to the bounded noise parameters are computed and given in Fig. 11. One can see that, $\langle P_2 \rangle$ monotonously increases with the bounded noise amplitude F_0. Moreover, it exhibits a resonance effect as the relaxation time τ_1 or the frequency ω of the bounded noise varies. Therefore, there exists a proper level of noise, determined by the quantity $\sqrt{\frac{2}{\tau_1}}$ (see Fig. 11(b)) and an optimum excitation frequency (see Fig. 11(c)) for which the mean output power is maximized. Fig. 11(b) demonstrates that the standard deviation of the amplitude of piezoelectric vibrations exhibits a single-peak mode as $\sqrt{\frac{2}{\tau_1}}$ varies. This resonance behavior correspond to the stochastic resonance phenomenon. It arises in several systems ranging from electronic systems [54,55] to biological systems [56–58] and, as far as the present system is concerned, a particular attention has to be paid to it in further studies.

5. Conclusion

Conclusively, the main objectives of this work was to investigate the effects of (a) the nonlinear magnetic coupling and (b) the parameters of non-smoothness and nonlinearities, on the performance of a hybrid vibration energy harvester with a non-smooth mechanical damping. It also focused on the investigation of the effect of environmental random fluctuations on the mean output powers. To reach this target, the energy harvesting device has been successively modeled by a deterministic non-smooth system under harmonic excitation and a non-smooth system under colored and bounded additive noise excitations. By the mean of a modified harmonic balance method, we have obtained the stationary harmonic response of the system to harmonic excitation. Using this response, we have then investigated the system's performance. We found that, the electromagnetic and piezoelectric transduction mechanisms are improved and the harvester efficiencies, increased, by weakening the nonlinearities and the damping of the harvester mechanical part and by choosing peculiar nonlinear magnetic coupling coefficients. Increasing the harmonic excitation strength is useful to augment the harvested powers, however, it can not be increased beyond a threshold value when one desires a harvested power of regular waveform. In fact, augmenting it further induces transition to chaotic behavior, and results in a non-periodic harvested power, which is inappropriate for energy storage devices.

Under bounded and colored noise excitation, we derived the stationary PDFs for the amplitudes of the mechanical and the electrical parts of the harvester, by the mean of the stochastic averaging procedure. We found that in the parameters' regime for which the averaging technique is meaningful, that is to say, in the regime of weak coupling, damping and nonlinearity parameters, the stationary PDFs only exhibited a single-peak mode as the system's parameters varied. This result has been verified by the Monte Carlo simulation. Moreover, we found in such parameters' regime that the mean output powers increase with the colored noises' intensities and the harvester piezoelectric part output power exhibits a resonance behavior as some bounded noise parameter vary. This behavior demonstrates that, for fixed colored noise intensities, the performance of the harvester piezoelectric part is maximized for optimum bounded noise relaxation time and average frequency. This result reveals the stochastic resonance phenomenon. For large coupling parameters, that is, in the parameter regime for which stochastic averaging technique is meaningless, we found by the mean of the Monte Carlo simulation that by increasing a particular parameter of nonlinearity, the stochastic P-bifurcation appears in the mechanical part of the energy harvester. This result sustains the idea of Siewe *et al.* [8] according to which the stochastic P-bifurcation can be exhibited by a stochastic dynamical system although not predicted theoretically by the stochastic averaging technique. The present work enables designers to get an insight on the constraint to be tackled in order to improve the device performance.

Declaration of Competing Interest

The authors declare that they have no known competing financial interests or personal relationships that could have appeared to influence the work reported in this paper.

CRediT authorship contribution statement

G.G. Sengha: Conceptualization, Methodology, Software, Investigation. **W. Fokou Kenfack:** Data curation, Writing - original draft. **M. Siewe Siewe:** Software, Visualization. **C.B. Tabi:** Software, Validation. **T.C. Kofane:** Supervision.

Acknowledgements

G.G. Sengha thanks the French Government for supporting his work in part through the Campus France's program for the promotion of the higher education and the international mobility.

Appendix A

The coefficients of polynomials $\Gamma^{\pm}$ are given by:

$$\chi_{10} = \omega^4 \gamma_2{}^2 \beta_2^2 \left(R_5^2 + R_1^2\right),$$

$$\chi_8 = 8\omega^2\gamma_2\beta_2\left(R_5^2R_6 + R_1^2R_6 + 4R_1R_2\right),$$

$$\begin{aligned}\chi_6^{\pm} =& 32\omega^2\gamma_2\beta_2\left(\gamma_0\omega^2\beta_0\left(R_5^2 + R_1^2\right) + R_4^{\pm}R_5 + R_1R_3\right)\\ &+ 16(R_6R_1 + 4R_2)^2 + 16R_6^2R_5^2,\end{aligned}$$

$$\begin{aligned}\chi_4^{\pm} =& 128\omega^2\beta_0\gamma_0\left(R_6\left(R_5^2 + R_1^2\right) + 4R_1R_2\right) + 512R_3R_2\\ &+ 128R_6\left(R_1R_3 + R_4^{\pm}R_5\right),\end{aligned}$$

$$\chi_2^{\pm} = 256\left(\left(\gamma_0\omega^2\beta_0R_1 + R_3\right)^2 + \left(R_4^{\pm} + \gamma_0\omega^2\beta_0R_5\right)^2\right),$$

where

$$R_1 = \frac{1-\omega^2}{\left(1-\omega^2\right)^2 + \mu_e^2\omega^2},$$

$$R_2 = \frac{3}{4}\lambda_2 - \frac{1}{2}\frac{\lambda_1\gamma_2}{\gamma_1},$$

$$R_3 = \omega_1^2 - \omega^2 + \frac{\delta\eta\omega^2\left(\omega_3^2-\omega^2\right)}{\mu_P^2\omega^2 + \left(\omega_3^2-\omega^2\right)^2},$$

$$R_4^{\pm} = -\frac{\delta\eta\omega^3\mu_P}{\mu_P^2\omega^2 + \left(\omega_3^2-\omega^2\right)^2} + (\nu_1 \pm \nu_2)\omega,$$

$$R_5 = -\frac{\mu_e\omega}{\left(1-\omega^2\right)^2 + \mu_e^2\omega^2},$$

and

$$R_6 = \omega^2(\beta_2\gamma_0 + \gamma_2\beta_0).$$

Appendix B. Appendix

Functions f_i and g_{ij} are defined as:

$$\begin{aligned}f_1(U,t) = \quad & \Big[-(\nu_1 - \nu_2\,\mathrm{sign}(\sin(\vartheta_1)))a\sin(\vartheta_1) + \tfrac{\lambda_1a^2}{\omega_1}\cos^2(\vartheta_1)\\ & -\left(\gamma_0 + \gamma_1a\cos(\vartheta_1) + \gamma_2a^2\cos^2(\vartheta_1)\right)\tfrac{b}{\omega_1}\sin(\vartheta_2)\\ & +\tfrac{\lambda_2a^3}{\omega_1}\cos^3(\vartheta_1) + \tfrac{\delta c}{\omega_1}\cos(\vartheta_3)\Big]\sin(\vartheta_1),\end{aligned} \tag{43}$$

$$g_{11}(U,t) = -\frac{\sin(\vartheta_1)}{\omega_1}, \tag{44}$$

$$\begin{aligned}f_2(U,t) = \quad & \Big[-(\nu_1 - \nu_2\,\mathrm{sign}(\sin(\vartheta_1)))\sin(\vartheta_1) + \tfrac{\lambda_1a}{\omega_1}\cos^2(\vartheta_1)\\ & -\left(\tfrac{\gamma_0}{a} + \gamma_1\cos(\vartheta_1) + \gamma_2a\cos^2(\vartheta_1)\right)\tfrac{b}{\omega_1}\sin(\vartheta_2)\\ & +\tfrac{\lambda_2a^2}{\omega_1}\cos^3(\vartheta_1) + \tfrac{\delta c}{\omega_1a}\cos(\vartheta_3)\Big]\cos(\vartheta_1),\end{aligned} \tag{45}$$

$$g_{21}(U,t) = -\frac{\cos(\vartheta_1)}{\omega_1a}, \tag{46}$$

$$\begin{aligned}f_3(U,t) = \quad & \left[-\mu_eb\sin(\vartheta_2) - \left(\beta_0 + \beta_1a\cos(\vartheta_1) + \beta_2a^2\cos^2(\vartheta_1)\right)\omega_1a\sin(\vartheta_1)\right]\\ & \times\sin(\vartheta_2),\end{aligned} \tag{47}$$

$$g_{32}(U,t) = -\sin(\vartheta_2), \tag{48}$$

$$f_4(U,t) = \begin{array}{l}\left[-\mu_e \sin(\vartheta_2) - \left(\beta_0 + \beta_1 a\cos(\vartheta_1) + \beta_2 a^2\cos^2(\vartheta_1)\right)\omega_1 \frac{a}{b}\sin(\vartheta_1)\right] \\ \times \cos(\vartheta_2),\end{array} \tag{49}$$

$$g_{42}(U,t) = -\frac{\cos(\vartheta_2)}{b}, \tag{50}$$

$$f_5(U,t) = \begin{array}{l} -\Big[-\frac{\eta\omega_1}{\omega_3} a\sin(\vartheta_1)(\nu_1 - \nu_2\,\mathrm{sign}(\sin(\vartheta_1))) \\ -\frac{b\eta}{\omega_3}\left(\gamma_0 + \gamma_1 a\cos(\vartheta_1) + \gamma_2 a^2(\cos(\vartheta_1))^2\right)\sin(\vartheta_2) \\ +\frac{\eta\lambda_1}{\omega_3} a^2\cos^2(\vartheta_1) + \frac{\eta\lambda_2}{\omega_3} a^3\cos^3(\vartheta_1) \\ +\mu_P c\sin(\vartheta_3) + \frac{\eta{\omega_1}^2 a\cos(\vartheta_1)}{\omega_3} + \frac{\eta\delta c\cos(\vartheta_3)}{\omega_3}\Big] \times \sin(\vartheta_3),\end{array} \tag{51}$$

$$g_{51}(U,t) = \eta\frac{\sin(\vartheta_3)}{\omega_3}, \tag{52}$$

$$g_{53}(U,t) = -\frac{\sin(\vartheta_3)}{\omega_3}, \tag{53}$$

$$f_6(U,t) = \begin{array}{l} -\Big[-\frac{\eta\omega_1}{\omega_3 c} a\sin(\vartheta_1)(\nu_1 - \nu_2\,\mathrm{sign}(\sin(\vartheta_1))) \\ -\frac{b\eta}{\omega_3 c}\left(\gamma_0 + \gamma_1 a\cos(\vartheta_1) + \gamma_2 a^2(\cos(\vartheta_1))^2\right)\sin(\vartheta_2) \\ +\frac{\eta\lambda_1}{\omega_3 c} a^2\cos^2(\vartheta_1) + \frac{\eta\lambda_2}{\omega_3 c} a^3\cos^3(\vartheta_1) \\ +\mu_P\sin(\vartheta_3) + \frac{\eta{\omega_1}^2 a\cos(\vartheta_1)}{\omega_3 c} + \frac{\eta\delta\cos(\vartheta_3)}{\omega_3}\Big] \times \cos(\vartheta_3),\end{array} \tag{54}$$

$$g_{61}(U,t) = \eta\frac{\cos(\vartheta_3)}{\omega_3 c}, \tag{55}$$

and

$$g_{63}(U,t) = -\frac{\cos(\vartheta_3)}{\omega_3 c}. \tag{56}$$

The drift and the diffusion coefficients are defined as:

$$m_1 = \frac{\tau_1 F_0^2\left(1+\tau_1^2\left(\omega^2+\omega_1^2\right)\right)}{4a\omega_1^2\left(1+\tau_1^2(\omega+\omega_1)^2\right)\left(1+\tau_1^2(\omega-\omega_1)^2\right)} - \frac{a\nu_1}{2}, \tag{57}$$

$$m_2 = \frac{3\lambda_2 a^2}{8\omega_1}, \tag{58}$$

$$m_3 = \frac{D_2}{2b\left(1+\tau_2^2\right)} - \frac{\mu_e b}{2}, \tag{59}$$

$$m_4 = 0, \tag{60}$$

$$m_5 = \frac{\eta^2 F_0^2\tau_1\left(1+\tau_1^2\left(\omega^2+\omega_3^2\right)\right)}{4c\omega_3^2\left(1+\tau_1^2(\omega+\omega_3)^2\right)\left(1+\tau_1^2(\omega-\omega_3)^2\right)} + \frac{D_3}{2c\omega_3^2\left(1+\omega_3^2\tau_3^2\right)} - \frac{\mu_P c}{2}, \tag{61}$$

$$m_6 = -\frac{\eta\delta}{2\omega_3}, \tag{62}$$

$$\sigma_1 = \sqrt{\frac{\tau_1 F_0^2\left(1+\tau_1^2\left(\omega^2+\omega_1^2\right)\right)}{2\omega_1^2\left(1+\tau_1^2(\omega+\omega_1)^2\right)\left(1+{\tau_1}^2(\omega-\omega_1)^2\right)}} = \sqrt{2a\left(m_1+\frac{a\nu_1}{2}\right)}, \tag{63}$$

$$\sigma_2 = \frac{\sigma_1}{a}, \tag{64}$$

$$\sigma_3 = \sqrt{\frac{D_2}{1+\tau_2^2}} = \sqrt{2b\left(m_3+\frac{\mu_e b}{2}\right)}, \tag{65}$$

$$\sigma_4 = \frac{\sigma_3}{b}, \tag{66}$$

$$\sigma_5 = \sqrt{\frac{\eta^2 F_0^2 \tau_1 \left(1+\tau_1{}^2\left(\omega^2+\omega_3^2\right)\right)}{2\omega_3^2\left(1+\tau_1^2(\omega+\omega_3)^2\right)\left(1+\tau_1^2(\omega-\omega_3)^2\right)} + \frac{D_3}{\omega_3^2\left(1+\omega_3^2\tau_3^2\right)}} = \sqrt{2c\left(m_5+\frac{\mu_P c}{2}\right)}, \tag{67}$$

and

$$\sigma_6 = \frac{\sigma_5}{c}. \tag{68}$$

References

[1] Martens W, von Wagner U, Litak G. Stationary response of nonlinear magnetopiezoelectric energy harvester systems under stochastic excitation. Eur Phys J 2013;222:1665.
[2] Borowiec M, Litak G, Lenci S. Noise effected energy harvesting in a beam with stopper. Int J Struct Stabil Dyn 2014;14:1440020.
[3] Xu M, Wang XJY, Huang Z. Stochastic averaging for nonlinear vibration energy harvesting system. Nonlinear Dyn 2014;78:1451.
[4] Li H, Qin W, Lan C, Deng W, Zhou Z. Dynamics and coherence resonance of tri-stable energy harvesting system. Smart Mater Struct 2016;25:015001.
[5] Xiao S, Jin Y. Response analysis of the piezoelectric energy harvester under correlated white noise. Nonlinear Dyn 2017;90:2069.
[6] Fokou ISM, Buckjohn CND, Siewe MS, Tchawoua C. Probabilistic distribution and stochastic p-bifurcation of a hybrid energy harvester under colored noise. Commun Nonlinear Sci Numer Simulat 2018;56:177.
[7] Yang T, Liu J, Cao Q. Response analysis of the archetypal smooth and discontinuous oscillator for vibration energy harvesting. Physica A 2018;507:358.
[8] Siewe MS, Kenfack WF, Kofane TC. Probabilistic response of an electromagnetic transducer with nonlinear magnetic coupling under bounded noise excitation. Chaos Soliton Fractals 2019;124:26.
[9] Daqaq MF. On intentional introduction of stiffness nonlinearities for energy harvesting under white gaussian excitations. Nonlinear Dyn 2012;69:1063?1079.
[10] Cottone F, Vocca H, Gammaitoni L. Nonlinear energy harvesting. Phys Rev Lett 2009;102:080601.
[11] Litak G, Friswell MI, Adhikari S. Magnetopiezoelastic energy harvesting driven by random excitations. Appl Phys Lett 2010;96:214103.
[12] Cottone F, Gammaitoni L, Vocca H, Ferrari M, Ferrari V. Piezoelectric buckled beams for random vibration energy harvesting. Smart Mater Struct 2012;21:035021.
[13] Wang X. Frequency analysis of vibration energy harvesting systems. Academic Press; 2016.
[14] Beeby S, White N. Energy harvesting for autonomous systems. Artech house; 2010.
[15] Tomlinson GR. Force distortion in resonance testing of structures with electrodynamic vibration exciters. J Sound Vib 1979;63:337.
[16] Siewe MS, Buckjohn CND. Heteroclinic motion and energy transfer in coupled oscillator with nonlinear magnetic coupling. Nonlinear Dyn 2014;75:903.
[17] Niaoqing H, Min C, Xisen W. The application of stochastic resonance theory for early detecting rub-impact fault of rotor system. Mech Syst Signal Pr 2003;17:883.
[18] Kenmoé GD, Ngouongo YJW, Kofane TC. Effect of the potential shape on the stochastic resonance processes. J Stat Phys 2015.
[19] Dykman MI, McClintock PVE. Power spectra of noise-driven nonlinear systems and stochastic resonance. Physica D 1992;58:10.
[20] Sharpe J, Sungar N, Macaria N. Observation of stochastic resonance using an optically addressed amorphous silicon/ferroelectric liquid crystal spatial light modulator. Opt Commun 1995;114:25.
[21] Freund JA, Schimansky-Geier L, Beisner B, Neiman A, Russell DF, Yakusheva T. Behavioral stochastic resonance: how the noise from a daphnia swarm enhances individual prey capture by juvenile paddlefish. J theor Biol 2002;71:214.
[22] Zheng R, Nakano K, Hu H, Su D, Cartmell MP. An application of stochastic resonance for energy harvesting in a bistable vibrating system. J Sound Vib 2014;333:2568.
[23] Li HT, Qin W, Deng W, Tian R. Improving energy harvesting by stochastic resonance in a laminated bistable beam. Eur Phys J Plus 2016;131:1.
[24] Nakano K, Cartmell MP, Hu H, Zheng R. Feasibility of energy harvesting using stochastic resonance caused by axial periodic force. J Mech Eng 2014;60:314.
[25] Litak G, Friswell MI, Adhikari S. Magnetopiezoelastic energy harvesting driven by random excitations. Appl Phys Lett 2010;96:214103.
[26] Dercole F, Rossa FD, Colombo A, Kuznetsov YA. Two degenerate boundary equilibrium bifurcations in planar filippov systems. SIAM J Appl Dyn Syst 2011;10:1525.
[27] Dercole F, Gragnani A, Rinaldi S. Bifurcation analysis of piecewise smooth ecological models. Theor Popul Biol 2007;72:197.
[28] Kuznetsov YA, Rinaldi S, Gragnani A. One-parameter bifurcations in planar filippov systems. Int J Bifurcat Chaos 2003;13:2157.
[29] Gouze J-L, Sari T. A class of piecewise linear differential equations arising in biological models. Dyn Syst 2002;17:299.
[30] Utkin VI. Sliding modes in control and optimization. Springer-Verlag; 1992.
[31] Utkin VI. Sliding mode control design principles and applications to electric drives. IEEE Trans Ind Electron 1993;40:23.
[32] Bartolini G, Parodi F, Utkin VI, Zolezzi T. The simplex method for nonlinear sliding mode control. Math Problem Eng 1999;4:461.
[33] Yakubovich VA, Leonov GA, Gelig AK. Stability of stationary sets in control systems with discontinuous nonlinearities. World Sci; 2004.
[34] Kowalczyk P, Piiroinen PT. Two-parameter sliding bifurcations of periodic solutions in a dry-friction oscillator. Physica D 2008;237:1053.
[35] Guardia M, Hogan SJ, Seara TM. An analytical approach to codimension-2 sliding bifurcations in the dry-friction oscillator. SIAM J Appl Dyn Syst 2010;9:769.
[36] Leine RI, Nijmeijer H. Dynamics and bifurcations of non-smooth mechanical systems. Berlin: Springer-Verlag; 2004.
[37] Acary V, Brogliato B. Numerical methods for nonsmooth dynamical systems, applications in mechanics and electonics. Berlin: Springer-Verlag; 2008.
[38] Yamapi R, Bowong S. Dynamics and chaos control of the self-sustained electromechanical device with and without discontinuity. Commun Nonlinear Sci Numer Simulat 2006;11:355.
[39] Soliman MSM, Abdel-Rahman EM, El-Saadany EF, Mansour RR. A design procedure for wideband micropower generators. J Mircoelectromech Syst 2009;18:1288.
[40] Lefeuvre E, Badel A, Richard C, Petit L, Guyomar D. A comparison between several vibration-powered piezoelectric generators for standalone systems. Sensor Actuator A 126:405.
[41] Wolf A. Quantifying chaos with lyapunouv exponent. Princeton: Princeton University press; 1986.
[42] Dimentberg MF. Statistical dynamics of nonlinear and time-Varying systems. New York: Wiley; 1988.
[43] Wedig WV. Analysis and simulation of nonlinear stochastic systems. Nonlinear dynamics in engineering systems, p 337. Schiehlen W, editor. Berlin: Springer; 1989.
[44] Gan C. Noise-induced chaos and basin erosion in softening duffing oscillator. Chaos Soliton Fractal 2005;25:1069.
[45] Stratonovich RL. Topics in the theory of random noise, vol. II. Gordon and breach. New York; 1967.
[46] Li JR, Xu W, Yang XL, Sun ZK. Chaotic motion of van der pol-mathieu-duffing system under bounded noise parametric excitation. J Sound Vib 2008;309:330.
[47] Bobryk RV, Chrzeszczyk A. Transitions induced by bounded noise. Physica A 2005;358:263.
[48] Liu WY, Zhu WQ, Huang ZL. Effect of bounded noise on chaotic motion of duffing oscillator under parametric excitation. Chaos Soliton Fractal 2001;12:527.
[49] d'Onofrio A. "fuzzy oncology": fuzzy noise induced bifurcations and their application to anti-tumor chemotherapy. Appl Math Lett 2008;21:662.

[50] Roberts JB, Spanos PD. Stochastic averaging: an approximate method of solving random vibration problems. Int J of Non-Linear Mechanics 1986;21:111.
[51] Zhu W. Recent developments and applications of the stochastic averaging method in random vibration. Appl Mech Rev 1996;49:s72.
[52] Honeycutt RL. Stochastic runge-kutta algorithms. i. white noise. Phys Rev A 1992;45:600.
[53] Honeycutt RL. Stochastic runge-kutta algorithms. II. colored noise. Phys Rev A 1992;45:604.
[54] Mantegna RN, Spagnolo B. Stochastic resonance in a tunnel diode. Phys Rev E 1994;49:R1792.
[55] Lanzara E, Mantegna RN, Spagnolo B, Zangara R. Experimental study of a nonlinear system in the presence of noise: the stochastic resonance. Am J Phys 1997;65:341.
[56] La Barbera A, Spagnolo B. Spatio-temporal patterns in population dynamics. Phys A 2002;314:120.
[57] Fiasconaro A, Valenti D, Spagnolo B. Nonmonotonic behavior of spatiotemporal pattern formation in a noisy lotka-volterra system. Acta Phys Pol B 2004;35:1491.
[58] Valenti D, Tranchina L, Brai M, Caruso A, Cosentino C, Spagnolo B. Environmental metal pollution considered as noise: effects on the spatial distribution of benthic foraminifera in two coastal marine areas of sicily (southern italy). Ecol Modell 2008;213:449.

Meccanica
https://doi.org/10.1007/s11012-021-01394-4

Fractional properties' effects on a hybrid energy harvesting system dynamics

G. G. Sengha · W. Fokou Kenfack · D. J. Owono Bekoa · M. Siewe Siewe · C. B. Tabi · T. C. Kofane

Received: 29 October 2020 / Accepted: 12 June 2021

Abstract A vibration-powered harvester modeled by non-smooth coupled oscillators with fractional properties and subjected to harmonic excitation is concerned in this work. By a modified harmonic balance method, the harmonic response of the system is studied, thence the effects of fractional derivatives' orders (FDOs) on the harvesting behavior of the system are sought. A numerical confirmation is then obtained by the mean of the Newton-Leipnik algorithm. The FDOs effects on the chaotic response and their implication on the harvesting characteristic of the system are also analyzed. For low amplitude excitations, it is found that, depending on the excitation frequency's band, the power generated by the mean of the electromagnetic transduction mechanism can be maximized either by increasing or reducing the order of the fractional derivative related to the electromagnetic circuit. Contrariwise, the performance of the piezoelectric conversion mechanism is improved by increasing the order of the fractional derivative related to the piezoelectric circuit, irrespective of the excitation frequency. For large amplitude excitations, proper choices of FDOs enable the system to exhibit a regular behavior instead of a chaotic one, so as to harvest a useful power of regular waveform.

Keywords Vibration energy harvesting · Fractional derivative · Harmonic balance method · Chaos

G. G. Sengha · W. F. Kenfack (✉) · D. J. O. Bekoa · M. S. Siewe · C. B. Tabi · T. C. Kofane
Department of Physics, Faculty of Sciences, University of Yaounde I, P.O. Box 812 Yaoundé, Cameroon
e-mail: wilsonkenfack@gmail.com

G. G. Sengha
e-mail: senghaghislain2@yahoo.fr

D. J. O. Bekoa
e-mail: davidbekoa95@gmail.com

M. S. Siewe
e-mail: martinsiewesiewe@yahoo.fr

C. B. Tabi
e-mail: tabic@biust.ac.bw

T. C. Kofane
e-mail: tckofane@yahoo.com

G. G. Sengha
Department of Physics, Faculty of sciences, University of Bangui, P.O. Box 1450 Bangui, Central African Republic

G. G. Sengha · T. C. Kofane
The African Center of Excellence in Information and Communication Technologies (CETIC), Yaoundé, Cameroon

C. B. Tabi · T. C. Kofane
Department of Physics and Astronomy, Botswana International University of Science and Technology, Private Bag 16, Palapye, Botswana

Published online: 07 July 2021

1 Introduction

Harvesting energy out of ambient sources such as human motion, wind and fluid flow, photonic or solar energy, thermal energy and environmental vibrations into usable electrical energy has drawn the attention of several researchers in the past recent years. Among the preceding energy sources, vibration energy harvesting technology employs mechanical vibrations as primary energy source, and the transduction mechanisms include electromagnetic [1, 2], piezoelectric [3], triboelectric [4], and electrostatic [5–7]. This research field has grown rapidly, whether measured by number of research papers and text-books [8–29] or diversity of potential applications. The harvested energy can, as a matter of fact, be provided to a variety of low power electronic portable devices to recharge their batteries or to enable remote operations [29]. Investigations in this scientific research field mainly aim at enhancing the efficiency and performance of vibration energy harvesters by searching appropriate system design, using better materials and structures and by taking advantage of nonlinear phenomena.

In pursuing this aim, several researchers have made use of nonlinear effects to broaden the frequency bandwidth of vibration energy harvesters and thus, to enhance the performance of the system. Erturk et al. [13], Harne and Wang [15], Vocca et al. [18] and Zhou et al. [21] to name but a few, reported that unlike linear harvesters, nonlinear bistable harvesters show promising results with enhanced frequency bandwidth. The bistable configuration of their potential energy should therefore be considered by designer as shown by Ramlan et al. [19]. Siewe and Buckjohn [30] and Stanton et al. [31] used the Melnikov theory to investigate the performance of nonlinear bistable harvesters by analyzing the critical condition for homoclinic bifurcation and interwell dynamics as a function of the systems parameters. In fact, nonlinear bistable systems may exhibit, through a snap-through action, large amplitude crossing well motion with an increase of harvested power benefit. The effects of random environmental fluctuations or noises on the performance of nonlinear harvesters have also been extensively studied [23, 25, 26, 32–34]. It has been acknowledged that stochastic resonance phenomenon is advantageous to increase the power generation [25, 32–34]. Indeed, linear harvesters amplify ambient vibration matching their natural frequency [11], however their efficiency dramatically drops in the close vicinity of this frequency. It has been considered by Siewe et al. [22] and more recently by Sengha et al. [35] that the interaction between the mechanical and the electrical parts of a scavenger making use of electromagnetic conversion mechanism is of nonlinear type. This assumption results in a nonlinear magnetic coupling between both parts of the harvester and it has been reported that for appropriate nonlinear coupling, the system performance is found to be improved.

In addition to accounting for nonlinear characteristic in modeling dynamical systems in general, and vibration energy harvesting systems in particular, another mean to develop more realistic models is to take the memory effect exhibited by some materials into account through fractional derivatives. Fractional order derivatives date back to the age of Leibniz and L'Hospital, when they both engaged into a controversy about the possibility of non-integer order derivative. From that era to nowadays, considerable efforts have been made by scientists to lay a solid foundation for fractional calculus and hundreds of publications and text-books [36–55] are now available in the literature for that subject matter. Many modern examples of its applications pervade several scientific fields ranging from biology to robotics, and from chemistry to economy and finance. In physics, more precisely in the field of vibration energy harvesting, Fokou et al. [56] recently discussed the performance of a piezoelectric buckled beam with fractional derivative and nonlinear damping subjected to purely harmonic excitation. It emerges that the order of fractional derivative plays an important role in the system response. Foupouapouognigni et al. [57] studied an electromechanical energy harvesting system exhibiting fractional properties and subjected to harmonic excitation by the mean of harmonic balance method. They showed that by augmenting the order of fractional derivative, the output power is maximized. Kwuimy et al. [58] considered an electromechanical system, acting as an energy harvester, with a fractional order current-voltage relationship for the electrical part and fractional power law in the restoring force of its mechanical part. It comes out from their studies that the resonant amplitude of the mechanical vibration considerably depends on the order of the fractional derivative. Cao et al. [42] considered a system with fractional order viscoelastic material for energy

harvesting perspective and showed that the fractional order property of the material enhances both high-energy chaotic motion and interwell periodic oscillation. These non-exhaustive recent developments in vibration energy harvesting show that accounting for hysteresis and/or memory effect through fractional derivative influences the performance of the system. It is thus interesting to pursue such analysis and investigate the effects of fractional order inductances on the response of another hybrid energy harvester with non-smooth behavior introduced earlier in the literature.

We extend our previous work in this paper by considering the non-smooth type hybrid energy harvester with nonlinear magnetic coupling introduced by Sengha et al. [35]. Sengha et al. [35] studies the deterministic and the stochastic dynamics of the hybrid energy harvester with regard to the nonlinear magnetic coupling coefficient, the coupling and nonlinearity parameters. In this work, unlike Sengha et al. [35], the hybrid energy harvester exhibits fractional properties. Its dynamics is therefore analytically and numerically studied with respect to FDOs. The essential issue of this work is to investigate the effects of the fractional properties on the harmonic response of the system and study the consequence on energy harvesting. In this paper, we also explore the effects of fractional properties on chaotic regime of such a class of hybrid vibration energy harvester. To this end, the remainder of this paper is organized as follows: In Sect. 2, a schematic description of the harvester is proposed, the derivation of the governing equations is performed, a modified harmonic balance method and a numerical scheme based on the Newton-Leipnik algorithm are developed. In Sect. 3, the effects of FDOs on the oscillatory amplitudes, the harvested powers and the system efficiency are investigated by the mean of the modified harmonic balance method. The results are then verified by the mean of the above numerical scheme. Then, by computing bifurcation diagrams, a numerical investigation of the effects of FDOs on the chaotic response of the system is carried out. We next provide a concise discussion of the above results. Finally, Sect. 4 summarizes the paper.

2 System description, modeling assumptions and methodology

2.1 Mathematical modeling

The electromechanical device sketched in Fig. 1 [35] is a hybrid energy harvester using two conversion mechanisms, namely the electromagnetic and the piezoelectric mechanisms. Its mechanical part possesses a damping with discontinuous behavior as pointed out by Sengha et al. [35]. Moreover, the coils within the electrical subsystem exhibit fractional properties.

The electrical part of the device consists of two circuitries: the piezoelectric and the electromagnetic circuits. The piezoelectric circuit consists of an inductor with inductance L_P, a piezoelectric element with force factor α and blocking capacitance C_P and the load resistance R_P, whose voltage and current obey the following equations:

$$i_1 = \frac{v}{R_P}, \tag{1a}$$

$$v = L_P \frac{d^\theta i_2}{d\tau^\theta}, \tag{1b}$$

$$i_P = i_1 + i_2, \tag{1c}$$

where i_P and v are respectively the current and the voltage across the electrodes of the piezoelectric element, i_1 and i_2 are the currents flowing through the load resistor and the inductor respectively. θ $(0<\theta<1)$ is the order of the fractional derivative

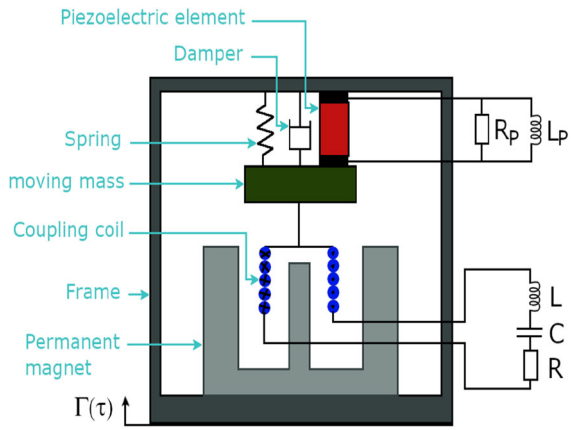

Fig. 1 Sketch of the hybrid energy harvester introduced by Sengha et al. [35]

with respect to time t. The electromagnetic circuit is formed of a linear capacitor of capacitance C, a linear resistor R and a linear inductor L with fractional property. Using the Kirchhoff's laws, this circuit can be described by the following equation:

$$L\frac{d^{1+\epsilon}q}{d\tau^{1+\epsilon}} + R\frac{dq}{d\tau} + \frac{1}{C}q + E_L = 0, \tag{2}$$

where E_L is the Lenz electromotive voltage, q is the instantaneous electrical charge and ϵ $(0<\epsilon<1)$ is the parameter describing the fractional property of the coil within the electromagnetic circuit.

The mechanical part reduces to a damped mass-spring system subjected to the inertial force due to the frame (base) acceleration $\Gamma(\tau)$. The motion of the suspended mass m can be mathematically formulated by the Newton's second law. It yields the following equation:

$$m\frac{d^2X}{d\tau^2} = -\mu_0\frac{dX}{d\tau} - F_P + F_L - m\Gamma(\tau), \tag{3}$$

with X the relative displacement of the mass with respect to the frame; F_P, the global restoring force due to the spring and the piezoelectric element; F_L, the Laplace force; $-m\Gamma(\tau)$ the inertial force and $\mu_0\dot{X}$ the damping forces originating from friction, air resistance, etc. The magnitude of the damping forces depends on the movement direction of the suspended mass in such a way that $\mu_0 = \begin{cases} \mu_0^+ & \text{if } \dfrac{dX}{d\tau} > 0 \\ \mu_0^- & \text{if } \dfrac{dX}{d\tau} < 0 \end{cases}$.

The harvester's mechanical part and electromagnetic circuit interact through the air-gap of a permanent magnet which creates a radial magnetic field $\mathbf{B}$. Following Siewe et al. [22, 30], the relationship between the magnitude B of that magnetic field and the coil position, is given as:

$$B = B_0\left(1 - \left(\frac{X + X_0}{X_{\max}}\right)^2\right), \tag{4}$$

where B_0 is the highest intensity that the field B reaches, X_0 is the armature initial position, and X_{max} is the maximum amplitude. Thence, the relationship between the Laplace force F_L and the current on the one hand, and the expression of the Lenz electromotive voltage E_L on the other hand, are of the form:

$$F_L = \alpha_0\left(1 - \left(\frac{X + X_0}{X_{max}}\right)^2\right)\frac{dq}{d\tau}, \tag{5a}$$

$$E_L = \kappa_0\left(1 - \left(\frac{X + X_0}{X_{\max}}\right)^2\right)\frac{dX}{d\tau}, \tag{5b}$$

where α_0 and κ_0 are coefficients of adjustment of dimension. They depend on B_0 and the coil geometrical parameters. Moreover, following reference [59], the expression of the global restoring force is given as:

$$F_P = \left(k_0X + k_1X^2 + k_2X^3 + \alpha v\right), \tag{6}$$

with k_0 the global linear stiffness of the system's mechanical part. Parameters k_1 and k_2 define the nonlinearity of the spring. The current i_P, across the piezoelectric element, is related to the mass displacement X by

$$i_P = \alpha\frac{dX}{d\tau} - C_P\frac{dv}{d\tau}. \tag{7}$$

Taking Eq. (1) into account in Eq. (7), it takes the following form:

$$\frac{1}{R_P}\frac{dv}{d\tau} + \frac{1}{L_P}\frac{d^{1-\theta}v}{d\tau^{1-\theta}} = \alpha\frac{d^2X}{d\tau^2} - C_P\frac{d^2v}{d\tau^2}. \tag{8}$$

Replacing Eq. (5b) into Eq. (2) and Eqs. (5a) and (6) into Eq. (3), then setting $\omega_m = \sqrt{\frac{k_0}{m}}$, $\omega_e = \sqrt{\frac{1}{LC}}$, $\omega_P = \sqrt{\frac{1}{L_PC_P}}$, $x = \frac{X}{l}$, $y = \frac{q}{Q_0}$, $z = \frac{v}{V_0}$, where l, Q_0 and V_0 are respectively the reference length, charge and voltage; and with the time transformation $t = \omega_e\tau$, one obtains the following dimensionless equations resulting from Eqs. (3), (2) and (8) respectively:

$$\ddot{x} + (v_1 + v_2\text{sign}(\dot{x}))\dot{x} + \omega_1^2x + \lambda_1x^2 + \lambda_2x^3 + \delta z + \left(\gamma_0 + \gamma_1x + \gamma_2x^2\right)\dot{y} = f(t), \tag{9a}$$

$$r_1D_t^{1+\epsilon}y + \mu_e\dot{y} + y + \left(\beta_0 + \beta_1x + \beta_2x^2\right)\dot{x} = 0, \tag{9b}$$

$$\ddot{z} + \mu_P\dot{z} + r_2D_t^{1-\theta}z + \eta\ddot{x} = 0, \tag{9c}$$

with the dimensionless parameters given by

$$v_1 = \frac{\mu_0^+ + \mu_0^-}{2m\omega_e}, \quad \omega_1 = \frac{\omega_m}{\omega_e}, \quad \lambda_1 = \frac{k_1 l}{m\omega_e^2},$$
$$\gamma_0 = -\frac{\alpha_0 Q_0}{ml\omega_e}\frac{X_{\max}^2 - X_0^2}{X_{\max}^2}, \quad \gamma_1 = \frac{2\alpha_0 X_0 Q_0}{m\omega_e X_{\max}^2},$$
$$\gamma_2 = \frac{\alpha_0 l Q_0}{m\omega_e X_{\max}^2}, \quad \delta = \frac{\alpha V_0}{ml\omega_e^2}, \quad \lambda_2 = \frac{k_2 l^2}{m\omega_e^2},$$
$$\mu_e = \frac{R}{L\omega_e}, \quad \beta_0 = \frac{\kappa_0 l}{LQ_0\omega_e}\frac{X_{\max}^2 - X_0^2}{X_{\max}^2}, \quad v_2 = \frac{\mu_0^+ - \mu_0^-}{2m\omega_e},$$
$$\beta_1 = -\frac{2\kappa_0 l^2 X_0}{LQ_0\omega_e X_{\max}^2}; \quad \beta_2 = -\frac{\kappa_0 l^3}{LQ_0\omega_e X_{\max}^2},$$
$$\mu_P = \frac{1}{R_P C_P \omega_e}, \quad \eta = -\frac{\alpha l}{C_P V_0}, \quad r_1 = \frac{1}{\omega_e^{1-\epsilon}},$$
$$r_2 = \frac{\omega_P^2}{\omega_e^{1+\theta}}.$$

The excitation function $f(t)$ is related to the frame motion acceleration as $f(t) = -\frac{\Gamma(\tau)}{l\omega_e^2}$. We assume throughout this report that $\Gamma(\tau)$ is a harmonic function with constant amplitude and constant frequency, i.e. $f(t)$ can be mathematically expressed as $f(t) = F_0\cos(\omega t)$, with F_0 the amplitude of the excitation and ω its frequency.

The potentials of the harvester mechanical and electrical parts are given by

$$V(x) = \frac{\omega_1^2}{2}x^2 + \frac{\lambda_1}{3}x^3 + \frac{\lambda_2}{4}x^4,$$
$$V(y) = \frac{1}{2}y^2 \quad \text{and} \quad V(z) = \frac{\omega_3^2}{2}z^2. \tag{10}$$

$V(y)$ and $V(z)$ are harmonic potentials. The conditions $\lambda_2 > 0$ and $\lambda_1^2 - 4\lambda_2\omega_1^2 > 0$ hold in the remainder of this report so that $V(x)$ is a bistable potential.

2.2 Harmonic response of the system: harmonic balance method

We seek in this section an approximate analytical solution of Eq. (9) in the form:

$$x(t) = a_1\cos(\omega t) + a_2\sin(\omega t), \tag{11a}$$

$$y(t) = b_1\cos(\omega t) + b_2\sin(\omega t), \tag{11b}$$

$$z(t) = c_1\cos(\omega t) + c_2\sin(\omega t). \tag{11c}$$

We set $a = \sqrt{a_1^2 + a_2^2}$, $b = \sqrt{b_1^2 + b_2^2}$ and $c = \sqrt{c_1^2 + c_2^2}$, the amplitudes of the preceding harmonic solutions. When replacing Eq. (11) into Eq. (9), we have to approximately evaluate $D_t^{1+\epsilon}[y(t)]$ and $D_t^{1-\theta}[z(t)]$. Among the numerous definitions of the fractional derivatives, we use the Caputo's definition [36] given as:

$$D_t^{\epsilon}[y(t)] = \frac{1}{\Gamma(1-\epsilon)}\int_0^t (t-s)^{-\epsilon}\dot{y}(s)ds = \frac{1}{\Gamma(1-\epsilon)}\int_0^t s^{-\epsilon}\dot{y}(t-s)ds, \tag{12}$$

where $\Gamma(\cdot)$ is the gamma function and $0 < \epsilon < 1$. Replacing Eq. (11b) into Eq. (12), one obtains

$$D_t^{\epsilon}[y(t)] = D_t^{\epsilon}[b_1\cos(\omega t) + b_2\sin(\omega t)] = \frac{1}{\Gamma(1-\epsilon)}\int_0^t s^{-\epsilon}(-b_1\omega\sin(\omega(t-s)))ds + \frac{1}{\Gamma(1-\epsilon)}\int_0^t s^{-\epsilon}b_2\omega\cos(\omega(t-s))ds. \tag{13}$$

Making the variable change $u = \omega s$ and setting $I_1 = \int_0^{\omega t}\frac{\cos u}{u^{\epsilon}}du$ and $I_2 = \int_0^{\omega t}\frac{\sin u}{u^{\epsilon}}du$, it can be shown that

$$D_t^{\epsilon}[y(t)] = \frac{\omega^{\epsilon}}{\Gamma(1-\epsilon)}[(-b_1 I_1 + +b_2 I_2)\sin(\omega t) + (b_1 I_2 + b_2 I_1)\cos(\omega t)]. \tag{14}$$

Using the approximation

$$I_1 \approx \Gamma(1-\epsilon)\sin\left(\epsilon\frac{\pi}{2}\right) \quad \text{and} \quad I_2 \approx \Gamma(1-\epsilon)\cos\left(\epsilon\frac{\pi}{2}\right), \tag{15}$$

we finally obtain

$$D_t^{\epsilon}[y(t)] = \omega^{\epsilon}\left[(b_1\cos(\omega t) + b_2\sin(\omega t))\cos\left(\epsilon\frac{\pi}{2}\right) + (b_2\cos(\omega t) - b_1\sin(\omega t))\sin\left(\epsilon\frac{\pi}{2}\right)\right]. \tag{16}$$

Thence, differentiating with respect to time t, we have the following expression of $D_t^{1+\epsilon}[y(t)]$

$$D_t^{1+\epsilon}[y(t)] = \frac{d}{dt}D_t^{\epsilon}[y(t)] = \omega^{1+\epsilon}\Big[(-b_1\sin(\omega t) + b_2\cos(\omega t))\cos\Big(\epsilon\frac{\pi}{2}\Big) - (b_1\cos(\omega t) + b_2\sin(\omega t))\sin\Big(\epsilon\frac{\pi}{2}\Big)\Big]. \tag{17}$$

We express $D_t^{1-\theta}[z(t)]$ in the same way as above. It follows that

$$D_t^{1-\theta}[z(t)] = \omega^{1-\theta}\Big[(c_1\cos(\omega t) + c_2\sin(\omega t))\cos\Big((1-\theta)\frac{\pi}{2}\Big) + (c_2\cos(\omega t) - c_1\sin(\omega t))\sin\Big((1-\theta)\frac{\pi}{2}\Big)\Big]. \tag{18}$$

In order to derive the algebraic equations that verify the amplitudes, let us substitute Eq. (11) into Eq. (9). We have to take Eqs. (17) and (18) into account and neglect the terms of higher harmonics. We obtain the following linear system:

$$\Big(\Big(\frac{3\lambda_2}{4} - \frac{\lambda_1\gamma_2}{2\gamma_1}\Big)a^2 + \omega_1^2 - \omega^2\Big)a_1 + (\nu_1 \pm \nu_2)\omega a_2 + \Big(\frac{1}{4}\omega\gamma_2 a^2 + \gamma_0\omega\Big)b_2 + \delta c_1 = F_0, \tag{19a}$$

$$-(\nu_1 \pm \nu_2)\omega a_1 + \Big(\Big(\frac{3\lambda_2}{4} - \frac{\lambda_1\gamma_2}{2\gamma_1}\Big)a^2 + \omega_1^2 - \omega^2\Big)a_2 - \Big(\frac{1}{4}\omega\gamma_2 a^2 + \gamma_0\omega\Big)b_1 + \delta c_2 = 0, \tag{19b}$$

$$(1 - r_1\varsigma_2)b_1 + (\mu_e\omega + r_1\varsigma_1)b_2 + \Big(\frac{\omega\beta_2}{4}a^2 + \beta_0\omega\Big)a_2 = 0, \tag{19c}$$

$$-(\mu_e\omega + r_1\varsigma_1)b_1 + (1 - r_1\varsigma_2)b_2 - \Big(\frac{\omega\beta_2}{4}a^2 + \beta_0\omega\Big)a_1 = 0, \tag{19d}$$

$$(r_2\varrho_2 - \omega^2)c_1 + (\mu_P\omega + r_2\varrho_1)c_2 - \eta\omega^2 a_1 = 0, \tag{19e}$$

$$-(\mu_P\omega + r_2\varrho_1)c_1 + (r_2\varrho_2 - \omega^2)c_2 - \eta\omega^2 a_2 = 0, \tag{19f}$$

where we set $\varsigma_1 = \omega^{1+\epsilon}\cos\big(\frac{\pi\epsilon}{2}\big)$, $\varsigma_2 = \omega^{1+\epsilon}\sin\big(\frac{\pi\epsilon}{2}\big)$, $\varrho_1 = \omega^{1-\theta}\cos\big(\frac{\pi\theta}{2}\big)$ and $\varrho_2 = \omega^{1-\theta}\sin\big(\frac{\pi\theta}{2}\big)$.

Using some elementary algebra, one can show from the preceding system that depending on the value taken by the sign function, the amplitude a is either the root of the algebraic equation $H^+(a) = 0$ or $H^-(a) = 0$, where the polynomial functions $H^{\pm}$ are defined as

$$H^{\pm}(a) = \iota_{10}a^{10} + \iota_8 a^8 + \iota_6^{\pm}a^6 + \iota_4^{\pm}a^4 + \iota_2^{\pm}a^2 - 256F_0^2. \tag{20}$$

The coefficients of these polynomials are provided in the "Appendix". The approximate amplitude of the harvester mechanical part's oscillation can be taken as the average of the roots yielded by the equations $H^+(a) = 0$ and $H^-(a) = 0$. From the above algebra, it is also shown that the amplitudes b and c of the electrical part's oscillations relate to amplitude a as follows:

$$b = \frac{\big|\beta_0 + \frac{1}{4}\beta_2 a^2\big|\omega a}{\sqrt{(1 - r_1\varsigma_2)^2 + (\mu_e\omega + r_1\varsigma_1)^2}}, \tag{21a}$$

$$c = \frac{|\eta|\omega^2 a}{\sqrt{(r_2\varrho_2 - \omega^2)^2 + (\mu_P\omega + r_2\varrho_1)^2}}. \tag{21b}$$

To evaluate the amplitude a of the mechanical vibration, the roots a^+ and a^- of the respective polynomials $H^+(a)$ and $H^-(a)$ are calculated by the mean of the Newton-Raphson algorithm. Then amplitude a is estimated as $a = \frac{a^+ + a^-}{2}$. Once amplitude a is determined, the amplitudes of the electrical oscillations are deduced through Eq. (21). Varying the frequency of the excitation, the amplitudes a, b and c are evaluated as mentioned above and the so-called *frequency-response curves* are plotted in Fig. 2. These are curves depicting the variations of the oscillators' amplitudes versus the excitation frequency. In a similar way, the variations of these amplitudes with respect to parameters ϵ and θ are provided (in solid lines) in Fig. 3. Moreover, the *amplitude-response curves*, which illustrate the oscillations amplitudes variation with respect to the excitation amplitude, are depicted with solid lines in Fig. 4.

2.3 Numerical simulations

In order to estimate these amplitudes by the mean of direct numerical integrations of system (9), each equation of system (9) can be decomposed into a set of equations of lower degree as follows:

$$\dot{x} = u, \tag{22a}$$

$$\dot{u} = G(x, u, v, z, t), \tag{22b}$$

$$\dot{y} = v, \tag{22c}$$

$$D_t^{\epsilon} v = \frac{1}{r_1}\left(-\mu_e v - y - \left(\beta_0 + \beta_1 x + \beta_2 x^2\right)u\right), \tag{22d}$$

$$\dot{z} = w, \tag{22e}$$

$$D_t^{1-\theta} z = \psi, \tag{22f}$$

$$\dot{w} = -\mu_P w - r_2 \psi - \eta G(x, u, v, z, t), \tag{22g}$$

where $G(x, u, v, z, t) = -(v_1 + v_2 sign(u))u - \omega_1^2 x -$

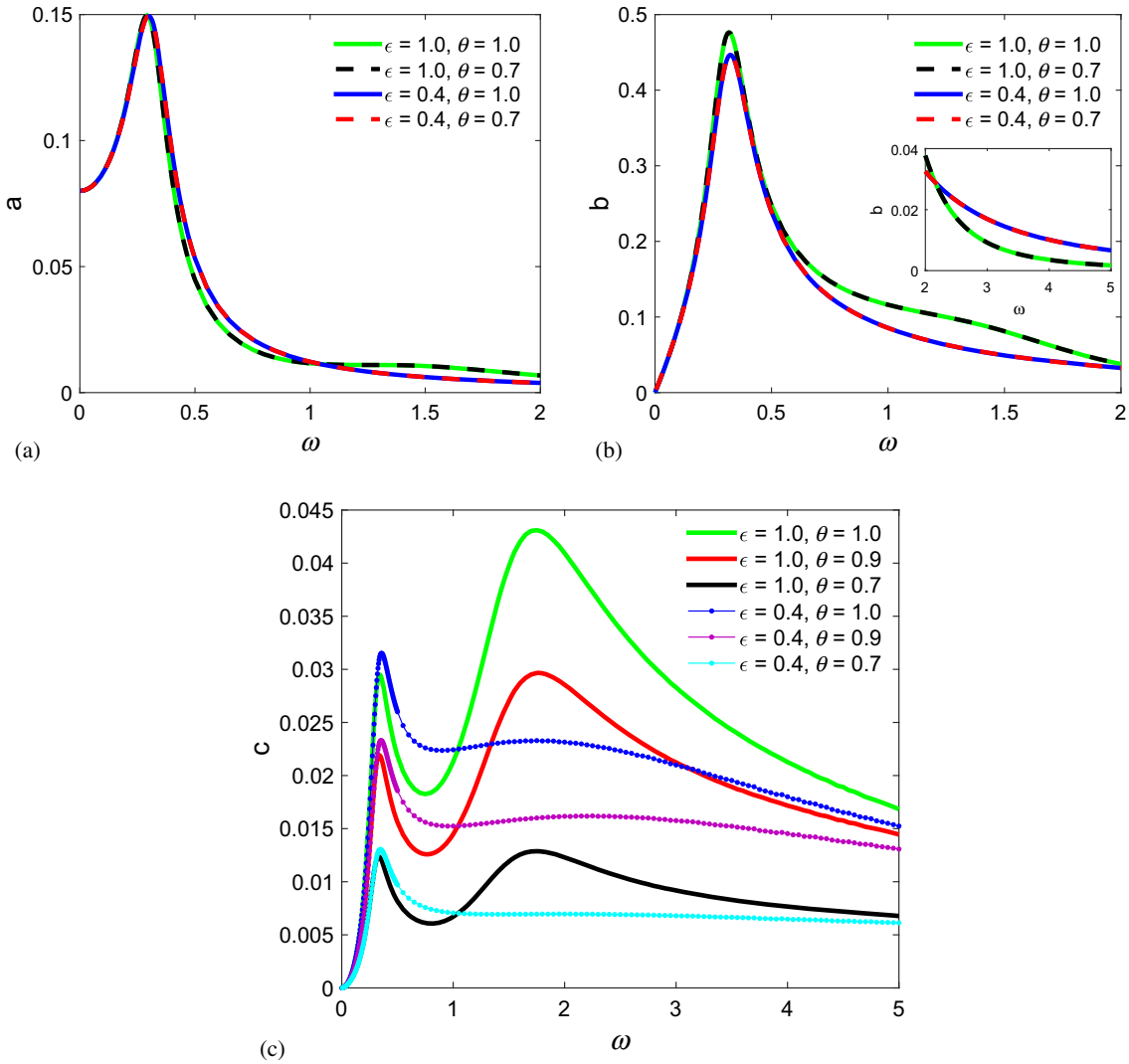

Fig. 2 Frequency-response curves: amplitudes of (**a**) mechanical vibrations, (**b**) electromagnetic vibrations and (**c**) piezoelectric ones versus driving frequency; for various FDOs ϵ and θ. These results are analytically obtained. Parameters are $v_1 = 0.3$, $v_2 = 0.05$, $\mu_e = 1.0$, $\mu_P = 16.0$, $\omega_1 = 0.5$, $\lambda_1 = 0.0045$, $\lambda_2 = 0.00002$, $\gamma_0 = -0.125$, $\gamma_1 = 0.002$, $\gamma_2 = 0.02$, $\beta_0 = 10.0$, $\beta_1 = -0.16$, $\beta_2 = -1.6$, $\delta = 0.001$, $\eta = -64.0$, $\omega_e = 50.0$, $\omega_P = 282.84$ and $F_0 = 0.02$ (color figure online)

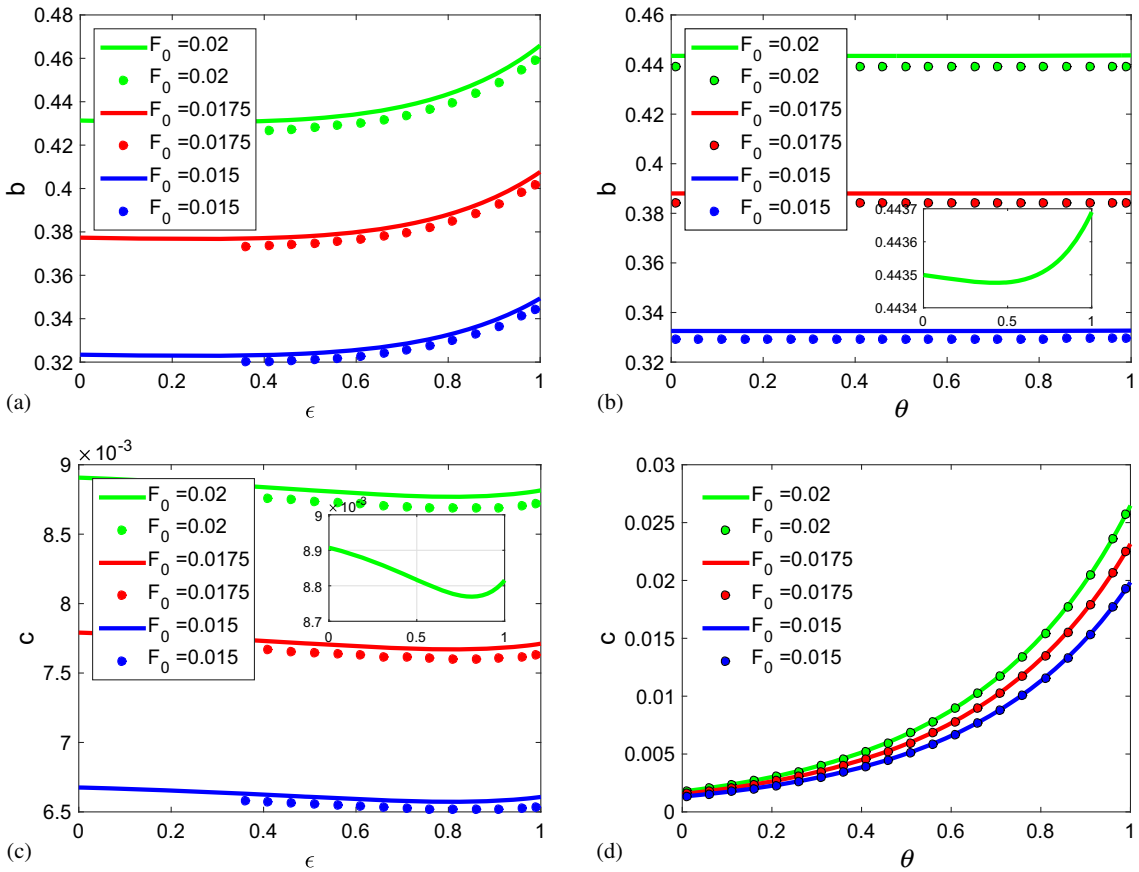

Fig. 3 Amplitudes of (**a**, **b**) electromagnetic vibrations and (**c**, **d**) piezoelectric ones versus FDOs. The solid thick curves result from analytical treatment, while circles and dots are obtained through numerical simulations. $\theta = 0.6$ for (**a**, **c**), $\epsilon = 0.8$ for (**b**, **d**) and $\omega = 0.3$. Other parameters in Fig. 2 are kept unchanged

$\lambda_1 x^2 \ -\lambda_2 x^3 - \delta z - (\gamma_0 + \gamma_1 x + \gamma_2 x^2)v + f(t)$. Using the fractional order Newton-Leipnik algorithm [45, 54], the above set of equations can be written in the following discretized form:

$$x_k = x_{k-1} + hu_{k-1}, \tag{23a}$$

$$u_k = u_{k-1} + hG(x_{k-1}, u_{k-1}, v_{k-1}, z_{k-1}, t_{k-1}), \tag{23b}$$

$$y_k = y_{k-1} + hv_{k-1}, \tag{23c}$$

$$v_k = \left[\frac{1}{r_1}\left(-\mu_e v_{k-1} - y_k - (\beta_0 + \beta_1 x_k + \beta_2 x_k^2)u_k\right)\right]h^{\epsilon} - \sum_{j=1}^{k} c_j^{(\epsilon)} v_{k-j}, \tag{23d}$$

$$\psi_{k-1} = \left[z_{k-1} + hw_{k-1} + \sum_{j=1}^{k} c_j^{(1-\theta)} z_{k-j}\right]\frac{1}{h^{1-\theta}}, \tag{23e}$$

$$z_k = z_{k-1} + hw_{k-1}, \tag{23f}$$

$$w_k = w_{k-1} + h\left[-\mu_p w_{k-1} - r_2\psi_{k-1} - \eta G(x_{k-1}, u_{k-1}, v_{k-1}, z_{k-1}, t_{k-1})\right], \tag{23g}$$

where h is the integration (or time) step defined such as $t_k = t_{k-1} + h$ and x_k denotes $x(t_k)$. The coefficients $c_j^{(\epsilon)}$ are computed by the following recursive relations:

$$c_0^{(\epsilon)} = 1, \quad c_j^{(\epsilon)} = \left(1 - \frac{1+\epsilon}{j}\right)c_{j-1}^{(\epsilon)}. \tag{24}$$

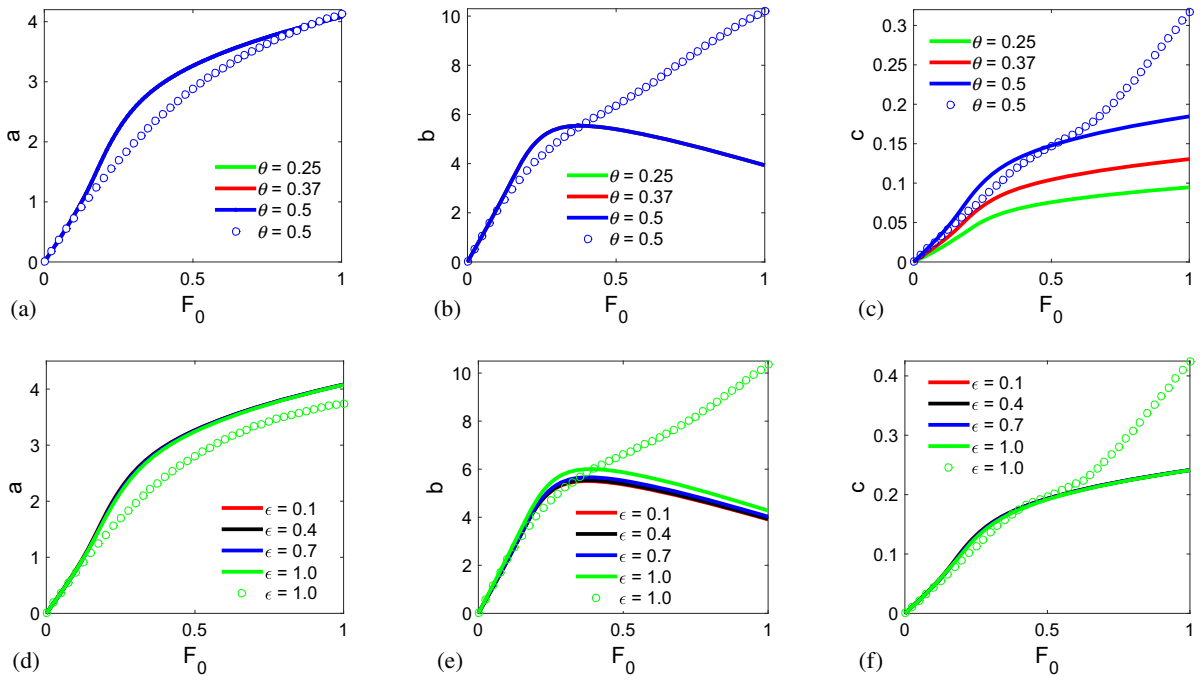

Fig. 4 Amplitude-response curves: amplitudes of (**a**) mechanical vibrations, (**b**) electromagnetic vibrations and (**c**) piezoelectric ones versus excitation strength. Solid thick lines result from analytical method and circles result from direct numerical integrations of system (9). Parameters in Fig. 2 are kept unchanged unless otherwise specified and $\omega = 0.3$

$c_j^{(1-\theta)}$ are computed in a similar way. By the mean of the above set of Eqs. ((23a)–(23g)), numerical solution of system (9) is evaluated with time step $h = 0.001$ and null initial conditions. This computation, done on MATLAB software, is excessively time consuming due to the memory effect. After computing a long time evolution of the state variables $x(t)$, $y(t)$ and $z(t)$; if $x(t)$, $y(t)$ and $z(t)$ exhibit a sine waveform, then the peak-to-peak lengths $x_{max} - x_{min}$, $y_{max} - y_{min}$ and $z_{max} - z_{min}$ are evaluated and the amplitudes a, b and c are extracted as $a = \frac{x_{max}-x_{min}}{2}$, $b = \frac{y_{max}-y_{min}}{2}$ and $c = \frac{z_{max}-z_{min}}{2}$. Note that x_{max}, y_{max} and z_{max} are respectively the upper peaks of $x(t)$, $y(t)$ and $z(t)$, while x_{min}, y_{min} and z_{min} are their lower peaks. With such a procedure, the amplitudes can be directly numerically evaluated with increasing frequency for instance, to obtain the frequency-response curves. Some of the results have been evaluated this way with a MATLAB code and superimposed to the results, analytically obtained through the harmonic balance method, provided in Figs. 3 and 4.

3 Results and discussion

3.1 Fractional derivatives orders' effects on the harmonic oscillatory regime

Analyzing Fig. 2, one can notice the variation of the amplitudes with increasing ϵ and θ. Moreover, Fig. 2 illustrates a resonance structure whose number of peak and peak high are affected by both ϵ and θ. Specifically, the variation of the amplitudes with respect of ϵ considerably depends on the frequency ω. As a matter of fact, as we can notice in Fig. 2(c), in low-frequency regime ($\omega < 1$ for instance), the amplitude c decreases with increasing ϵ; whereas, the amplitude c increases with ϵ in the high-frequency regime. This remark can be drawn by comparing the green solid line and the blue dotted line of Fig. 2(c). A similar analysis can be made by observing Fig. 2(a), (b). It is clearly shown in Fig. 2(c) that c increases with θ. To further probe the evolution of the amplitudes with respect to ϵ and θ, let's evaluate both analytically and numerically the amplitudes as ϵ increases on the one hand, and as θ grows on the other hand. Some of the results obtained in the low-frequency regime ($\omega = 0.3$) are provided in

Fig. 3. Contrariwise to Figs. 2(b), 3(b) demonstrates that amplitude b varies with θ (see the insert in Fig. 3(b)), however this variation is slow. Figure 3(a) approves the observation that can be made on Fig. 2(b), according to which amplitude b increases with ϵ in the low-frequency regime. Figure 3(c) shows that the variation of amplitude c with respect to ϵ is not monotonic, however this variation confirms the observation made on Fig. 2(c) because, in the low-frequency regime, the value of amplitude c obtained with $\epsilon = 0.4$ is greater than that obtained with $\epsilon = 1$. Figure 3(d) shows that amplitude c monotonically increases with θ as suggested by Fig. 2(c). Note that in the low-frequency regime, amplitude a slowly increases with θ. Its variation with ϵ is similar to that of c. It was enough to provide in this report the variation of amplitudes with respect to ϵ and θ, in the high-frequency regime. The results provided in Fig. 3 have been obtained with sufficiently small excitation amplitude F_0. One can see in this figure that numerical results (represented by circles) have the same trend as analytical results (represented by solid lines). This agreement in term of trend and the gap between both analytical and numerical results may depend on the system parameters. Inspecting Fig. 4, we note that the amplitudes increase with the excitation amplitude as suggested through Fig. 3. Note that solid lines stand for analytical results while circles stand for numerical results. It is clear, analyzing Fig. 4, that the gap between both results drastically depends on the excitation amplitude F_0. The more F_0 increases, the more the gap augments. When F_0 increases further, the trends of both results do no longer agree. This is due to the fact that, the more F_0 increases, the more the system's output deviates from harmonics oscillations.

3.2 Fractional order properties and consequences on energy harvesting

We are interested in this section in studying the influence of the orders ϵ and θ of the fractional derivatives upon the harvested powers on the one hand and upon the efficiencies of both transduction mechanisms on the other hand. Following [35], we respectively define, for the present hybrid energy harvester, the electromagnetic and the piezoelectric output powers as follows:

$$\tilde{P}_1 = R\left(\frac{dq}{d\tau}\right)^2 \quad \text{and} \quad \tilde{P}_2 = \frac{v^2}{R_P}. \tag{25}$$

Define the corresponding dimensionless output powers

$$P_1 = \frac{LC}{RQ_0^2}\tilde{P}_1 = \dot{y}^2 \quad \text{and} \quad P_2 = \frac{R_P}{V_0^2}\tilde{P}_2 = z^2, \tag{26}$$

their maximum values (or magnitudes) P_{1max} and P_{2max} are evaluated as:

$$P_{1\,\max} = \frac{\omega}{\pi}\int_0^{\frac{2\pi}{\omega}} \dot{y}^2 dt \quad \text{and} \quad P_{2\,\max} = \frac{\omega}{\pi}\int_0^{\frac{2\pi}{\omega}} z^2 dt. \tag{27}$$

They are related to the amplitudes b and c of the electrical vibrations. It has been shown above that the fractional orders ϵ and θ affect the vibrations amplitudes in general. Specifically, the influence of ϵ on the amplitudes strongly depends on the excitation frequency. Consequently, output powers are affected by fractional orders as well and their variations may considerably be dictated by the value of the oscillation frequency ω. To ascertain these combined effects of the FDOs and excitation frequency, the output powers have been evaluated for several values of ϵ, θ and ω. The results, depicted in Fig. 5, illustrate the 3-dimensional variations of output powers versus ω and ϵ on the one hand, and versus ω and θ on the other hand.

As suggested by the dependence of the amplitudes on fractional derivatives orders, Fig. 5(a)–(d) demonstrate that the harvested powers also depend on ϵ and θ. By inspection of Fig. 5(a), (b), it is clear that the variation of the output powers with fractional derivative order (FDO) ϵ depends on the frequency regime. As a matter of fact, depending on the frequency band, output powers can increase or can decrease with ϵ. This is clearly illustrated in the inserts within Fig. 5(a) and (b). In these inserts are plotted and superimposed the output powers for two values of ϵ, namely $\epsilon = 0.1$ (black solid line) and $\epsilon = 1$ (blue solid line). We notice that the electromagnetic harvested power increases with ϵ in the low-frequency regime, that is to say $0 < \omega < 2$ for instance. Contrariwise, it decreases with ϵ in the high-frequency regime. As for the piezoelectric output power, it rather decreases with ϵ in the low-frequency regime, that is for $0 < \omega < 1$ for instance. Conversely, it increases with ϵ for greater values of ω.

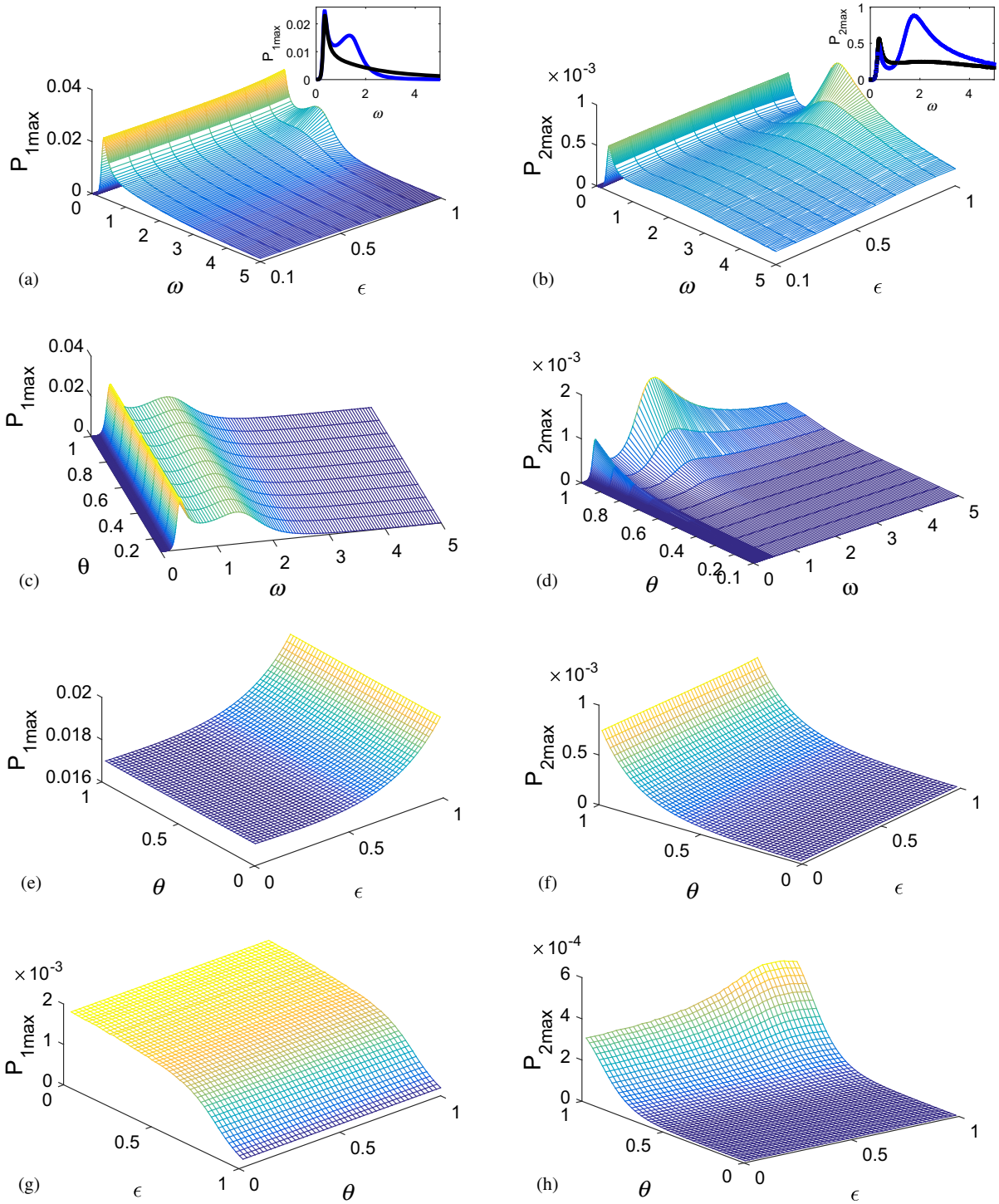

Fig. 5 Output powers versus excitation frequency and FDOs. For **a** and **b** $\theta = 0.9$, for **c** and **d** $\epsilon = 1$, for **e** and **f** $\omega = 0.3$ and for **g** and **h** $\omega = 4$. Other parameters are kept unchanged

Moreover, the output powers of the present harvester exhibit a resonant behavior as its counterpart without fractional properties. However, the number of resonant peaks and the peak height strongly depend on orders of fractional derivatives. In fact, for parameters used in this report, the piezoelectric output power exhibits two peaks. The first one is reached nearly at $\omega = 0.3$ and the second one at $\omega = 1.75$. As ϵ increases, the height of the first resonant peak slowly decreases while that of the second peak quickly increases (see Fig. 5(b) and insert therein). The electromagnetic output power progressively escapes the one-peak mode to join the two-peaks mode with increasing ϵ as observed in Fig. 5(a) and in insert therein. It is remarked observing Fig. 5(c) and (d) that the electromagnetic output power is less influenced by θ while the piezoelectric output power quickly increases with θ irrespective of the frequency band. Figure 5(e) and (f) have been obtained with $\omega = 0.3$. These figures clearly show that at very low frequency, the electromagnetic harvested power is more sensitive to ϵ than it is to θ. In fact, it monotonously increases with ϵ as remarked above. Conversely, the piezoelectric harvested power is more sensitive to θ than it is to ϵ. As expected, it monotonously increases with θ. As for Fig. 5(g) and (h), they were obtained with $\omega = 4$. Figure 5(g) confirms that P_{1max} rather decreases with ϵ for large values of the driving frequency. Figure 5(h) confirms that P_{2max} always increases with θ irrespective of ω.

It is worth noticing that, for very low frequencies, the electromagnetic harvested power is larger than the piezoelectric output power irrespective of the fractional orders. This can be verify by superimposing surfaces provided in Fig. 5(e) and (f). For greater frequencies, there is an area in (ϵ, θ) plane within which the piezoelectric output power is larger, and, another area where the electromagnetic harvested power is larger. This remark is ascertained by superimposing the results provided in Fig. 5(g) and (h).

Let's now define the efficiencies related to both transduction mechanisms with the purpose of comparing these transduction mechanisms on the one hand, and firmly characterizing the fractional derivatives orders' effects on the system efficacy on the other hand. To this end, define as in reference [35] the instantaneous input power

$$\tilde{P}_{in} = -m\Gamma(\tau)\frac{dX}{d\tau}, \tag{28}$$

that is the power of the inertial force acting on the moving mass, and letting

$$P_{in} = \frac{1}{ml^2\omega_e^3}\tilde{P}_{in} = \dot{x}f(t) \tag{29}$$

the corresponding dimensionless input power, the normalized efficiency ρ is defined by the relation $\rho = \frac{P_{out\max}}{P_{in\max}}$; where $P_{in\max}$ is the magnitude of the dimensionless input power from the driving vibrations and $P_{out\max}$ is the magnitude of the dimensionless power delivered to the electrical load. Note that $P_{out\max}$ represents either the electromagnetic output power magnitude $P_{1\max}$ or the piezoelectric output power magnitude $P_{2\max}$. Thence, we define two normalized efficiencies, which are related to both transduction mechanisms exhibited by the harvester. It follows that the normalized efficiencies for the electromagnetic and the piezoelectric transduction mechanisms are respectively expressed as:

$$\rho_1 = \frac{b^2\omega}{F_0 a} \quad \text{and} \quad \rho_2 = \frac{c^2}{F_0 a\omega}. \tag{30}$$

It is worth noticing that the variations of the normalized efficiencies with the system parameters have the same trends as the variations of the genuine efficiencies, which are expressed as follows:

$$\tilde{\rho}_1 = \frac{RQ_0^2}{ml^2\omega_e}\rho_1, \qquad \tilde{\rho}_2 = \frac{V_0^2}{R_P ml^2\omega_e^3}\rho_2. \tag{31}$$

The genuine efficiencies are analytically evaluated for several values of the fractional derivatives orders and for three different values of the frequency. Results are depicted in Fig. 6, that is the 3-Dimensional plot of efficiencies $\tilde{\rho}_1$ and $\tilde{\rho}_2$ (in percentage) with respect to ϵ and θ. In Fig. 6(a), the upper surface stands for $\tilde{\rho}_1$; the efficiency of the electromagnetic transduction mechanism, while the lower one represents $\tilde{\rho}_2$, the efficiency of the piezoelectric transduction mechanism. This result has been obtained for $\omega = 0.3$. Conversely, in Fig. 6(b) and (c) respectively obtained with $\omega = 4$ and $\omega = 10$, there exists an area of the $(\epsilon - \theta)$ plane within which $\tilde{\rho}_1$ is greater than $\tilde{\rho}_2$, and another area within which the opposite is observed. It therefore comes out from Fig. 6 that in the low-frequency regime, the electromagnetic mechanism is

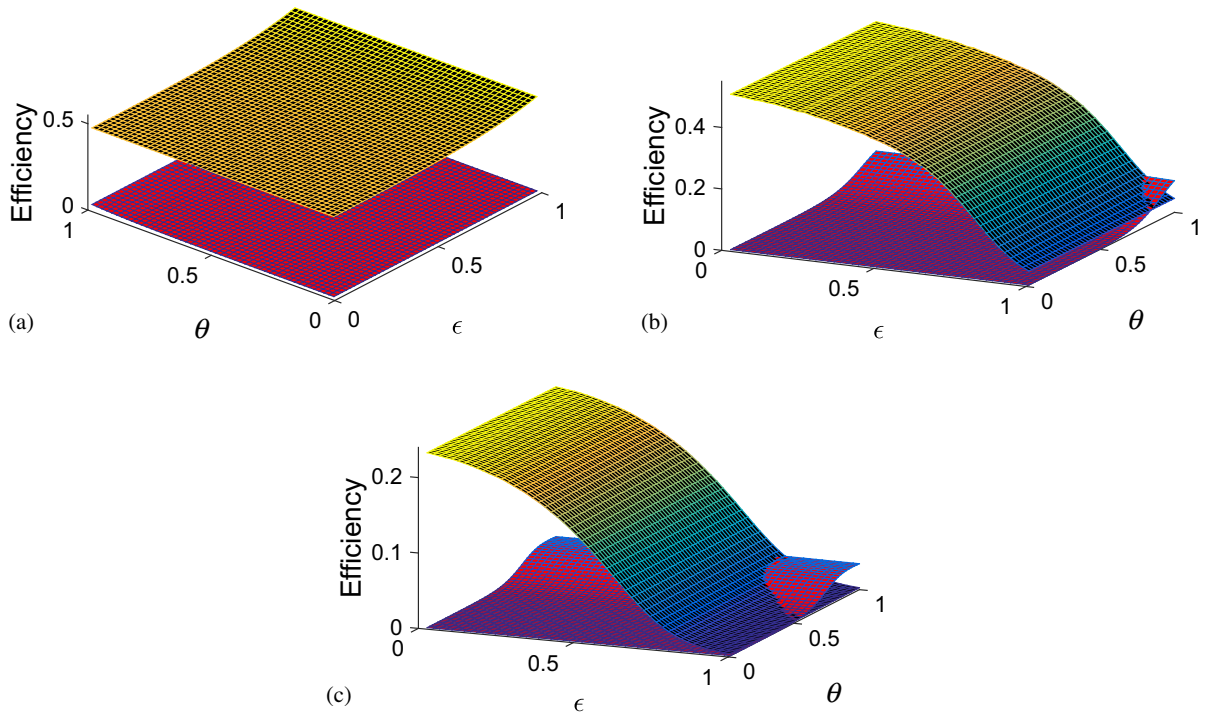

Fig. 6 Efficiency versus ϵ and θ. Parameters in Fig. 2 are kept unchanged unless otherwise specified, $F_0 = 0.02$, $\omega = 0.3$ for (**a**) $\omega = 4$ for (**b**) and $\omega = 10$ for (**c**)

more efficient that the piezoelectric one irrespective of ϵ and θ. Moreover, for low frequencies, ϵ can be augmented to especially improve the electromagnetic mechanism while θ can be increased to improve the piezoelectric one. Contrariwise, for greater frequencies, augmenting ϵ results in reducing the efficacy of the electromagnetic transduction mechanism. This can be also achieved to render the electromagnetic mechanism less efficient than the piezoelectric one. Moreover, an appropriate choice of ϵ and θ, in the high frequency regime, enables the present hybrid energy harvester to achieve mechanisms of similar efficacy.

Let us note in addition that, when the excitation strength F_0 increases, while remaining weak, the transduction mechanisms efficiencies monotonously increase irrespective of the fractional derivatives orders and irrespective of the driving frequency. As the transition to chaos, which is not always desirable, is expected with increasing F_0 on the one hand, and as increasing F_0 enables to improve the efficiencies on the other hand, it is necessary to investigate the effects of orders of fractional derivatives on the chaotic behavior of the system.

3.3 Fractional derivatives orders' effects onto chaotic response and energy harvesting perspectives

Unlike the non-fractional counterpart of system 9, simulating system 9 is very time consuming due to the memory effect as we did not make use of the short memory principle throughout all this report. This constraint rendered simulations very cumbersome, especially when the fractional derivatives orders are lower than 0.4. In addition, due to the above constraint assessing the maximum Lyapunov exponent [60], which is an indicator commonly used to predict emergence of chaotic response of a dynamical system, is very cumbersome on the one hand; and on the other hand, this number as legally defined has no direct meaning because the system dimension could be undetermined. Therefore, to investigate the response type of the present system, as the excitation strength and the fractional derivatives orders evolve, we can make use of other indicators for qualitatively characterizing the dynamical behavior like the power spectral density, the $0-1$ test, the poincar map, the basin of attraction and the bifurcation diagram. We

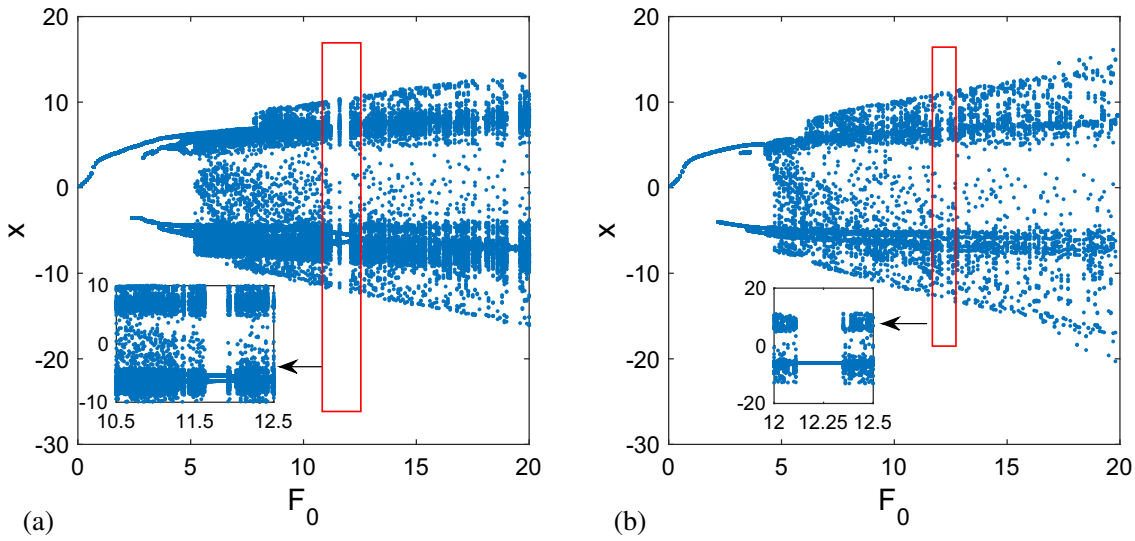

Fig. 7 Bifurcation diagrams versus the excitation strength for different couples (ϵ, θ). For **a** $\epsilon = 1.0$ and $\theta = 1.0$, for **b** $\epsilon = 0.90$ and $\theta = 0.80$, other parameters in Fig. 2 are kept unchanged and $\omega = 0.5$

made several computations by the mean of the fractional order Newton-Leipnik algorithm, however due to the conciseness constraint, we only provided bifurcation diagrams in the present paper. Unless otherwise specified, we used the initial conditions $(x_0, u_0, y_0, v_0, z_0, w_0) = (0, 0, 0, 0, 0, 0)$ throughout the simulations. The results are provided in Figs. 7 and 8.

It comes out from computations that the present system, like its non-fractional counterpart, exhibits a rich dynamical behavior that mainly depends on the amplitude and frequency of the excitation. Figure 7 illustrates a qualitative change in the system response as the excitation amplitude varies through the corresponding bifurcation diagram. As expected, periodic vibrations are exhibited for small values of F_0. These vibrations are almost harmonic when F_0 is sufficiently small. Other waveforms such as relaxation oscillations appear as F_0 increases. When F_0 increases further, a transition from periodic to non-periodic vibrations occurs. Figure 7(a) has been obtained with $\epsilon = 1$ and $\theta = 1$ by the mean of the fourth-order Runge Kutta algorithm. It is a bifurcation diagram of the non-fractional counterpart of system (9). One can see that when F_0 increases more, we observe in this figure another transition from non-periodic motion to periodic motion which is subsequently followed by another transition to non-periodic motion. Figure 7(b) has been obtained with $\epsilon = 0.90$ and $\theta = 0.80$. In this figure, similar transition from non-periodic vibrations to periodic ones, subsequently follows by another transition to non-periodic motion only occurs once. Comparing Fig. 7(a) and (b), we clearly remark that the region corresponding to periodic motion depends on the FDOs. As a matter of fact, regular motion appears within the region $F_0 \in [12.12; 12.34]$ on Fig. 7(b), while on Fig. 7(a), in the same region appear non-periodic vibrations which are found to be chaotic.

To further probe the effect of FDOs, we studied the qualitative evolution of the system response with increasing FDOs and, to this end, corresponding bifurcation diagrams are provided in Fig. 8(a) and (c). The results depicted in Fig. 8(a)–(d) are obtained with $F_0 = 12.25$. For such a value of the excitation amplitude, the non-fractional version of system (9) exhibits a chaotic vibration. However, as it is seen in Fig. 8(a), when the FDO θ varies with fixed ϵ ($\epsilon = 0.90$), this chaotic vibration can give birth to regular motion for peculiar values of θ. For instance, for $\theta = 0.97$ with $\epsilon = 0.90$ one obtains the time series depicted in Fig. 8(b) (blue solid line). The insert within this figure represents the corresponding state space diagram. This is a fractional order-induced periodic oscillation. Similarly, when ϵ varies for fixed θ ($\theta = 0.97$), as one can notice by analyzing Fig. 8(c), there are peculiar values of ϵ for which the behavior of the system's response switch from chaotic to regular. As expected, this phenomenon appears at $\epsilon = 0.90$.

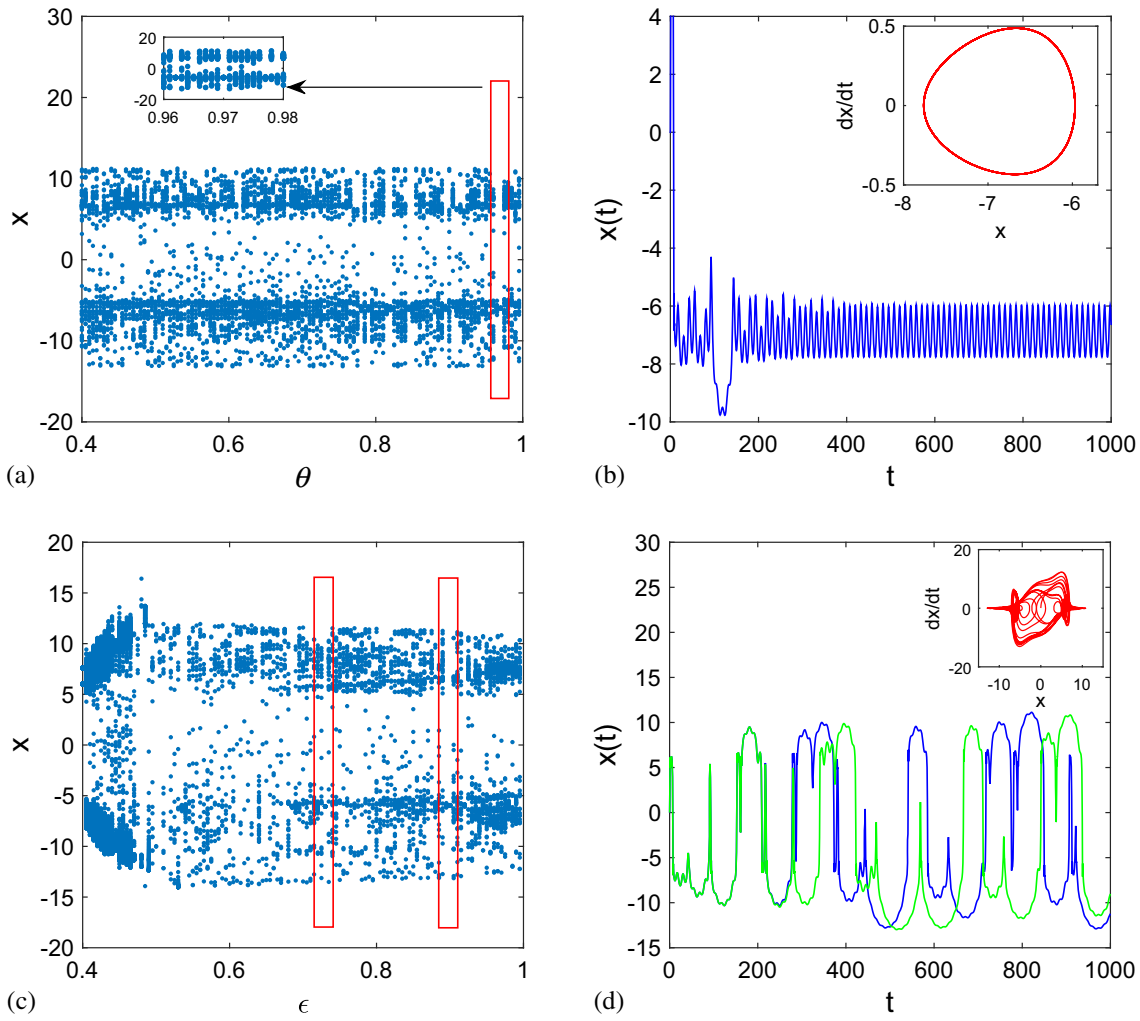

Fig. 8 Bifurcation diagrams versus the FDOs and time series illustrating regular and chaotic dynamics. (**a**) Bifurcation diagram versus θ with $\epsilon = 0.90$, (**b**) periodic oscillations for $\epsilon = 0.90$ and $\theta = 0.97$, (**c**) bifurcation diagram versus ϵ with $\theta = 0.97$ and (**d**) chaotic vibrations for $\epsilon = 0.90$ and $\theta = 0.964$. $\omega = 0.5$, $F_0 = 12.25$ and other parameters are those used in Fig. 2(color figure online)

Other periodic motions appear at $\epsilon = 0.685$, $\epsilon = 0.73$ and $\epsilon = 0.92$. These values of ϵ are not exhaustive. They rather give an overview of the tight domains of ϵ where regular motions are expected to occur. As a matter of fact, since the diagram of Fig. 8(c) has been obtained with the ϵ step of 0.005, by analyzing this figure, it follows that the domains of ϵ within which regular oscillations are expected to occur correspond to $\epsilon \in]0.680; 0.690[\cup]0.725; 0.735[\cup]0.895; 0.905[\cup]0.915; 0.925[$. In the domains complementary to the above ones, chaotic oscillations are expected to appear. For instance, for $\epsilon \in [0.905; 0.915]$, the harvester is expected to exhibit non-regular oscillations which are highly sensitive to initial conditions. These are chaotic motions which involve long displacements from the initial state (0, 0, 0, 0, 0, 0) due to the fact that the excitation amplitude is sufficiently large. In such regime of oscillation, the instantaneous output power can reach very large values, however it is not regular in waveform. In order to ascertain the preceding discussion, we computed various time series of system (9) for ϵ taken in the domain corresponding to chaotic vibrations. The result obtained with $\epsilon = 0.91$ (for θ fixed at 0.97) is provided

in Fig. 8(d). In this figure, the blue solid line starts with null initial conditions while the green solid curve initiates with $(x_0, u_0, y_0, v_0, z_0, w_0) = (10^{-8}, 0, 0, 0, 0, 0)$. Both curves are initially superimposable, however at the long run, they completely diverge from one another. This motion is therefore highly sensitive to the initial conditions, which is another signature of chaotic behavior. The insert within Fig. 8(d) is the state space diagram corresponding to the previous motion, obtained with null initial conditions. It is not worth mentioning that the results depicted in Fig. 8 have been obtained with the time step $h = 0.005$ (to solve system (9)), the ϵ step of 0.005 and θ step of 0.005; while the result provided in Fig. 7 is obtained with the time step $h = 0.01$ and the step of 0.1 for F_0.

3.4 Discussion

Sustainable power generation is the major interest of investigations in the field of energy harvesting systems as well as in this work. It may be achieved by converting ambient energy into electrical energy. Among possible sources of ambient energy [61], we are concerned in this work with the transformation of mechanical vibrations. Several techniques aiming at improving the work performance of vibration energy harvesters have been developed in the past two decades. Some important techniques are, for instance, preloading technique [62], bi-stability [63], hybridization [64], stochastic excitation [25, 26, 35]. Apart from the above-mentioned methods, recent advances in fractional calculus lately allowed some investigators [42, 56–58] to search the effects of fractional order components on the performance of vibration energy harvesters. The present paper, like the work reported in Ref. [57], focuses on this task by considering a fractional order inductor in the electrical part of the system. In other works [56, 58], the capacitor within the electrical part of the harvester is assumed to be of fractional order. The intent of these investigations is, of course, to search how the fractional properties can be beneficial in enhancing the harvester performance. In this paper, as it is commonly found in the works on fractional-order energy harvesting systems [42, 56–58], fractional order derivative may effectively enhance the performance of the harvester. However, this can be achieved only for peculiar operating conditions. For instance, in Ref. [58], the harvester efficiency is improved only for a large amplitude of perturbation by exploiting the hardening behavior of the system. In this work, the performance of the system is strongly affected by the excitation frequency. In low-frequency regime, increasing the FDO ϵ within $]0, 1[$ results in enhancing one of the output powers. However, such findings reveals that the standard inductor ($\epsilon = 1$) is more appropriate than an inductor exhibiting fractional properties. A similar result is highlighted by Foupouapouognigni et al. [57]. Contrariwise, unlike the findings commonly highlighted so far [57, 58], the output power related to the electromagnetic circuitry decreases with the FDO for an appropriate range of the excitation frequency. In this case, the fractional order inductor is better than a standard inductor, and diminishing the FDO rather improves the efficiency of the system. It has also been reported as in this paper, by calculating basins of attraction and bifurcation diagrams, that fractional order properties induce a broad spectrum of non-linear behavior connected with sensitivity to the initial conditions and chaos [45]. Energy harvesting systems have been extensively studied for the last two decades and several papers are devoted to them in the literature. Indeed, these papers report studies aiming at improving the performance of energy harvesters. However, as the harvesting performance can be improved in a variety of aspects, each of these studies has its own peculiarity. As a matter of fact, references [61, 65] are concerned with vibration energy harvesters making use of piezoelectric conversion mechanism while the present work deals with a hybrid harvester with two conversion mechanisms, which are electromagnetic and piezoelectric. The present work studies the role that fractional properties may play in enhancing the performance of a hybrid harvester, while reference [65] studies the response of a piezoelectric harvester with regard to non-smooth nonlinearities. Moreover, it pays attention on the role that can play non-smooth nonlinearities in obtaining a broadband harvesting capacity. Unlike this work, reference [61] presents a comprehensive review of recently developed piezoelectric energy harvesting techniques for converting mechanical energy into electricity.

4 Conclusion

Summarily, we mainly investigated in this work the effects of FDOs, on the performance of a hybrid vibration energy harvester with a non-smooth mechanical damping. To this end, the energy harvesting apparatus has been modeled by a deterministic non-smooth fractional differential system under harmonic excitation. By the mean of a modified harmonic balance method, we have obtained the stationary harmonic response of the system. We have then investigated the harvester performance by the mean of this response. In the harmonic oscillatory regime, we found that FDOs astonishingly affect the device efficiency in the sense that: an increase of the FDO θ results, irrespective of the frequency, in the increase of the output voltage of the piezoelectric circuitry, and consequently leading to the increase of the corresponding output power. In addition, the derivative order θ slightly affects the electromagnetic output power in a non-monotonic way. The influence of the FDO ϵ on the electromagnetic output power significantly depends on the frequency. Indeed, in low-frequency regime, the electromagnetic output power increases with ϵ. However, in high-frequency regime, the decrease of ϵ leads to large values of the output power for the electromagnetic circuitry and thence, improves the performance of the electromagnetic transduction mechanism. The variation of ϵ also slightly affects the piezoelectric harvested power in a non-monotonic way irrespective of the frequency. The efficiency of the electromagnetic transduction mechanism is more sensitive to ϵ while that of the piezoelectric transduction mechanism is more sensitive to θ. Monitoring the FDOs in high-frequency band is useful to render the piezoelectric transduction mechanism more efficient than the electromagnetic one or to get transduction mechanisms of similar performance.

Apart from harmonic oscillations which are delivered by the harvester when the excitation strength is sufficiently small, the system exhibits a richer dynamical behavior especially when the excitation amplitude is increased. In fact, we found through numerical simulations that the harvester may be excited to a degree so as to exhibit non-regular or chaotic behavior. These chaotic output voltages contain large value instantaneous voltages and may yield substantially greater root mean square output powers, but such chaotic or aperiodic voltages may hardly yield a useful electrical power because they are irregular in waveform. We also found that for large excitation strength, a proper choice of the FDOs can be used to draw the system to a regular behavior and thus to prevent the emergence of chaotic vibrations. In short, it comes out of this work that: fractional derivatives' orders (FDOs) astonishingly affect the device efficiency, monitoring FDOs enables to achieve conversion mechanisms of similar performance, chaotic behavior appears for large harmonic excitation amplitudes, and this chaotic behavior can be overcome by a proper choice of the FDOs.

Acknowledgements G.G. Sengha thanks the French Government for supporting his work in part through the Campus France's program for the promotion of the higher education and the international mobility.

Funding This study was funded by Campus France.

Declarations

Conflict of interest The authors declare that they have no conflict of interest.

Appendix

The coefficients of polynomials $H^{\pm}$ are given by:

$$\iota_{10} = \omega^4 {\gamma_2}^2 \beta_2^2 \left(\Delta_5^2 + \Delta_1^2\right),$$
$$\iota_8 = 8\omega^2 \gamma_2 \beta_2 \left(\Delta_5^2 \Delta_6 + \Delta_1^2 \Delta_6 + 4\Delta_1 \Delta_2\right),$$
$$\iota_6^{\pm} = 32\omega^2 \gamma_2 \beta_2 \left(\gamma_0 \omega^2 \beta_0 \left(\Delta_5^2 + \Delta_1^2\right) + \Delta_4^{\pm} \Delta_5 + \Delta_1 \Delta_3\right) + 16(\Delta_6 \Delta_1 + 4\Delta_2)^2 + 16\Delta_6^2 \Delta_5^2,$$
$$\iota_4^{\pm} = 128\omega^2 \beta_0 \gamma_0 \left(\Delta_6 \left(\Delta_5^2 + \Delta_1^2\right) + 4\Delta_1 \Delta_2\right) + 512\Delta_3 \Delta_2 + 128\Delta_6 \left(\Delta_1 \Delta_3 + \Delta_4^{\pm} \Delta_5\right),$$
$$\iota_2^{\pm} = 256\left(\left(\gamma_0 \omega^2 \beta_0 \Delta_1 + \Delta_3\right)^2 + \left(\Delta_4^{\pm} + \gamma_0 \omega^2 \beta_0 \Delta_5\right)^2\right),$$

where

$$\Delta_1 = \frac{1 - r_1\varsigma_2}{(1 - r_1\varsigma_2)^2 + (\mu_e\omega + r_1\varsigma_1)^2},$$

$$\Delta_2 = \frac{3}{4}\lambda_2 - \frac{1}{2}\frac{\lambda_1\gamma_2}{\gamma_1},$$

$$\Delta_3 = \omega_1^2 - \omega^2 + \frac{\delta\eta\omega^2(r_2\varrho_2 - \omega^2)}{(r_2\varrho_2 - \omega^2)^2 + (\mu_P\omega + r_2\varrho_1)^2},$$

$$\Delta_4^{\pm} = -\frac{\delta\eta\omega^2(\mu_P\omega + r_2\varrho_1)}{(r_2\varrho_2 - \omega^2)^2 + (\mu_P\omega + r_2\varrho_1)^2} + (v_1 \pm v_2)\omega,$$

$$\Delta_5 = -\frac{\mu_e\omega + r_1\varsigma_1}{(1 - r_1\varsigma_2)^2 + (\mu_e\omega + r_1\varsigma_1)^2},$$

and

$$\Delta_6 = \omega^2(\beta_2\gamma_0 + \gamma_2\beta_0).$$

References

1. Torah R, Glynne-Jones P, Tudor M, O'Donnell T, Roy S, Beeby S (2008) Self-powered autonomous wireless sensor node using vibration energy harvesting. Meas Sci Technol 19:125202
2. Sari I, Balkan T, Kulah H (2008) An electromagnetic micro power generator for wideband environmental vibrations. Sens Actuators A 145:405
3. Aktakka EE, Najafi K (2014) A micro inertial energy harvesting platform with self-supplied power management circuit for autonomous wireless sensor nodes. IEEE J Solid-State Circ 49:2017
4. Sano C, Mitsuya H, Ono S, Miwa K, Toshiyoshi H, Fujita H (2018) Triboelectric energy harvesting with surface-charge-fixed polymer based on ionic liquid. Sci Technol Adv Mater 19:317
5. Sakane Y, Suzuki Y, Kasagi N (2008) The development of a high-performance perfluorinated polymer electret and its application to micro power generation. J Micromech Microeng 18:104011
6. Suzuki Y (2011) Recent progress in MEMS electret generator for energy harvesting. IEEJ Trans Electr Electron Eng 6:101
7. Mitcheson PD, Miao P, Stark BH, Yeatman EM, Holmes AS, Green TC (2004) MEMS electrostatic micropower generator for low frequency operation. Sens Actuators A 115:523
8. Martens W, von Wagner U, Litak G (2013) Stationary response of nonlinear magnetopiezoelectric energy harvester systems under stochastic excitation. Eur Phys J 222:1665
9. Buckjohn CND, Martin MS, Fokou ISM, Tchawoua C, Kofane TC (2013) Investigating bifurcations and chaos in magnetopiezoelastic vibrating energy harvesters using Melnikov theory. Phys Scr 88:015006
10. Borowiec M, Litak G, Lenci S (2014) Noise effected energy harvesting in a beam with stopper. Int J Struct Stab Dyn 14:1440020
11. Williams CB, Yates RB (1996) Analysis of a micro-electric generator for microsystems. Sens Actuators A 52:8
12. Xu M, Jin X, Wang Y, Huang Z (2014) Stochastic averaging for nonlinear vibration energy harvesting system. Nonlinear Dyn 78:1451
13. Erturk A, Hoffmann J, Inman DJ (2009) A piezomagnetoelastic structure for broadband vibration energy harvesting. Appl Phys Lett 94:128
14. Li H, Qin W, Lan C, Deng W, Zhou Z (2016) Dynamics and coherence resonance of tri-stable energy harvesting system. Smart Mater Struct 25:015001
15. Harne RL, Wang KW (2013) A review of the recent research on vibration energy harvesting via bistable systems. Smart Mater Struct 22:23001
16. Xiao S, Jin Y (2017) Response analysis of the piezoelectric energy harvester under correlated white noise. Nonlinear Dyn 90:2069
17. Fokou ISM, Buckjohn CND, Siewe MS, Tchawoua C (2018) Probabilistic distribution and stochastic P-bifurcation of a hybrid energy harvester under colored noise. Commun Nonlinear Sci Numer Simul 56:177
18. Vocca H, Neri I, Travasso F, Gammaitoni L (2012) Kinetic energy harvesting with bistable oscillators. Appl Energy 97:771
19. Ramlan R, Brennan MJ, Mace BR, Kovacic I (2010) Potential benefits of a non-linear stiffness in an energy harvesting device. Nonlinear Dyn 59:545
20. Yang T, Liu J, Cao Q (2018) Response analysis of the archetypal smooth and discontinuous oscillator for vibration energy harvesting. Physica A 507:358
21. Zhou S, Cao J, Inman DJ, Ji Lin S, Wang Z (2014) Broadband tristable energy harvester: modeling and experiment verification. Appl Energy 133:33
22. Siewe MS, Kenfack WF, Kofane TC (2019) Probabilistic response of an electromagnetic transducer with nonlinear magnetic coupling under bounded noise excitation. Chaos Solitons Fractals 124:26
23. Daqaq MF (2012) On intentional introduction of stiffness nonlinearities for energy harvesting under white Gaussian excitations. Nonlinear Dyn 69:1063
24. Cottone F, Vocca H, Gammaitoni L (2009) Nonlinear energy harvesting. Phys Rev Lett 102:080601
25. Litak G, Friswell MI, Adhikari S (2010) Magnetopiezoelastic energy harvesting driven by random excitations. Appl Phys Lett 96:214103
26. Cottone F, Gammaitoni L, Vocca H, Ferrari M, Ferrari V (2012) Piezoelectric buckled beams for random vibration energy harvesting. Smart Mater Struct 21:035021
27. Wang X (2016) Frequency analysis of vibration energy harvesting systems. Academic Press, Cambridge
28. Beeby S, White N (2010) Energy harvesting for autonomous systems. Artech House, Norwood
29. Erturk A, Inman DJ (2011) Piezoelectric energy harvesting. Wiley, Chichester
30. Siewe MS, Buckjohn CND (2014) Heteroclinic motion and energy transfer in coupled oscillator with nonlinear magnetic coupling. Nonlinear Dyn 75:903

31. Stanton SC, Mann BP, Owens BA (2012) Melnikov theoretic methods for characterizing the dynamics of the bistable piezoelectric inertial generator in complex spectral environments. Physica D 241:711
32. Zheng R, Nakano K, Hu H, Su D, Cartmell MP (2014) An application of stochastic resonance for energy harvesting in a bistable vibrating system. J Sound Vib 333:2568
33. Li HT, Qin W, Deng W, Tian R (2016) Improving energy harvesting by stochastic resonance in a laminated bistable beam. Eur Phys J Plus 131:1
34. Nakano K, Cartmell MP, Hu H, Zheng R (2014) Feasibility of energy harvesting using stochastic resonance caused by axial periodic force. J Mech Eng 60:314
35. Sengha GG, Kenfack WF, Siewe MS, Tabi CB, Kofane TC (2020) Dynamics of a non-smooth type hybrid energy harvester with nonlinear magnetic coupling. Commun Nonlinear Sci Numer Simul 90:105364
36. Debnath L (2003) Recent applications of fractional calculus to science and engineering. Int J Math Sci 54:3413
37. Duarte F, Machado JAT (2002) Chaotic phenomena and fractional-order dynamics in the trajectory control of redundant manipulators. Nonlinear Dyn 29:315
38. Lenzi EK, Netoa RM, Tateishi AA, Lenzi MK, Ribeiro HV (2016) Fractional diffusion equations coupled by reaction terms. Physica A 458:9
39. Agrawal O (2004) Application of fractional derivatives in thermal analysis of disk brake. Nonlinear Dyn 38:191
40. Ngueuteu GM, Woafo P (2012) Dynamics and synchronization analysis of coupled fractional-order nonlinear electromechanical systems. Mech Res Commun 46:20
41. Prodanov D, Delbeke J (2016) A model of space-fractional-order diffusion in the glial scar. J Theor Biol 403:97–109
42. Cao J, Zhou S, Inman DJ, Chen Y (2015) Chaos in the fractionally damped broadband piezoelectric energy generator. Nonlinear Dyn 80:1705
43. Machado JAT, Silva MF, Barbosa RS, Jesus IS, Reis CM, Marcos MG, Galhano AF (2010) Some applications of fractional calculus in engineering. Math Probl Eng 639801:1
44. Silva MF, Machado JAT (2006) Fractional order PD^{α} joint control of legged robots. J Vib Control 12:1483
45. Syta A, Litak G, Lenci S, Scheffler M (2014) Chaotic vibrations of the duffing system with fractional damping. Chaos 24:013107
46. Atangana A, Baleanu D (2016) New fractional derivatives with nonlocal and non-singular kernel: theory and application to heat transfer model. Therm Sci 20:763
47. Cveticanin L, Zukovic M (2009) Melnikov's criteria and chaos in systems with fractional order deflection. J Sound Vib 326:768
48. Miller KS, Ross B (1993) An introduction to the fractional calculus and fractional differential equations. Wiley, New York
49. Atangana A, Alkahtani BST (2013) Extension of the resistance, inductance, capacitance electrical circuit to fractional derivative without singular kernel. Adv Mech Eng 7:16
50. Oldham KB, Spanier J (1974) The fractional calculus. Academic Press, New-York
51. Aguilar JFG, Martnez HY, Ramn CC, Ordua IC, Jimnez RFE, Peregrino VHO (2015) Modeling of a mass-spring-damper system by fractional derivatives with and without a singular kernel. Entropy 17:6289
52. Ross B (1975) Fractional calculus and applications, vol 457. Lecture notes in mathematics, chapter a brief history and exposition of the fundamental theory of the fractional calculus. Springer, New-York
53. Herrmann R (2013) Fractional calculus: an introduction for physicists. GigaHedron, Germany
54. Petras I (2010) Fractional-order nonlinear systems: modelling, analysis and simulation. Springer, New York
55. Zhang B, Ducharne B, Guyomar D (2013) Inverse model of the piezoelectric ceramic polarization under wide bandwidth mechanical excitations with fractional derivative consideration. Opt Quant Electron 46:103110
56. Fokou ISM, Buckjohn CND, Siewe MS, Tchawoua C (2017) Nonlinear analysis and analog simulation of a piezoelectric buckled beam with fractional derivative. Eur Phys J Plus 132:1
57. Foupouapouognigni O, Buckjohn CND, Siewe MS, Tchawoua C (2017) Nonlinear electromechanical energy harvesters with fractional inductance. Chaos Solitons Fractals 103:12
58. Kwuimy CAK, Litak G, Nataraj C (2015) Nonlinear analysis of energy harvesting systems with fractional order physical properties. Nonlinear Dyn 80:491
59. Lefeuvre E, Badel A, Richard C, Petit L, Guyomar D (2006) A comparison between several vibration-powered piezoelectric generators for standalone systems. Sens Actuators A 126:405
60. Wolf A (1986) Quantifying chaos with lyapunouv exponent. Princeton University Press, Princeton
61. Yang Z, Zhou S, Zu J, Inman D (2018) High-performance piezoelectric energy harvesters and their applications. Joule 2:642
62. Leland ES, Wright PK (2006) Resonance tuning of piezoelectric vibration energy scavenging generators using compressive axial preload. Smart Mater Struct 15:1413
63. He Q, Daqaq MF (2015) New insights into utilizing bistability for energy harvesting under white noise. J Vib Acoust 137:021009
64. Challa VR, Prasad MG, Fisher FT (2009) A coupled piezoelectric- electromagnetic energy harvesting technique for achieving increased power output through damping matching. Smart Mater Struct 18:095029
65. Ai R, Monteiro LLS, Monteiro PCC, Pacheco PMCL, Savi MA (2019) Piezoelectric vibration-based energy harvesting enhancement exploiting nonsmoothness. Actuators 8:1